Lehrstuhl für Bauinformatik
Fakultät für Bauingenieur- und Vermessungswesen
Technische Universität München

Modeling Localization and Failure with High-Order Finite Elements

Holger Heidkamp

Vollständiger Abdruck der von der Fakultät für Bauingenieur- und Vermessungswesen der Technischen Universität München zur Erlangung des akademischen Grades eines

Doktor-Ingenieurs

genehmigten Dissertation.

Vorsitzender:	Univ.-Prof. Dr.-Ing. Kai-Uwe Bletzinger
Prüfer der Dissertation:	
	1. Univ.-Prof. Dr.rer.nat. Ernst Rank
	2. Univ.-Prof. Dr.-Ing. Karl Schweizerhof, Universität Fridericiana zu Karlsruhe

Die Dissertation wurde am 11.01.2007 bei der Technischen Universität München eingereicht und durch die Fakultät für Bauingenieur- und Vermessungswesen am 11.04.2007 angenommen.

Für Susi.

Abstract

This thesis presents a consistent modeling approach to the phenomenon of deformation localization and material failure, based on high-order finite elements. With particular focus on large scale analyses, it adopts a macroscopic perception of the failure process. Viewing the typically small failure zones from the level of practical interest, continuous fields with a steep gradient appear discontinuous; this constitutes the notion of *strong discontinuities*, i.e., jumps in the displacement field. Accounting for the possible occurrence of strong discontinuities, the pathological mesh sensitivity exhibited by classical continuum softening approaches is overcome. Discontinuities are incorporated into the finite element formulation in an *embedded* manner, avoiding the need of additional global degrees of freedom and thus, giving rise to an efficient discretization and numerical treatment of the problem. As opposed to previous concepts, the presented approach is consistently deduced regarding its possible application in the context of *high-order finite elements*. Put forth by a novel reassessment of the strong discontinuity kinematics, the extended p-adaptive formulation is established. Three dimensional numerical investigations show, that — in contrast to commonly adopted low-order finite element approximations — the proposed p-adaptive high-order approach facilitates a minimization of potential *locking* effects while at the same time the algorithmic implementation efficiently preserves a high degree of locality.

Zusammenfassung

Die vorliegende Arbeit präsentiert einen konsistenten Modellierungsansatz zu den Problemkreisen Verformungslokalisierung und Materialversagen, der auf finiten Elementen hoher Ordnung basiert. Mit besonderem Augenmerk auf Großberechnungen nimmt sie eine makroskopische Sichtweise auf das Problem ein. Von der Ebene der Ingenieuranwendung aus betrachtet, erscheinen stetige Felder in den typischerweise kleinen Versagenszonen unstetig. Dieser Zusammenhang motiviert die Einführung *starker Diskontinuitäten*, d.h. eines sprungstetigen Verschiebungsfeldes. Diese Maßnahme überwindet die pathologische Netzabhängigkeit des klassischen kontinuumsmechanischen Ansatzes zur Simulation von Materialentfestigung. Die finite Element Formulierung bindet die Verschiebungsdiskontinuitäten im Rahmen eines *eingebetteten* Ansatzes ein, wodurch zusätzliche Freiheitsgrade auf globaler Ebene vermieden werden; eine effiziente Diskretisierung und numerische Behandlung des Problems wird ermöglicht. Abweichend von bislang etablierten Verfahren, ist der präsentierte Ansatz konsistent hinsichtlich der Anwendung im Kontext *finiter Elemente hoher Ordnung* abgeleitet. Ausgehend von einer neuartigen Interpretation der Kinematik sprungstetiger Verschiebungsfelder entwickelt sich die erweiterte p-adaptive Formulierung. Dreidimensionale numerische Untersuchungen zeigen, dass der vorgeschlagene p-adaptive Ansatz hoher Ordnung — im Gegensatz zu üblicherweise angewendeten Ansätzen im Rahmen finiter Elemente niedriger Ordnung — eine Minimierung potenzieller *Locking*-Effekte erreicht, *ohne* dass die algorithmische Umsetzung ihren weitestgehend lokalen Charakter verliert.

Vorwort

Die vorliegende Arbeit entstand im Rahmen meiner Forschungstätigkeit am Lehrstuhl für Bauinformatik der Fakultät Bauingenieur- und Vermessungswesen der Technischen Universität München im Zeitraum zwischen Februar 2003 und Dezember 2006.

Aufrichtiger Dank gilt meinem geschätzten Doktorvater, Herrn Professor Dr.rer.nat. Ernst Rank. Seine Aufgeschlossenheit hat dieses berufsbegleitende Forschungsprojekt erst ermöglicht. Durch den gewährten Freiraum und das entgegengebrachte Vertrauen bei der Ausgestaltung des Themas hat er mich nachhaltig motiviert; seine bewundernswerte Fähigkeit, zielsicher Unschärfen der Argumentation zu entlarven, war grundlegend für den Erfolg der Arbeit.

Herrn Professor Dr.-Ing. Karl Schweizerhof danke ich ganz herzlich für die Übernahme des Koreferates. Sein aufrichtiges Interesse an meiner Arbeit und die aufmerksame Kritik waren ein sehr wertvolles Feedback.

Großen Anteil an der Realisierung des Forschungsvorhabens hatte die Sofistik AG als mein Arbeitgeber. Für ihre Unterstützung danke ich den Vorständen Thomas Fink und Dr.-Ing. Casimir Katz sowie den übrigen Sofistik-Kollegen; Dr.-Ing. Casimir Katz besonders auch für die ideelle Förderung des Projektes von der ersten Stunde an.

Herr PD Dr.-Ing. Alexander Düster war gewissermaßen der Pyrotechniker hinsichtlich meines Interesses für die Finite Elemente p-Version. Für den Initialfunken und für die vielen Anregungen und Diskussionen, durch die er mich in diesem Projekt begleitet hat, danke ich ihm sehr.

Für die beinahe familiäre Atmosphäre und das freundschaftliche Miteinander am Lehrstuhl, dass auch mir als Externem zuteil wurde, bedanke ich mich bei allen Kollegen und nicht zuletzt bei der *guten Seele* des Lehrstuhls, Frau Hanne Cornils.

Eltern, Familie und Freunde waren mir eine enorme Stütze und wichtige Energiequelle, gerade in stark beanspruchenden Zeiten.

Ganz besonders bedanken möchte ich mich bei meiner Frau Susi. Durch ihre uneingeschränkte Zuversicht war sie der entscheidende Rückhalt für mich — danke für diese großartige Liebe und Geduld.

Holger Heidkamp
Juni 2007

Contents

Chapter 1

Introduction

If you have an apple and I have an apple and we exchange these apples then you and I will still each have one apple. But if you have an idea and I have an idea and we exchange these ideas, then each of us will have two ideas.
– George Bernard Shaw.

The present introductory chapter is split into three main parts. The first Section 1.1 aims at motivating the problematic nature of modeling localization and failure processes, by means of discussion of a simple model problem. This is then followed by a short review about efforts made in the field of modeling of deformation localization in Section 1.2. Both sections together provide the basis for the objective and the scope of this work, which are outlined in the final Section 1.3 of this chapter.

1.1 Motivation

In order to approach the basic distinctive features associated with the simulation of material softening behavior, subsequently a basic virtual experiment is presented. The experiment also motivates the fundamental notion of *strong discontinuities*.

As a simple but representative model problem, we consider a bar loaded in uniaxial tension. We assume, that the material behaves linear elastic up to a certain threshold f_t *(capacity)*, which is reached at strain ε_0. Once loaded beyond this threshold, the material is assumed to follow a linear softening law in stress-strain space, such that its capacity vanishes completely at strain $\varepsilon > \varepsilon_u$ (Figure 1.1). The bar be of length L and cross-sectional area A. One bar end be clamped, while the opposite end be loaded by a prescribed displacement u.

As a starting point, we assume the bar to be perfectly uniform both regarding material properties and geometry. Then, during loading, every section along the bar will reach its capacity

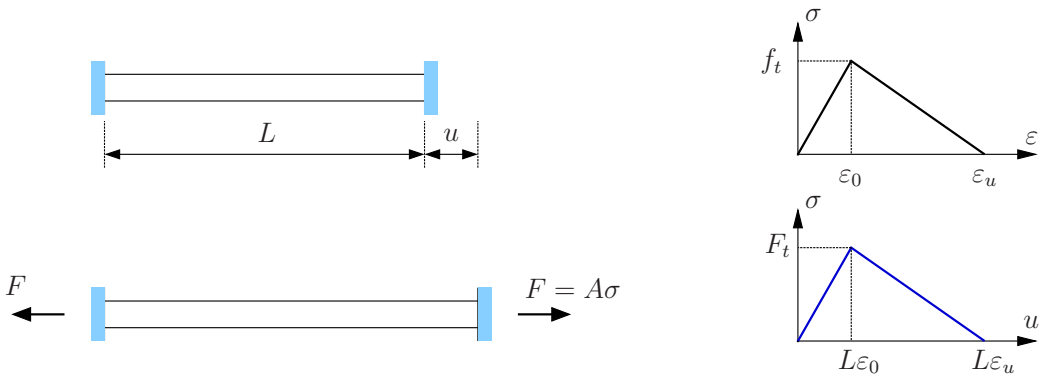

Figure 1.1: Model problem: perfectly uniform bar subjected to uniaxial tension.

at the same instant — namely when the prescribed displacement loading has reached the value of $u = L\varepsilon_0$, corresponding to the force $F_t = A \cdot f_t$. Consequently, if loaded further, all sections along the bar will undergo simultaneous softening until zero capacity is reached at a loading state of $u = L\varepsilon_u$ (Figure 1.1).

Obviously, the setting of a perfectly uniform bar is not very realistic — in practice there are variations in capacity and/or geometry. In our thought experiment, we account for this by introducing an imperfection zone of extension $\frac{L}{n}$ located at mid-bar. The imperfection be such, that the capacity of the adjacencies is slightly higher. Accordingly, at a loading state of $u = L\varepsilon_0$, only sections in the imperfection zone will have reached their capacity, the remaining sections are still in a linear elastic state. As a consequence, during further loading, only sections within the imperfection zone will experience softening and thus follow the softening branch in the stress-strain relation. The remaining sections will unload elastically to satisfy equilibrium. Hence, at the instance when the bar's load carrying capacity has decreased to zero, the corresponding elongation of the bar amounts to $u = \frac{L}{n}\varepsilon_u$. Notably, this elongation depends via n on the size of the softening zone, so we obtain different softening responses for different values of n. Remarkably, in the limit $n \to \infty$, i.e., for an infinitesimal softening zone, the "softening" path degenerates to the elastic unloading path (Figure 1.2).

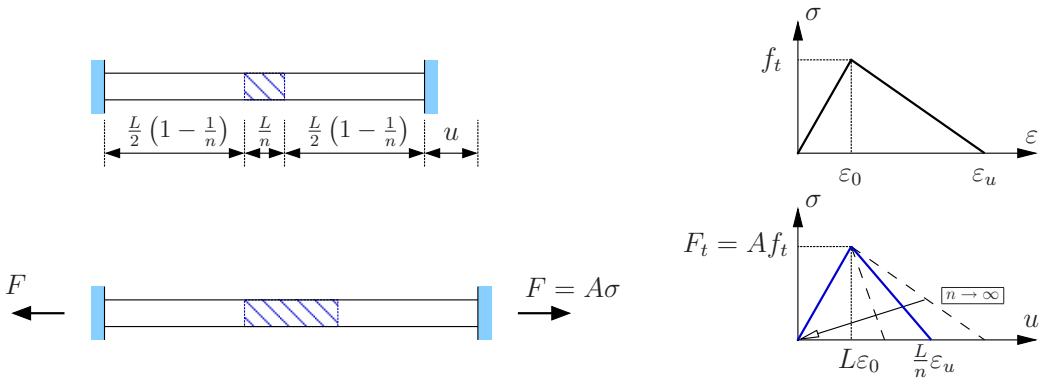

Figure 1.2: Model problem: bar with imperfection zone subjected to uniaxial tension.

To summarize, several pathological features of the classical strain-softening continuum mechanical approach to this problem can be stated (Jirásek [54]):

(i) In the limit, the softening zone is infinitesimal.

(ii) As motivated above, in the limit case, the simulated softening response approaches the elastic unloading path, thus featuring a *snap-back* in the obtained load-displacement response. This behavior is always obtained, irrespective of structural size and material ductility.

(iii) Degeneration of "softening" path to the elastic unloading path implies *zero dissipated energy* during the failure process.

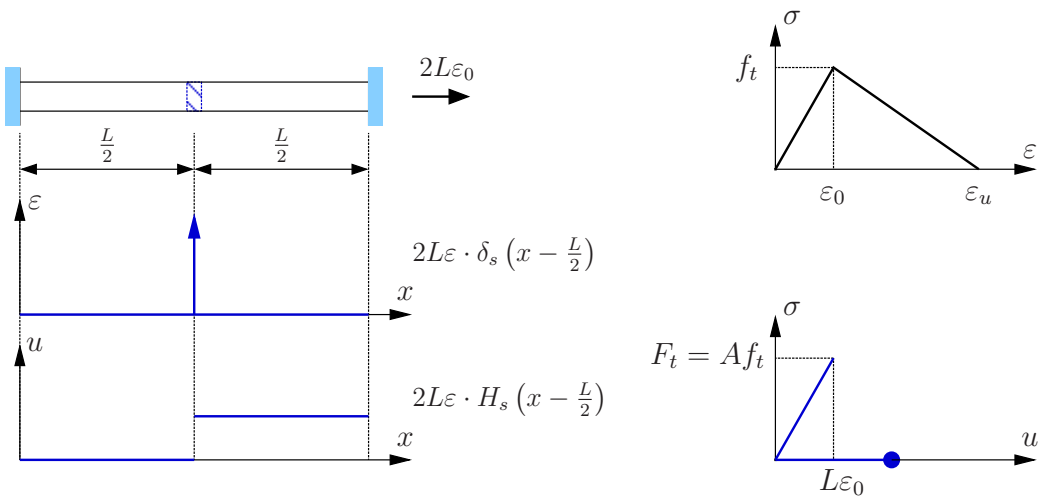

Figure 1.3: Model problem: strain and displacement distribution for the strain-softening continuum solution.

From the mathematical point of view, these features are related to the *loss of ellipticity* of the governing differential equation, effecting the boundary value problem to become ill-posed — with the consequence that is does not have a unique solution, anymore. From the numerical point of view, ill-posedness is evidenced by a pathological mesh sensitivity of the results. If we, for example, consider the previous example to be discretized uniformly by N linear finite elements, then the softening response induced by the imperfection at mid-bar is represented by one finite element of length $\frac{L}{n}$. Completely analogous to the foregoing discussion, the slope of the softening branch depends strongly on the number of elements and degenerates to the elastic unloading path as the number of elements tends to infinity, i.e., $n \to \infty$. In conclusion, the deficiency of the classical strain-softening continuum mechanical approach is manifested by an inherent loss of objectivity.

However, the example not only illustrates the insufficiency of the classical approach, it also motivates an alternative notion of the problem. To see this, let us consider the situation of the bar being loaded by a displacement of, say $2L\varepsilon_0$. Then, in the limit case for $n \to \infty$,

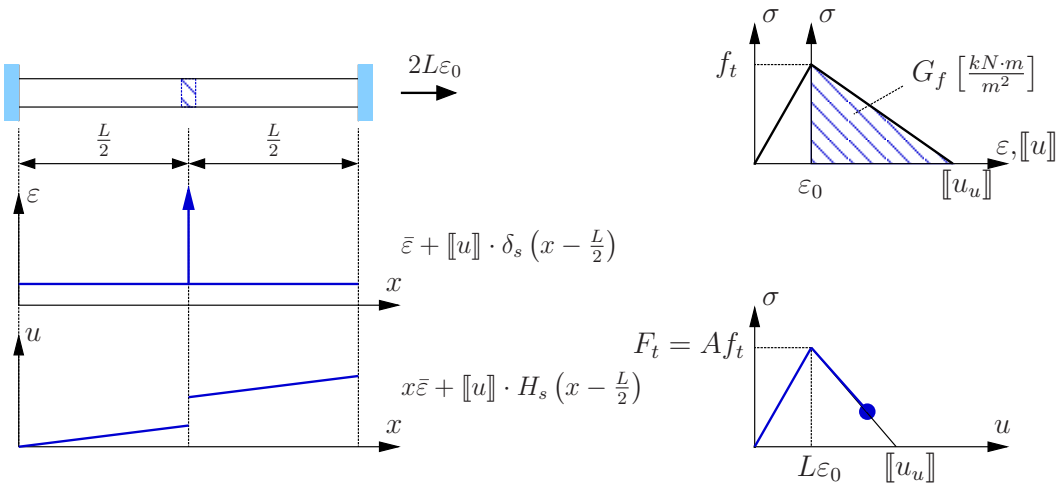

Figure 1.4: Model problem: notion of *strong discontinuity* associated with objective traction-separation softening law, replacing the problematic stress-strain relation.

the strain distribution along the bar is characterized by $2L\varepsilon_0 \cdot \delta_s \left(x - \frac{L}{2}\right)$ and the corresponding displacement distribution reads $2L\varepsilon_0 \cdot H_s \left(x - \frac{L}{2}\right)$ — thus exhibiting a discontinuity at mid-bar of magnitude $2L\varepsilon_0$ (Figure 1.3). This observation suggests that material induced localizing behavior — provided that a proper association to a softening law is achieved — can be represented by *strong discontinuities*, i.e., jumps in the displacement field.

For the considered case of mode I failure, there is experimental evidence that the dissipated energy during the failure process (*fracture energy*), often denoted by G_f, is an objective material parameter. As a consequence, the softening behavior can be described in an objective manner by a traction-separation law rather than a stress-strain relation. Thus, introducing the notion of a *strong discontinuity* into our model and linking it to the traction-separation law type description of material softening, renders an objective approach to characterize the structure's softening behavior (Figure 1.4).

1.2 Modeling deformation localization — a review

Prevention of failure of structures and structural components has always been a major concern in engineering. Among the many possible causes for structural failure, material induced failure is not only a very significant one, its computational treatment also represents one of the most interesting and challenging fields in engineering science. In the following, some key achievements during evolution of research on this topic shall be reflected, which — due to the diversity of literature — can only be done in a highlighting manner. A comprehensive review can, e.g., be found in de Borst [28], Mosler [75] or Jirásek [52].

Closer investigation of fracture of materials reveals, that failure is often preceeded by the formation of a process zone in which damage and other inelastic effects accumulate, and in

which high strain gradients prevail. This phenomenon is commonly termed *strain localization* or *deformation localization*. Such processes can be associated with a wide range of materials (see, e.g., NÁDAI [83]) — some examples are shear banding in soils, shearing of rock faults, necking of metals, crazes in polymers and the accumulation and coalescence of microcracks in concrete and rocks under low confining pressures. It is evident, that these phenomena are *no longer* covered by the scope of classical continuum mechanics, as it is, for example, defined in TRUESDELL & NOLL [124].

The probably first scientific contribution to localization phenomena is HADAMARD's [47] characterization of conditions for the occurence of stationary waves in continua and dates back to 1903. Later, theoretical considerations regarding strain localization and material instability phenomena were published by HILL [48], THOMAS [123], MANDEL [68], RUDNICKI & RICE [104] and RICE & RUDNICKI [101].

In the mid-1980's, attempts to numerically simulate localization phenomena on the basis of standard continuum mechanics that employed a local stress-strain softening relation, were carried out. They failed in the sense that the solution proved to be determined to a strong degree by the discretization of the problem, see, e.g., DE BORST [26]. The deficiency of the classical continuum approach to capture zones of localized straining correctly, can be attributed to the fact that the employed softening stress-strain relations are substantially the result of a mapping of force-displacement relations, obtained from testing devices, on basis of the original load-carrying area and original length. This process does not account for changes in the microstructure and, as a consequence, the mathematical model ceases to be a meaningful representation of physical reality.

Early approaches to resolve this lack of objectivity of the classical continuum mechanical approach are based on the experimentally validated notion of the *fracture energy* as an objective material parameter. To this end, PIETRUSZCZAK & MROŹ [94] as well as OLIVER [86] enhance the classical plasticity formulation by introducing the softening modulus as a fracture energy dependent model parameter, which implies a direct dependency of the softening modulus on the finite element geometry. HILLERBORG, MODEER & PETERSSON [49] propose a fracture energy preserving approach for brittle materials, where the geometry enters the formulation implicitly by establishing the softening response as a function of the crack opening.

Alternative attempts aim at the direct extension of the classical continuum mechanical model. Several approaches can be distinguished, but they all have in common the introduction of an internal length scale that is associated to the extension of the localized zone. *Nonlocal* models (PIJAUDIER-CABOT & BAŽANT [95]; BAŽANT & PIJAUDIER-CABOT [9]) are characterized by the fact, that the principle of *locality* — postulating that a material point's response only depends on the loading state at this point — is abandoned. *Gradient enhanced* theories (DE BORST & MÜHLHAUS [29]; MÜHLHAUS & AIFANTIS [81]) can be derived from a TAYLOR-expansion of the nonlocal models. The COSSERAT-*continuum* approach (COSSERAT & COSSERAT [21]; DE BORST [27]; STEINMANN & WILLAM [120]; EHLERS & VOLK [40]), finally, is based on the introduction of additional rotational degrees of freedom to describe the kinematics of the considered material point. VOLK [125], for example, successfully used the COSSERAT-theory as a regularizing means in the context of simulation of porous media.

All three approaches understand localization as a steady process — resulting in a continuous deformation gradient field with a distinct local maximum at the localization zone. The numerical resolution of such a gradient field, therefore, requires a corresponding fine discretization — which increases the numerical effort considerably.

A completely different notion is constituted by a macroscopic view of the deformation localization problem. With this perception, localization of deformation can be interpreted as C^0-discontinuity of the displacement field, with the corresponding gradient being DIRAC distributed. This idea goes back to JOHNSON [61], who established discontinuous displacement fields as admissible solutions to the differential equations of a perfectly-plastic pin-jointed bar. In this context, the paper of MATTHIES et al. [69] represents another important work. The adoption of C^0-discontinuous displacement fields within the framework of the finite element method was first accomplished by JOHNSON & SCOTT [62] to model the response of a perfectly-plastic pin-jointed bar. Various proposals to incorporate discontinuous approaches directly into the finite element formulation in terms of *embedded discontinuities* can be observed in the following decade. Aiming at an improved resolution of shear bands, ORTIZ et al. [92] suggested an enrichment of the strain field for quadrilateral elements, such that one *weak discontinuity* [1] line per element can be captured. BELYTSCHKO et al. [10] advanced the idea and presented an element formulation that allowed for two weak discontinuity lines in one element, the formulation thus being capable of representing the whole localization band within one finite element. Direct incorporation of a *strong discontinuity* into a two-dimensional finite element formulation was subsequently accomplished by DVORKIN, CUITIÑO & GIOIA [39] as well as KLISINSKI et al. [65]. So far, all embedded discontinuity formulations alluded to were derived purely from physical considerations — due to their simplicity no variational principle was needed. Significant progress was finally achieved by the formulation of the *strong discontinuity approach* in the fundamental work of SIMO et al. [116]. Therein, the authors analyze local material models in the softening regime under the assumption of C^0-discontinuous displacement fields. A vital issue is the interpretation of the softening moduli as singular distributions, which allows for treatment of the displacement discontinuity within the framework of classical perfect plasticity. Based on the concept of *enhanced assumed strains* established by SIMO & RIFAI [117] and SIMO & ARMERO [112], SIMO & OLIVER [115] and OLIVER [87] then provided a sound variational basis for the method and also proposed a corresponding two-dimensional finite element formulation based on constant strain elements. A key feature of this method, is constituted by the fact that the additional degrees of freedom associated with the discontinuous displacement modes are eliminated on element level by static condensation — therefore, the system of global degrees of freedom remains unchanged. ARMERO & GARIKIPATI [4] subsequently modified the formulation in the sense that the stress-strain relation describing the inelastic softening response of the material is replaced by a traction-displacement relation.

Succeedingly, numerous concepts for application of the strong discontinuity approach to the description of material softening in the scope of damage models (e.g.,GARIKIPATI [43], ARMERO

[1] A *weak* discontinuity is characterized by the fact that certain components of the strain field exhibit a jump across the discontinuity. As a consequence, the corresponding displacement field is still rendered C^0-continuous. In case of a *strong* discontinuity, on the contrary, the discontinuity directly refers to components of the displacement field itself, the resulting displacement field is no longer C^0-continuous.

[2]), elasto-plastic models (e.g., Borja & Regueiro [17], Regueiro & Borja [100]) or coupled models (e.g., Mosler & Meschke [79]) were developed. All these concepts have in common that the discontinuous constitutive model was obtained by a suitable "projection" of the continuum model onto the localization surface, which transforms the stress-strain based continuum law into a traction-displacement based constitutive relation. An alternative way was advocated by Armero [3], who established the energy density function as composed of a continuous portion and a dissipative, singular distributed portion — the latter being associated with the displacement discontinuity. Based on the principle of maximum dissipation, Armero then derived the constitutive evolution equations directly in terms of the displacement discontinuity. The same concept was later adopted by Mosler [76].

As alluded to above, the original implementation of the strong discontinuity approach in a two-dimensional setting was established for constant strain elements — allowing one discontinuous mode per element and, thus, facilitating a straightforward elimination of the additional degrees of freedom associated with the discontinuous displacement modes on element level by static condensation. This concept was later modified by introducing a Gauss-point local notion of the displacement discontinuity, furnishing a numerical implementation that is in complete formal analogy to the algorithmic framework of classical C^0-continuous continuum models. The particular advantage of this setting is the elimination of the need for a static condensation procedure on element level (Mosler & Meschke [77], Borja [16]). Based on this approach, Mosler & Meschke [77] then extended the two-dimensional scheme to a general three-dimensional finite element implementation. A three-dimensional discontinuity formulation for the simulation of brittle fracture, using tetrahedral elements with linear shape functions, was also presented by Wells & Sluys [130].

More Recent publications within the strong discontinuity modeling framework are devoted to finite element implementations that aim at the reduction of *locking* effects; for instance, in the field of simulation of cracking of brittle materials, where Jirásek & Zimmermann [60] employed a nonlocal damage model to estimate the crack topology and combine it with a C^0-discontinuous displacement field. As an alternative concept Mosler & Meschke [80] advocated the adoption of a *rotating discontinuity* approach.

A further class of strategies, devoted to alleviating spurious locking and *mesh bias* effects, is based on the enforcement of a geometrically continuous discontinuity path. These strategies, commonly termed *tracking strategies*, are beyond the scope of the strong discontinuity approach itself and they essentially rely on *nonlocal* information. Successful combinations of tracking strategy and strong discontinuity approach are presented, e.g., by Oliver et. al. [91] and Feist [41] in the context of low-order finite element approximations.

The overall rather expensive character of discontinuity tracking strategies, has triggered recent research efforts towards formulations that aim at a realistic identification of the discontinuity path, based on predominantly *local* information, i.e., information available at element and material point level, respectively, see, e.g., Oliver et al. [90], Sancho et al. [107, 106, 108].

A further trend in development of solution techniques to simulate localization was constituted by the idea to treat the newly introduced discontinuity variables as additional global

unknowns (Bolzon & Corigliano [14]). New developments in this direction are closely related to the *partition-of-unity* concept (Babuška & Melenk [70, 5]). This approach, often termed *extended finite element method*, introduces separate degrees of freedom associated with the displacement discontinuities on basis of a partition-of-unity (Moës, Dolbow & Belytschko [73]). As opposed to the approach of embedded discontinuities, this method relies on a *nodal enrichment* and the additional degrees of freedom pertain to the global system of degrees of freedom, i.e., they can not be eliminated on a local level. Though this method offers the perspective of a very general and completely discretization independent modeling of failure zones, see, e.g., Jiràsek & Belytschko [56] and Wells [128, 129], its numerical implementation — especially with respect to a three-dimensional setting — proves complex and does not seem to be fully resolved, yet.

1.3 Objective and scope of the work

To the author's best knowledge, modeling approaches in the field of deformation localization and material failure are presently almost exclusively developed and applied in the context of a low-order, mostly constant strain, finite element framework.

Based on the observation that spurious *locking* effects and *mesh bias*, are to a strong degree influenced by the insufficient kinematic approach of low-order finite elements, the leading thought of this thesis develops as follows: For linear and nonlinear elliptic boundary value problems, high-order finite elements are proven to provide very efficient discretizations [121, 33, 84]. Moreover, due to their superior kinematics, high-order polynomial approximations have been found to be robust against locking [96, 35, 98]. Therefore, as express concerns of this work,

- it is not only desirable from an academic point of view to extend the scope of application of high-order finite elements to the field of deformation localization and material failure;
- moreover, the assumption is justified that the rich kinematic potentials of high-order polynomial extensions significantly alleviate stress *locking* and *mesh bias* issues — thus, also in this problem domain a high-order finite element approach is expected to contribute to an effective formulation that does *not* rely on elaborate strategies of highly nonlocal character.

Subsequent to this introductory chapter, Chapters 2–6 form the core of this work. They are structured according to:

Continuum mechanics & Discretization

- Chapter 2 summarizes the fundamental laws of continuum mechanics, on which developments presented in this work are based. Focusing on a small deformation context the basic relations of kinematics, stress and equilibrium are outlined. The coherence between strains and stresses, described by constitutive laws, is treated in view of the

energy dissipation associated with material failure. For development of the variational formulation, a general three field functional is employed. The so obtained variational formulation constitutes the foundation for the numerical procedure and facilitates the consistent formulation of *embedded strong discontinuities* in the framework of *enhanced assumed strains*.

- Chapter 3 initially introduces the finite element method as a general discretization procedure. Accounting for the incorporation of strong discontinuities, the generalized framework set by the variational formulation is maintained. As the aspired extensions are developed consistently in respect of possible applicability within a high-order finite element framework, the characteristics of the finite element p-version are a natural matter in the following. Accordingly, high-order hierarchical Ansatz spaces, mapping concepts, as well as numerical integration are described as specifications of the p-version approach.

Strong discontinuities

- Chapter 4 extends the classical continuum mechanical formulation regarding the possible occurence of *strong discontinuities*, i.e jumps in the displacement field. As an essential attribute to this approach, the postulate of *traction continuity* evolves; it is exploited for a direct coupling between strong discontinuity kinematics and a *discrete interface law*. Following the previously established framework of enhanced assumed strains, it develops a finite element formulation that furnishes both a consistent representation of the strong discontinuity kinematics and the traction continuity requirement. Starting from there, Chapter 4 develops the central notion of a p-adaptive consistent extension of the approach to a high-order finite element framework. Two essential ingredients form the basis for this progression:

  a) Dispensing with the restriction of one discontinuity plane per finite element features the transition to a pure continuum formulation and facilitates the elimination of degrees of freedom, associated with the displacement discontinuities, already on material point level.

  b) A novel reassessment of the strong discontinuity kinematics then puts forth the extended p-adaptive formulation. As opposed to previous formulations, the approach is consistent with the adoption of high-order polynomial approximations.

- Chapter 5 specializes the previously developed embedded strong discontinuity formulation in respect of a modeling approach for brittle predominant mode-I material failure. From the discussion of *rotating* and *fixed* discontinuity approaches, it deduces the idea of a *hybrid* approach which accounts for the observed multi-phase character of the failure zone formation process.

Numerical examples

- Chapter 6 finally, sheds light on the question regarding the approach's consistency in a high-order finite element context, by means of four spatially discretized numerical examples. It illustrates both *necessity* and *effectiveness* of the advocated p-adaptive

extension. Following a continuing study, which elaborates the distinct contribution of the proposed *hybrid discontinuity approach* to the simulation of a locking free propagation of the failure zone, the chapter concludes with a benchmark simulation. This simulation not only supports the validity of the model, it also illustrates the superior resolution of the failure process compared to corresponding low-order finite element approximations.

The work concludes with a survey over the essential outcomes in Chapter 7. From the very beginning it was obvious that due to the complex nature of the problem field, there will be questions left unanswered. So, Chapter 7 also tries to throw light on possible future directions of research in this field.

Chapter 2

Classical continuum mechanics

I could never make out what those damned dots meant.
– Winston Churchill.

As a foundation for the subsequent treatment of discretization concepts (Chapter 3), the present chapter starts with summarizing the continuum mechanical basics. A continuum body is understood as an assembly of material particles, each particle being characterized by distinct material properties. During motion, this assembly of particles remains a portion of the EUCLIDEAN space $\mathbb{R}^3$ at any time t. Subsequent considerations are essentially based on explanations of BONET & WOOD [15], WRIGGERS [133, 132] and TRUESDELL & NOLL [124].

2.1 Kinematics

2.1.1 Motion

The three-dimensional EUCLIDEAN space $\mathbb{R}^3$ is spanned by an orthonormal basis $\boldsymbol{E}$ defined in the reference point O of the system. Let $\Omega_0 \subset \mathbb{R}^3$ refer to the reference configuration of a continuuum body at time $t = 0$ with boundary $\partial\Omega_0$ and closure $\bar{\Omega}_0 := \Omega_0 \cup \partial\Omega_0$. A particle of $\bar{\Omega}_0$ at its initial position at time $t = 0$ be labeled by the coordinates $\boldsymbol{X} \in \Omega_0$, defined with respect to the cartesian basis $\boldsymbol{E}$. At time $t \in (0, T] \subset \mathbb{R}_+$ the current configuration of the body be referenced by $\Omega \subset \mathbb{R}^3$, boundary $\partial\Omega_0$ and closure $\bar{\Omega} := \Omega \cup \partial\Omega$. Assume further, that the position of a particle at time $t \in (0, T]$ be described by the current coordinates $\boldsymbol{x} \in \Omega$, which in general may refer to an alternative cartesian basis $\boldsymbol{e}$. Then, the motion of the body can be described by a mapping between initial and current particle positions as

$$\begin{aligned} \phi \;&:\; \bar{\Omega}_0 \times [0, T] \;\mapsto \bar{\Omega} \quad \text{with} \quad \bar{\Omega}_0, \bar{\Omega} \in \mathbb{R}^3 \\ \boldsymbol{x} \;&=\; \phi(\boldsymbol{X}, t) \end{aligned} \tag{2.1}$$

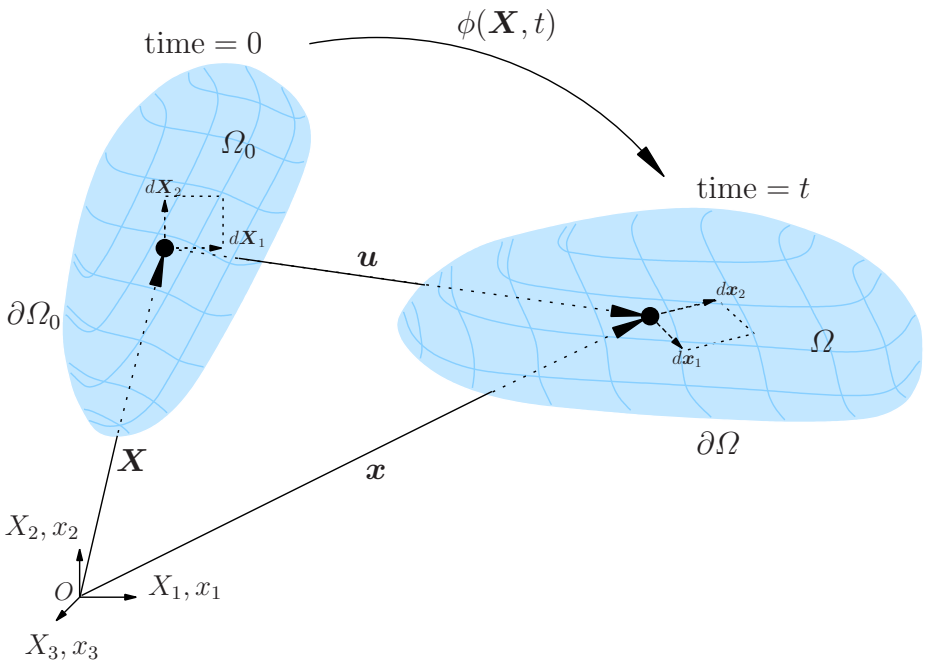

Figure 2.1: Motion of a material particle

For a fixed value of t, equation (2.1) represents the mapping between reference (undeformed) and current (deformed) configuration of body Ω — if view is focused on a distinct particle, i.e., $\boldsymbol{X}$ is kept fixed, equation (2.1) describes the motion of this particle as a function of time.

When describing the motion of a body mathematically, two different views can be adopted — which should be carefully distinguished:

- The EULERIAN approach employs a *spatial* description. The observer is connected to a distinct spatial position and monitors changes at this position, which may also be due to 'passing by' of different material particles. Thus, the observer does not possess information that is associated to a distinct particle, like, e.g., the change of particle's physical properties over time.

- The LAGRANGIAN approach adopts a *material* based description. The observer is connected to a distinct material particle and monitors changes of its physical properties and spatial position over time.

The EULER approach is commonly applied in the field of computational fluid mechanics, while for strucural mechanics problems generally the LAGRANGIAN view is preferred since it facilitates incorporation of material specific response in a natural way. Throughout the remainder of this work the LAGRANGIAN view is adopted.

2.1.2 Deformation gradient

Consider a body whose deformation over time is described by the motion equation (2.1). The *displacement vector* $\boldsymbol{u}$ associated with a particle then defines the difference between initial and current position.

$$\boldsymbol{u} = \boldsymbol{x} - \boldsymbol{X} \tag{2.2}$$

As an important measure to relate quantities associated with the reference configuration (before deformation) to corresponding quantities in the current configuration (during deformation), the *deformation gradient tensor* $\boldsymbol{F}$ is introduced.

$$\boldsymbol{F} := \frac{\partial \phi(\boldsymbol{X}, t)}{\partial \boldsymbol{X}} = \frac{\partial \left(\boldsymbol{X} + \boldsymbol{u}(\boldsymbol{X}, t)\right)}{\partial \boldsymbol{X}} = \boldsymbol{1} + \frac{\partial \boldsymbol{u}(\boldsymbol{X}, t)}{\partial \boldsymbol{X}} \tag{2.3}$$

In $(2.3)_3$, $\boldsymbol{1}$ denotes the second-order unit tensor. For the spatial derivatives with respect to reference and current configuration we stipulate

$$\boldsymbol{\nabla}_0(\bullet) := \frac{\partial(\bullet)}{\partial \boldsymbol{X}} \quad \text{and} \quad \boldsymbol{\nabla}(\bullet) := \frac{\partial(\bullet)}{\partial \boldsymbol{x}} \, . \tag{2.4}$$

The deformation gradient $\boldsymbol{F}$ represents the instantaneous "direction of motion" of a material particle and thus maps tangent vectors in the reference configuration to tangent vectors in the current configuration — for example, it associates to the elemental vectors $d\boldsymbol{X}_i \in \Omega_0$, $i = 1...2$, the elemental vectors $d\boldsymbol{x}_i \in \Omega$ (Figure 2.1).

$$d\boldsymbol{x} = \boldsymbol{F} \, d\boldsymbol{X} \tag{2.5}$$

The postulation of uniqueness of the mapping (2.1) is complemented by exclusion of self-penetration of the body. These two requirements give rise to the condition

$$J := det\boldsymbol{F} > 0 \, , \tag{2.6}$$

where the JACOBIAN determinant J has been introduced.

Based on the deformation gradient, convenient transformations of area and volume between reference and current configurations can be defined as

$$d\boldsymbol{a} = \boldsymbol{n} da = J \, \boldsymbol{F}^{-T} \, d\boldsymbol{A} \qquad \text{(NANSON's formula)} \tag{2.7}$$

and

$$dv = J \, dV \, , \tag{2.8}$$

respectively. In equation (2.7), $\boldsymbol{n}$ denotes the normal vector to the considered infinitesimal surface section da in the current configuration. Quantities dv and dV in equation (2.8) represent the respective infinitesimal volumes in current and reference configuration.

2.1.3 Strain

For a suitable definition of strain, the notion of objectivity or frame invariance plays a fundamental role; a body which is subjected to a pure rigid body motion should not experience any consequential straining. The GREEN-LAGRANGE strain tensor — as a quantity that meets this requirement — shall be introduced in the following.

The scalar product of two elemental vectors $\boldsymbol{X}_1$ and $\boldsymbol{X}_2$ is both influenced by the vectors' respective lengths and the enclosed angle between them. Consequently, the *change of scalar product* during transformation to the current configuration $\boldsymbol{x}_1$ and $\boldsymbol{x}_2$ furnishes a quantity, that reflects both stretching of the vectors and change of the enclosed angle — and thus represents a suitable basis for the definition of strain.

$$\begin{aligned} \frac{1}{2}\left(d\boldsymbol{x}_1 \bullet d\boldsymbol{x}_2 - d\boldsymbol{X}_1 \bullet d\boldsymbol{X}_2\right) &= \frac{1}{2}\left(\boldsymbol{F} d\boldsymbol{X}_1 \bullet \boldsymbol{F}\, d\boldsymbol{X}_2 - d\boldsymbol{X}_1 \bullet d\boldsymbol{X}_2\right) \\ &= \frac{1}{2}\left(d\boldsymbol{X}_1 \bullet \boldsymbol{F}^T\boldsymbol{F}\, d\boldsymbol{X}_2 - d\boldsymbol{X}_1 \bullet d\boldsymbol{X}_2\right) \\ &=: d\boldsymbol{X}_1 \bullet \boldsymbol{E}\, d\boldsymbol{X}_2 \end{aligned} \tag{2.9}$$

In equations (2.9), we have employed the mapping of elemental vectors according to (2.5). The definition of the GREEN-LAGRANGE strain, finally, is derived from (2.9) as

$$\boldsymbol{E} = \frac{1}{2}\left(\boldsymbol{F}^T\boldsymbol{F} - \boldsymbol{1}\right) \tag{2.10}$$

or equivalently, in view of $(2.3)_3$ and (2.4),

$$\boldsymbol{E} = \frac{1}{2}\left(\boldsymbol{\nabla}_0\boldsymbol{u} + \boldsymbol{\nabla}_0^T\boldsymbol{u} + \boldsymbol{\nabla}_0^T\boldsymbol{u}\,\boldsymbol{\nabla}_0\boldsymbol{u}\right) \ . \tag{2.11}$$

It should be noted that GREEN-LAGRANGE strain tensor $\boldsymbol{E}$, due to its construction, is symmetric — hence, for $\boldsymbol{x}, \boldsymbol{X}, \boldsymbol{u} \in \mathbb{R}^3$ we have six independent components.

In the context of infinitesimal theory, which is followed in this work, no distinction is required between reference configuration Ω_0 and current configuration Ω, such that $\boldsymbol{\nabla}_0(\bullet) \approx \boldsymbol{\nabla}(\bullet)$. In particular, the displacement gradient $\boldsymbol{\nabla}\boldsymbol{u}$ is considered to be small, furnishing $\boldsymbol{\nabla}^T\boldsymbol{u}\,\boldsymbol{\nabla}\boldsymbol{u} \ll 1$. Hence, the quadratic term in (2.11) is considered to be negligible and one arrives at the well-known symmetric linearized, or engineering, strain tensor definition according to

$$\boldsymbol{\varepsilon} = \frac{1}{2}\left(\boldsymbol{\nabla}\boldsymbol{u} + \boldsymbol{\nabla}^T\boldsymbol{u}\right) = \boldsymbol{\nabla}^{\mathrm{sym}}\boldsymbol{u} \ . \tag{2.12}$$

Remark. It is important to note, that in a finite deformation context, the linearized strain definition according to (2.12) is not frame invariant. Consider, for example a body subject to an in-plane rigid body rotation about ninety degrees, such that

$$u_x = -X - Y \ , \quad u_y = X - Y \quad \text{and} \quad u_z = 0 \ . \tag{2.13}$$

Then, the linearized strain tensor according to (2.12) would yield non-zero entries

$$\varepsilon_{xx} = \varepsilon_{yy} = -1 \tag{2.14}$$

— and thus, violate the frame invariance (objectivity) postulate and introduce spurious straining to the body. □

2.2 Stress and equilibrium

2.2.1 Stress state

The *"concept of force describes the action of the outside world on a body in motion and the interaction between the different parts of the body"* [124]. Considering, at a given time t, an arbitrary part $\mathcal{P} \subset \Omega$ of the body with boundary $\partial\mathcal{P}$, the notion of *stress* is developed as follows. Assuming the resultant contact force on $\partial\mathcal{P}$ being given by $\boldsymbol{f}_a$, then there exists a corresponding vector field $\boldsymbol{t}(\boldsymbol{x}, t)$ defined for each point $\boldsymbol{x} \subset \partial\mathcal{P}$ on the boundary, such that

$$\boldsymbol{f}_a(\mathcal{P}) = \int_{\partial\mathcal{P}} \boldsymbol{t}(\boldsymbol{x}, t)\, da \,. \tag{2.15}$$

Therein, $\boldsymbol{t}(\boldsymbol{x}, t)$ represents the so-called CAUCHY stress or traction vector; it can be interpreted as *density of the contact force*. Since $\mathcal{P}$ is arbitrary this notion can be extended to all interior points of Ω, such that $\boldsymbol{t}(\boldsymbol{x}, \boldsymbol{n}, t)$ is the stress vector at $\boldsymbol{x}$ acting across the oriented surface element with normal $\boldsymbol{n}$. [1] The so obtained stress vector is also referred to as *true* stress — it relates the current force $d\boldsymbol{f}_a$ at a point $\boldsymbol{x}$ to an area da related to the current configuration:

$$\boldsymbol{t}(\boldsymbol{x}, \boldsymbol{n}, t) = \frac{d\boldsymbol{f}_a}{da} \tag{2.16}$$

The CAUCHY theorem postulates a linear relation between stress vector $\boldsymbol{t}(\boldsymbol{x}, \boldsymbol{n}, t)$ and normal unit vector $\boldsymbol{n}$ of a considered surface according to

$$\boldsymbol{t}(\boldsymbol{x}, \boldsymbol{n}, t) = \boldsymbol{\sigma}(\boldsymbol{x}, t)\, \boldsymbol{n} \,. \tag{2.17}$$

The second-order tensor $\boldsymbol{\sigma}$ represents the CAUCHY stress tensor, which is merely a function of position and time — thus independent of $\boldsymbol{n}$. Figure 2.2 illustrates the sign convention for the definition of stress tensors, commonly adopted in solid mechanics. In the absence of micropolar stresses, which is presumed throughout this work, the local balance of angular of momentum dictates symmetry of the CAUCHY stress tensor, i.e.,

$$\boldsymbol{\sigma}^T = \boldsymbol{\sigma} \quad \text{or} \quad \sigma_{ij} = \sigma_{ji} \,. \tag{2.18}$$

A continuum classified by these properties, is frequently called BOLTZMANN continuum, cf., for example, D'ADETTA [25].

Depending on the kinematic description adopted, there exist different corresponding stress definitions. The concept to establish the appropriate stress description is derived from the central notion of *work conjugacy*. Representatively, the Second PIOLA-KIRCHHOFF stress tensor $\boldsymbol{S}$ shall subsequently be introduced. The internal virtual work (see Section 2.3.2) characterizes

[1] If $\boldsymbol{x} \in \partial\Omega$ and $\boldsymbol{n}$ coincides with the exterior unit normal to $\partial\Omega$, then the stress vector $\boldsymbol{t}(\boldsymbol{x}, t)$ reduces to a function of position and is frequently named *surface traction* on the boundary $\partial\Omega$.

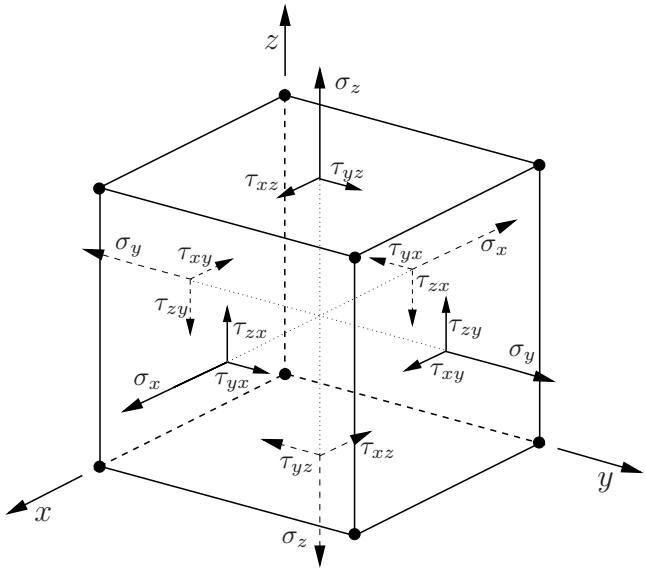

Figure 2.2: Sign convention for stress tensor components

the degree of straining of a body. It is defined in the current (deformed) configuration by means of linearized strain and CAUCHY stress tensor according to

$$\mathcal{W}_{\text{int}} = \int_{\Omega} \boldsymbol{\varepsilon}(\delta\boldsymbol{u}) : \boldsymbol{\sigma}(\boldsymbol{u})\, dv \;, \tag{2.19}$$

where $\delta\boldsymbol{u}$ represents a field of admissible virtual displacements. [2] Using the previously defined GREEN-LAGRANGE strain tensor $\boldsymbol{E}$ (2.11), the above internal virtual work expression can equivalently be recast as

$$\mathcal{W}_{\text{int}} = \int_{\Omega_0} \boldsymbol{E}(\delta\boldsymbol{u}) : \boldsymbol{S}(\boldsymbol{u})\, dV \;; \tag{2.20}$$

furnishing the energy conjugate Second PIOLA-KIRCHHOFF stress tensor $\boldsymbol{S}$ as

$$\boldsymbol{S} := J\boldsymbol{F}^{-1}\boldsymbol{\sigma}\boldsymbol{F}^{-T} \;. \tag{2.21}$$

2.2.2 Equilibrium

The local equilibrium condition for a general deformable body in the EUCLIDEAN space $\mathbb{R}^3$ is derived on basis of the balance of mass and momentum. For the quasi-static case, neglecting inertia effects, the differential equations of the three-dimensional model problem are obtained

[2] The : symbol adopted in (2.19) denotes the double contraction operation, here applied to two second-order tensors, thus featuring a scalar result. In indical notation, we have $W_{\text{int}} = \varepsilon_{ij}\sigma_{ij}$.

from the postulate of equilibrium at the differential element as:

$$\begin{aligned} \frac{\partial \sigma_{xx}}{\partial x} + \frac{\partial \sigma_{xy}}{\partial y} + \frac{\partial \sigma_{xz}}{\partial z} + b_x = 0 \\ \frac{\partial \sigma_{yx}}{\partial x} + \frac{\partial \sigma_{yy}}{\partial y} + \frac{\partial \sigma_{yz}}{\partial z} + b_y = 0 \\ \frac{\partial \sigma_{zx}}{\partial x} + \frac{\partial \sigma_{zy}}{\partial y} + \frac{\partial \sigma_{zz}}{\partial z} + b_z = 0 \end{aligned} \quad , \tag{2.22}$$

or, more compact

$$\mathrm{div}\boldsymbol{\sigma} + \boldsymbol{b} = \mathbf{0} \; . \tag{2.23}$$

For a state of equilibrium, condition (2.23) must be fulfilled for every part of the body. The vector $\boldsymbol{b} = \begin{bmatrix} b_x & b_y & b_z \end{bmatrix}^T$ represents the body force per unit volume and is supposed to be a prescribed quantity for the boundary value problem.

2.3 Variational formulation

So far, the model problem has been characterized by the fundamental mechanical equations; the kinematic relations of Section 2.1 and the equilibrium condition of Section 2.2.2, which is derived on basis of a local balance of mass and momentum. Discussion of the extant constitutive relations, linking strains and stresses, will be postponed to Section 2.4. The present section is devoted to establishing a formulation of the boundary value problem that can conveniently be adopted as a basis for the subsequent finite element approach. Generally, the finite element formulation is established in terms of a *weak form* of the differential equations under consideration.

To this end, starting from the method of weighted residuals, Section 2.3.2 establishes the classical *principle of virtual work* as the common basis for standard finite element formulations. With a view to later developments, Section 2.3.4 then adopts an alternative and more general approach, employing the variational functional according to Hu [50] and Washizu [127]. This functional furnishes the consistent variational framework for the incorporation of enriched strain fields into the finite element formulation — such as the *enhanced assumed strain* method (EAS), constituted by Simo & Rifai [117] — and also facilitates the consistent formulation of *embedded strong discontinuities* (Simo & Oliver [115]), which will be the matter of Chapter 4.

For the sake of clarity and conforming with the scope of the work, discussion is restricted to the infinitesimal case; in particular, no distinction is required between initial configuration Ω_0 and current configuration Ω. It should be noted however, that the method of enhanced assumed strains can equally valid be posed for the case of finite deformations (Simo & Armero [112]; Wall et al. [126]).

2.3.1 Definition of the boundary value problem

Let $\Omega \subset \mathbb{R}^3$ be the reference configuration of a continuum body with a smooth boundary $\partial\Omega$, closure $\bar{\Omega} := \Omega \cup \partial\Omega$, and particles X labeled by their position vectors $\boldsymbol{x} \in \Omega$ relative to the standard basis in $\mathbb{R}^3$. The deformation of the body from its reference configuration is described by the displacement field $\boldsymbol{u}$. Deformation is assumed to be prescribed as $\boldsymbol{u}^* := \boldsymbol{u}|_{\partial_u}$ on the DIRICHLET boundary $\partial_u\Omega \subset \partial\Omega$. Among the many possible types of loading that can act on a continuum body, this work limits regard to body forces $\boldsymbol{b}$ and surface tractions $\boldsymbol{t}^* := \boldsymbol{\sigma}|_{\partial_\sigma}\boldsymbol{n}$. These surface tractions be prescribed on the NEUMANN boundary $\partial_\sigma\Omega \subset \partial\Omega$, such that $\partial_u\Omega \cup \partial_\sigma\Omega = \partial\Omega$ and $\partial_u\Omega \cap \partial_\sigma\Omega = \varnothing$.

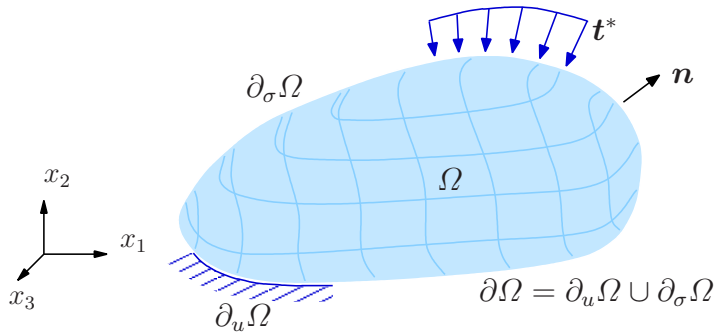

Figure 2.3: Definition of the boundary value problem

2.3.2 The weak form of equilibrium

The departure point is the differential equilibrium condition (2.23). Accounting for the previously defined boundary conditions, the displacement field $\boldsymbol{u}$ is sought that satisfies

$$\mathrm{div}\boldsymbol{\sigma} + \boldsymbol{b} = \boldsymbol{0} \,. \tag{2.24}$$

Let now $\delta\boldsymbol{u} \in \mathcal{V}$ define a test function vector which can equivalently be interpreted as virtual displacement. $\mathcal{V} = \{\delta\boldsymbol{u}(\boldsymbol{x}) \in [H^1(\Omega)]^{n_{\mathrm{dim}}} : \delta\boldsymbol{u} = \boldsymbol{0} \text{ on } \partial_u\Omega\}$ defines a SOBOLEV space [6, 31], which is based on functions with square-integrable, generalized derivatives. n_{dim} corresponds to the number of *physical degrees of freedom*, which for the considered BOLTZMANN continuum is equivalent to the dimensionality of the problem, i.e., $n_{\mathrm{dim}} = i$ for $\boldsymbol{x} \in \mathbb{R}^i$ with $i = 1, 2, 3$. Then, multiplying — according to the method of weighted residuals — the differential equation (2.24) by the test function vector $\delta\boldsymbol{u}$ and integrating over the computational domain Ω yields

$$\int_\Omega (\mathrm{div}\boldsymbol{\sigma} + \boldsymbol{b}) \bullet \delta\boldsymbol{u} \, dv = 0 \quad \forall \delta\boldsymbol{u} \in \mathcal{V} \,; \tag{2.25}$$

now rendering equilibrium in an integral sense. Integrating by parts [3] and using the GAUSS theorem, finally puts forth the so-called *weak form* of equilibrium

$$\int_{\Omega} \boldsymbol{\nabla}^{\mathrm{sym}} \delta\boldsymbol{u} : \boldsymbol{\sigma} \, dv = \int_{\Omega} \boldsymbol{b} \bullet \delta\boldsymbol{u} \, dv + \int_{\partial_\sigma \Omega} \boldsymbol{t}^* \bullet \delta\boldsymbol{u} \, da \, . \tag{2.26}$$

Note, that the symmetry (2.18) of the CAUCHY stress tensor implies the equivalence $\boldsymbol{\nabla}\delta\boldsymbol{u} : \boldsymbol{\sigma} = \boldsymbol{\nabla}^{\mathrm{sym}}\delta\boldsymbol{u} : \boldsymbol{\sigma}$. The attribute *weak* refers to the fact that equation (2.26) poses less strict requirements regarding the regularity of the displacement field than its *strong form* counterpart (2.24). Equation (2.26) frequently is referred to as *principle of virtual work*, where the work due to internal forces is defined by

$$\mathcal{W}_{\mathrm{int}}(\boldsymbol{u}, \delta\boldsymbol{u}) := \int_{\Omega} \boldsymbol{\nabla}^{\mathrm{sym}} \delta\boldsymbol{u} : \boldsymbol{\sigma} \, dv = \int_{\Omega} \boldsymbol{\varepsilon} : \boldsymbol{\sigma} \, dv \tag{2.27}$$

and the work due to external forces is given as

$$\mathcal{W}_{\mathrm{ext}}(\delta\boldsymbol{u}) := \int_{\Omega} \boldsymbol{b} \bullet \delta\boldsymbol{u} \, dv + \int_{\partial_\sigma \Omega} \boldsymbol{t}^* \bullet \delta\boldsymbol{u} \, da \, . \tag{2.28}$$

The resulting strain energy is specified as

$$\mathcal{U}(\boldsymbol{u}) := \frac{1}{2} \mathcal{W}_{\mathrm{int}}(\boldsymbol{u}, \boldsymbol{u}) \, , \tag{2.29}$$

with the corresponding energy norm

$$\|\boldsymbol{u}\|_{E(\Omega)} \; := \; \sqrt{\mathcal{U}(\boldsymbol{u})} = \sqrt{\frac{1}{2} \mathcal{W}_{\mathrm{int}}(\boldsymbol{u}, \boldsymbol{u})} \, . \tag{2.30}$$

Equation (2.26) determines the exact solution $\boldsymbol{u} = \boldsymbol{u}_{ex}$ with finite strain energy that satisfies the geometrical boundary conditions.

Remark. With every statement of the principle of virtual work it is also possible to associate a quadratic functional $\mathit{\Pi}(\boldsymbol{u})$, such that the exact solution $\boldsymbol{u}_{ex}$ to the *weak form* is the minimizing function of this functional. For conservative systems, this quadratic functional can directly be associated with the *potential energy*.

$$\mathit{\Pi}(\boldsymbol{u}) := \mathcal{U}(\boldsymbol{u}) - \mathcal{W}_{\mathrm{ext}}(\boldsymbol{u}) = \frac{1}{2} \mathcal{W}_{\mathrm{int}}(\boldsymbol{u}, \boldsymbol{u}) - \mathcal{W}_{\mathrm{ext}}(\boldsymbol{u}) \tag{2.31}$$

□

2.3.3 Generalized variational formulation

Extending the pure displacement formulation of the previous section, it is also possible to introduce strain $\boldsymbol{\varepsilon}$ and stress $\boldsymbol{\sigma}$ as additional primary variables. As a consequence, the corresponding functional (2.31) then renders three independent fields $\mathit{\Pi} := \mathit{\Pi}(\boldsymbol{u}, \boldsymbol{\varepsilon}, \boldsymbol{\sigma})$. Such a —

[3] The product rule gives rise to the divergence property $\mathrm{div}\,(\boldsymbol{\sigma}\delta\boldsymbol{u}) = \delta\boldsymbol{u} \bullet \mathrm{div}\boldsymbol{\sigma} + \boldsymbol{\nabla}\delta\boldsymbol{u} : \boldsymbol{\sigma}$.

most general — approach is constituted by the Hu-Washizu three-field variational functional. It is stated as (e.g., Andelfinger [1], Simo & Hughes [113])

$$\Pi(\boldsymbol{u},\boldsymbol{\varepsilon},\boldsymbol{\sigma}) = \Pi_{\text{int}}(\boldsymbol{u},\boldsymbol{\varepsilon},\boldsymbol{\sigma}) + \Pi_{\text{ext}}(\boldsymbol{u},\boldsymbol{\varepsilon},\boldsymbol{\sigma}) \tag{2.32}$$

where

$$\Pi_{\text{int}}(\boldsymbol{u},\boldsymbol{\varepsilon},\boldsymbol{\sigma}) = \int_{\Omega} W(\boldsymbol{x},\boldsymbol{\varepsilon}) - \boldsymbol{\sigma} : (\boldsymbol{\varepsilon} - \boldsymbol{\nabla}^{\text{sym}}\boldsymbol{u}) \; dV \tag{2.33}$$

represents the internal potential [4], with $W(\boldsymbol{x},\boldsymbol{\varepsilon})$ denoting the stored material energy function. The external potential is specified as

$$\Pi_{\text{ext}}(\boldsymbol{u},\boldsymbol{\varepsilon},\boldsymbol{\sigma}) = -\int_{\Omega} \boldsymbol{b} \bullet \boldsymbol{u} \; dV - \int_{\partial_\sigma \Omega} \boldsymbol{t}^* \bullet \boldsymbol{u} \; dA \tag{2.34}$$

In anticipation of later developments, we also define in the standard fashion (cf. Section 2.3.2) spaces of admissible displacement variations

$$\mathcal{V} = \{\delta\boldsymbol{u}(\boldsymbol{x}) \in [H^1(\Omega)]^{n_{\text{dim}}} : \delta\boldsymbol{u} = \boldsymbol{0} \text{ on } \partial_u\Omega\} \tag{2.35}$$

and spaces of admissible strain and stress variations

$$\mathcal{E} = \{\delta\boldsymbol{\varepsilon}(\boldsymbol{x}) \in [L_2(\Omega)]^{n_{\text{strn}}}\} \quad \text{and} \quad \mathcal{S} = \{\delta\boldsymbol{\sigma}(\boldsymbol{x}) \in [L_2(\Omega)]^{n_{\text{strn}}}\} \; , \tag{2.36}$$

n_{dim} again denoting the dimensionality of the problem and n_{strn} referring to the number of strain and stress components, respectively.

Based on the notion of the *principle of minimum potential energy*, it is convenient to expand the potential $\Pi(\boldsymbol{u},\boldsymbol{\varepsilon},\boldsymbol{\sigma})$ around the unknown state $(\boldsymbol{u}_{ex},\boldsymbol{\varepsilon}_{ex},\boldsymbol{\sigma}_{ex})$ by means of a truncated Taylor series.

$$\begin{aligned} \Pi(\boldsymbol{u},\boldsymbol{\varepsilon},\boldsymbol{\sigma}) &= \Pi(\boldsymbol{u}_{ex} + \kappa\ \delta\boldsymbol{u}, \boldsymbol{\varepsilon}_{ex} + \kappa\ \delta\boldsymbol{\varepsilon}, \boldsymbol{\sigma}_{ex} + \kappa\ \delta\boldsymbol{\sigma}) \\ &\approx \Pi(\boldsymbol{u}_{ex},\boldsymbol{\varepsilon}_{ex},\boldsymbol{\sigma}_{ex}) + D\Pi(\boldsymbol{u},\boldsymbol{\varepsilon},\boldsymbol{\sigma}) \cdot (\delta\boldsymbol{u},\delta\boldsymbol{\varepsilon},\delta\boldsymbol{\sigma}) \end{aligned} \tag{2.37}$$

The directional derivative (Gâteaux derivative) $D\Pi(\bullet)\cdot(\bullet)$ represents the first variation $\delta\Pi$ of the functional (2.32) around a point $(\boldsymbol{u}_{ex},\boldsymbol{\varepsilon}_{ex},\boldsymbol{\sigma}_{ex})$ in the direction $(\delta\boldsymbol{u},\delta\boldsymbol{\varepsilon},\delta\boldsymbol{\sigma})$ and is defined as

$$\begin{aligned} \delta\Pi &\equiv D\Pi(\boldsymbol{u},\boldsymbol{\varepsilon},\boldsymbol{\sigma}) \cdot (\delta\boldsymbol{u},\delta\boldsymbol{\varepsilon},\delta\boldsymbol{\sigma}) \\ &:= \left.\frac{d}{d\kappa}\right|_{\kappa\to 0} \Pi(\boldsymbol{u}+\kappa\delta\boldsymbol{u}, \boldsymbol{\varepsilon}+\kappa\delta\boldsymbol{\varepsilon}, \boldsymbol{\sigma}+\kappa\delta\boldsymbol{\sigma}) \end{aligned} \tag{2.38}$$

A necessary requirement in order to let candidate $(\boldsymbol{u}_{ex},\boldsymbol{\varepsilon}_{ex},\boldsymbol{\sigma}_{ex})$ indeed be a minimizer of the potential $\Pi(\boldsymbol{u},\boldsymbol{\varepsilon},\boldsymbol{\sigma})$, is the stationarity of equation (2.37) [112]. This implies, that the first variation of the functional vanishes. Accordingly, we write

$$\delta\Pi = \left(\frac{\partial\Pi(\boldsymbol{u}+\kappa\delta\boldsymbol{u})}{\partial\kappa} + \frac{\partial\Pi(\boldsymbol{\varepsilon}+\kappa\delta\boldsymbol{\varepsilon})}{\partial\kappa} + \frac{\partial\Pi(\boldsymbol{\sigma}+\kappa\delta\boldsymbol{\sigma})}{\partial\kappa} \right)\Bigg|_{\kappa\to 0} \overset{!}{=} 0 \tag{2.39}$$

[4] Taking a different point of view on this formulation, the stress field $\boldsymbol{\sigma}$ can be interpreted as a Lagrange multiplier — applied to enforce the kinematic constraint $\boldsymbol{\varepsilon} = \boldsymbol{\nabla}^{\text{sym}}\boldsymbol{u}$ [113].

which — accounting for the *independence* of the three variable fields — finally yields

$$\left.\begin{aligned} &\int_\Omega \boldsymbol{\nabla}^{\mathrm{sym}}\delta\boldsymbol{u} : \boldsymbol{\sigma}\; dV - \underbrace{\left(\int_\Omega \boldsymbol{b} \bullet \delta\boldsymbol{u}\; dV + \int_{\partial_\sigma\Omega} \boldsymbol{t}^* \bullet \delta\boldsymbol{u}\; dA\right)}_{\mathcal{W}_{\mathrm{ext}}} = 0 \\ &\int_\Omega \delta\boldsymbol{\varepsilon} : (\hat{\boldsymbol{\sigma}}(\boldsymbol{\varepsilon}) - \boldsymbol{\sigma})\; dV = 0 \\ &\int_\Omega \delta\boldsymbol{\sigma} : (\boldsymbol{\nabla}^{\mathrm{sym}}\boldsymbol{u} - \boldsymbol{\varepsilon})\; dV = 0 \end{aligned}\right| \quad \delta\Pi \tag{2.40}$$

Notably, equation $(2.40)_1$ reflects the well-known weak form of the equilibrium equations (principle of virtual work) (2.26), giving rise to the strong form of equilibrium

$$\mathrm{div}\boldsymbol{\sigma} + \boldsymbol{b} = \boldsymbol{0} \tag{2.41}$$

and the static Neumann boundary conditions

$$\boldsymbol{t}^* = \boldsymbol{\sigma}|_{\partial_\sigma}\boldsymbol{n} \quad \text{on} \quad \partial_\sigma\Omega\,. \tag{2.42}$$

Additionally, equations $(2.40)_2$ and $(2.40)_3$ enforce the constitutive relation

$$\hat{\boldsymbol{\sigma}}(\boldsymbol{\varepsilon}) = \boldsymbol{\sigma} \tag{2.43}$$

and the kinematic equation

$$\boldsymbol{\nabla}^{\mathrm{sym}}\boldsymbol{u} = \boldsymbol{\varepsilon}\,. \tag{2.44}$$

To summarize, except for the Dirchlet boundary conditions $\boldsymbol{u} = \boldsymbol{u}^*$ on $\partial_u\Omega$, all other governing equations are replaced by the variational equality (2.40) in a weak sense, see also Jirásek [52].

Remark. Though the derivation of (2.40) is initially motivated by the notion of minimization of the potential energy — which silently assumes the existence of such a potential — the application of the variational equality (2.40) is not restricted to the class of problems where such a potential indeed exists. Instead it is possible to start directly with (2.40) — all governing equations are contained therein, as was shown above. To emphasize this aspect, in $(2.40)_2$ the partial derivative of the material stored energy function $\partial_{,\boldsymbol{\varepsilon}}W(\boldsymbol{\varepsilon})$ has been replaced by the stress $\hat{\boldsymbol{\sigma}}(\boldsymbol{\varepsilon})$ computed from the assumed strain $\boldsymbol{\varepsilon}$ using the respective constitutive equation. For non-conservative systems — i.e., systems that do not preserve the energy introduced to them — of course, the interpretation of minimization of a potential is lost and no longer justified. □

2.3.4 Modified three-field variational problem

The fundamental idea of the *enhanced assumed strain method* is the decomposition of the strain field into a displacement compatible and an enhanced portion. Introducing this split

both for the strains and the corresponding admissible variations, namely

$$\begin{aligned} \boldsymbol{\varepsilon} &= \boldsymbol{\nabla}^{\mathrm{sym}}\boldsymbol{u} + \tilde{\boldsymbol{\varepsilon}} \\ \delta\boldsymbol{\varepsilon} &= \boldsymbol{\nabla}^{\mathrm{sym}}\delta\boldsymbol{u} + \delta\tilde{\boldsymbol{\varepsilon}} \end{aligned} \tag{2.45}$$

with $\tilde{\boldsymbol{\varepsilon}}, \delta\tilde{\boldsymbol{\varepsilon}} \in \tilde{\mathcal{E}}$ and $\tilde{\mathcal{E}}$ being the space of enhanced strain fields, equation $(2.40)_2$ is rewritten as

$$\int_{\Omega} \delta\tilde{\boldsymbol{\varepsilon}} : (\hat{\boldsymbol{\sigma}}(\boldsymbol{\varepsilon}) - \boldsymbol{\sigma}) \; dV + \int_{\Omega} \boldsymbol{\nabla}^{\mathrm{sym}}\delta\boldsymbol{u} : (\hat{\boldsymbol{\sigma}}(\boldsymbol{\varepsilon}) - \boldsymbol{\sigma}) \; dV = 0$$

Using this relation and inserting (2.45) into (2.40), the modified three-field variational problem is finally obtained as (Simo & Rifai [117]; Klinkel & Wagner [64])

$$\left.\begin{aligned} &\int_{\Omega} \boldsymbol{\nabla}^{\mathrm{sym}}\delta\boldsymbol{u} : \hat{\boldsymbol{\sigma}}(\boldsymbol{\nabla}^{\mathrm{sym}}\boldsymbol{u} + \tilde{\boldsymbol{\varepsilon}}) \; dV - \mathcal{W}_{\mathrm{ext}}(\delta\boldsymbol{u}) = 0 \\ &\int_{\Omega} \delta\tilde{\boldsymbol{\varepsilon}} : (\hat{\boldsymbol{\sigma}}(\boldsymbol{\nabla}^{\mathrm{sym}}\boldsymbol{u} + \tilde{\boldsymbol{\varepsilon}}) - \boldsymbol{\sigma}) \; dV = 0 \\ &\int_{\Omega} \delta\boldsymbol{\sigma} : \tilde{\boldsymbol{\varepsilon}} \; dV = 0 \end{aligned}\right| \; \delta\Pi \tag{2.46}$$

2.3.5 Linearization of the modified variational problem

In general, the system of equations (2.46) can be nonlinear. In the context of such a nonlinear framework, an efficient iterative solution strategy with quadratic convergence properties is the Newton-Raphson algorithm. The algorithm is based on a consistent linearization of the underlying variational problem and can be outlined as follows. Having arrived at a state $(\boldsymbol{u}_k, \tilde{\boldsymbol{\varepsilon}}_k, \boldsymbol{\sigma}_k)$ — silently assuming equations (2.46) are not satisfied — a corrected state

$$(\boldsymbol{u}_{k+1}, \tilde{\boldsymbol{\varepsilon}}_{k+1}, \boldsymbol{\sigma}_{k+1}) = (\boldsymbol{u}_k, \tilde{\boldsymbol{\varepsilon}}_k, \boldsymbol{\sigma}_k) + (\dot{\boldsymbol{u}}, \dot{\tilde{\boldsymbol{\varepsilon}}}, \dot{\boldsymbol{\sigma}})$$

can be obtained by a linear extension of (2.46) around the state k. Again, applying a truncated Taylor series expansion, we write

$$\delta\Pi(\boldsymbol{u}_{k+1}, \tilde{\boldsymbol{\varepsilon}}_{k+1}, \boldsymbol{\sigma}_{k+1}) \approx \delta\Pi(\boldsymbol{u}_k, \tilde{\boldsymbol{\varepsilon}}_k, \boldsymbol{\sigma}_k) + \underbrace{D\delta\Pi(\boldsymbol{u}_k, \tilde{\boldsymbol{\varepsilon}}_k, \boldsymbol{\sigma}_k) \cdot (\dot{\boldsymbol{u}}, \dot{\tilde{\boldsymbol{\varepsilon}}}, \dot{\boldsymbol{\sigma}})}_{=:\delta\dot{\Pi}} \tag{2.47}$$

and require $\delta\Pi(\boldsymbol{u}_{k+1}, \tilde{\boldsymbol{\varepsilon}}_{k+1}, \boldsymbol{\sigma}_{k+1}) \overset{!}{=} 0$; $\delta\dot{\Pi}$ denotes the directional derivative of the first variation of the functional (2.32). Standard arguments in the calculus of variations yield

$$\begin{aligned}
\delta\dot{\Pi} &= \left.\frac{d}{d\kappa}\right|_{\kappa\to 0} \delta\Pi(\boldsymbol{u}+\kappa\dot{\boldsymbol{u}}, \boldsymbol{\varepsilon}+\kappa\dot{\tilde{\boldsymbol{\varepsilon}}}, \boldsymbol{\sigma}+\kappa\dot{\boldsymbol{\sigma}}) \\
&= \int_\Omega \left(\boldsymbol{\nabla}^{\mathrm{sym}}\delta\boldsymbol{u} : \partial_{,\boldsymbol{\varepsilon}}\hat{\boldsymbol{\sigma}} : \boldsymbol{\nabla}^{\mathrm{sym}}\dot{\boldsymbol{u}} + \boldsymbol{\nabla}^{\mathrm{sym}}\delta\boldsymbol{u} : \partial_{,\boldsymbol{\varepsilon}}\hat{\boldsymbol{\sigma}} : \dot{\tilde{\boldsymbol{\varepsilon}}} \right) dV \\
&\quad + \int_\Omega \left(\delta\tilde{\boldsymbol{\varepsilon}} : \partial_{,\boldsymbol{\varepsilon}}\hat{\boldsymbol{\sigma}} : \boldsymbol{\nabla}^{\mathrm{sym}}\dot{\boldsymbol{u}} + \delta\tilde{\boldsymbol{\varepsilon}} : \partial_{,\boldsymbol{\varepsilon}}\hat{\boldsymbol{\sigma}} : \dot{\tilde{\boldsymbol{\varepsilon}}} \right) dV \\
&\quad + \int_\Omega \delta\boldsymbol{\sigma} : \dot{\tilde{\boldsymbol{\varepsilon}}}\, dV + \int_\Omega \delta\tilde{\boldsymbol{\varepsilon}} : \dot{\boldsymbol{\sigma}}\, dV
\end{aligned} \tag{2.48}$$

2.3.6 Eliminating the stress field from the formulation

So far, three independent variable fields $\boldsymbol{u}$, $\tilde{\boldsymbol{\varepsilon}}$ and $\boldsymbol{\sigma}$ show up in the variational problem (2.46) and its linearized form (2.47). The stress field's occurence — and hence, its later discretization — can be avoided by formally introducing an L_2-orthogonality between stress field and the enhanced strain field variations (Simo & Rifai [117]). Imposing

$$\int_\Omega \delta\tilde{\boldsymbol{\varepsilon}} : \boldsymbol{\sigma}\, dV = 0 \tag{2.49}$$

and introducing the definition of the fourth-order continuum constitutive tangent tensor

$$\mathbb{C}_{\mathrm{t}} := \partial_{,\boldsymbol{\varepsilon}}\hat{\boldsymbol{\sigma}}(\boldsymbol{\varepsilon}) = \partial_{,\boldsymbol{\varepsilon}}\hat{\boldsymbol{\sigma}}(\boldsymbol{\nabla}^{\mathrm{sym}}\boldsymbol{u} + \tilde{\boldsymbol{\varepsilon}}) \tag{2.50}$$

the variational problem (2.46) and its linearized form (2.47) with respect to the remaining two independent variables and their corresponding variations reduce to

$$\boxed{\begin{aligned}
&\int_\Omega \boldsymbol{\nabla}^{\mathrm{sym}}\delta\boldsymbol{u} : \hat{\boldsymbol{\sigma}}\, dV - \mathcal{W}_{\mathrm{ext}}(\delta\boldsymbol{u}) = 0 \\
&\int_{\Omega_e} \delta\tilde{\boldsymbol{\varepsilon}} : \hat{\boldsymbol{\sigma}}\, dV = 0
\end{aligned}} \tag{2.51}$$

and

$$\boxed{\begin{aligned}
&\int_\Omega \boldsymbol{\nabla}^{\mathrm{sym}}\delta\boldsymbol{u} : \mathbb{C}_{\mathrm{t}} : \boldsymbol{\nabla}^{\mathrm{sym}}\dot{\boldsymbol{u}}\, dV + \int_\Omega \boldsymbol{\nabla}^{\mathrm{sym}}\delta\boldsymbol{u} : \mathbb{C}_{\mathrm{t}} : \dot{\tilde{\boldsymbol{\varepsilon}}}\, dV + \\
&\qquad + \int_\Omega \boldsymbol{\nabla}^{\mathrm{sym}}\delta\boldsymbol{u} : \hat{\boldsymbol{\sigma}}\, dV - \mathcal{W}_{\mathrm{ext}}(\delta\boldsymbol{u}) = 0 \\
&\int_{\Omega_e} \delta\tilde{\boldsymbol{\varepsilon}} : \mathbb{C}_{\mathrm{t}} : \boldsymbol{\nabla}^{\mathrm{sym}}\dot{\boldsymbol{u}}\, dV + \int_{\Omega_e} \delta\tilde{\boldsymbol{\varepsilon}} : \mathbb{C}_{\mathrm{t}} : \dot{\tilde{\boldsymbol{\varepsilon}}}\, dV + \int_{\Omega_e} \delta\tilde{\boldsymbol{\varepsilon}} : \hat{\boldsymbol{\sigma}}\, dV = 0
\end{aligned}} \tag{2.52}$$

respectively. In light of this outcome, equation $(2.51)_2$ can be interpreted as the weak form of an *internal equilibrium condition* — complementing the classical weak equilibrium requirement $(2.51)_1$ between internal and external forces.

Remark. Note, that the components of the admissible enhanced strain field $\tilde{\boldsymbol{\varepsilon}}$ and its variation $\delta\tilde{\boldsymbol{\varepsilon}}$ are required only to lie in $L_2(\Omega)$ [117, 112, 12] — therefore, the respective fields need not be continuous on the domain Ω. In view of a later finite element discretization, see Section 3.1.2, this facitilates the L_2-orthogonality between stress field and enhanced strain field variation (2.49) to be established on subdomains $\Omega_e \subset \Omega$, represented by finite elements; which finally features a convenient construction of corresponding interpolation functions. To indicate this aspect, the subscript $(\bullet)_e$ has been added to the integration domains in equations (2.51) and (2.52), respectively. □

2.4 Continuum constitutive modeling

The basic lines of continuum kinematics and equilibrium in local and variational form set out so far, have essentially been developed irrespective of material specific constitutive properties. In mathematical terms, this disregard becomes manifest in the insuffient number of equations to uniquely determine the solution to the boundary value problem defined in Section 2.3.1. To complete the formulation, the present section takes on the discussion of constitutive relations which mark the residual link between deformation of a continuum material and consequential induced stress state — finally furnishing a well-posed boundary value problem.

Owing to the tremendous variety of materials and loading regimes of interest, the diversity of constitutive modeling approaches is almost just as comprehensive. An extensive overview with particular focus on inelastic material response and failure is, e.g., given in Bažant & Cedolin [7], Stein [119], Jirásek [51] or Jirásek & Bažant [55]. An excellent outline of classical infinite and finite elastoplasticity can, e.g., be found in Miehe [72]. Due to its generality, the flow theory of plasticity is also covered by many standard books on (computational) continuum mechanics, such as Zienkiewicz [135], Crisfield [23, 24] Wriggers [132] or Simo & Hughes [114].

Still, especially in consideration of the large amount of available constitutive modeling approaches with very different complexity, from the analyst's point of view the key point of using constitutive equations must be characterized as finding the *simplest* model that offers the accuracy required in the present situation.

In view of the later adopted modeling approach to capture traction-separation response at the discontinuity surface (cf. Section 4.3 and Chapter 5), this section concentrates on the description of basic ingredients of (hyper-)elasticity and the flow theory of plasticity. Also, consistent with the framework developed so far, a strong focus on the geometrical linear theory is maintained.

2.4.1 Hyperelasticity

Common to all elastic continuum models is the fundamental notion of a *stored material energy potential* $W(\boldsymbol{\varepsilon})$ as a function of the deformation state, characterized by the strain tensor $\boldsymbol{\varepsilon}$. This notion implies that:

(i) There is a *unique* relation between deformation state and corresponding internal stress state.

(ii) A consecutively loaded and unloaded body exactly returns to its initial position, i.e., *no permanent deformation* is induced. As a consequence, the deformation state is completely elastic with $\boldsymbol{\varepsilon} = \boldsymbol{\varepsilon}_{\mathrm{e}}$.

Having described the material characteristics by a suitable energy function, the stress state is formally established by

$$\boldsymbol{\sigma} := \frac{\partial W(\boldsymbol{\varepsilon}_{\mathrm{e}})}{\partial \boldsymbol{\varepsilon}_{\mathrm{e}}} = \partial_{,\boldsymbol{\varepsilon}_{\mathrm{e}}} W(\boldsymbol{\varepsilon}_{\mathrm{e}}) \tag{2.53}$$

and the change of stress with respect to strain is consequently described via

$$\dot{\boldsymbol{\sigma}} = \partial_{,\boldsymbol{\varepsilon}_{\mathrm{e}}} \boldsymbol{\sigma}(\boldsymbol{\varepsilon}_{\mathrm{e}})\, \dot{\boldsymbol{\varepsilon}}_{\mathrm{e}} = \mathbb{C}\, \dot{\boldsymbol{\varepsilon}}_{\mathrm{e}} \,, \tag{2.54}$$

with

$$\mathbb{C} := \frac{\partial \boldsymbol{\sigma}(\boldsymbol{\varepsilon}_{\mathrm{e}})}{\partial \boldsymbol{\varepsilon}_{\mathrm{e}}} = \frac{\partial^2 W(\boldsymbol{\varepsilon}_{\mathrm{e}})}{\partial \boldsymbol{\varepsilon}_{\mathrm{e}}\, \partial \boldsymbol{\varepsilon}_{\mathrm{e}}} = \partial_{,\boldsymbol{\varepsilon}_{\mathrm{e}}} \partial_{,\boldsymbol{\varepsilon}_{\mathrm{e}}} W(\boldsymbol{\varepsilon}_{\mathrm{e}}) \tag{2.55}$$

denoting the fourth-order constitutive tangent tensor.

The simplest example of a hyperelastic constitutive framework is indeed the famous Hooke's law of *isotropic linear elasticity*, dealing with only two material parameters. Specifying the stored energy potential as

$$W(\boldsymbol{\varepsilon}_{\mathrm{e}}) = 2\mu \bar{I}_2 + \frac{1}{2}\lambda I_1^2 \,, \tag{2.56}$$

where λ and μ denote the Lamé material constants and $I_1 := \mathrm{tr}(\boldsymbol{\varepsilon}_{\mathrm{e}})$ and $\bar{I}_2 := \frac{1}{2}\mathrm{tr}(\boldsymbol{\varepsilon}_{\mathrm{e}} \otimes \boldsymbol{\varepsilon}_{\mathrm{e}})$, respectively, are invariants of the strain tensor, the stress state is obtained via (2.53) as

$$\boldsymbol{\sigma} = 2\mu \boldsymbol{\varepsilon}_{\mathrm{e}} + \lambda \mathrm{tr}(\boldsymbol{\varepsilon}_{\mathrm{e}})\, \mathbf{1} \,. \tag{2.57}$$

From definition (2.55), the constitutive tangent is then deduced as (Crisfield [24])

$$\mathbb{C} = \frac{\partial^2 W(\boldsymbol{\varepsilon}_{\mathrm{e}})}{\partial \boldsymbol{\varepsilon}_{\mathrm{e}}\, \partial \boldsymbol{\varepsilon}_{\mathrm{e}}} = 2\mu\, \boldsymbol{I} + \lambda\, \mathbf{1} \otimes \mathbf{1} \,. \tag{2.58}$$

In equations (2.57) and (2.58) $\mathbf{1}$ and $\boldsymbol{I}$ denote the second-order and fourth-order unit tensor, respectively. As a consequence of the specific choice of the energy potential (2.56), which

depends on the strains in a quadratic manner, the resulting constitutive tangent (2.58) is constant, therefore furnishing a linear relationship between strains and corresponding stresses. In the infinitesimal case, where the strains are also linearly dependent on the displacements, the resultant load-displacement relation renders linear, too. By increasing the number of elastic material constants it is possible to account for anisotropic effects ranging from transversal isotropy and orthotropy to general anisotropy with at most 21 independent elastic moduli [5]. The LAMÉ constant λ can equivalently be expressed by

$$\lambda = \frac{3\kappa - 2\mu}{3} \,, \tag{2.60}$$

with $\kappa = E/(3(1-2\nu))$ being the bulk modulus, $\mu = E/(2(1+\nu))$ the shear modulus, E YOUNG's modulus and ν POISSON's ratio. Using this equivalence, the constitutive tangent (2.58) is recast as

$$\mathbb{C} = 2\mu[\boldsymbol{I} - \frac{1}{3}\,\mathbf{1}\otimes\mathbf{1}] + \kappa\,\mathbf{1}\otimes\mathbf{1}\,. \tag{2.61}$$

In the general case — depending on the specific choice of the stored energy potential W — the constitutive tangent tensor is non-constant but depends on the strains. Well-known hyperelastic formulations, frequently used in the field of simulation of rubber-like materials, are, e.g., due to MOONEY [74], RIVLIN [102] or OGDEN [85].

Remark. It should be noted, that in the geometrical nonlinear case it is vital to define the stored energy potential in terms of a suitable frame invariant strain measure, e.g., the previously introduced GREEN-LAGRANGE strain tensor $\boldsymbol{E}$. Otherwise, the formulation is susceptible to the introduction of spurious straining in consequence of rigid body rotations (cf. Section 2.1.3). Naturally, when using such a frame invariant strain measure, the stress is then described in terms of the appropriate work conjugate stress measure, e.g., the Second PIOLA-KIRCHHOFF stress tensor $\boldsymbol{S}$. □

[5] The fourth-order constitutive tensor due (2.55) features $3^4 = 81$ entries. Since the symmetry property of the stress tensor (2.18) renders three out of nine equations obsolete, each equation having nine coefficients, that is a total reduction of $3 \cdot 9 = 27$ constants. In the remaining six equations each three coefficients are not independent as a result of the symmetry of the strain tensor (cf. Section 2.1.3), which eliminates another $3 \cdot 6 = 18$ constants. Thus, because of symmetry in stress and strain tensors the number of independent elastic constants is reduced to $81 - 27 - 18 = 36$.
Further, accounting for the fact that the constitutive tensor is derived from an energy potential, it emerges that the result should be the same irrespective of the order of differentiation, i.e.,

$$C_{ijkl} = \frac{\partial}{\partial\varepsilon_{ij}}\left(\frac{\partial W}{\partial\varepsilon_{kl}}\right) = \frac{\partial}{\partial\varepsilon_{kl}}\left(\frac{\partial W}{\partial\varepsilon_{ij}}\right) = C_{klij}\,. \tag{2.59}$$

This symmetry reduces the total amount of constants by another 15, which yields a final total of 21 independent constants.

2.4.2 Flow theory of plasticity

A central notion of the flow theory of plasticity is the introduction of a space of admissible stresses:

$$\mathbb{E}_{\boldsymbol{\sigma}} := \{(\boldsymbol{\sigma}, \boldsymbol{q}) \in \mathbb{S} \times \mathbb{R}^n \mid \phi\,(\boldsymbol{\sigma}, \boldsymbol{q}) \leqslant 0\} \qquad \forall \boldsymbol{X} \in \Omega \tag{2.62}$$

Inner points of this space, i.e., $\boldsymbol{\sigma} \in \mathbb{E}_{\boldsymbol{\sigma}} \backslash \partial\mathbb{E}_{\boldsymbol{\sigma}}$ are characterized by elastic response, while on the boundary $\partial\mathbb{E}_{\boldsymbol{\sigma}}$ plastic states are permitted, as well. The function $\phi : \mathbb{S} \times \mathbb{R}^n \mapsto \mathbb{R}$ describes the restricted space subject to the stress state $\boldsymbol{\sigma}$ and the stress-like variable $\boldsymbol{q}$ and is commonly known as yield function. Variable $\boldsymbol{q}$ accounts for a possible evolution of the admissible stress space in dependence of an energy conjugate strain-like variable $\boldsymbol{\alpha}$, an effect which is known as *hardening* in case of expansion and *softening* in the contractive case, respectively. For brevity, in the remainder of the section we will use the term hardening as a generic term unless explicitly stated otherwise. As opposed to *kinematic* hardening behavior, which is characterized by a translation of the space of admissible stresses in stress space, this work is concerned with the case of *isotropic* hardening, exhibiting a uniform isotropic evolution of the space of admissible stresses. In case $\boldsymbol{q}$ does not evolve during plastic flow, as a consequence the elastic domain remains fixed — this behavior is commonly termed *perfect plasticity*. The space of admissible stresses is subject to the following constraints:

- Convexity: $\mathbb{E}_{\boldsymbol{\sigma}}$ must be a convex space. More descriptive, this condition requires that all points on the linear path between two admissible stress states also render admissible, i.e., belong to $\mathbb{E}_{\boldsymbol{\sigma}}$. This implies that for an elastic state $\boldsymbol{\sigma}^{(1)}$ which changes during monotonic loading to the elastic state $\boldsymbol{\sigma}^{(2)}$, the intermediate states are completely characterized by elastic response, too. A principle two-dimensional graphical representation of such a convex elastic domain is given in Figure 2.4.

- C^1-continuity: The continuity of the first derivative of the yield function must not be guaranteed in a strict sense. With particular view to multi-surface plasticity, it is sufficient to require that the yield function is C^1-continuous for almost all (= all but a finite number of) points. Mathematically,

$$\begin{aligned} &\partial\mathbb{E}_{\boldsymbol{\sigma}} \text{ Lipschitz-continuous} \quad \text{and} \\ &\partial\mathbb{E}_{\boldsymbol{\sigma}} \in C^1(\mathbb{S} \times \mathbb{R}^n, \mathbb{R}) \text{ for almost all } \boldsymbol{\sigma} \in \partial\mathbb{E}_{\boldsymbol{\sigma}}\ . \end{aligned} \tag{2.63}$$

In contrast to the hyperelastic case, the flow theory of plasticity accounts for the possibility that the energy furnished during deformation is *not* maintained completely in form of reversible, stored material strain energy — a portion of the deformation energy is then irreversibly dissipated, e.g., in form of thermal energy. A direct consequence of the process' irreversibility is the development of permanent (= *plastic*) deformation, i.e., a loaded and sequentially unloaded continuum body does not recover its initial position. Such characteristics can indeed be observed for a wide range of materials; mechanical energy dissipation frequently is manifested by changes in the material microstructure, finally giving rise to the phenomenon of plastic deformation. Foregoing considerations motivate a second fundamental assumption

— the split of the strain tensor into an elastic and a plastic contribution. For the infinitesimal theory, which is followed in this work, this can be done in an additive manner:

$$\boldsymbol{\varepsilon} = \boldsymbol{\varepsilon}_{\mathrm{e}} + \boldsymbol{\varepsilon}_{\mathrm{p}} \tag{2.64}$$

Due to the allowance of energy dissipation, the stored energy potential W is henceforth a function of the elastic portion of the strains rather than the total strains. Further, the possible evolution of the admissible stress space in dependence of the stress-like variable $\boldsymbol{q}$ is accounted for by introducing the conjugate strain-like variable $\boldsymbol{\alpha}$. Hence, we obtain $W := W(\boldsymbol{\varepsilon}_{\mathrm{e}}, \boldsymbol{\alpha})$. Following the hyperelastic framework (2.53), the stress state is then derived as

$$\boldsymbol{\sigma} = \frac{\partial W(\boldsymbol{\varepsilon}_{\mathrm{e}}, \boldsymbol{\alpha})}{\partial \boldsymbol{\varepsilon}_{\mathrm{e}}} \tag{2.65}$$

and definition of the stress-like hardening variable $\boldsymbol{q}$ yields

$$\boldsymbol{q} := -\frac{\partial W(\boldsymbol{\varepsilon}_{\mathrm{e}}, \boldsymbol{\alpha})}{\partial \boldsymbol{\alpha}} \, . \tag{2.66}$$

Restricting attention to the isothermal case, i.e., no thermal energy is explicitly supplied to the material, the internal stress power

$$\mathcal{P} = \boldsymbol{\sigma} : \dot{\boldsymbol{\varepsilon}} \tag{2.67}$$

is additively composed of a contribution stemming from the stored energy potential and a term associated with internal energy dissipation. Accordingly, we can write the dissipation inequality as

$$\mathcal{D} = \mathcal{P} - \dot{W} \geqslant 0 \, , \tag{2.68}$$

where $\dot{W}$ denotes the change of stored energy during the elastoplastic process. Equation (2.68) often is referred to as Clausius-Planck form of the second fundamental theorem of thermodynamics [72]. In view of definitions (2.65) and (2.66) together with (2.67) and (2.64) the dissipation inequality, specialized for the considered flow theory of plasticity, is finally recast as

$$\begin{aligned} \mathcal{D} &= \boldsymbol{\sigma} : \dot{\boldsymbol{\varepsilon}} - (\boldsymbol{\sigma} : \dot{\boldsymbol{\varepsilon}}_{\mathrm{e}} - \boldsymbol{q} \bullet \dot{\boldsymbol{\alpha}}) \\ &= \boldsymbol{\sigma} : \dot{\boldsymbol{\varepsilon}}_{\mathrm{p}} + \boldsymbol{q} \bullet \dot{\boldsymbol{\alpha}} \geqslant 0 \, . \end{aligned} \tag{2.69}$$

2.4.2.1 The principle of maximum dissipation

So far, the stress tensor $\boldsymbol{\sigma}$ and the stress-like hardening variable $\boldsymbol{q}$ have been derived from the stored energy potential according to equations (2.65) and (2.66). To complete the formulation, it remains to establish the evolution equations for the conjugate plastic strain tensor $\boldsymbol{\varepsilon}_{\mathrm{p}}$ and the internal strain-like variable $\boldsymbol{\alpha}$. This can be achieved by employing the *principle of maximum*

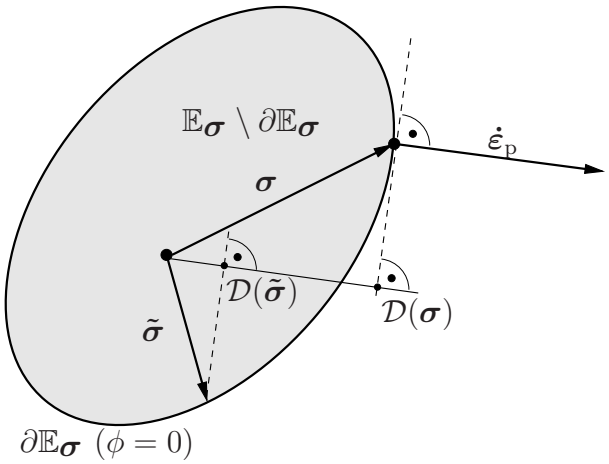

Figure 2.4: Convex elastic domain $\mathbb{E}_{\boldsymbol{\sigma}}$ and geometrical interpretation of the principle of maximum plastic dissipation for perfect plasticity.

plastic dissipation. The principle states that for a given inelastic strain rate $\dot{\boldsymbol{\varepsilon}}_{\mathrm{p}}$, from all admissible stress states $\tilde{\boldsymbol{\sigma}}$ the current state $\boldsymbol{\sigma}$ is the one that maximizes the internal dissipation $\mathcal{D}$. A geometrical interpretation of this principle for the perfectly plastic case is depicted in Figure 2.4.

Adopting this principle (e.g., [114, 72]) — i.e., postulating the dissipation according to (2.69) to be maximized within the space of admissible stresses $\mathbb{E}_{\boldsymbol{\sigma}}$ — a constrained maximization problem is obtained. This is then transferred to an equivalent unconstrained minimization problem by means of the LAGRANGE-functional (see, e.g., LUENBERGER [67])

$$\mathcal{L}\left(\boldsymbol{\sigma}, \boldsymbol{q}, \lambda\right) = -\mathcal{D} + \lambda\phi\left(\boldsymbol{t}, \boldsymbol{q}\right) \ , \tag{2.70}$$

where the LAGRANGE factor λ in the present context usually goes by the name *plastic multiplier*. The solution of this problem is determined by the stationarity requirement of (2.70), leading to

$$\frac{\mathcal{L}}{\partial\boldsymbol{\sigma}} \stackrel{!}{=} 0 \quad \Rightarrow \quad \dot{\boldsymbol{\varepsilon}}_{\mathrm{p}} = \lambda\, \partial_{,\boldsymbol{\sigma}}\phi \qquad (\textit{flow rule}) \tag{2.71}$$

$$\frac{\mathcal{L}}{\partial\boldsymbol{q}} \stackrel{!}{=} 0 \quad \Rightarrow \quad \dot{\boldsymbol{\alpha}} = \lambda\, \partial_{,\boldsymbol{q}}\phi \qquad (\textit{hardening rule}) \tag{2.72}$$

accomplished by the so-called KARUSH-KUHN-TUCKER conditions

$$\lambda \geqslant 0, \quad \phi\left(\boldsymbol{t}, \boldsymbol{q}\right) \leqslant 0, \quad \lambda\phi\left(\boldsymbol{t}, \boldsymbol{q}\right) = 0 \ . \tag{2.73}$$

The so obtained flow rule (2.71) and hardening rule (2.72) are termed *associative* since they are obtained by the respective partial derivatives of the same potential function, namely the yield function ϕ. The concept can be generalized by introducing the additional potentials g and h for flow rule and hardening rule, respectively. The generalized, non-associative versions of the evolution equations then read:

$$\dot{\boldsymbol{\varepsilon}}_{\mathrm{p}} = \lambda\, \partial_{,\boldsymbol{\sigma}} g \qquad \text{and} \qquad \dot{\boldsymbol{\alpha}} = \lambda\, \partial_{,\boldsymbol{q}} h \tag{2.74}$$

When adopting the non-associative evolution equations, of course, the notion of maximum dissipation is lost.

According to the KARUSH-KUHN-TUCKER condition $(2.73)_3$, plastic flow characterized by $\lambda > 0$ can only occur for $\phi = 0$. Further, stress states with $\phi > 0$ are not permitted due (2.62), so the rate of the yield function's change is also zero during plastic flow. This consideration leads to the *consistency condition*

$$\lambda\dot{\phi} = 0 \; . \tag{2.75}$$

Equation (2.75) alternatively is termed *persistency condition* [114], since it requires the stress state to 'persist' on $\partial\mathbb{E}_{\boldsymbol{\sigma}}$ during plastic flow.

2.4.2.2 The constitutive tangent stiffness

Assuming that the current values of all variables as well as the rate of the total strain are given, the so far developed basic equations allow the computation of the remaining variables' rates. If plastic loading takes place, i.e., $\lambda > 0$, the rate of the plastic multiplier λ can be obtained from the consistency condition (2.75). To this end, applying the chain rule, it is recast as

$$\dot{\phi} = \frac{\partial\phi}{\partial\boldsymbol{\sigma}} : \dot{\boldsymbol{\sigma}} + \frac{\partial\phi}{\partial\boldsymbol{q}} \bullet \dot{\boldsymbol{q}} = 0 \; . \tag{2.76}$$

Further, $\dot{\boldsymbol{\sigma}}$ is expressed using (2.64) and $(2.74)_1$ as

$$\dot{\boldsymbol{\sigma}} = \mathbb{C} : (\dot{\boldsymbol{\varepsilon}} - \lambda\, \partial_{,\boldsymbol{\sigma}} g) \tag{2.77}$$

and $\dot{\boldsymbol{q}}$ is expanded by means of $(2.74)_2$ as

$$\dot{\boldsymbol{q}} = \frac{\partial\boldsymbol{q}}{\partial\boldsymbol{\alpha}}\dot{\boldsymbol{\alpha}} = -\lambda\, \boldsymbol{H}\frac{\partial h}{\partial\boldsymbol{q}} \; . \tag{2.78}$$

In (2.78) the definition $\boldsymbol{H} := -\partial\boldsymbol{q}/\partial\boldsymbol{\alpha}$ was introduced while in (2.77) the fourth-order constitutive tangent according to (2.55) was employed. Substituting (2.77) and (2.78) into consistency condition (2.76), yields a linear equation for the plastic multiplier λ:

$$\lambda = \frac{\partial_{,\boldsymbol{\sigma}}\phi : \mathbb{C} : \dot{\boldsymbol{\varepsilon}}}{\partial_{,\boldsymbol{\sigma}}\phi : \mathbb{C} : \partial_{,\boldsymbol{\sigma}} g + \partial_{,\boldsymbol{q}}\phi \bullet \boldsymbol{H} \bullet \partial_{,\boldsymbol{q}} h} \tag{2.79}$$

Substitution of this result back into (2.77) puts forth the rate form of the elastoplastic stress-strain law as

$$\dot{\boldsymbol{\sigma}} = \left(\mathbb{C} - \frac{\mathbb{C} : \partial_{,\boldsymbol{\sigma}} g \otimes \partial_{,\boldsymbol{\sigma}}\phi : \mathbb{C}}{\partial_{,\boldsymbol{\sigma}}\phi : \mathbb{C} : \partial_{,\boldsymbol{\sigma}} g + \partial_{,\boldsymbol{q}}\phi \bullet \boldsymbol{H} \bullet \partial_{,\boldsymbol{q}} h} \right) : \dot{\boldsymbol{\varepsilon}} \; . \tag{2.80}$$

The term in parantheses represents the fourth-order *elastoplastic constitutive tangent* tensor, commonly denoted as $\mathbb{C}_{\text{ep}}$.

1. Linear elastic isotropic constitutive relationship:

$$\dot{\boldsymbol{\sigma}} = \mathbb{C}(\dot{\boldsymbol{\varepsilon}} - \dot{\boldsymbol{\varepsilon}}_{\mathrm{p}})$$

2. Admissible stress space:

$$\mathbb{E}_{\boldsymbol{\sigma}} := \{(\boldsymbol{\sigma}, \boldsymbol{q}) \in \mathbb{S} \times \mathbb{R}^n \mid \phi\,(\boldsymbol{\sigma}, \boldsymbol{q}) \leqslant 0\} \qquad \forall \boldsymbol{X} \in \Omega$$

3. Non-associated flow rule and hardening rule:

$$\dot{\boldsymbol{\varepsilon}}_{\mathrm{p}} = \lambda \frac{\partial g}{\partial \boldsymbol{\sigma}} \quad , \quad \dot{\boldsymbol{\alpha}} = \lambda \frac{\partial h}{\partial \boldsymbol{q}} \quad \text{and} \quad \dot{\boldsymbol{q}} = -\lambda \boldsymbol{H} \frac{\partial h}{\partial \boldsymbol{q}}$$

4. Karush-Kuhn-Tucker conditions:

$$\lambda \geqslant 0, \quad \phi\,(\boldsymbol{t}, \boldsymbol{q}) \leqslant 0, \quad \lambda \phi\,(\boldsymbol{t}, \boldsymbol{q}) = 0$$

5. Consistency condition:

$$\lambda \dot{\phi}(\boldsymbol{\sigma}, \boldsymbol{q}) = 0$$

Table 2.1: Rate independent flow theory of plasticity with non-associated flow and hardening rules

It should be noted that the elastoplastic constitutive tangent $\mathbb{C}_{\mathrm{ep}}$ in general is not symmetric anymore. Merely for the particular case of an associative flow rule, for which the equivalence $\partial_{,\boldsymbol{\sigma}} g \equiv \partial_{,\boldsymbol{\sigma}} \phi$ holds, symmetry of the constitutive tangent tensor is maintained.

Table 2.1 summarizes the essential ingredients of the flow theory of plasticity for the more general case of non-associated flow and hardening rules, respectively.

Chapter 3

The finite element method

The Law of Conservation of Energy tells us
we can't get something for nothing,
but we refuse to believe it.
– Isaac Asimov

The finite element method (FEM) represents a general numerical procedure for obtaining an approximate solution to the mathematical formulation of a model problem, given by a partial differential equation. Applying this method, the underlying formulation is not solved analytically but the solution is approximated by a finite number of operations. This is essentially achieved by discretization of the unknown variable fields along with the introduction of trial functions, i.e., reducing the problem size to a finite number of unknowns (degrees of freedom). Naturally, the quality of the approximation is directly influenced by the number of degrees of freedom.

3.1 Discretization

The basis for the subsequently discussed discretization procedure is the generalized variational formulation (2.51), set out in Section 2.3. The corresponding procedure for the pure displacement formulation, as constituted by the weak form of equilibrium (2.26), is then simply derived by neglecting the enhanced terms. As alluded to above, the scope of this work is limited to infinitesimal theory, i.e., small strains and small deformations are assumed. Accordingly, in what follows, reference and current configuration of the continuum body are not distinguished and all coordinate specifications consistently refer to the reference configuration.

To begin with, in the context of a finite element approximation it is convenient to render the fundamental ingredients of the underlying variational formulation (2.51) in matrix notation.

3.1.1 Transition to matrix notation

To this end, we express the displacement vector $\mathbf{u}$ and its variation $\delta\mathbf{u}$ as

$$\mathbf{u} \;=\; [u_x,\, u_y,\, u_z]^T \qquad \text{and} \qquad \delta\mathbf{u} \;=\; [\delta u_x,\, \delta u_y,\, \delta u_z]^T \,. \tag{3.1}$$

Exploiting the symmetry properties of the compatible strain tensor $\boldsymbol{\varepsilon}^c = \boldsymbol{\nabla}^{\mathrm{sym}}\boldsymbol{u}$, we have six independent scalar variables that can be written in VOIGT notation [1] as

$$\boldsymbol{\varepsilon}^c = [\,\varepsilon_x,\, \varepsilon_y,\, \varepsilon_z,\, \gamma_{xy},\, \gamma_{yz},\, \gamma_{xz}\,]^T \,, \tag{3.2}$$

where $\gamma_{ij} = \varepsilon_{ij} + \varepsilon_{ji}, i \neq j$. Accordingly, for the enhanced strains, we have

$$\tilde{\boldsymbol{\varepsilon}} = [\,\tilde{\varepsilon}_x,\, \tilde{\varepsilon}_y,\, \tilde{\varepsilon}_z,\, \tilde{\gamma}_{xy},\, \tilde{\gamma}_{yz},\, \tilde{\gamma}_{xz}\,]^T \,. \tag{3.3}$$

The compatible strains (3.2) depend on the displacements via the differential operator matrix $\mathbf{L}$:

$$\boldsymbol{\varepsilon}^c \;=\; \mathbf{L}\,\mathbf{u} \qquad \text{with} \quad \mathbf{L} \;=\; \begin{bmatrix} \dfrac{\partial}{\partial X} & 0 & 0 \\ 0 & \dfrac{\partial}{\partial Y} & 0 \\ 0 & 0 & \dfrac{\partial}{\partial Z} \\ \dfrac{\partial}{\partial Y} & \dfrac{\partial}{\partial X} & 0 \\ 0 & \dfrac{\partial}{\partial Z} & \dfrac{\partial}{\partial Y} \\ \dfrac{\partial}{\partial Z} & 0 & \dfrac{\partial}{\partial X} \end{bmatrix} \tag{3.4}$$

The stresses $\boldsymbol{\sigma}$ are related to the strains (3.2) via a rate form constitutive (cf. equations (2.54) and (2.80)) of the form

$$\dot{\boldsymbol{\sigma}} = [\,\dot{\sigma}_x,\; \dot{\sigma}_y,\; \dot{\sigma}_z,\; \dot{\tau}_{xy},\; \dot{\tau}_{yz},\; \dot{\tau}_{zx}\,]^T = \mathbf{C}\,\dot{\boldsymbol{\varepsilon}} \,. \tag{3.5}$$

For linear elasticity, the matrix $\mathbf{C}$ is identified as the counterpart to the constitutive tensor $\mathbb{C}$ (2.61) and renders [2]

$$\mathbf{C} \;=\; \frac{1}{3}\begin{bmatrix} 3\kappa+4\mu & 3\kappa-2\mu & 3\kappa-2\mu & 0 & 0 & 0 \\ 3\kappa-2\mu & 3\kappa+4\mu & 3\kappa-2\mu & 0 & 0 & 0 \\ 3\kappa-2\mu & 3\kappa-2\mu & 3\kappa+4\mu & 0 & 0 & 0 \\ 0 & 0 & 0 & 3\,\mu & 0 & 0 \\ 0 & 0 & 0 & & 3\,\mu & 0 \\ 0 & 0 & 0 & & 0 & 3\,\mu \end{bmatrix} , \tag{3.6}$$

[1] See BELYTSCHKO et al. [11] and references therein for a definition of VOIGT notation and further reading.

[2] Due to the definition of engineering shear strains as $\gamma_{ij} = \varepsilon_{ij} + \varepsilon_{ji}, i \neq j$, the respective components in (3.6) are multiplied by $\frac{1}{2}$.

with the bulk modulus κ and the shear modulus μ being defined according to Section 2.4.1.

3.1.2 Finite element representation

Let the continuum body $\Omega_0 \in \mathbb{R}^3$ be represented by means of a union of finite elements Ω_e, so that $\Omega_0 = \bigcup_{e=1}^{n_{el}} \Omega_e$. Let furthermore a set of basis functions $N_i, i = 1, \dots, n_{\text{edof}}$ and $G_i, i = 1, \dots, n_{\tilde{\varepsilon}}$ be defined on each element Ω_e. Then, the trial functions for the approximate solution $(\bullet)_h$ to the exact solution $(\bullet)_{ex}$ of the variational formulation (2.51) can be stated as

$$\mathbf{u}_h = \sum_{e=1}^{n_{el}} \sum_{i=1}^{n_{\text{edof}}} \chi_e \, d_i \mathbf{N}_i(\mathbf{X}) =: \sum_{e=1}^{n_{el}} \chi_e \, \mathbf{N}^{n_{\text{dim}} \times n_{\text{edof}}} \, \mathbf{d} \tag{3.7}$$

for the displacement field and

$$\tilde{\boldsymbol{\varepsilon}}_h = \sum_{e=1}^{n_{el}} \sum_{i=1}^{n_{\tilde{\varepsilon}}} \chi_e \, \mu_i \mathbf{G}_i(\mathbf{X}) =: \sum_{e=1}^{n_{el}} \chi_e \, \mathbf{G}^{n_{\text{strn}} \times n_{\tilde{\varepsilon}}} \, \boldsymbol{\mu} \tag{3.8}$$

for the enhanced strain field approximation. By $\mathcal{V}^h \subset \mathcal{V}$ and $\tilde{\mathcal{E}}^h \subset \tilde{\mathcal{E}}$ we denote the finite element spaces of displacements and enhanced strains, so that $\mathbf{u}_h \in \mathcal{V}^h$ and $\tilde{\boldsymbol{\varepsilon}}_h \in \tilde{\mathcal{E}}^h$. The characteristic function $\chi_e : \Omega_e \mapsto \mathbb{R}$ is defined as

$$\chi_e = \begin{cases} 1 & \text{iff} \quad \mathbf{X} \in \Omega_e, \\ 0 & \text{otherwise.} \end{cases} \tag{3.9}$$

and serves as a filter to prevent spurious contributions from other elements but the active one.

There is an infinite number of functions $\delta\boldsymbol{u}$ and $\delta\tilde{\boldsymbol{\varepsilon}}$, that are admissible and must satisfy equations (2.51). Since it is generally not possible to "test" against an infinite number of variations, an analogous approximation as for the variable fields is also introduced for the corresponding variations, which constitutes the so-called Bubnov-Galerkin method. In a more general setting however, the corresponding *test* function space may be different from the *trial* function space, furnishing a Petrov-Galerkin scheme (Simo & Oliver [115]; Oliver [88]). In view of later developments we employ such a concept for the enhanced strain variations and define a corresponding weighting space of admissible test functions $\mathcal{E}^h_\delta$, such that $\mathcal{E}^h_\delta \neq \mathcal{E}^h$; we set

$$\begin{aligned} \delta\mathbf{u} &= \sum_{e=1}^{n_{el}} \sum_{i=1}^{n_{\text{edof}}} \chi_e \, \delta d_i \mathbf{N}_i(\mathbf{X}) =: \sum_{e=1}^{n_{el}} \chi_e \, \mathbf{N}^{n_{\text{dim}} \times n_{\text{edof}}} \, \delta\mathbf{d} \\ \delta\tilde{\boldsymbol{\varepsilon}} &= \sum_{e=1}^{n_{el}} \sum_{i=1}^{n_{\tilde{\varepsilon}}} \chi_e \, \delta\mu_i \hat{\mathbf{G}}_i(\mathbf{X}) =: \sum_{e=1}^{n_{el}} \chi_e \, \hat{\mathbf{G}}^{n_{\text{strn}} \times n_{\tilde{\varepsilon}}} \, \delta\boldsymbol{\mu} \end{aligned} \tag{3.10}$$

where $\delta\boldsymbol{u} \in \mathcal{V}^h$ and $\delta\tilde{\boldsymbol{\varepsilon}} \in \mathcal{E}^h_\delta$. The particular form of the element basis functions $\mathbf{N}$ is treated in Section 3.2 and the characteristics of $\mathbf{G}$ and $\hat{\mathbf{G}}$ are closely connected with the incorporation of

strong discontinuities into the formulation, see Section 4.4. Restricting conditions that apply to the choices of spaces for $\tilde{\boldsymbol{\varepsilon}}$ and $\delta\tilde{\boldsymbol{\varepsilon}}$ are discussed in Section 4.4, as well.

Adopting the interpolations (3.7), (3.8) and (3.10), along with the definition

$$\mathbf{B} := \mathbf{L}\mathbf{N} \,, \tag{3.11}$$

the variational equations (2.51) and its linearized form (2.52) are finally recast as

$$\boxed{\begin{aligned} &\mathop{\mathsf{A}}_{e=1}^{n_{el}} \Big| \; \delta\mathbf{d}^T \left[\int_{\Omega_e} \mathbf{B}^T \, \hat{\boldsymbol{\sigma}} \; dV - \int_{\Omega_e} \mathbf{N}^T \, \mathbf{b} \; dV - \int_{\partial\Omega_e} \mathbf{N}^T \, \mathbf{t}^* \; dA \right] = 0 \\ &\mathop{\mathsf{A}}_{e=1}^{n_{el}} \Big| \; \delta\boldsymbol{\mu}^T \left[\int_{\Omega_e} \hat{\mathbf{G}}^T \, \hat{\boldsymbol{\sigma}} \; dV \right] = 0 \end{aligned}} \tag{3.12}$$

and

$$\boxed{\begin{aligned} &\mathop{\mathsf{A}}_{e=1}^{n_{el}} \Big| \; \delta\mathbf{d}^T \left[\int_{\Omega_e} \mathbf{B}^T\mathbf{C}\mathbf{B} \; dV \; \dot{\mathbf{d}} + \int_{\Omega_e} \mathbf{B}^T\mathbf{C}\mathbf{G} \; dV \; \dot{\boldsymbol{\mu}} + \right. \\ &\qquad\qquad \left. + \int_{\Omega_e} \mathbf{B}^T \hat{\boldsymbol{\sigma}} \; dV - \int_{\Omega_e} \mathbf{N}^T \mathbf{b} \; dV - \int_{\partial\Omega_e} \mathbf{N}^T \, \mathbf{t}^* \; dA \right] = 0 \\ &\mathop{\mathsf{A}}_{e=1}^{n_{el}} \Big| \; \delta\boldsymbol{\mu}^T \left[\int_{\Omega_e} \hat{\mathbf{G}}^T\mathbf{C}\mathbf{B} \; dV \; \dot{\mathbf{d}} + \int_{\Omega_e} \hat{\mathbf{G}}^T\mathbf{C}\mathbf{G} \; dV \dot{\boldsymbol{\mu}} + \int_{\Omega_e} \hat{\mathbf{G}}^T \hat{\boldsymbol{\sigma}} \; dV \right] = 0 \end{aligned}} \tag{3.13}$$

where $\mathop{\mathsf{A}}_{e=1}^{n_{el}}$ denotes the standard assembly operator. Considering that the variations $\delta\mathbf{d}$ and $\delta\boldsymbol{\mu}$ are arbitrary, from (3.13) we conclude

$$\mathop{\mathsf{A}}_{e=1}^{n_{el}} \Big| \underbrace{\begin{bmatrix} {}^{\mathrm{bb}}\mathbf{K}_e & {}^{\mathrm{bg}}\mathbf{K}_e \\ {}^{\mathrm{gb}}\mathbf{K}_e & {}^{\mathrm{gg}}\mathbf{K}_e \end{bmatrix}}_{=:\mathbf{K}_e} \begin{Bmatrix} \dot{\mathbf{d}} \\ \dot{\boldsymbol{\mu}} \end{Bmatrix} = \begin{Bmatrix} \mathbf{f}_e^{\mathrm{ext}} - \mathbf{f}_e^{\mathrm{int}} \\ -\mathbf{h}_e \end{Bmatrix} \,, \tag{3.14}$$

where we have employed the definitions

$$\begin{aligned} {}^{\mathrm{bb}}\mathbf{K}_e &:= \int_{\Omega_e} \mathbf{B}^T\mathbf{C}\mathbf{B} \; dV \qquad & {}^{\mathrm{bg}}\mathbf{K}_e &:= \int_{\Omega_e} \mathbf{B}^T\mathbf{C}\mathbf{G} \; dV \\ {}^{\mathrm{gb}}\mathbf{K}_e &:= \int_{\Omega_e} \hat{\mathbf{G}}^T\mathbf{C}\mathbf{B} \; dV \qquad & {}^{\mathrm{gg}}\mathbf{K}_e &:= \int_{\Omega_e} \hat{\mathbf{G}}^T\mathbf{C}\mathbf{G} \; dV \end{aligned} \tag{3.15}$$

and

$$\begin{aligned} \mathbf{f}_e^{\mathrm{ext}} &:= \int_{\Omega_e} \mathbf{N}^T\mathbf{b} \; dV + \int_{\partial\Omega_e} \mathbf{N}^T \, \mathbf{t}^* \; dA \qquad & \mathbf{f}_e^{\mathrm{int}} &:= \int_{\Omega_e} \mathbf{B}^T \hat{\boldsymbol{\sigma}} \; dV \\ \mathbf{h}_e &:= \int_{\Omega_e} \hat{\mathbf{G}}^T \hat{\boldsymbol{\sigma}} \; dV \,. \end{aligned} \tag{3.16}$$

With a view to later developments, we consider as a particular case a *locally* enforced enhanced strain field interpolation — i.e., we drop the requirement of inter element continuity of the additional variables $\boldsymbol{\mu}$. Then, it is possible to eliminate the enhanced variables by static condensation on element level, so that the condensed stiffness matrix $\tilde{\mathbf{K}}_e$ resembles the classical displacement degrees of freedom, only. From (3.14), straightforward calculus yields:

$$\begin{aligned} \underbrace{\left({}^{\mathrm{bb}}\mathbf{K}_e - {}^{\mathrm{bg}}\mathbf{K}_e({}^{\mathrm{gg}}\mathbf{K}_e)^{-1}\,{}^{\mathrm{gb}}\mathbf{K}_e\right)}_{\tilde{\mathbf{K}}_e}\dot{\mathbf{d}} \;&=\; \mathbf{f}_e^{\mathrm{ext}} - \mathbf{f}_e^{\mathrm{int}} + {}^{\mathrm{bg}}\mathbf{K}_e({}^{\mathrm{gg}}\mathbf{K}_e)^{-1}\,\mathbf{h}_e \\ \dot{\boldsymbol{\mu}} \;&=\; -({}^{\mathrm{gg}}\mathbf{K}_e)^{-1}\left(\mathbf{h}_e + {}^{\mathrm{gb}}\mathbf{K}_e\dot{\mathbf{d}}\right) \end{aligned} \tag{3.17}$$

Finally, after assembly, the discretized system of equations emerges:

$$\tilde{\mathbf{K}}\,\dot{\mathbf{d}} = \mathbf{F} \tag{3.18}$$

Where prior to discretization the exact solution $\mathbf{u}_{ex}$ was sought, now the coefficients $\dot{d}_i,\ i = 1,\ldots,n_{\mathrm{dof}}$ are the unknowns that must fulfill the above system of equations and satisfy the geometrical boundary conditions. $\tilde{\mathbf{K}}$ denotes the global (or system) stiffness matrix whereas $\mathbf{F}$ renders the effective total force vector *(out-of-balance force)*. It should be noted that in general, due to the adopted Petrov-Galerkin scheme with $\hat{\mathbf{G}} \neq \mathbf{G}$, we have ${}^{\mathrm{gb}}\mathbf{K}_e \neq ({}^{\mathrm{bg}}\mathbf{K}_e)^T$ — with the consequence that the condensed stiffness matrix $\tilde{\mathbf{K}}$ is no longer symmetric. Further, the system of equations (3.18) can be nonlinear, i.e., $\tilde{\mathbf{K}}$ is not constant but in some way dependent on the unknowns $\mathbf{d}$ — therefore, in general an iterative solution procedure is required.

Remark. Derivation of (3.17) is based on the assumption of regularity — and hence, invertibility — of ${}^{\mathrm{gg}}\mathbf{K}_e$. Consequential implications are discussed in Section 4.4.2. □

Remark. In the case of a pure displacement approach as obtained from the weak form of equilibrium (2.26), the corresponding finite element formulation can simply be derived from the above by neglecting the terms related to the enhanced strains. Thus, from (3.14) we readily obtain

$${}^{\mathrm{bb}}\mathbf{K}_e\,\dot{\mathbf{d}} = \mathbf{f}_e^{\mathrm{ext}} - \mathbf{f}_e^{\mathrm{int}} \tag{3.19}$$

by setting $\dot{\boldsymbol{\mu}} = \mathbf{0}$. □

3.1.2.1 Coordinate transformation for integration over the finite element domain

Element stiffness matrix and load vector initially are functions of $\mathbf{X}$. An efficient and convenient computational scheme is established by defining the element shape functions, discussed in the following section, in a unified manner — namely, on basis of a standard element with local coordinates $\boldsymbol{\xi}$ and domain $\Omega_{\mathrm{st}}^{\mathrm{h}} = [(-1,1)\times(-1,1)\times(-1,1)]$. This, on the other hand, requires a bijective mapping function between global (physical) and local coordinates $\mathbf{X}$ und $\boldsymbol{\xi}$. Let it be defined by the function $\mathbf{Q}^e$ and the unique inverse relation $(\mathbf{Q}^e)^{-1}$.

$$\mathbf{X} = \mathbf{Q}^e(\boldsymbol{\xi}) \qquad \text{und} \qquad \boldsymbol{\xi} \;=\; (\mathbf{Q}^e)^{-1}(\mathbf{X}) \tag{3.20}$$

Using this transformation rule, mapping of the shape functions — which are defined locally in terms of $\boldsymbol{\xi}$ — to the global setting can be expressed as:

$$N_i(\mathbf{X}) = N_i\Big((\mathbf{Q}^e)^{-1}(\mathbf{X})\Big) \;=\; N_i\Big(\boldsymbol{\xi}(\mathbf{X})\Big) \tag{3.21}$$

For the strain-displacement matrix $\mathbf{B}$, the shape function's derivatives with respect to the physical coordinates are required. Accounting for the chain rule, we obtain

$$\begin{bmatrix} \dfrac{\partial N_i}{\partial X} \\ \dfrac{\partial N_i}{\partial Y} \\ \dfrac{\partial N_i}{\partial Z} \end{bmatrix} = \begin{bmatrix} \dfrac{\partial \xi}{\partial X} & \dfrac{\partial \eta}{\partial X} & \dfrac{\partial \zeta}{\partial X} \\ \dfrac{\partial \xi}{\partial Y} & \dfrac{\partial \eta}{\partial Y} & \dfrac{\partial \zeta}{\partial Y} \\ \dfrac{\partial \xi}{\partial Z} & \dfrac{\partial \eta}{\partial Z} & \dfrac{\partial \zeta}{\partial Z} \end{bmatrix} \begin{bmatrix} \dfrac{\partial N_i}{\partial \xi} \\ \dfrac{\partial N_i}{\partial \eta} \\ \dfrac{\partial N_i}{\partial \zeta} \end{bmatrix} = \quad \mathbf{J}^{-1} \quad \begin{bmatrix} \dfrac{\partial N_i}{\partial \xi} \\ \dfrac{\partial N_i}{\partial \eta} \\ \dfrac{\partial N_i}{\partial \zeta} \end{bmatrix}, \tag{3.22}$$

where the JACOBI-matrix $\mathbf{J}$, respectively its inverse, encapsulates the geometry dependent information, thus facilitating the finite element Ansatz spaces being set up in a unified manner, independent of the geometry. Setting

$$\mathbf{J} = \begin{bmatrix} \dfrac{\partial X}{\partial \xi} & \dfrac{\partial Y}{\partial \xi} & \dfrac{\partial Z}{\partial \xi} \\ \dfrac{\partial X}{\partial \eta} & \dfrac{\partial Y}{\partial \eta} & \dfrac{\partial Z}{\partial \eta} \\ \dfrac{\partial X}{\partial \zeta} & \dfrac{\partial Y}{\partial \zeta} & \dfrac{\partial Z}{\partial \zeta} \end{bmatrix}, \qquad \text{we have:} \qquad dX\,dY\,dZ \;=\; \det\mathbf{J}\cdot d\xi\,d\eta\,d\zeta \tag{3.23}$$

Within a high-order finite element framework both the Ansatz spaces and the mapping concept are different from those of the standard h-version. These aspects are considered in detail in Section 3.2 and 3.3, respectively.

3.1.2.2 Computation of the element matrices

Thus, the integration problem has been transformed to the domain $\Omega^{\mathrm{h}}_{\mathrm{st}}$ of the standard element. For computation of the element matrices, the following relations are obtained:

1. element stiffness matrix

$${}^{\mathrm{bb}}\mathbf{K}_e \;=\; \int_{-1}^{1}\int_{-1}^{1}\int_{-1}^{1} \mathbf{B}^T\,\mathbf{C}\,\mathbf{B}\,\det\mathbf{J} \quad d\xi\,d\eta\,d\zeta \tag{3.24}$$

(If required, analogous computation for ${}^{bg}\mathbf{K}_e$, ${}^{gb}\mathbf{K}_e$ and ${}^{gg}\mathbf{K}_e$.)

2. element load vector

$$\mathbf{f}_e^{\text{ext}} = \int_{-1}^{1}\int_{-1}^{1}\int_{-1}^{1} \mathbf{N}^T\,\mathbf{b}\,\det\mathbf{J}\;d\xi\,d\eta\,d\zeta \tag{3.25}$$

$$+ \sum_{i=1}^{6}\int_{-1}^{1}\int_{-1}^{1} \mathbf{N}^T\,\mathbf{t}^*\;|\partial_{,r}\mathbf{X}\times\partial_{,s}\mathbf{X}|\;dr\,ds\,, \tag{3.26}$$

where according to Section 3.3 holds:

$$\begin{aligned} &r=\xi, \quad s=\eta \qquad \text{for} \quad i=1,6\\ &r=\xi, \quad s=\zeta \qquad \text{for} \quad i=2,4\\ &r=\eta, \quad s=\zeta \qquad \text{for} \quad i=3,5 \end{aligned} \tag{3.27}$$

(Analogous computation for $\mathbf{f}_e^{int}$ and possibly $\mathbf{h}_e$.)

3.2 High-order hierarchical ansatz spaces

In order to improve the quality of the finite element approximation, the key characteristic of the finite element *p*-version is the employment of high-order polynomial degrees for the Ansatz functions on a rather coarse spatial finite element discretization of the problem domain. Composition of the Ansatz function space is based on a hierarchical concept, which features several beneficial qualities. The hierarchical concept is characterized by the fundamental idea, that *all Ansatz functions of lower order are contained in the space of Ansatz functions of higher order*. Or, vice-versa: A higher-order Ansatz function space is obtained by simply adding the corresponding higher-order functions to the lower order Ansatz function space. To begin with, the one-dimensional hierarchical basis established by Szabó and Babuška [121] is introduced in Section 3.2.1 and differences to the standard basis are pointed out.

3.2.1 The one-dimensional hierarchical basis

On a two-noded one-dimensional standard element $\Omega_{\text{st}} = [-1, 1]$, the first two Ansatz functions $N_1(\xi)$ and $N_2(\xi)$ defined by equations (3.31) and (3.32) represent the typical linear nodal Ansatz functions, as they are also known from the *h*-version of the finite element method. They each take the value 1 at one node and vanish at the other. $N_1(\xi)$ and $N_2(\xi)$ are, accordingly, part of both the standard and the hierarchical basis (cf. Figure 3.1, left and right).

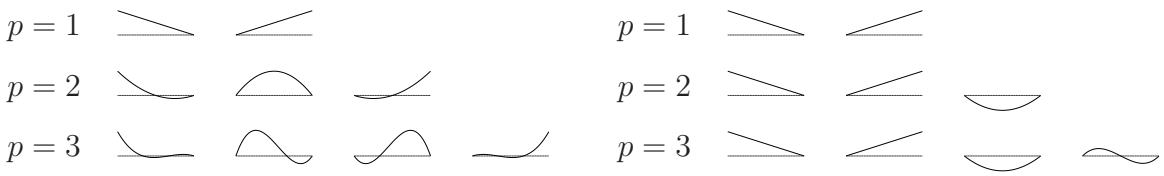

Figure 3.1: One-dimensional standard basis and hierarchical basis for $p = 1, 2, 3$

The higher-order functions of the standard basis (Figure 3.1, left) are defined by LAGRANGE polynomials

$$N_i^p(\xi) = \prod_{j=1,\, j\neq i}^{p+1} \frac{\xi - \xi_j}{\xi_i - \xi_j} \,. \tag{3.28}$$

The description of these polynomials is based on collocation points x_j in the interval $[-1, 1]$, normally arranged equidistant — such that a polynomial N_i^p takes the value 1 at node x_i and 0 at all remaining nodes x_j with $j \neq i$:

$$N_i^p(\xi_j) = \delta_{ij} \tag{3.29}$$

A further distinct feature of the standard basis is rendered by the fact that the sum of all LAGRANGE polynomials for a given polynomial degree p equals 1 for any point $\xi \in [-1, 1]$, the LAGRANGIAN polynomial basis thus features the *partition of unity* property

$$\sum_{i=1}^{p+1} N_i^p\,(\xi) = 1 \,. \tag{3.30}$$

The hierachical concept adopts a completely different approach. On extending the Ansatz to $p > 1$, the existing Ansatz space of the linear functions $N_1(\xi)$ und $N_2(\xi)$ is simply enhanced by each one Ansatz function with the corresponding polynomial degree $N_i(\xi)$, $i = 3, 4, \ldots$, according to (3.33):

$$N_1(\xi) = \frac{1}{2}(1 - \xi) \tag{3.31}$$

$$N_2(\xi) = \frac{1}{2}(1 + \xi) \tag{3.32}$$

$$N_i(\xi) = \phi_{i-1}(\xi), \quad i = 3, 4, \ldots, p + 1 \tag{3.33}$$

One important point is that the higher-order Ansatz functions vanish on the boundary of the interval:

$$N_i(-1) = N_i(1) = 0, \quad i = 3, 4, \ldots \,; \tag{3.34}$$

thus establishing the naming *internal modes* or *bubble modes*. It should be noted, that the polynomials $\phi_j(\xi)$ are defined (see below) without adopting the notion of additional nodes as supporting or collocation points, thus the higher-order Ansatz functions are not associated with a *physical* location on the element.

The polynomials $\phi_j(\xi)$ are obtained by integration of the well-known LEGENDRE polynomials.

$$\phi_j(\xi) = \sqrt{\frac{2j-1}{2}} \int_{-1}^{\xi} L_{j-1}(x)\, dx = \frac{1}{\sqrt{4j-2}} (L_j(\xi) - L_{j-2}(\xi)), \quad j = 2, 3, \ldots \tag{3.35}$$

LEGENDRE polynomials $\{L_n(x)\}_{n=0}^{\infty}$ are solutions to the LEGENDRE differential equation

$$((1-x^2)y')' + n(n+1)y = 0, \quad x \in (-1,1), \quad n = 0, 1, 2, \ldots \tag{3.36}$$

and can be determined, either, using the RODRIGUEZ formula [134]

$$L_n(x) = \frac{1}{2^n\, n!} \frac{d^n}{d\, x^n} (x^2-1)^n, \quad x \in (-1,1), \quad n = 0, 1, 2, \ldots \tag{3.37}$$

or, by recursive multiplication from BONNET's formula [121]:

$$L_n(x) = \frac{1}{n} [(2n-1)xL_{n-1}(x) - (n-1)L_{n-2}(x)], \quad x \in (-1,1),\ n = 2, 3, 4, \ldots \tag{3.38}$$

Exemplarily, the first nine LEGENDRE polynomials read:

$$\begin{aligned}
L_0(x) &= 1\,, \\
L_1(x) &= x\,, \\
L_2(x) &= 3/2\, x^2 - 1/2\,, \\
L_3(x) &= 5/2\, x^3 - 3/2\, x\,, \\
L_4(x) &= 35/8\, x^4 - 15/4\, x^2 + 3/8\,, \\
L_5(x) &= 63/8\, x^5 - 35/4\, x^3 + 15/8\, x\,, \\
L_6(x) &= 231/16\, x^6 - 315/16\, x^4 + 105/16\, x^2 - 5/16\,, \\
L_7(x) &= 429/16\, x^7 - 693/16\, x^5 + 315/16\, x^3 - 35/16\, x\,, \\
L_8(x) &= 6435/128\, x^8 - 3003/32\, x^6 + 3465/64\, x^4 - 315/32\, x^2 + 35/128
\end{aligned} \tag{3.39}$$

An important property of LEGENDRE polynomials is their orthogonality in the integration interval $(-1, 1)$, so that:

$$\int_{-1}^{1} L_n(x) L_m(x)\, dx = \begin{cases} \dfrac{2}{2n+1} & \text{if} \quad n = m \\ 0 & \text{else} \end{cases} \tag{3.40}$$

This distinct property is the reason, why for the polynomials $\phi_j(\xi)$ (3.35) — and thus the Ansatz functions $N_i(\xi)$ (3.33) — the integrated form (3.35) of the LEGENDRE polynomials is adopted. Consider the computation of the element stiffness matrix according to equation (3.24) for our one-dimensional standard element $\Omega_{\text{st}} = [-1, 1]$. Assume $\mathbf{C}$ constant and note, that the strain-displacement matrix $\mathbf{B}$ is essentially the derivative of the Ansatz functions $\mathbf{N}$. Then, it is evident that off-diagonal terms in the element stiffness matrix that correspond to higher-order modes are identically zero due to the orthogonality property (3.40). In general, a non-constant $\mathbf{C}$ or the Jacobian (3.23) may effect non-zero values also for these off-diagonal

terms — nevertheless, the consideration motivates a superior conditioning of the element stiffness matrix, thus, also of the system stiffness matrix, when compared to the standard Ansatz space.

Every function, that can be represented by the standard basis, can equally be described by the hierarchical basis. The latter is superior to the standard basis in several respects:

- As already alluded to, it improves the conditioning of the stiffness matrix, facilitating a faster and more stable iterative solution of the system of equations.
- If degrees of freedom are organized properly, the resulting stiffness matrix inherits the hierarchical structure of the Ansatz space, featuring a straightforward elimination of internal modes by static condensation and thus, improvement of the efficiency of the solution process.

3.2.2 Hierarchical Ansatz space for quadrilaterals

Composition of the two-dimensional Ansatz space for quadrilaterals follows the basis introduced by Szabó and Babuška [121]. The corresponding standard element $\Omega^{\mathrm{q}}_{\mathrm{st}} = [(-1,1) \times (-1,1)]$ is depicted in Figure 3.2.

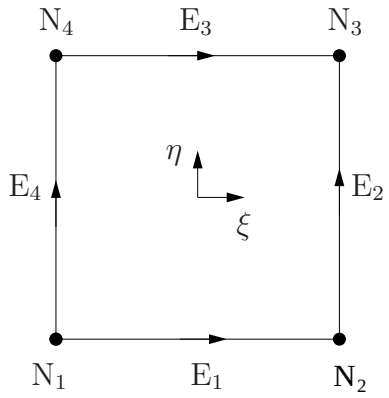

Figure 3.2: Definition of nodes and edges in the quadrilateral standard element

The two-dimensional Ansatz space is simply formed by the tensor product of the one-dimensional hierarchical basis. By construction, three types of Ansatz functions can be identified.

1. **Nodal modes**:
   The nodal modes

$$N^{\mathrm{N}_i}_{1,1}(\xi,\eta) = \frac{1}{4}\,(1+\xi_i\,\xi)(1+\eta_i\,\eta)\,, \quad i = 1,\ldots,4 \tag{3.41}$$

correspond to the standard bilinear Ansatz functions, as they are known from the isoparametric quadrilateral element. As in the one-dimensional case (ξ_i, η_i) denote the local coordinates of the i-th node. Figure 3.3, exemplarily illustrates the Ansatz function for node 1.

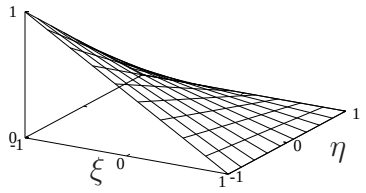

Figure 3.3: Node 1: $N_{1,1}^{\mathrm{N}_1}(\xi,\eta) = \frac{1}{4}(1-\xi)(1-\eta)$

2. **Edge modes**:
   Edge modes are those constituents of the tensor product space that are formed by the product of each one internal and one corresponding orthogonal nodal Ansatz function of the one-dimensional basis. Thus, an edge mode takes the value of the corresponding internal mode along one edge and vanishes at all remaining edges. The respective modes for edge E_1 read

$$N_{i,1}^{\mathrm{E}_1}(\xi,\eta) = \frac{1}{2}(1-\eta)\phi_i(\xi)\ . \tag{3.42}$$

   For $i = 2$ along edge 1, the corresponding mode is plotted in 3.4.

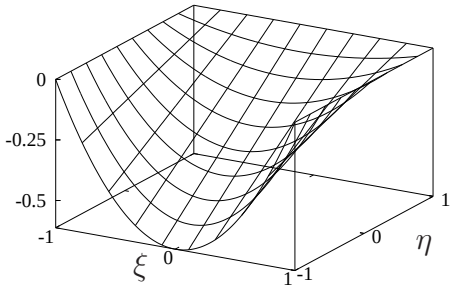

Figure 3.4: Edge 1 $(i = 2)$: $N_{2,1}^{\mathrm{E}_1}(\xi,\eta) = \frac{1}{2}(1-\eta)\phi_2(\xi)$

3. **Internal modes** (*bubble modes*):
   Internal modes, finally, are formed by multiplication of two orthogonal internal Ansatz functions of the one-dimensional basis, see equation (3.43).

$$N_{i,j}^{\mathrm{int}}(\xi,\eta) = \phi_i(\xi)\phi_j(\eta) \tag{3.43}$$

As a consequence, internal modes are purely local to the element and vanish at the edges. Exemplarily, Figure 3.5 depicts the internal mode for $i = j = 2$.

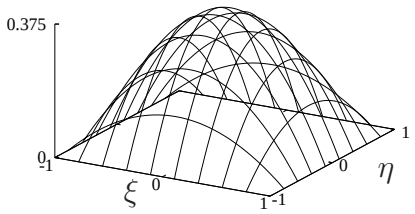

Figure 3.5: Internal mode ($i = j = 2$): $N^{\text{int}}_{2,2}(\xi, \eta) = \phi_2(\xi)\phi_2(\eta)$

The indices i, j of the Ansatz functions correspond to the polynomial degress p_ξ and p_η of the standard element's $\Omega^{\text{q}}_{\text{st}}$ local directions ξ, η.

3.2.3 Hierarchical Ansatz space for hexahedral elements

The extension to a three-dimensional Ansatz space for hexahedrals follows completely analogous lines as for the quadrilateral case. Again, the starting point is the one-dimensional hierarchical basis, introduced by Szabó and Babuška [121]. The three-dimensional Ansatz space is then formed by the tensor product of three mutually orthogonal one-dimensional bases, accounting for the three distinct directions ξ, η and ζ. The hexahedral standard element $\Omega^{\text{q}}_{\text{st}} = [(-1, 1) \times (-1, 1) \times (-1, 1)]$ is depicted in Figure 3.6.

For this three-dimensional extended case, four types of Ansatz functions can be identified.

1. **Nodal modes**:
   The eight nodal modes (3.44), defined by the product of each three mutually orthogonal nodal Ansatz functions of the one-dimensional basis, reflect the trilinear Ansatz functions of the standard isoparametric hexahedral element. (ξ_i, η_i, ζ_i) denote the local coordinates of node i.

$$N^{\text{N}_i}_{1,1,1}(\xi, \eta, \zeta) = \frac{1}{8}(1 + \xi_i\,\xi)(1 + \eta_i\,\eta)(1 + \zeta_i\zeta), \quad i = 1, \ldots, 8 \tag{3.44}$$

2. **Edge modes**:
   They are associated with each one of the twelve element edges and vanish at all remaining edges. The Ansatz functions of edge E_1 (cf. Figure 3.6), e.g., are defined by equation (3.45).

$$N^{\text{E}_1}_{i,1,1}(\xi, \eta, \zeta) = \frac{1}{4}(1 - \eta)(1 - \zeta)\phi_i(\xi) \tag{3.45}$$

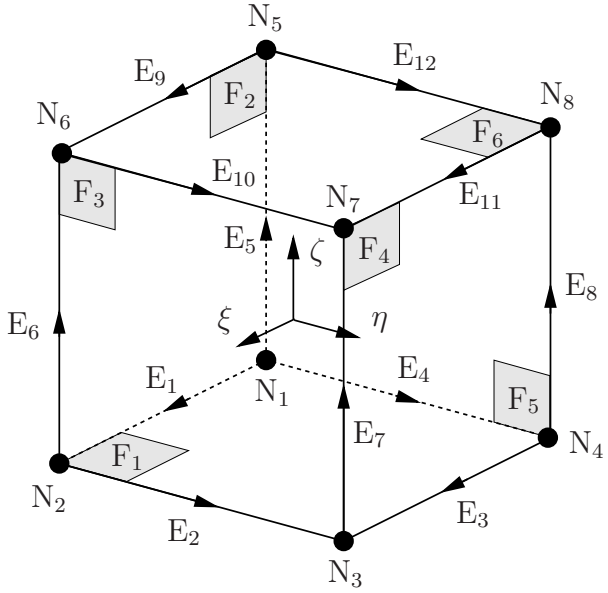

$$\Omega^{\mathrm{h}}_{\mathrm{st}} = [(-1,1) \times (-1,1) \times (-1,1)]$$

Figure 3.6: Definition of nodes edges and faces for the hexahedral standard element

3. **Face modes**:
   The six face modes are the product of two internal one-dimensional Ansatz functions and one nodal one-dimensional Ansatz function — each mutually orthogonal. Thus, each face mode takes values different from zero on precisely one associated face, while it vanishes at the other faces. The Ansatz functions for face F_1, e.g., read

$$N^{\mathrm{F}_1}_{i,j,1}(\xi,\eta,\zeta) \;=\; \frac{1}{2}\,(1-\zeta)\phi_i(\xi)\phi_j(\eta)\;. \tag{3.46}$$

4. **Internal modes** (*bubble modes*):
   Analogous to the one- and two-dimensional case, internal modes are purely local to the element and vanish at its boundary.

$$N^{\mathrm{int}}_{i,j,k}(\xi,\eta,\zeta) \;=\; \phi_i(\xi)\phi_j(\eta)\phi_k(\zeta) \tag{3.47}$$

The indices i, j, k of the Ansatz functions denote the polynomial degrees p_ξ, p_η and p_ζ with respect to the local directions ξ, η, ζ of the standard element $\Omega^{\mathrm{h}}_{\mathrm{st}}$.

Having finally defined the complete set of Ansatz functions for the three-dimensional hexaedral element, matrix $\mathbf{N}$ introduced in $(3.10)_1$ can now be further particularized as

$$\mathbf{N} = \left[\, \mathbf{N}^{\mathrm{N}} \quad \mathbf{N}^{\mathrm{E}} \quad \mathbf{N}^{\mathrm{F}} \quad \mathbf{N}^{\mathrm{B}} \,\right]\;, \tag{3.48}$$

superscript N, E, F and B denoting the *nodal*, *edge*, *face* and *internal (bubble)* modes, respectively.

3.2.4 Various specifications of Ansatz spaces

The Ansatz space $\mathcal{S}$ of a finite element computation is spanned by a set of Ansatz functions of above discussed type. For the two- and three-dimensional case however, different specifications regarding the completeness of the Ansatz space are possible.

- In the one-dimensional case, the degree p of the Ansatz space $\mathcal{S}_{\mathrm{ps}}^{p_\xi}(\Omega_{\mathrm{st}})$ corresponds directly to the polynomial degree of the Ansatz function in direction ξ.

- In two dimensions, description of the Ansatz spaces depends on the local directions ξ und η and the respective chosen polynomial degress p_ξ and p_η. Szabó und Babuška [121] distinguish two types of Ansatz spaces, the *trunk space* $\mathcal{S}_{\mathrm{ts}}^{p_\xi,p_\eta}(\Omega_{\mathrm{st}}^{\mathrm{q}})$ and the *tensor product space* $\mathcal{S}_{\mathrm{ps}}^{p_\xi,p_\eta}(\Omega_{\mathrm{st}}^{\mathrm{q}})$. The latter is also termed *full* space, since it comprehends the complete set of functions emerging from the tensor product of the two one-dimensional hierarchical bases $\mathcal{S}_{\mathrm{ps}}^{p_\xi}(\Omega_{\mathrm{st}})$ and $\mathcal{S}_{\mathrm{ps}}^{p_\eta}(\Omega_{\mathrm{st}})$. Formally, the *tensor product space* $\mathcal{S}_{\mathrm{ps}}^{p_\xi,p_\eta}(\Omega_{\mathrm{st}}^{\mathrm{q}})$ consists of all polynomials on the standard element $\Omega_{\mathrm{st}}^{\mathrm{q}} = [(-1,1)\times(-1,1)]$ that are spanned by the set of monomials

  $$\xi^i\,\eta^j \qquad \text{with} \quad i=0,1,\ldots,p_\xi, \quad j=0,1,\ldots,p_\eta\ .$$

  The *trunk space* $\mathcal{S}_{\mathrm{ts}}^{p_\xi,p_\eta}(\Omega_{\mathrm{st}}^{\mathrm{q}})$, on the other hand, is spanned by the reduced set of monomials

  $$\xi^i\eta^j \qquad \text{with} \quad i=0,\ldots,p_\xi, \quad j=0,\ldots,p_\eta, \quad i+j=0,\ldots,\max\{p_\xi,p_\eta\}\ ,$$

  complemented by

  $$\begin{array}{rll} \xi\,\eta & \text{for} & p_\xi = p_\zeta = 1 \\ \xi^{p_\xi}\,\eta & \text{for} & p_\xi \geq 2 \\ \xi\,\eta^{p_\eta} & \text{for} & p_\eta \geq 2\ . \end{array}$$

  The difference between the two Ansatz spaces can nicely be visualized by means of Pascal's triangle. For comparison, the Ansatz spaces $\mathcal{S}_{\mathrm{ts}}^{3,3}(\Omega_{\mathrm{st}}^{\mathrm{q}})$ and $\mathcal{S}_{\mathrm{ps}}^{3,3}(\Omega_{\mathrm{st}}^{\mathrm{q}})$ are contrasted in Figure 3.7.

- For the three-dimensional case, in addition to *trunk space* $\mathcal{S}_{\mathrm{ts}}^{p_\xi,p_\eta,p_\zeta}(\Omega_{\mathrm{st}}^{\mathrm{h}})$ and *tensor product space* $\mathcal{S}_{\mathrm{ps}}^{p_\xi,p_\eta,p_\zeta}(\Omega_{\mathrm{st}}^{\mathrm{h}})$, a third variant can be identified — the *anisotropic tensor product space* $\mathcal{S}^{p,p,q}(\Omega_{\mathrm{st}}^{\mathrm{h}})$. The definition of these three specifications again goes back to Szabó and Babuška and is described in detail in [121]. Polynomial degress p_ξ, p_η and p_ζ for the *trunk space* $\mathcal{S}_{\mathrm{ts}}^{p_\xi,p_\eta,p_\zeta}(\Omega_{\mathrm{st}}^{\mathrm{h}})$ and *tensor product space* $\mathcal{S}_{\mathrm{ps}}^{p_\xi,p_\eta,p_\zeta}(\Omega_{\mathrm{st}}^{\mathrm{h}})$ can be chosen individually for the respective local directions ξ, η and ζ. Differences between these two Ansatz spaces are manifested in the representation of face modes and internal modes. As in the two-dimensional case, the *tensor product space* is formed by the complete set of monomials, whereas the *trunk space* is spanned by a reduced set. Exemplarily, we

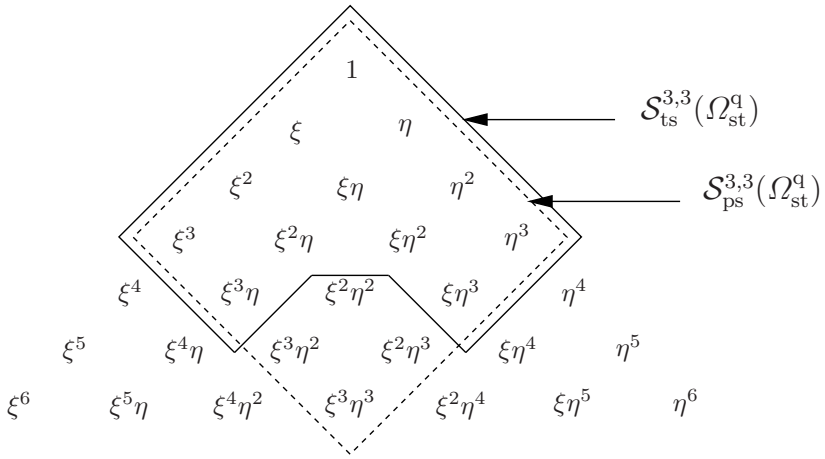

Figure 3.7: Ansatz spaces *trunk space* $\mathcal{S}_{\mathrm{ts}}^{3,3}(\Omega_{\mathrm{st}}^{\mathrm{q}})$ and *tensor product space* $\mathcal{S}_{\mathrm{ps}}^{3,3}(\Omega_{\mathrm{st}}^{\mathrm{q}})$

consider the modes for face F_1, given by (3.46). For the *trunk space*, the set of monomials is then constrained according to

$$\begin{aligned} \xi^i\eta^j\zeta^k \qquad & \text{with} \quad i = 2,\dots,p_\xi - 2, \quad j = 0,\dots,p_\eta - 2, \quad k = 0,1 \\ & \text{and} \quad i + j = 0,\dots,\max\{p_\xi, p_\eta\}\ . \end{aligned}$$

Similarly, for the internal modes (3.47) we have

$$\begin{aligned} \xi^i\eta^j\zeta^k \qquad & \text{with} \quad i = 2,\dots,p_\xi - 4, \quad j = 0,\dots,p_\eta - 4, \quad k = 0,\dots,p_\zeta - 4 \\ & \text{and} \quad i + j + k = 0,\dots,\max\{p_\xi, p_\eta, p_\zeta\}\ . \end{aligned}$$

The *anisotropic tensor product space* $\mathcal{S}^{p,p,q}(\Omega_{\mathrm{st}}^{\mathrm{h}})$, finally is characterized by two polynomial degrees p and q, where the polynomial degrees of all higher-order Ansatz functions associated with the local directions ξ and η are assumed to be equal, i.e., $p_\xi = p_\eta = p$. These Ansatz functions correspond to edges E_i and $i = 1,\dots,4,9,\dots,12$, faces F_1 and F_6, as well as to all internal modes (cf. Figure 3.6). Ansatz functions for faces F_1 and F_6 conform with those of the *trunk space* $\mathcal{S}_{\mathrm{ts}}^{p_\xi,p_\eta,p_\zeta}(\Omega_{\mathrm{st}}^{\mathrm{h}})$ for $p_\xi = p_\eta = p$. The degree of Ansatz functions for the remaining direction ζ is specified by q. q affects the Ansatz functions for edges E_i for $i = 5,\dots,8$, faces F_i for $i = 2,\dots 5$, and all internal modes. In contrast to faces F_1 and F_6, the Ansatz functions for faces F_i with $i = 2,\dots,5$ conform with those of the *tensor product space* $\mathcal{S}_{\mathrm{ps}}^{p_\xi,p_\eta,p_\zeta}(\Omega_{\mathrm{st}}^{\mathrm{h}})$. Thus, for a constant polynomial degree $p = q = p_\xi = p_\eta = p_\zeta$, the *trunk space* $\mathcal{S}_{\mathrm{ts}}^{p_\xi,p_\eta,p_\zeta}(\Omega_{\mathrm{st}}^{\mathrm{h}})$ renders the lowest, the *anisotropic tensor product space* $\mathcal{S}^{p,p,q}(\Omega_{\mathrm{st}}^{\mathrm{h}})$ an intermediate number and the *tensor product space* $\mathcal{S}_{\mathrm{ps}}^{p_\xi,p_\eta,p_\zeta}(\Omega_{\mathrm{st}}^{\mathrm{h}})$ the highest number of Ansatz functions.

High-order finite elements are not only flexible regarding the choice of polynomial degree for the local directions — they also allow for a differentiated choice with respect to the primary variables u_x, u_y and u_z. A comprehensive description of this flexibility is given in Düster [33] and Düster et al. [35]. Equation (3.49) exemplarily illustrates the definition of a so-called *polynomial degree template* $\mathbf{p}$ with the three independent

primary variables $\mathbf{u} = [u_x, u_y, u_z]^T$:

$$\mathbf{p} = \begin{array}{c} \\ \xi \\ \eta \\ \zeta \end{array} \begin{array}{c} \begin{array}{ccc} u_x & u_y & u_z \end{array} \\ \begin{pmatrix} 1 & 4 & 7 \\ 2 & 5 & 8 \\ 3 & 6 & 9 \end{pmatrix} \end{array} \tag{3.49}$$

Considering the *trunk space* $\mathcal{S}_{\mathrm{ts}}^{p_\xi,p_\eta,p_\zeta}(\Omega_{\mathrm{st}}^{\mathrm{h}})$, this template defines the Ansatz for the displacement field $u_x \in \mathcal{S}_{\mathrm{ts}}^{1,2,3}(\Omega_{\mathrm{st}}^{\mathrm{h}})$, $u_y \in \mathcal{S}_{\mathrm{ts}}^{4,5,6}(\Omega_{\mathrm{st}}^{\mathrm{h}})$ and $u_z \in \mathcal{S}_{\mathrm{ts}}^{7,8,9}(\Omega_{\mathrm{st}}^{\mathrm{h}})$. For *tensor product space* $\mathcal{S}_{\mathrm{ps}}^{p_\xi,p_\eta,p_\zeta}(\Omega_{\mathrm{st}}^{\mathrm{h}})$ and *anisotropic tensor product space* $\mathcal{S}^{p,p,q}(\Omega_{\mathrm{st}}^{\mathrm{h}})$, the proceeding is analogous.

A *polynomial degree template* can be assigned individually to each finite element. Continuity of the Ansatz at element faces and element edges is then assured by each adopting the higher polynomial degree at the interfacing element parts.

Based on the foregoing considerations, a hexahedral element formulation features some advantageous characteristics when compared to corresponding tetrahedral and pentrahedral formulations. Apart from the intuitive numerical integration using a Gaussian quadrature scheme, hexahedral finite element discretizations lead to a higher accuracy of the solution. The most significant benefit, however, is gained for the analysis of thin-walled structures. In this case, the previously discussed flexibility of the Ansatz space proves particularly powerful. Accounting for the mechanical behavior of thin-walled structures, it is possible to choose the polynomial degree in thickness direction different from the in-plane direction — leading to very efficient discretizations. Comprehensive studies on this topic and practical applications are given, for example, in [99, 82, 122, 33, 35].

Irrespective of the Ansatz space's dimensionality, degrees of freedom related to internal modes are purely local to the corresponding finite element, i.e., there is no dependence on degrees of freedom attributed to neighboring finite elements. Exploiting this property, it is possible to eliminate element internal degrees of freedom already on element level by adopting a static condensation procedure. Depending on the specific problem and the adopted Ansatz space, the consequential reduction of the number of global unknowns can be significant. The static elimination procedure proves particular efficient, if an appropriate ordering of the elemental degrees of freedom is considered [33].

3.3 Mapping concept for high-order elements

For the h-version of the finite element method, discretization error is controlled by local or global mesh refinement. At the same time, the geometric boundary of the structure is captured more and more accurately — in the limit case, for the element size h approaching zero, the approximate boundary representation converges to the exact geometry. The p-version of the finite element method, on the contrary, achieves convergence to the exact solution by locally or

globally increasing the polynomial degree of the Ansatz functions. In doing so, the element size is kept constant. Hence, to facilitate control over the geometrical error of the discretization, an element size independent representation technique of the structural boundary is required. The *blending function method*, originally proposed by Gordon and Hall [45, 46] in 1973, is a tool that matches these requirements. It allows for the exact description of an arbitrary geometry of the finite element boundary. Subsequently, the fundamentals of the method are outlined for the two-dimensional (Section 3.3.1) and three-dimensional case (Section 3.3.2). In Section 3.3.3, different concepts regarding the geometric representation of the boundary are shortly discussed and their repective assets and drawbacks contrasted.

3.3.1 Two-dimensional blending

To motivate subsequent developments, consider the mapping $\mathbf{Q}^e(\boldsymbol{\xi}) = [Q_x^e(\boldsymbol{\xi}), Q_y^e(\boldsymbol{\xi})]^T$ of a quadrilateral standard element $\Omega_{\text{st}}^{\text{q}} = [(-1,1) \times (-1,1)]$ with local coordinates $\boldsymbol{\xi} = [\xi, \eta]^T$ to a general quadrilateral with global coordinates $\mathbf{X} = [X, Y]^T$, as illustrated in Figure 3.8. The geometry of the general quadrilateral in $\mathbb{R}^2$ be defined by its nodal coordinates $\mathbf{X}_i = [X_i, Y_i]^T$ with $i = 1, \ldots, 4$ and its edges $\mathbf{E}_i = [E_{ix}, E_{iy}]^T$ with $i = 1, \ldots, 4$. We postulate, that edges

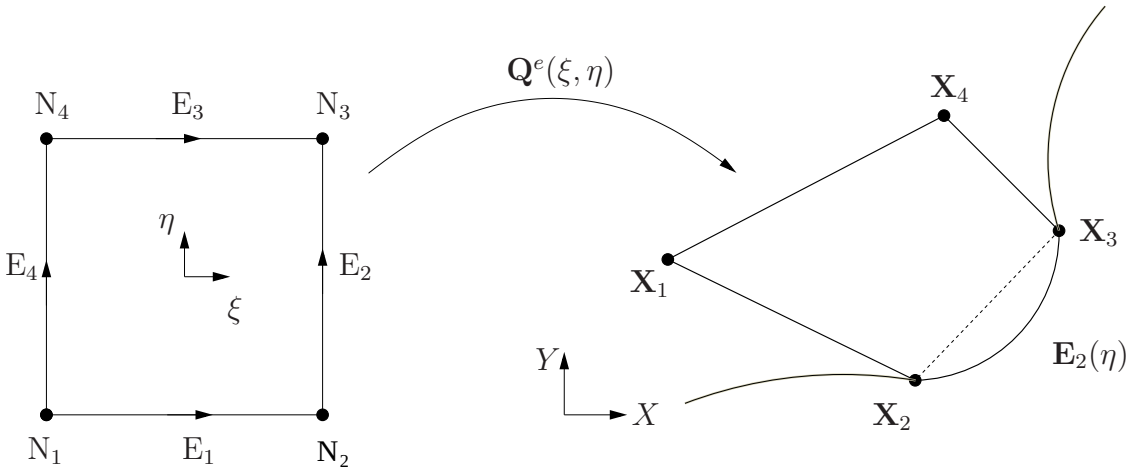

Figure 3.8: Mapping of a quadrilateral element

$\mathbf{E}_i(r)$ with $i = 1, \ldots, 4$ can be described as parametric curves depending on parameters ξ and η, with $\{\xi, \eta\} \in [-1, 1]$ — so that $\mathbf{E}_i(r) = [E_{ix}(r),\, E_{iy}(r)]^T$, where

$$\begin{aligned} r &= \xi \qquad \text{for} \quad i = 1, 3 \\ r &= \eta \qquad \text{for} \quad i = 2, 4\,. \end{aligned} \tag{3.50}$$

Then, equation (3.51) describes a general transformation from standard element to geometrical element.

$$\mathbf{X} \;=\; \mathbf{Q}^e(\xi,\eta) \;=\; \sum_{i=1}^{4} N_{1,1}^{\mathrm{N}_i}(\xi,\,\eta)\,\mathbf{X}_i + \sum_{i=1}^{4} \mathbf{e}_i(\xi,\,\eta) \tag{3.51}$$

The first term represents the standard bilinear mapping of an isoparametric quadrilateral, where the Ansatz functions $N_{1,1}^{\mathrm{N}_i}(\xi,\,\eta)$ are defined via equation (3.41). The second term accounts for a possibly curved geometry of the edges, it is frequently referred to as *edge blending term*. To seize the construction principle of the blending term, consider the example of local edge $\mathrm{E}_2(\eta)$ being mapped onto a curve whose geometry in the range of the element edge be defined by $\mathbf{E}_2(\eta) = [E_{2x}(\eta),\, E_{2y}(\eta)]^T$ (Figure 3.8).

$$\mathbf{e}_2(\xi,\,\eta) \;=\; \left[\,\mathbf{E}_2(\eta) \;-\; \left(\frac{1-\eta}{2}\,\mathbf{X}_2 + \frac{1+\eta}{2}\,\mathbf{X}_3\right)\right] \;\frac{1+\xi}{2} \tag{3.52}$$

Considering equation (3.52), the term in square brackets corresponds to the difference between the curved edge $\mathbf{E}_2(\eta) = [E_{2x}(\eta),\, E_{2y}(\eta)]^T$ and the imaginary straight edge between nodes $\mathbf{X}_2$ und $\mathbf{X}_3$, as it would be obtained by standard bilinear mapping. Multiplication by $[(1+\xi)/2]$ applies a linear *blending* to this difference term. This blending assures that the difference is completely accounted for along edge E_2, where $(\xi = 1)$ and thus $[(1+\xi)/2] = 1$ — while along the opposite edge E_4, where $(\xi = -1)$ prevails, $[(1+\xi)/2]$ and thus the influence of the curved edge E_2 vanishes.

Upon substitution of the edge terms $\mathbf{e}_i(\xi,\,\eta)$ — specified in detail in Appendix B.1 — into equation (3.51), one finally obtains (3.53). [3]

$$\begin{aligned}\mathbf{x} \;&=\; \mathbf{Q}^e(\xi,\eta) \\ &=\; \frac{1}{2}\Big[\,(1-\eta)\mathbf{E}_1(\xi) \,+(1+\xi)\mathbf{E}_2(\eta) \,+(1+\eta)\mathbf{E}_3(\xi) \,+(1-\xi)\mathbf{E}_4(\eta)\,\Big] \\ &\quad -\,[\; N_{1,1}^{\mathrm{N}_1}(\xi,\,\eta)\,\mathbf{X}_1 + N_{1,1}^{\mathrm{N}_2}(\xi,\,\eta)\,\mathbf{X}_2 + N_{1,1}^{\mathrm{N}_3}(\xi,\,\eta)\,\mathbf{X}_3 + N_{1,1}^{\mathrm{N}_4}(\xi,\,\eta)\,\mathbf{X}_4\;]\end{aligned} \tag{3.53}$$

3.3.2 Three-dimensional blending

Description of the method for a three-dimensional setting is developed following analogous lines as for the two-dimensional case. The essential enhancement is given by terms representing the geometry of the element faces. Subsequently, the application of the blending function method to three-dimensional hexahedral elements is briefly outlined. A comprehensive discussion of

[3] The minus sign, which applies to the linear terms of the mapping function (3.53) emerges as a result of the substitution.

this topic is given in [63], [13], [18] and [35]. Figure 3.9 illustrates the situation of a standard hexahedral element $\Omega^{\mathrm{h}}_{\mathrm{st}} = [(-1,1) \times (-1,1) \times (-1,1)]$ with local coordinates $\boldsymbol{\xi} = [\xi, \eta, \zeta]^T$ being transformed to a general hexahedral element with global cordinates $\mathbf{X} = [X, Y, Z]^T$ via the mapping $\mathbf{Q}^e(\boldsymbol{\xi}) = [Q^e_x(\boldsymbol{\xi}), Q^e_y(\boldsymbol{\xi}), Q^e_z(\boldsymbol{\xi})]^T$. The element geometry in $\mathbb{R}^3$ is uniquely defined by the nodal coordinates $\mathbf{X}_i = [X_i, Y_i, Z_i]^T$ mit $i = 1, \ldots, 8$, the edges $\mathbf{E}_i = [E_{ix}, E_{iy}, E_{iz}]^T$, $i = 1, \ldots, 12$ and the faces $\mathbf{F}_i = [F_{ix}, F_{iy}, F_{iz}]^T$, $i = 1, \ldots, 6$. As for the two-dimensional case we

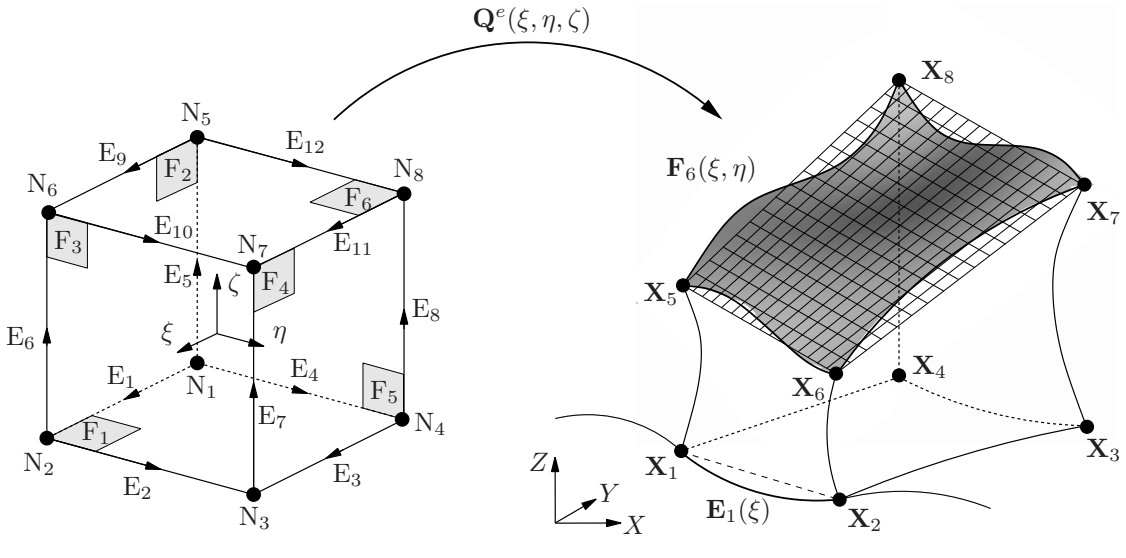

Figure 3.9: Mapping of a hexahedral element

require that edges $\mathbf{E}_i(r)$ with $i = 1, \ldots, 12$ can be described as parametric curves depending on parameters ξ, η and ζ with $\{\xi, \eta, \zeta\} \in [-1, 1]$ — so that $\mathbf{E}_i(r) = [E_{ix}(r),\, E_{iy}(r),\, E_{iz}(r)]^T$, where

$$\begin{aligned} r &= \xi \qquad \text{for} \quad i = 1, 3, 9, 11 \\ r &= \eta \qquad \text{for} \quad i = 2, 4, 10, 12 \\ r &= \zeta \qquad \text{for} \quad i = 5, 6, 7, 8\ . \end{aligned} \tag{3.54}$$

Similarly, faces $\mathbf{F}_i$ with $i = 1, \ldots, 6$ are supposed to be represented by parametric surfaces dependent on each two parameters (ξ, η), (ξ, ζ) and (η, ζ), repectively, with $\{\xi, \eta, \zeta\} \in [-1, 1]$ — so that $\mathbf{F}_i(r, s) = [F_{ix}(r, s),\, F_{iy}(r, s),\, F_{iz}(r, s)]^T$, where

$$\begin{aligned} (r, s) &= (\xi, \eta) \qquad \text{for} \quad i = 1, 6 \\ (r, s) &= (\xi, \zeta) \qquad \text{for} \quad i = 2, 4 \\ (r, s) &= (\eta, \zeta) \qquad \text{for} \quad i = 3, 5\ . \end{aligned} \tag{3.55}$$

Then, equation (3.56) defines a general transformation from standard element to geometrical element.

$$\mathbf{X} \;=\; \mathbf{Q}^e(\xi,\eta,\zeta) \;=\; \sum_{i=1}^{8} N^{\mathrm{N}_i}_{1,1,1}(\xi,\eta,\zeta)\,\mathbf{X}_i + \sum_{i=1}^{6} \mathbf{f}_i(\xi,\,\eta,\,\zeta) - \sum_{i=1}^{12} \mathbf{e}_i(\xi,\,\eta,\,\zeta) \tag{3.56}$$

The first term represents the standard trilinear mapping of an isoparametric hexahedral element, where the functions $N^{\mathrm{N}_i}_{1,1,1}(\xi,\eta,\zeta)$ resemble the previously introduced nodal Ansatz functions (3.44). The second term accounts for a possibly curved geometry of the element faces, it is frequently referred to as *face blending term*. Composition of this term is covered in detail in Appendix B.2.2. Here, it is exemplarily discussed for the element face F_6 (cf. Figure 3.9). The square bracketed term in equation (3.57) corresponds to the difference between the actual curved surface geometry $\mathbf{F}_6(\xi,\eta) = [F_{6x}(\xi,\eta),\, F_{6y}(\xi,\eta),\, F_{6z}(\xi,\eta)]^T$ and an imaginary bilinear surface (as it would be obtained by standard trilinear mapping), spanned by the element nodes $\mathbf{X}_5, \mathbf{X}_6, \mathbf{X}_7$ and $\mathbf{X}_8$. Multiplication by the term $[(1+\zeta)/2]$ manifests — as in the two-dimensional case — a linear blending, and thus a vanishing contribution, of this difference towards the opposite face F_1.

$$\begin{aligned}\mathbf{f}_6(\xi,\,\eta,\,\zeta) \;=\; \Bigg[\mathbf{F}_6(\xi,\eta) \;-\; \Bigg(&\frac{(1-\xi)(1-\eta)}{4}\mathbf{X}_5 + \frac{(1+\xi)(1-\eta)}{4}\mathbf{X}_6 + \\ &+\frac{(1+\xi)(1+\eta)}{4}\mathbf{X}_7 + \frac{(1-\xi)(1+\eta)}{4}\mathbf{X}_8\Bigg)\Bigg]\left(\frac{1+\zeta}{2}\right)\end{aligned} \tag{3.57}$$

The final term in equation (3.56) refers to the edge blending, which is exemplarily illustrated for edge E_1, as follows. The derivation is in complete analogy to the two-dimensional case, i.e., the bracketed term in (3.58) again denotes the difference between curved geometry $\mathbf{E}_1(\xi) = [E_{1x}(\xi),\, E_{1y}(\xi),\, E_{1z}(\xi)]^T$ and the imaginary straight edge as direct connection between nodes $\mathbf{X}_1$ and $\mathbf{X}_2$. The only difference to the two-dimensional case is that the factors $[(1-\eta)/2]$ and $[(1-\zeta)/2]$ assure the vanishing contribution of the difference term towards *all* opposite edges — i.e., all edges with equivalent local edge parameter, namely $\mathbf{E}_3(\xi)$, $\mathbf{E}_9(\xi)$ and $\mathbf{E}_{11}(\xi)$.

$$\mathbf{e}_1(\xi,\,\eta,\,\zeta) \;=\; \left[\mathbf{E}_1(\xi) - \left(\frac{1-\xi}{2}\mathbf{X}_1 + \frac{1+\xi}{2}\mathbf{X}_2\right)\right]\left(\frac{1-\eta}{2}\right)\left(\frac{1-\zeta}{2}\right). \tag{3.58}$$

Every edge is part of two faces. Hence, the corresponding edge difference terms are considered twice during face blending. This reveals, why the edge blending terms in equation (3.56) must be subtracted.

Substituting the edge terms $\mathbf{e}_i(\xi,\,\eta\,\zeta)$ and face terms $\mathbf{f}_i(\xi,\,\eta\,\zeta)$ contained in equation (3.56)

by the corresponding terms specified in Appendix B.2, one finally obtains

$$
\begin{aligned}
\mathbf{x} &= \mathbf{Q}^e(\xi,\eta,\zeta) \qquad (3.59)\\
&= \frac{1}{2}\Big[(1-\zeta)\,\mathbf{F}_1(\xi,\,\eta)+(1-\eta)\,\mathbf{F}_2(\xi,\,\zeta)+(1+\xi)\,\mathbf{F}_3(\eta,\,\zeta)+\\
&\quad +(1+\eta)\,\mathbf{F}_4(\xi,\,\zeta)+(1-\xi)\,\mathbf{F}_5(\eta,\,\zeta)+(1+\zeta)\,\mathbf{F}_6(\xi,\,\eta)\Big]\\
&\quad -\frac{1}{4}\Big[(1-\zeta)(1-\eta)\,\mathbf{E}_1(\xi)+(1-\zeta)(1+\xi)\,\mathbf{E}_2(\eta)+(1-\zeta)(1+\eta)\,\mathbf{E}_3(\xi)+\\
&\quad +(1-\zeta)(1-\xi)\,\mathbf{E}_4(\eta)+(1-\xi)(1-\eta)\,\mathbf{E}_5(\zeta)+(1+\xi)(1-\eta)\,\mathbf{E}_6(\zeta)+\\
&\quad +(1+\xi)(1+\eta)\,\mathbf{E}_7(\zeta)+(1-\xi)(1+\eta)\,\mathbf{E}_8(\zeta)+(1+\zeta)(1-\eta)\,\mathbf{E}_9(\xi)+\\
&\quad +(1+\zeta)(1+\xi)\,\mathbf{E}_{10}(\eta)+(1+\zeta)(1+\eta)\,\mathbf{E}_{11}(\xi)+(1+\zeta)(1-\xi)\,\mathbf{E}_{12}(\eta)\Big]\\
&\quad +N^{\mathrm{N}_1}_{1,1,1}(\xi,\,\eta,\,\zeta)\,\mathbf{X}_1+N^{\mathrm{N}_2}_{1,1,1}(\xi,\,\eta,\,\zeta)\,\mathbf{X}_2+N^{\mathrm{N}_3}_{1,1,1}(\xi,\,\eta,\,\zeta)\,\mathbf{X}_3+\\
&\quad +N^{\mathrm{N}_4}_{1,1,1}(\xi,\,\eta,\,\zeta)\,\mathbf{X}_4+N^{\mathrm{N}_5}_{1,1,1}(\xi,\,\eta,\,\zeta)\,\mathbf{X}_5+N^{\mathrm{N}_6}_{1,1,1}(\xi,\,\eta,\,\zeta)\,\mathbf{X}_6+\\
&\quad +N^{\mathrm{N}_7}_{1,1,1}(\xi,\,\eta,\,\zeta)\,\mathbf{X}_7+N^{\mathrm{N}_8}_{1,1,1}(\xi,\,\eta,\,\zeta)\,\mathbf{X}_8
\end{aligned}
$$

3.3.3 Various mapping concepts — assets and drawbacks

Based on their fundamental properties, mapping concepts can generally be classified into three groups:

- *isoparametric approach*
  The same functions that define the Ansatz space for the solution $\mathbf{u}_h$, approximating the exact solution $\mathbf{u}$, are also adopted for mapping of the geometry. This approach is the standard procedure for low order linear or quadratic elements in the context of the h-version of the finite element method.

- *subparametric approach*
  Mapping functions for the geometry are comprised in the function space for the approximate solution to $\mathbf{u}$. The Ansatz space adopted to obtain the approximate solution $\mathbf{u}_h$ is more general.

- *superparametric approach*
  Mapping functions for the geometry are more general than those, that are employed to obtain the approximate solution $\mathbf{u}_h$. This can be the case if, e.g., for the description of the geometry higher-order polynomials are used than for the description of the primary variables $\mathbf{u}_h$.

The subsequent section tempts an outline of the approaches' distinct characteristics and a short discussion of their respective impact on the finite element analysis. To this end, it follows the

principal argumentation of Szabó & Babuška [121] and [18, 33, 84]. The arguments set out below are valid in a strict sense for a pure displacement based finite element formulation. Mixed finite element formulations might exhibit a somewhat lower sensitivity, due to possibly improved locking behavior as for the enhanced assumed strain method [117] — the basic rationale, however, also applies to this class of formulations.

To elaborate the fundamental differences, the representation of rigid body modes plays a vital role. A rigid body movement or rotation does not induce any straining to an eleastic body, the body remains strain free. The general rigid body motion, i.e., translations in x-, y-, and z-direction and the three rotations about the body's origin, is represented by the displacement field (3.60) with C_i, $i = 1, \ldots, 6$ being constant.

$$\mathbf{u}_{\mathrm{rbm}} = C_1 \begin{bmatrix} 1 \\ 0 \\ 0 \end{bmatrix} + C_2 \begin{bmatrix} 0 \\ 1 \\ 0 \end{bmatrix} + C_3 \begin{bmatrix} 0 \\ 0 \\ 1 \end{bmatrix} + C_4 \begin{bmatrix} 0 \\ -z \\ y \end{bmatrix} + C_5 \begin{bmatrix} z \\ 0 \\ -x \end{bmatrix} + C_6 \begin{bmatrix} -y \\ x \\ 0 \end{bmatrix} \tag{3.60}$$

The representation of these modes by the finite element solution $\mathbf{u}_h$ can be guaranteed if, and only if: the geometry mapping function space is a subspace of — or, falls together with — the finite element solution's Ansatz space. In other words, the finite element Ansatz must be capable of reproducing the rigid body modes, which for the rotational terms implicitly involves representation of the geometry.

$$\mathbf{u}_h \stackrel{!}{=} \mathbf{u}_{\mathrm{rbm}} \qquad \text{with} \qquad \mathbf{u}_h = \sum_{i=1}^{n_{\mathrm{modes}}} N_i(\boldsymbol{\xi})\, \mathbf{a}_i \tag{3.61}$$

For *isoparametric* and *subparametric* mapping approaches, condition (3.61) is always satisfied; for the *superparametric* case the complexity of the geometry description excels the one of the finite element Ansatz. In this case, rigid body translations are still captured by the nodal modes — exact representation of rigid body rotations, however, fails due to insufficient richness of the finite element Ansatz. As a consequence, the solution exhibits spurious strains. For smooth geometries, the corresponding error can in general be significantly reduced by adapting the finite element Ansatz to a higher polynomial degree, see Szabó & Babuška [121] and Düster [33]. For complex geometries, however, this error might have a crucial impact on the quality of the solution, as was shown in detail by Bröker in [18].

Some commonly adopted mapping strategies are subsequently outlined:

- The *isoparametric* standard concept is predominantly applied in the context of the finite element h-version. It emerges as a special case of the general blending function method. For isoparametric mapping, both the finite element discretization and the geometry mapping are described by

$$\mathbf{x} \approx \sum_{i=1}^{(p+1)^n_{\mathrm{dim}}} N_i^p(\boldsymbol{\xi})\, \mathbf{a}_i \,, \tag{3.62}$$

where, depending on the spatial dimension n_{dim} of the problem: $\mathbf{x} = [x, y]^T \in \mathbb{R}^2$, $\boldsymbol{\xi} = [\xi_x, \xi_y]^T$ and $\mathbf{a}_i = [a_{ix}, a_{iy}]^T$, respectively $\mathbf{x} = [x, y, z]^T \in \mathbb{R}^3$, $\boldsymbol{\xi} = [\xi_x, \xi_y, \xi_z]^T$ and $\mathbf{a}_i = [a_{ix}, a_{iy}, a_{iz}]^T$. $N_i^p(\boldsymbol{\xi})$ denote the LAGRANGE-polynomials, with $\mathbf{a}_i$ being the collocation points which are commonly arranged in an equidistant manner. As discussed above, due to the isoparametric character of the mapping, errors due to insufficient representation of the rigid body modes cannot occur. A disadvantage of this concept lies in a potential lack of accuracy regarding the geometrical description, which can possibly affect the quality of the obtained results.

Mapping strategies suitable for the p-version of the finite element method are conveniently based on the previously introduced blending function method, compare equations (3.51) and (3.56). Three different strategies regarding the geometric representation of element edges $\mathbf{E}_i$ and faces $\mathbf{F}_i$ shall be considered:

- In case geometry is available in a parametrized form using curves $\mathbf{E}_i(r)$ and surfaces $\mathbf{F}_i(r, s)$, re-parametrization with respect to the element local parameters $\boldsymbol{\xi}$ facilitates the computation of JACOBIAN matrices that are based on the exact geometry. To this end, the strategies set out in Sections 3.3.1 and 3.3.2 are adopted. The advantage of accurately capturing the geometry by an analytical description is opposed to the possibility of merging in a *superparametric* approach — which would feature the drawbacks, just discussed.

- A different strategy was introduced by KIRÁLYFALVI & SZABÓ [63] in 1997, the *quasi-regional mapping*. The fundamental idea is to employ a polynomial approximation of the geometry instead of a parametric exact description.

$$\begin{aligned} \mathbf{E}_i(r) \quad &\approx \quad \mathbf{E}_i^{\text{interp}}(r) \quad = \quad \sum_{k=1}^{p+1} N_k^p(r)\, \mathbf{E}_i(r_k) \\ \mathbf{F}_i(r,s) \quad &\approx \quad \mathbf{F}_i^{\text{interp}}(r,s) \quad = \quad \sum_{k=1}^{p+1} \sum_{l=1}^{q+1} N_k^p(r)\, N_l^q(s)\, \mathbf{F}_i(r_k, s_l) \end{aligned} \tag{3.63}$$

  The terms $\mathbf{E}_i(r)$ and $\mathbf{F}_i(r, s)$, occuring in equation (3.63), are specified by equations (3.50) and accordingly (3.54) and (3.55). The interpolation of the geometry is supplied by means of LAGRANGE-polynomials, evaluated at distinct collocation points r_k and s_l according to CHEN & BABUŠKA [20]. The distribution of these collocation points, also termed BABUŠKA-CHEN points, are not equidistant — their positioning scheme aims at a minimization of oscillations due to the polynomial approximation. Details are given in [20].

  With a view of applying this method of boundary representation to quadrilateral and hexahedral finite elements KIRÁLYFALVI and SZABÓ point out two distinct characteristics of their approach:

  1. "The only information required are coordinates of the curves and surfaces in the collocation points."

2. "If the curves or surfaces are analytic then their piecewise polynomial approximation converges to the analytic expressions as the number of collocation points is increased."

Due to the fact that LAGRANGE-polynomials take the value 1 at each one node and vanish at all remaining nodes (3.29), computation of the collocation points $\mathbf{E}_i(r_k)$ and $\mathbf{F}_i(r_k, s_l)$ is done in a straightforward explicit manner — no solution of a corresponding system of equations is required. It should be noted that the space spanned by LAGRANGE-polynomials of a certain order is more comprehensive than the corresponding *trunk space* of LEGENDRE-polynomials. Therefore, transition to a *superparametric* state cannot generally be excluded for this approach; unless the — costly — *tensor product space* of at least the same order as the polynomial geometry approximation is chosen for the finite element approximation.

- A third variant, therefore, adopts the same Ansatz for the geometry approximation as for the finite element solution. In this case, the approximation reads:

$$\begin{aligned} \mathbf{E}_i(r) &\approx \mathbf{E}_i^{\text{approx}}(r) = \sum_{i=1}^{n_{\text{Moden}}} N_i(r)\,\mathbf{a}_i \\ \mathbf{F}_i(r,s) &\approx \mathbf{F}_i^{\text{approx}}(r,s) = \sum_{i=1}^{m_{\text{Moden}}} N_i(r,s)\,\mathbf{b}_i \end{aligned} \tag{3.64}$$

Therein, functions $N_i(r)$ and $N_i(r, s)$ denote the hierarchical Ansatz functions according to Section 3.2; $\mathbf{a}_i$ and $\mathbf{b}_i$ refer to the corresponding coefficients. Due to the character of the Ansatz functions, computation of the respective coefficents requires the solution of a system of equations. As a result of the equality of approximation spaces for geometry and finite element solution, the approach is classified as *isoparametric*. Further discussion of this concept is provided by DEMKOWICZ [30, 31] in the context of *hp*-adaptive finite element methods.

As we have seen, it is possible to directly apply the *blending function method* to the parametrized exact description of the respective faces $\mathbf{F}_i(r, s)$ and edges $\mathbf{E}_i(r)$. Different from that, both the *quasi-regional mapping* and the *isoparametric* geometry approximation introduce an intermediate geometry configuration — obtained by interpolation and approximation, respectively, of the true geometry — which then in turn serves as a basis for the *blending function method*. This notion is, inspired by NÜBEL [84], graphically illustrated in Figure 3.10.

3.4 Numerical integration

The finite element method, irrespective of its different derivations and specifications, commonly adopts an integral approach of the underlying system of differential equations. The

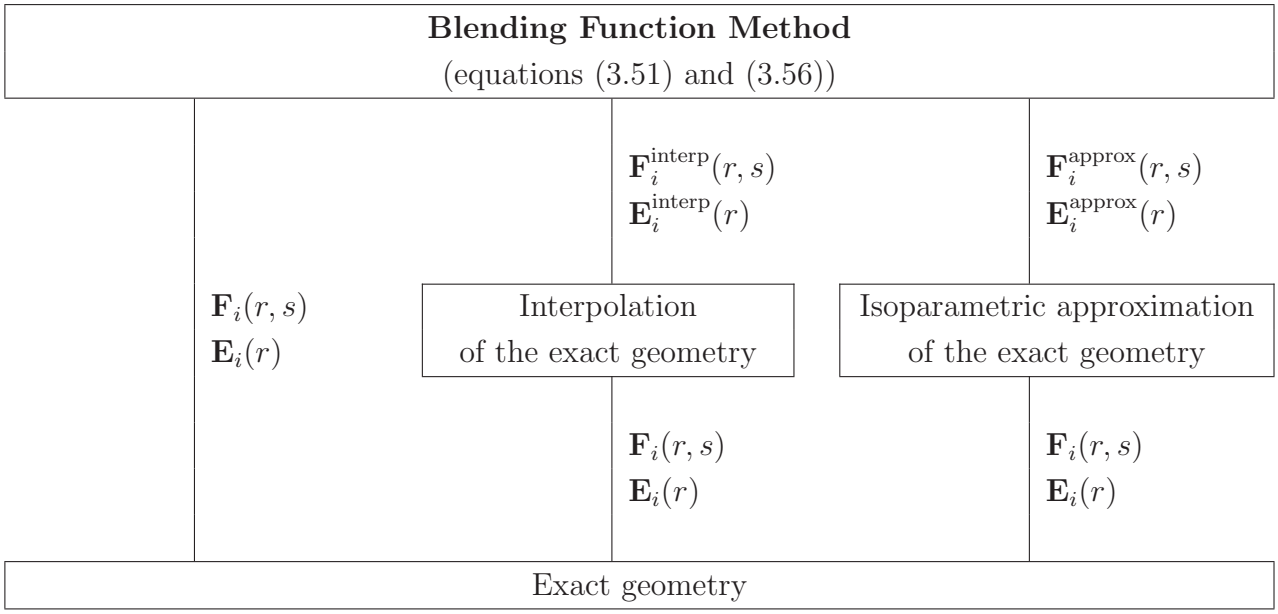

Figure 3.10: Mapping strategies in the framework of the blending function method; $\mathbf{E}_i(r)$ and $\mathbf{F}_i(r,s)$ are specified by (3.50) and accordingly (3.54) and (3.55)

discretized forms (3.12) and (3.13) of the variational principle (2.51) and (2.52) naturally reflect this notion. Since for an arbitrarily posed boundary value problem the evaluation of the corresponding integrals in closed form is generally not possible, numerical quadrature is a central issue of the solution process.

Subsequently, the essential characteristics of the GAUSS quadrature — which is probably the most widely-used quadrature scheme in finite element computations and also is the basis for the numerical analyses carried out in Chapter 6 — are briefly outlined.

3.4.1 GAUSS quadrature

Using the GAUSS quadrature scheme, the initial integration problem

$$\int_{-1}^{+1}\int_{-1}^{+1}\int_{-1}^{+1} f(\xi,\eta,\zeta)\,d\xi\,d\eta\,d\zeta \tag{3.65}$$

is transferred to an approximate summation problem according to

$$\sum_{i=1}^{l}\sum_{j=1}^{m}\sum_{k=1}^{n} w_i\,w_j\,w_k\,f(\xi_i,\eta_j,\zeta_k)\;. \tag{3.66}$$

Thus, the volume integral is reduced to a triple — corresponding to the three directions — one-dimensional integration, which, of course, manifests an approximation in the general case.

$$\int_{-1}^{+1} f(x)\,dx \;\approx\; \sum_{i=1}^{n} w_i\, f(x_i) \quad \text{with} \quad x_i \in [-1,1] \tag{3.67}$$

In equation (3.67), w_i reflect the GAUSS-weights and x_i represent the collocation points or GAUSS-points. In contrast to the NEWTON-COTES scheme, which employs equidistant collocation points, the GAUSS quadrature scheme is derived on a more general basis, allowing the position of the collocation points to vary — thus, furnishing a higher degree of accuracy. For GAUSSian quadrature, the following proposition holds: *There exists precisely one quadrature formula* (3.67) *with n collocation points that yields the maximum degree of accuracy* $(2n-1)$*, i.e., integrates a polynomial of degree* $(2n-1)$ *exactly.* It can be proved (see, e.g., [109]), that collocation points x_i correspond to the roots of the n-th LEGENDRE polynomial (3.37) or (3.38) and the corresponding weights are defined by

$$w_i = \int_{-1}^{1} \prod_{\substack{j=1 \\ j\neq i}}^{n} \left(\frac{x - x_j}{x_i - x_j} \right)^2 dx > 0, \quad (i = 1, 2, \ldots, n). \tag{3.68}$$

Collocation points $x_i \neq 0$ are located pairwise symmetric to the origin. From (3.68), it can easily be seen that the associated weights are pairwise identical, too. Generally, it can be stated that the high precision of the GAUSS integration is payed for by the discomfort, that the location of collocation points and the magnitude of the respective weights depends on the order of n. A robust numerical procedure for determination of collocation point coordinates and corresponding weights is provided in [109].

Chapter 4

Embedded strong discontinuities

Might as well jump!
– Van Halen.

4.1 Strong discontinuity kinematics

The so far described classical continuum model (Chapter 2) is based on the fundamental assumption of the body's response remaining continuous during loading. It was, however, already alluded to in Section 1.2, that failure of materials is frequently preceeded by the formation of a process zone in which damage and other inelastic effects accumulate, and in which high strain gradients prevail — furnishing the notion of *deformation localization*. Clearly, when attempting to extend the model to these kinds of phenomena, the scope of classical continuum mechanics (Truesdell & Noll [124]) is left. Assessing the typically small localization zones from a distance, continuous fields with a steep gradient appear discontinuous. For practical engineering problems this means that many continuous problems arise discontinuous when viewed from the level of practical interest. [1] Adopting this view, the remainder of this section is devoted to extending the classical continuum model regarding the possible incident of strong discontinuities, i.e., jumps in the displacement field. Thereby, the notation follows the fundamental concept of a re-parametrization of the strong discontinuity kinematics which was constituted in Simo et al. [116] and subsequently elaborated by Simo & Oliver [115] and Oliver [88]. Later, this notion was succeeded by several authors, amongst others Regueiro & Borja [100, 17], Borja [16], Mosler & Meschke [77] and Feist [41].

[1] Notably, also fields that appear continuous may in fact be discontinuous when observed at a lower scale (microlevel).

4.1.1 Standard approach

To begin with, consider the classical boundary value problem set out in Section 2.3.1. Supplementary, body Ω is assumed to be separated into two portions Ω^+ and Ω^- by a discontinuity surface $\partial_\mathrm{s}\Omega$ of arbitrary shape (Figure 4.1). This decomposition is formally described by $\Omega = \Omega^+ \cup \Omega^- \cup \partial_\mathrm{s}\Omega$. Further, the orientation of the discontinuity surface is assumed to be defined by its normal $\boldsymbol{N}$.

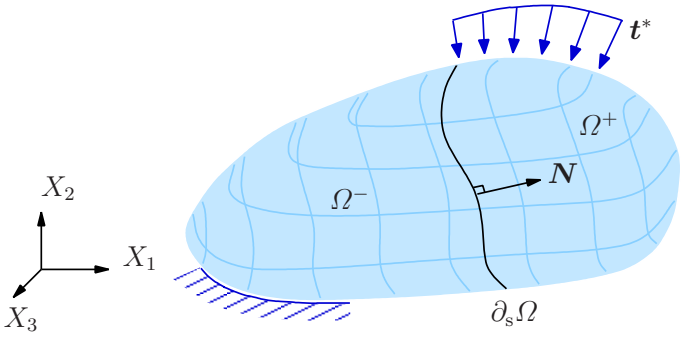

Figure 4.1: Body with discontinuity surface $\partial_\mathrm{s}\Omega$

In such a setting, the strong discontinuity approach is based on the assumption of a jump in the displacement field across the discontinuity surface. Mathematically, this jump can conveniently be expressed using the Heaviside function $H_\mathrm{s}(\boldsymbol{X})$, operating on a smooth continuous function. Accordingly, the displacement field can be written as

$$\boldsymbol{u}(\boldsymbol{X},t) = \underbrace{\breve{\boldsymbol{u}}(\boldsymbol{X},t)}_{\text{regular}} + \underbrace{[\![\boldsymbol{u}]\!](\boldsymbol{X},t)\, H_\mathrm{s}(\boldsymbol{X})}_{\text{jump term}} , \qquad \forall \boldsymbol{X} \in \Omega \tag{4.1}$$

with the Heaviside function $H_\mathrm{s}(\boldsymbol{X})$ being defined as

$$H_\mathrm{s}(\boldsymbol{X}) := \begin{cases} 1 & \forall \boldsymbol{X} \in \Omega^+ , \\ 0 & \forall \boldsymbol{X} \in \Omega^- . \end{cases} \tag{4.2}$$

It is emphasized, that both $\breve{\boldsymbol{u}}(\boldsymbol{X},t)$ *and* $[\![\boldsymbol{u}]\!](\boldsymbol{X},t)$ are smooth continuous functions on Ω [128, 105, 41]. Introducing the definition $[\![(\bullet)(\boldsymbol{X})]\!]_\mathrm{s} := (\bullet)(\boldsymbol{X})^+ - (\bullet)(\boldsymbol{X})^-$, $\forall \boldsymbol{X} \in \partial_\mathrm{s}\Omega$, the magnitude of the displacement jump at the discontinuity surface is determined from (4.1) as

$$[\![\boldsymbol{u}]\!]_\mathrm{s} := [\![\boldsymbol{u}]\!](\boldsymbol{X},t) , \qquad \forall \boldsymbol{X} \in \partial_\mathrm{s}\Omega . \tag{4.3}$$

The displacement rate field is then obtained by differentiating (4.1) once with respect to time. Assuming that the Heaviside function is stationary, which implies that the discontinuity does not translate, we obtain:

$$\dot{\boldsymbol{u}}(\boldsymbol{X},t) = \dot{\breve{\boldsymbol{u}}}(\boldsymbol{X},t) + [\![\dot{\boldsymbol{u}}]\!](\boldsymbol{X},t)\, H_\mathrm{s}(\boldsymbol{X}) , \qquad \forall \boldsymbol{X} \in \Omega . \tag{4.4}$$

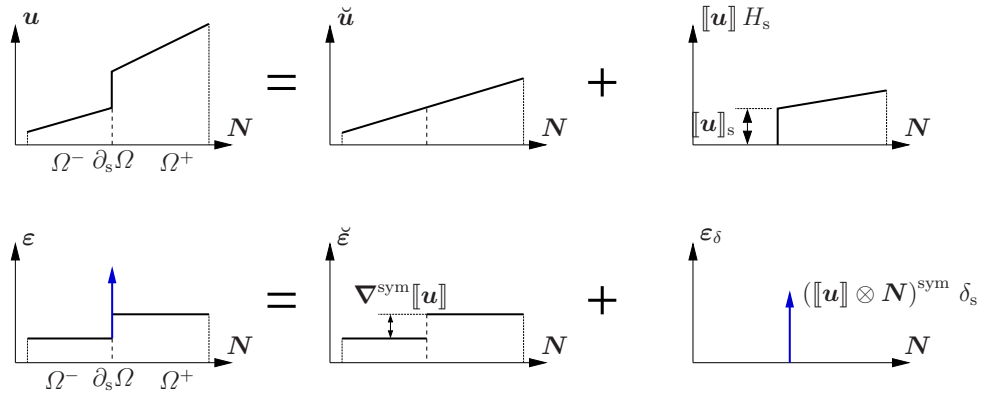

Figure 4.2: Strong discontinuity kinematics: Decomposition of displacement field into continuous and discontinuous portions and strain field into corresponding regular and singular contributions.

To complete the strong discontinuity kinematics, it remains to establish the corresponding strain tensor. Employing the mathematical concept of generalized functions (distributions) furnishes the derivative of the discontinuous Heaviside function as $\boldsymbol{\nabla} H_\mathrm{s} = \boldsymbol{N}\delta_\mathrm{s}$, and thus avoids the need to explicitly consider body Ω as two separate entities Ω^+ and Ω^- linked by traction forces at the discontinuity surface $\partial_\mathrm{s}\Omega$. Hence, the linearized (small) strain tensor is derived as

$$\begin{aligned}\boldsymbol{\varepsilon}(\boldsymbol{X},t) &= \boldsymbol{\nabla}^\mathrm{sym}\boldsymbol{u} \\ &= \underbrace{\boldsymbol{\nabla}^\mathrm{sym}\breve{\boldsymbol{u}} + \boldsymbol{\nabla}^\mathrm{sym}[\![\boldsymbol{u}]\!]\, H_\mathrm{s}(\boldsymbol{X})}_{\breve{\boldsymbol{\varepsilon}}\ \text{(regular)}} + \underbrace{([\![\boldsymbol{u}]\!]_\mathrm{s} \otimes \boldsymbol{N})^\mathrm{sym}\ \delta_\mathrm{s}}_{\boldsymbol{\varepsilon}_\delta\ \text{(singular)}}\ .\end{aligned} \tag{4.5}$$

With δ_s we denote the Dirac-delta distribution at the discontinuity surface $\partial_\mathrm{s}\Omega$, defined by $\delta_\mathrm{s} := \delta(\boldsymbol{X} - \boldsymbol{X}_\mathrm{s})$ with $\boldsymbol{X}_\mathrm{s} \in \partial_\mathrm{s}\Omega$. Considering the stationarity of the Heaviside function, the strain rate is established from (4.5) by differentiating once with respect to time:

$$\dot{\boldsymbol{\varepsilon}}(\boldsymbol{X},t) = \underbrace{\boldsymbol{\nabla}^\mathrm{sym}\dot{\breve{\boldsymbol{u}}} + \boldsymbol{\nabla}^\mathrm{sym}[\![\dot{\boldsymbol{u}}]\!]\, H_\mathrm{s}(\boldsymbol{X})}_{\dot{\breve{\boldsymbol{\varepsilon}}}\ \text{(regular)}} + \underbrace{([\![\dot{\boldsymbol{u}}]\!]_\mathrm{s} \otimes \boldsymbol{N})^\mathrm{sym}\ \delta_\mathrm{s}}_{\dot{\boldsymbol{\varepsilon}}_\delta\ \text{(singular)}} \tag{4.6}$$

4.1.2 Reformulated kinematics

From a computational point of view, as will be seen later, it proves favorable to slightly modify the kinematics established above. To this end, a domain $\Omega_\varphi \subset \Omega$ is introduced, such that the discontinuity surface renders a subset of Ω_φ, i.e., $\partial_\mathrm{s}\Omega \subset \Omega_\varphi$ [115, 88], for illustration see Figure 4.3. The two portions of Ω_φ that are separated by the discontinuity surface are denoted by Ω_φ^- and Ω_φ^+, such that $\Omega_\varphi^- \subset \Omega^-$, $\Omega_\varphi^+ \subset \Omega^+$ and $\Omega_\varphi^- \cup \Omega_\varphi^+ = \Omega_\varphi$.

Introducing the definition

$$\bar{\boldsymbol{u}}(\boldsymbol{X},t) := \breve{\boldsymbol{u}}(\boldsymbol{X},t) + [\![\boldsymbol{u}]\!](\boldsymbol{X},t)\,\varphi(\boldsymbol{X})\ , \tag{4.7}$$

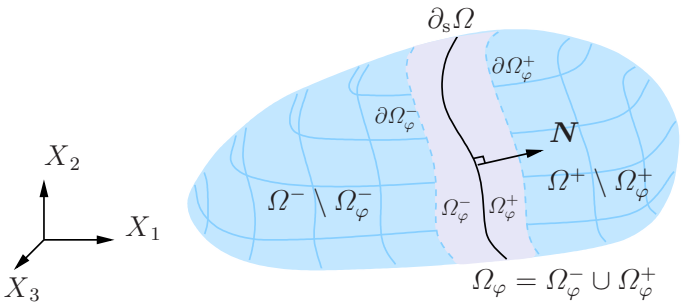

Figure 4.3: Body with discontinuity surface $\partial_s\Omega$ and subdomain Ω_φ

equation (4.1) can — without loss of generality — be cast in a competely equivalent format (Figure 4.4):

$$\begin{aligned}\boldsymbol{u}(\boldsymbol{X},t) &= \bar{\boldsymbol{u}}(\boldsymbol{X},t) + [\![\boldsymbol{u}]\!](\boldsymbol{X},t)\ (H_s(\boldsymbol{X}) - \varphi(\boldsymbol{X})) \\ &= \bar{\boldsymbol{u}}(\boldsymbol{X},t) + [\![\boldsymbol{u}]\!](\boldsymbol{X},t)\, M_s(\boldsymbol{X}) \\ &= \underbrace{\bar{\boldsymbol{u}}(\boldsymbol{X},t)}_{\text{regular}} + \underbrace{\hat{\boldsymbol{u}}(\boldsymbol{X},t)}_{\text{jump term}}\end{aligned} \tag{4.8}$$

In (4.8), the 'regularizing' function $M_s(\boldsymbol{X})$ is defined as

$$M_s(\boldsymbol{X}) := H_s(\boldsymbol{X}) - \varphi(\boldsymbol{X})\ . \tag{4.9}$$

The substantial notion that motivates the forms (4.8) and (4.7) and constitutes the definition of the function $M_s(\boldsymbol{X})$ (4.9), is the introduction of an — to begin with, completely arbitrary — interpolation function $\varphi(\boldsymbol{X})$. The essential characteristic of this function is the 'transmission' of the displacement jump effect at the discontinuity surface, $[\![\boldsymbol{u}]\!]_s$, to the boundaries of domain Ω_φ. Therefore, as a necessary condition to assure the equivalence between the re-parametrized form (4.8) and the original one (4.1) we require [115, 88, 16, 77, 128, 41]:

$$\varphi(\boldsymbol{X}) := \begin{cases} 0 & \forall \boldsymbol{X} \in \Omega^- \setminus \Omega_\varphi^- \\ 1 & \forall \boldsymbol{X} \in \Omega^+ \setminus \Omega_\varphi^+ \\ C^0\text{-continuous in result interval } [0,1] & \forall \boldsymbol{X} \in \Omega_\varphi \end{cases} \tag{4.10}$$

It will be seen later that above condition is indeed necessary, but *not sufficient* in order to assure consistency of the approach with respect to the order of polynomial approximation for the regular displacement field $\bar{\boldsymbol{u}}$ (cf. Section 4.5.2).

Differentiating (4.8) with respect to time yields the corresponding rate form of the displacement field as

$$\begin{aligned}\dot{\boldsymbol{u}}(\boldsymbol{X},t) &= \dot{\bar{\boldsymbol{u}}}(\boldsymbol{X},t) + \dot{\hat{\boldsymbol{u}}}(\boldsymbol{X},t) \\ &= \dot{\bar{\boldsymbol{u}}}(\boldsymbol{X},t) + [\![\dot{\boldsymbol{u}}]\!](\boldsymbol{X},t)\ (H_s(\boldsymbol{X}) - \varphi(\boldsymbol{X}))\ .\end{aligned} \tag{4.11}$$

To appreciate the advantage of this reformulated version of the strong discontinuity kinematics, we consider the jump term of equation (4.8). According to requirement (4.10) it follows

that $M_\mathrm{s}(\boldsymbol{X}) = 0 \quad \forall \boldsymbol{X} \in \Omega \setminus \Omega_\varphi$ which in turn implies $\boldsymbol{u}(\boldsymbol{X},t) = \bar{\boldsymbol{u}}(\boldsymbol{X},t) \quad \forall \boldsymbol{X} \in \Omega \setminus \Omega_\varphi$. Hence, by conveniently choosing Ω_φ, this property can be exploited, such that the DIRICHLET boundary conditions need to be prescribed solely for $\bar{\boldsymbol{u}} = \breve{\boldsymbol{u}} + [\![\boldsymbol{u}]\!]\varphi$ rather than for $\breve{\boldsymbol{u}}$ *and* $[\![\boldsymbol{u}]\!]$. The important point is that, using the reformulated version, the regular displacement field $\bar{\boldsymbol{u}}$ already incorporates the jump effect and can, as will be seen later, be associated with the compatible displacement field spanned by the standard finite element basis functions, cf. Section 4.5.2.

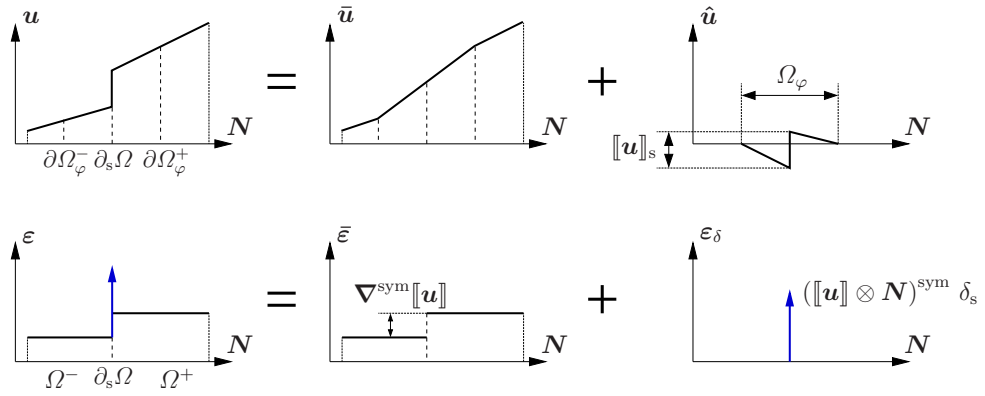

Figure 4.4: Reformulated strong discontinuity kinematics: Decomposition of displacement field into continuous and discontinuous portions and strain field into regular and singular contributions.

Following identical lines as before, the linearized strain tensor for the reformulated kinematics is established as (4.4)

$$\boldsymbol{\varepsilon}(\boldsymbol{X},t) := \underbrace{\boldsymbol{\nabla}^{\mathrm{sym}}\bar{\boldsymbol{u}} - (\llbracket\boldsymbol{u}\rrbracket_\mathrm{s} \otimes \boldsymbol{\nabla}\varphi)^{\mathrm{sym}} + \boldsymbol{\nabla}^{\mathrm{sym}}\llbracket\boldsymbol{u}\rrbracket\, M_\mathrm{s}}_{\bar{\boldsymbol{\varepsilon}}\ \text{regular}} + \underbrace{(\llbracket\boldsymbol{u}\rrbracket_\mathrm{s} \otimes \boldsymbol{N})^{\mathrm{sym}}\ \delta_\mathrm{s}}_{\boldsymbol{\varepsilon}_\delta\ \text{singular}}\ , \tag{4.12}$$

where again δ_s denotes the DIRAC-delta distribution at the discontinuity surface $\partial_\mathrm{s}\Omega$.

It is always possible to establish a re-parametrization of $\boldsymbol{u}$ by means of $\bar{\boldsymbol{u}}$ and $[\![\boldsymbol{u}]\!]$ such that $[\![\boldsymbol{u}]\!] = \text{const.}$ in the direction $\boldsymbol{N}$ normal to the discontinuity. For the remaining in-plane directions the contribution of $\boldsymbol{\nabla}^{\mathrm{sym}}[\![\boldsymbol{u}]\!]$ is considered to be negligible compared to the contribution of $(\llbracket\boldsymbol{u}\rrbracket_\mathrm{s} \otimes \boldsymbol{\nabla}\varphi)^{\mathrm{sym}}$ in (4.12). Hence, we assume $\boldsymbol{\nabla}[\![\boldsymbol{u}]\!] \approx \boldsymbol{0}$, cf. references [16, 128, 75, 41]. Following SIMO & OLIVER [115], our aim is to introduce the strong discontinuity kinematics within the framework of enhanced assumed strains (EAS). According to the EAS concept, the enhanced strains are modeled in an incompatible fashion — meaning that with view on a later finite element discretization no inter element continuity of the enhanced strains is required, cf. Section 2.3.6. Therefore, also from a variational point of view, it is admissible to neglect the term $\boldsymbol{\nabla}[\![\boldsymbol{u}]\!]$ in equation (4.12). Hence, from (4.12) we define:

$$\boldsymbol{\varepsilon} := \boldsymbol{\nabla}^{\mathrm{sym}}\bar{\boldsymbol{u}} - \underbrace{(\llbracket\boldsymbol{u}\rrbracket_\mathrm{s} \otimes \boldsymbol{\nabla}\varphi)^{\mathrm{sym}}}_{=:\boldsymbol{\varepsilon}_\varphi} + (\llbracket\boldsymbol{u}\rrbracket_\mathrm{s} \otimes \boldsymbol{N})^{\mathrm{sym}}\ \delta_\mathrm{s} \tag{4.13}$$

Again, assuming that the Heaviside function, and thus M_s, is stationary and again neglecting the term $\boldsymbol{\nabla}[\![\dot{\boldsymbol{u}}]\!]$, the strain rate can be found from (4.12) by differentiating once with respect

to time:

$$\dot{\boldsymbol{\varepsilon}} := \boldsymbol{\nabla}^{\mathrm{sym}}\dot{\boldsymbol{u}} - \underbrace{(\llbracket \dot{\boldsymbol{u}} \rrbracket_{\mathrm{s}} \otimes \boldsymbol{\nabla}\varphi)^{\mathrm{sym}}}_{=:\dot{\boldsymbol{\varepsilon}}_{\varphi}} + (\llbracket \dot{\boldsymbol{u}} \rrbracket_{\mathrm{s}} \otimes \boldsymbol{N})^{\mathrm{sym}} \ \delta_{\mathrm{s}} \tag{4.14}$$

Remark. In view of a possibly non-uniform evolution of the jump amplitude along the discontinuity surface, the assumption of $\llbracket \dot{\boldsymbol{u}} \rrbracket(\boldsymbol{X}) \approx \boldsymbol{0}$ may initially seem improper. It is admissible, however, since the evolution of the discontinuity in the present formulation does not rely on a continuous representation of the inner surface. As a consequence of the finite element discretization process, the crucial kinematics (4.13) will be sampled in a discrete set of points (finite elements or rather, as discussed later, integration points). In this context, the situation of a non-uniform evolution of the jump amplitude along the discontinuity surface would then be approximated by piecewise constant contributions of the respective sampling points. □

Remark. For the time being, any function satisfying conditions (4.10) is considered to be a suitable choice for the transmission function $\varphi(\boldsymbol{X})$. However, as already mentioned, closer inspection reveals that certain restrictions apply to guarantee a consistent formulation of the approach. This will be discussed in detail in Section 4.5.2. □

4.2 The weak and local form of the equilibrium equations

The description of the kinematics of a body crossed by a discontinuity surface established in the previous section, maintained the idea of a strain field that is defined everywhere in the body — inclusive of the discontinuity surface. Therefore, the discussion of equilibrium conditions for such a setting, can be done following classical lines and conveniently be based on the classical weak form of equilibrium. In dependence on Simo & Oliver [115] and Oliver [88] this notion shall be adopted in the following in order to establish the adequate form of the local (strong) conditions of equilibrium.

To this end, following up Section 2.3, we start from the weak form of the equilibrium equations as stated by the principle of virtual work (2.26):

$$\int_{\Omega} \boldsymbol{\nabla}^{\mathrm{sym}}\delta\boldsymbol{u} : \boldsymbol{\sigma} \, dV = \int_{\Omega} \boldsymbol{b} \bullet \delta\boldsymbol{u} \, dV + \int_{\partial_{\sigma}\Omega} \boldsymbol{t}^{*} \bullet \delta\boldsymbol{u} \, dA \ , \tag{4.15}$$

for all admissible test functions $\delta\boldsymbol{u} \in \mathcal{V}$. In view of the previously established strong discontinuity kinematics (4.8), a similar split as for the displacement field is introduced for the test functions, yielding

$$\delta\boldsymbol{u} = \delta\bar{\boldsymbol{u}} + \boldsymbol{\beta} M_{\mathrm{s}}(\boldsymbol{X}) \ . \tag{4.16}$$

The local form of the equilibrium equations in a strong discontinuity setting can then be derived in two steps. In a first step, the test functions are chosen to be regular functions on Ω. This is simply achieved by setting $\delta\boldsymbol{u} = \delta\bar{\boldsymbol{u}}$. This choice is then adopted for the weak form of the equilibrium equation (4.15). Integrating by parts [2] and using the Gauss theorem

[2] The product rule gives rise to the divergence property $\mathrm{div}\,(\boldsymbol{\sigma}\delta\boldsymbol{u}) = \delta\boldsymbol{u} \bullet \mathrm{div}\boldsymbol{\sigma} + \boldsymbol{\nabla}\delta\boldsymbol{u} : \boldsymbol{\sigma}$.

furnishes the left hand side of equation (4.15) as

$$\int_{\Omega} \boldsymbol{\nabla}^{\mathrm{sym}} \delta\boldsymbol{u} : \boldsymbol{\sigma}\, dV = -\int_{\Omega} \delta\boldsymbol{u} \bullet \operatorname{div} \boldsymbol{\sigma}\, dV + \int_{\partial_{\mathrm{s}}\Omega} \delta\boldsymbol{u} \bullet \left[\boldsymbol{\sigma}^{+}\boldsymbol{N}^{+} - \boldsymbol{\sigma}^{-}\boldsymbol{N}^{-}\right]\, dA + \int_{\partial_{\sigma}\Omega} \delta\boldsymbol{u} \bullet \boldsymbol{\sigma}\boldsymbol{N}\, dA\,. \tag{4.17}$$

Note, that application of the GAUSS theorem to the internal surface $\partial_{\mathrm{s}}\Omega$ gives rise to the intermediate term in the right hand side of equation (4.17). Inserting this result into the weak form of equilibrium (4.15), by a standard argument the local equilibrium equations

$$\operatorname{div} \boldsymbol{\sigma} + \boldsymbol{b} = \boldsymbol{0} \qquad \text{in} \quad \Omega \backslash \partial_{\mathrm{s}}\Omega \tag{4.18}$$

$$\boldsymbol{\sigma}\boldsymbol{N} = \boldsymbol{t}^{*} \qquad \text{on} \quad \partial_{\sigma}\Omega \tag{4.19}$$

and

$$\underbrace{\boldsymbol{\sigma}^{+}\boldsymbol{N} - \boldsymbol{\sigma}^{-}\boldsymbol{N}}_{[\![\boldsymbol{t}]\!]_{\mathrm{s}}} = \boldsymbol{0} \qquad \text{on} \quad \partial_{\mathrm{s}}\Omega \tag{4.20}$$

are obtained. In (4.20), again the notation $[\![(\bullet)(\boldsymbol{X})]\!]_{\mathrm{s}} := (\bullet)(\boldsymbol{X})^{+} - (\bullet)(\boldsymbol{X})^{-}\,,\ \forall \boldsymbol{X} \in \partial_{\mathrm{s}}\Omega$ was adopted. In a second step, now choosing the test functions to be discontinuous, i.e., $\delta\boldsymbol{u} = \boldsymbol{\beta} M_{\mathrm{s}}(\boldsymbol{X})$, the additional local condition

$$\boldsymbol{t}_{\mathrm{s}} - \boldsymbol{\sigma}^{+}\boldsymbol{N} = \boldsymbol{0} \qquad \text{on} \quad \partial_{\mathrm{s}}\Omega \tag{4.21}$$

can be derived following similar lines as above. Details are given in [115]. In (4.21), $\boldsymbol{t}_{\mathrm{s}}$ explicitly refers to the tractions prevailing *at* the discontinuity surface.

Condition (4.20) imposes the equality of the right-hand and left-hand limit of the tractions in the bulk material adjacent the discontinuity surface, while (4.21) requires the tractions *at* the discontinuity surface $\partial_{\mathrm{s}}\Omega$ to balance the right-hand traction limit. In conclusion, for a continuum body with a discontinuity surface, we have the classical local equilibrium conditions supplemented with two additional conditions, stating traction continuity over the discontinuity surface $\partial_{\mathrm{s}}\Omega$.

Proposition 4.2.1 (Traction continuity)**.** After onset of localization, the stress $\boldsymbol{\sigma}$ remains regularly distributed over the domain Ω. In particular, traction continuity over the discontinuity surface $\partial_{\mathrm{s}}\Omega$ is maintained.

4.3 Constitutive modeling in a strong discontinuity context

The previously derived kinematics associated with the presence of strong displacement discontinuities are composed of two different displacement fields, $[\![\boldsymbol{u}]\!]$ and $\bar{\boldsymbol{u}}$, compare equation (4.13). In the present section, the constitutive equations associated with these fields are discussed.

According to the definition of the kinematics of Section 4.1, the strains in the bulk material, denoted by $\Omega^{\pm}$, are regularly distributed — thus facilitating the application of standard stress-strain based continuum models. For the sake of clarity, in what follows linear elastic HOOKE's law is adopted for points belonging to $\Omega^{\pm}$. That is, the stresses $\boldsymbol{\sigma}$ in $\Omega^{\pm}$ are computed by means of the elastic fourth-order constitutive tensor $\mathbb{C} := \partial_{,\boldsymbol{\varepsilon}}\partial_{,\boldsymbol{\varepsilon}} W_{el}(\boldsymbol{X}, \boldsymbol{\varepsilon})$ according to $\dot{\boldsymbol{\sigma}} = \mathbb{C} : \dot{\boldsymbol{\varepsilon}}$. It should be noted, however, that any classical continuum model, such as plasticity or a damage theory can be applied equally well.

4.3.1 Traction-separation laws

On the discontinuity surface $\partial_{\mathrm{s}}\Omega$ — in contrast to $\Omega^{\pm}$ — the material response is ruled by the discontinuous displacement jump $[\![\boldsymbol{u}]\!]_{\mathrm{s}} = [\![\boldsymbol{u}]\!](\boldsymbol{X}, t)\ \forall \boldsymbol{X} \in \partial_{\mathrm{s}}\Omega$ and can be represented by a traction-separation law. Using the traction continuity condition (4.21) at the interface, a traction-separation law of the type

$$\boldsymbol{t}^{+} = \boldsymbol{t}_{\mathrm{s}}\left([\![\boldsymbol{u}]\!]_{\mathrm{s}}\right) \quad \text{with} \quad \boldsymbol{t} := \boldsymbol{\sigma}\boldsymbol{N}, \quad \boldsymbol{t}_{\mathrm{s}} := \boldsymbol{t}|_{\partial_{\mathrm{s}}\Omega} \tag{4.22}$$

renders an admissible choice.

Basically, there are two concepts that can be applied for development of a constitutive law of type (4.22). The first method involves a projection of a classical stress-strain relationship onto the discontinuity surface $\partial_{\mathrm{s}}\Omega$, e.g., SIMO et al. [116]. Alternatively, a traction-separation law can be derived from an assumed singular distributed stored energy functional W. This notion is adopted, e.g., by ARMERO [3], OLIVER [88] or MOSLER [76].

Following the latter concept, we postulate an additive split of the stored energy into a regularly distributed part W_{reg} corresponding to points in $\Omega^{\pm}$ and a singular part W_{ie} associated with points in $\partial_{\mathrm{s}}\Omega$ according to

$$W = W_{\mathrm{reg}} + W_{\mathrm{ie}}\,\delta_{\mathrm{s}}\ . \tag{4.23}$$

The fundamental assumption, the concept is based upon, is the direct association of the displacement discontinuity $[\![\boldsymbol{u}]\!]_{\mathrm{s}}$ with the inelastic deformation stemming from the singular portion of the stored energy functional; $W_{\mathrm{ie}} = W_{\mathrm{ie}}\left(\boldsymbol{\alpha}\left([\![\boldsymbol{u}]\!]_{\mathrm{s}}\right)\right)$ in terms of the displacement-like variable $\boldsymbol{\alpha} \in \mathbb{R}^n$ depending on the displacement discontinuity. Then, it is possible to define the space of admissible stresses (or rather tractions) in analogy to standard plasticity in a general fashion as

$$\mathbb{E}_{\boldsymbol{t}} := \{\left(\boldsymbol{t}^{+}, \boldsymbol{q}\right) \in \mathbb{R}^3 \times \mathbb{R}^n \mid \phi\left(\boldsymbol{t}^{+}, \boldsymbol{q}\right) \leqslant 0\} \qquad \forall \boldsymbol{X} \in \partial_{\mathrm{s}}\Omega\ . \tag{4.24}$$

Hence, the space of admissible stresses is confined by the yield (or failure) function $\phi\left(\boldsymbol{t}^{+}, \boldsymbol{q}\right)$, which is constituted of the traction vector $\boldsymbol{t}^{+}$ and a vector of stress-like hardening/softening parameters $\boldsymbol{q}$ that is conjugated to $\boldsymbol{\alpha}$. If we adopt the special choice $\phi\left(\boldsymbol{t}^{+}, \boldsymbol{q}\right) = \|\boldsymbol{t}^{+} - \boldsymbol{q}\|$ and $\boldsymbol{q} = \boldsymbol{t}_{\mathrm{s}}$ — then, $\phi = 0$ renders the traction continuity condition stated in Proposition 4.2.1. That is, the traction continuity condition (4.21) can be recast in a format that is identical to the yield condition known from standard plasticity theory. In what follows — as $\boldsymbol{t}_{\mathrm{s}}$ is

included in the stress-like variable $\boldsymbol{q}$ — we omit the + sign indicating the right-hand limit of the traction vector without risk of confusion, i.e., $\boldsymbol{t} := \boldsymbol{t}^+$.

The direct association of the displacement discontinuity $[\![\boldsymbol{u}]\!]_\mathrm{s}$ with the singular portion of the stored energy functional W_ie at the discontinuity surface, actually restricts the dissipative mechanism to the discontinuity surface $\partial_\mathrm{s}\Omega$. This, in turn, implies the concentration of inelastic deformation to the localization zone in case of softening response taking place. Such a behavior is indeed motivated by experimental observations and reflects the key characteristics of localization phenomena; in accordance with the fundamental work of Simo et al. [116], we devise:

Proposition 4.3.1 (Deformation concentration)**.** After onset of localization, inelastic deformation related to softening response, is concentrated to the localization zone represented by the discontinuity surface $\partial_\mathrm{s}\Omega$ — which is, for this reason, also termed *localization surface*.

Since the space of admissible stresses (4.24) is formally equivalent to that of standard plasticity theory, the evolution equations defining the interface law can be derived following similar lines as for the stress-strain based continuous case, cf. Section 2.4.2. Accordingly, by introducing two potentials $g(\boldsymbol{t}, \boldsymbol{q})$ and $h(\boldsymbol{t}, \boldsymbol{q})$, the rates of $[\![\boldsymbol{u}]\!]_\mathrm{s}$ and $\boldsymbol{\alpha}$ are defined in a general manner as

$$[\![\dot{\boldsymbol{u}}]\!]_\mathrm{s} := \lambda \partial_{,\boldsymbol{t}} g \quad \text{and} \quad \dot{\boldsymbol{\alpha}} := \lambda \partial_{,\boldsymbol{q}} h \; . \tag{4.25}$$

The precise definition of the space of admissible stresses (4.24) — which is analogous to the notion of *yield surface* in classical elastoplasticity — clearly depends on the particular choice of the norm $\|\bullet\|$. With a view to later developments we choose $q = \|\boldsymbol{t}_\mathrm{s}\|$ and specify

$$\begin{aligned} \phi \; : \; & \mathbb{R}^3 \times \mathbb{R}_+ \mapsto \mathbb{R} \\ & (\boldsymbol{t}, q) \mapsto \|\boldsymbol{t}\| - q \; , \end{aligned} \tag{4.26}$$

which reflects the case of *isotropic hardening / softening*.

Remark. For the specific choice $g = \phi$ and $h = \phi$, the associative case is obtained. Then, the evolution equations (4.25) can alternatively be derived as a result from the principle of maximum dissipation, cf. Section 2.4.2. Employing the energy functional (4.23), the dissipation inequality is then stated as [3, 76]

$$\mathcal{D} = \boldsymbol{t} \bullet [\![\dot{\boldsymbol{u}}]\!]_\mathrm{s} + \boldsymbol{q} \bullet \dot{\boldsymbol{\alpha}} \geqslant 0 \; . \tag{4.27}$$

In analogy to the continuum case of Section 2.4.2, the principle of maximum dissipation is adoped by postulating the dissipation according to (4.27) to be maximized within the space of admissible stresses $\mathbb{E}_{\boldsymbol{t}}$. Then, a constrained maximization problem is obtained, which can again be transferred to an equivalent unconstrained minimization problem by means of the Lagrange-functional (see, e.g., Luenberger [67]):

$$\mathcal{L}(\boldsymbol{t}, \boldsymbol{q}, \lambda) = -\mathcal{D} + \lambda \phi(\boldsymbol{t}, \boldsymbol{q}) \tag{4.28}$$

The KARUSH-KUHN-TUCKER conditions then determine the solution of the problem. In the present context, they read

$$[\![\dot{\boldsymbol{u}}]\!]_{\mathrm{s}} = \lambda \partial_{,\boldsymbol{t}} \phi, \quad \dot{\boldsymbol{\alpha}} = \lambda \partial_{,\boldsymbol{q}} \phi \tag{4.29}$$

and

$$\lambda \geqslant 0, \quad \phi\,(\boldsymbol{t}, \boldsymbol{q}) \leqslant 0, \quad \lambda \phi\,(\boldsymbol{t}, \boldsymbol{q}) = 0\,, \tag{4.30}$$

where equations (4.29) represent the associative form of the evolution equations (4.25). □

4.3.2 Correlation with strong discontinuity kinematics

Having established the traction-separation law including its evolution equations (4.25) and (4.29), respectively, a direct coherence with the strong discontinuity kinematics defined by equation (4.14) can readily be established. Accounting for the plastic dissipation at the discontinuity surface $\partial_{\mathrm{s}}\Omega$ and in view of (4.14), the resulting strain field is defined by

$$\dot{\boldsymbol{\varepsilon}} = \underbrace{\boldsymbol{\nabla}^{\mathrm{sym}} \dot{\boldsymbol{u}} - ([\![\dot{\boldsymbol{u}}]\!]_{\mathrm{s}} \otimes \boldsymbol{\nabla}\varphi)^{\mathrm{sym}}}_{\text{regular}} + \underbrace{([\![\dot{\boldsymbol{u}}]\!]_{\mathrm{s}} \otimes \boldsymbol{N})^{\mathrm{sym}}\, \delta_{\mathrm{s}} - \lambda\, \partial_{,\boldsymbol{\sigma}} g}_{\text{singular}}\,. \tag{4.31}$$

Also, complying with the assumption $\boldsymbol{\nabla}[\![\boldsymbol{u}]\!] \approx \boldsymbol{0}$ that has been made in the derivation of (4.14), the jump discontinuity can equivalently be expressed as

$$[\![\dot{\boldsymbol{u}}]\!]_{\mathrm{s}} = \dot{\zeta} \boldsymbol{m}\,, \tag{4.32}$$

where $\boldsymbol{m}$ denotes the direction of the displacement jump and $\dot{\zeta}$ represents its magnitude.

4.3.2.1 The regular portion of the enhanced strain field

Drawing attention to the regular portion of the strain field (4.31), the direct relation to the evolution equations (4.25) or (4.29) is derived as follows. Considering $(4.25)_1$ we obtain

$$([\![\dot{\boldsymbol{u}}]\!]_{\mathrm{s}} \otimes \boldsymbol{\nabla}\varphi)^{\mathrm{sym}} = \lambda \left(\partial_{,\boldsymbol{t}} g \otimes \boldsymbol{\nabla}\varphi\right)^{\mathrm{sym}}\,. \tag{4.33}$$

and can, with view of (4.14), conclude that

$$\dot{\boldsymbol{\varepsilon}}_{\varphi} = \lambda \left(\partial_{,\boldsymbol{t}} g \otimes \boldsymbol{\nabla}\varphi\right)^{\mathrm{sym}}\,. \tag{4.34}$$

The above result is now employed to describe the response of a material point in $\Omega_{\varphi}^{\pm}$ that is subject to HOOKE's law. Using (4.34) and adopting the strong discontinuity kinematics (4.14) renders

$$\begin{aligned} \dot{\boldsymbol{\sigma}} &= \mathbb{C} : \dot{\boldsymbol{\varepsilon}} \\ &= \mathbb{C} : \left(\boldsymbol{\nabla}^{\mathrm{sym}} \dot{\boldsymbol{u}} - \dot{\boldsymbol{\varepsilon}}_{\varphi}\right) \\ &= \mathbb{C} : \left(\boldsymbol{\nabla}^{\mathrm{sym}} \dot{\boldsymbol{u}} - \lambda \left(\partial_{,\boldsymbol{t}} g \otimes \boldsymbol{\nabla}\varphi\right)^{\mathrm{sym}}\right) \end{aligned} \tag{4.35}$$

Remarkably, constitutive relation (4.35) is formally identical to classical flow theory of plasticity — with term $(\partial_{,\boldsymbol{t}} g \otimes \boldsymbol{\nabla}\varphi)^{\mathrm{sym}}$ taking the role of the 'direction of flow', cf. equation $(2.74)_1$.

4.3.2.2 Physical relevance of the Lagrange multiplier λ

Complying with Proposition 4.3.1, we assume that the dissipative mechanism is restricted completely to the discontinuity surface $\partial\Omega_{\mathrm{s}}$. This assumption implies a singular distribution of the plastic multiplier, i.e., $\lambda \equiv \lambda\,\delta_{\mathrm{s}}$. Further, due to the direct association of the displacement discontinuity $[\![\boldsymbol{u}]\!]_{\mathrm{s}}$ with the dissipative mechanism at the discontinuity surface $\partial\Omega_{\mathrm{s}}$, the resulting plastic strains must correspond to the singular portion $([\![\dot{\boldsymbol{u}}]\!]_{\mathrm{s}} \otimes \boldsymbol{N})^{\mathrm{sym}}\ \delta_{\mathrm{s}}$ of the strain field (4.31):

$$([\![\dot{\boldsymbol{u}}]\!]_{\mathrm{s}} \otimes \boldsymbol{N})^{\mathrm{sym}}\ \delta_{\mathrm{s}} = \lambda\,\partial_{,\boldsymbol{\sigma}} g\ \delta_{\mathrm{s}} \tag{4.36}$$

Multiplication with $\partial_{,\boldsymbol{\sigma}}\phi : \mathbb{C}$ [88] and using (4.32), then furnishes λ as

$$\lambda = \frac{\partial_{,\boldsymbol{\sigma}}\phi : \mathbb{C} : ([\![\dot{\boldsymbol{u}}]\!]_{\mathrm{s}} \otimes \boldsymbol{N})^{\mathrm{sym}}}{\partial_{,\boldsymbol{\sigma}}\phi : \mathbb{C} : \partial_{,\boldsymbol{\sigma}} g} = \dot{\zeta}\,\frac{\partial_{,\boldsymbol{\sigma}}\phi : \mathbb{C} : (\boldsymbol{m} \otimes \boldsymbol{N})^{\mathrm{sym}}}{\partial_{,\boldsymbol{\sigma}}\phi : \mathbb{C} : \partial_{,\boldsymbol{\sigma}} g}\ . \tag{4.37}$$

For a frequently employed class of potential functions, such as the later adopted Rankine type (cf. Chapter 5), the partial derivative $\partial_{,\boldsymbol{\sigma}} g$ is determined as $(\boldsymbol{m} \otimes \boldsymbol{N})$, such that from (4.37) it is evident that

$$\lambda = \dot{\zeta}\ . \tag{4.38}$$

Hence, the Lagrange multiplier λ has a clear physical meaning, it represents the current change in the amplitude of the displacement discontinuity.

4.3.3 Strong discontinuity condition

The condition for the initial formation of a strong discontinuity, i.e., a jump in the displacement field, is termed *strong discontinuity condition* [3]. It allows to identify the orientation vector $\boldsymbol{N}$ of the discontinuity surface Ω_{s}. It should be noted, that formation of a strong discontinuity often is preceeded by a weak discontinuity, representing a jump in the displacement *gradient* field. For models only accounting for strong discontinuities, which are the focus of this work, this distiction is, however, dispensable. Yet, for the later adopted Rankine criterion (Chapter 5), conditions for weak and strong discontinuity, respectively, appear to be equivalent [75]. The following representation is essentially based on the work of Simo et al. [116] and Oliver [88].

[3] Sometimes, it is also referred to as *localization condition*, e.g. Regueiro & Borja [100].

Derivation of the strong discontinuity condition relies on the notion of a regular distribution of the stress field, e.g. [100]. Considering equation (4.31), the stress vector for an elastoplastic continuum material is defined by

$$\dot{\boldsymbol{t}} = \mathbb{C} : \left[\boldsymbol{\nabla}^{\mathrm{sym}} \dot{\boldsymbol{u}} - \dot{\boldsymbol{\varepsilon}}_{\varphi} + (\llbracket \dot{\boldsymbol{u}} \rrbracket_{\mathrm{s}} \otimes \boldsymbol{N})^{\mathrm{sym}} \, \delta_{\mathrm{s}} - \lambda \, \partial_{,\boldsymbol{\sigma}} g \right] \bullet \boldsymbol{N} \, . \tag{4.39}$$

Again assuming the dissipative mechanism to be restricted to the discontinuity surface $\partial_{\mathrm{s}}\Omega$, we can substitute λ by the previously derived definition (4.37) and rewrite (4.39) as

$$\dot{\boldsymbol{t}} = \boldsymbol{N} \bullet \mathbb{C} : \left[\boldsymbol{\nabla}^{\mathrm{sym}} \dot{\boldsymbol{u}} - \dot{\boldsymbol{\varepsilon}}_{\varphi} \right] + \boldsymbol{N} \bullet \underbrace{\left[\mathbb{C} - \frac{\mathbb{C} : \partial_{,\boldsymbol{\sigma}} g \otimes \partial_{,\boldsymbol{\sigma}} \phi : \mathbb{C}}{\partial_{,\boldsymbol{\sigma}} \phi : \mathbb{C} : \partial_{,\boldsymbol{\sigma}} g} \right]}_{\mathbb{C}_{\mathrm{ep}}^{\mathrm{perf}}} : (\llbracket \dot{\boldsymbol{u}} \rrbracket_{\mathrm{s}} \otimes \boldsymbol{N})^{\mathrm{sym}} \, \delta_{\mathrm{s}} \, , \tag{4.40}$$

with $\mathbb{C}_{\mathrm{ep}}^{\mathrm{perf}}$ as the elastoplastic continuum tangent for perfect plasticity. If the stress vector is to remain regularly distributed, the singular contributions in (4.40) must vanish. This implies

$$\boldsymbol{Q}(\boldsymbol{N}) \bullet \llbracket \dot{\boldsymbol{u}} \rrbracket_{\mathrm{s}} \stackrel{!}{=} \boldsymbol{0} \, , \tag{4.41}$$

where the acoustic tensor $\boldsymbol{Q}$ is defined as

$$\boldsymbol{Q}(\boldsymbol{N}) := \boldsymbol{N} \bullet \mathbb{C}_{\mathrm{ep}}^{\mathrm{perf}} \bullet \boldsymbol{N} \, , \tag{4.42}$$

e.g. Simo et al. [116], Oliver [88] and Regueiro & Borja [100].

In order to admit non-trivial solutions $\llbracket \dot{\boldsymbol{u}} \rrbracket_{\mathrm{s}} \neq \boldsymbol{0}$ of equation (4.42), the acoustic tensor must become singular, i.e.,

$$\det(\boldsymbol{Q}(\boldsymbol{N})) \stackrel{!}{=} 0 \, . \tag{4.43}$$

The normal vector $\boldsymbol{N}$ identifying the direction of the discontinuity can now be computed from condition (4.43). In some cases analytical solutions can be derived, see, e.g., Oliver [88]; generally however, it is required to revert to numerical solution procedures.

4.3.4 Condition of uniqueness

Having identified the formal analogy between the constitutive response of a material point in $\Omega_{\varphi}^{\pm}$ (4.35) and the classical flow theory of plasticity, cf. Section 2.4.2, it is possible to transfer some insights from the latter to the present setting.

The elastoplastic tangent constitutive tensor $\mathbb{C}_{\mathrm{ep}}$ (2.80) is adapted by simply replacing $\partial_{,\boldsymbol{\sigma}} g$ with $(\partial_{,\boldsymbol{t}} g \otimes \boldsymbol{\nabla}\varphi)^{\mathrm{sym}}$ from (4.35). Focusing on associative evolution equations, i.e., $h \equiv \phi$ and $g \equiv \phi$, the tangent constitutive tensor in a strong discontinuity context arises as

$$\mathbb{C}_{\varphi} = \mathbb{C} - \frac{\mathbb{C} : (\partial_{,\boldsymbol{t}} \phi \otimes \boldsymbol{\nabla}\varphi)^{\mathrm{sym}} \otimes \partial_{,\boldsymbol{\sigma}} \phi : \mathbb{C}}{\partial_{,\boldsymbol{\sigma}} \phi : \mathbb{C} : (\partial_{,\boldsymbol{t}} \phi \otimes \boldsymbol{\nabla}\varphi)^{\mathrm{sym}} + \partial_{,\boldsymbol{q}} \phi \bullet \boldsymbol{H} \bullet \partial_{,\boldsymbol{q}} \phi} \, . \tag{4.44}$$

In order to render a *unique* behavior, the denominator of (4.44) is required to be positive (Jirásek [53]):

$$\partial_{,\boldsymbol{\sigma}}\phi : \mathbb{C} : (\partial_{,\boldsymbol{t}}\phi \otimes \boldsymbol{\nabla}\varphi)^{\mathrm{sym}} + \partial_{,\boldsymbol{q}}\phi \bullet \boldsymbol{H} \bullet \partial_{,\boldsymbol{q}}\phi > 0 \tag{4.45}$$

In view of equation (4.35), the above condition corresponds to a *snap-back* in the $\boldsymbol{\sigma} - \boldsymbol{\nabla}^{\mathrm{sym}}\bar{\boldsymbol{u}}$ relation (Mosler [75]).

Remark. As will emerge in the discretized setting, see Section 4.5.2, via $\boldsymbol{\nabla}\varphi$ condition (4.45) actually poses a restriction on the maximum extension of the discretized localization zone Ω_φ and/or the order of polynomial approximation within the discretized localization zone Ω_φ. □

4.4 A mixed finite element formulation

From the strong discontinuity kinematics in Section 4.1 the strain field accounting for strong discontinuities is in a general fashion written as — cf. equation (4.13) —

$$\boldsymbol{\varepsilon} = \boldsymbol{\nabla}^{\mathrm{sym}}\bar{\boldsymbol{u}} + \tilde{\boldsymbol{\varepsilon}} \,, \tag{4.46}$$

composed of a regular strain field $\boldsymbol{\nabla}^{\mathrm{sym}}\bar{\boldsymbol{u}}$ stemming from the compatible part of the displacement field and an enhanced term $\tilde{\boldsymbol{\varepsilon}}$, containing a singular contribution, as well:

$$\tilde{\boldsymbol{\varepsilon}} := -\left(\boldsymbol{\mu} \otimes \boldsymbol{\nabla}\varphi\right)^{\mathrm{sym}} + \left(\boldsymbol{\mu} \otimes \boldsymbol{N}\right)^{\mathrm{sym}} \ \delta_{\mathrm{s}} \tag{4.47}$$

The displacement jump at the discontinuity surface is denoted by $\boldsymbol{\mu}$ rather than $[\![\boldsymbol{u}]\!]_{\mathrm{s}}$ to emphasize its element local character — as will be seen, in the present context the discontinuity does not necessarily need to be continuous across element boundaries. Interpreting the enhanced term as a consequence of an incompatible deformation mode, the strain field (4.46) can readily be associated with the concept of *enhanced assumed strains*, which was discussed in the previous Section 2.3.

There it was shown, that starting from a general Hu-Washizu three-field variational basis the introduction of a split of the strain field into a compatible and an enhanced portion (cf. equation (2.45)) along with the enforcement of an L_2-orthogonality condition between enhanced strain field and stress field (cf. equation (2.49)) removes the stress field from the variational formulation. Thus, the modified variational problem appears as constituted of the displacement field and the enhanced strain field and their variations, only (cf. equations (2.51) and (2.52)). Upon discretization (cf. Section 3.1) and the introduction of corresponding interpolations for the variable fields — in the general case furnishing a Petrov-Galerkin scheme —, the *local* enhanced strain field variables are eliminated on element level (cf. equations (3.17)). For convenience, we shall rewrite the linearized system of equations around a state of equilibrium:

$$\begin{aligned} &\underbrace{\left({}^{\mathrm{bb}}\mathbf{K}_e - {}^{\mathrm{bg}}\mathbf{K}_e({}^{\mathrm{gg}}\mathbf{K}_e)^{-1}\,{}^{\mathrm{gb}}\mathbf{K}_e\right)}_{\tilde{\mathbf{K}}_e}\dot{\mathbf{d}} \;=\; \dot{\mathbf{f}}_e \quad \text{and} \\ &\dot{\boldsymbol{\mu}} \;=\; -({}^{\mathrm{gg}}\mathbf{K}_e)^{-1}\,{}^{\mathrm{gb}}\mathbf{K}_e\,\dot{\mathbf{d}} \,, \end{aligned} \tag{4.48}$$

where $\dot{\mathbf{f}}_e$ is a generic symbol denoting a change of the elemental force vector, without differentiation between external and internal forces.

So far, the question of constructing appropriate enhanced strain field interpolations has not been addressed. As can be imagined, the choice is not completely arbitrary. In fact, certain restrictions apply (Simo & Armero [112]). Namely,

(i) *variational consistency*

(ii) *patch-test* conformity (constant nominal stress field)

(iii) *stability*

of the formulation have to be assured. In the present context, with view of Proposition 4.2.1, a fourth condition is of practical relevance:

(iv) *traction continuity* over the discontinuity surface $\partial_{\mathrm{s}}\Omega$

Subsequently, these issues are discussed more detailed.

4.4.1 Strong discontinuity kinematics and traction continuity

We have already identified the enhanced part $\tilde{\boldsymbol{\varepsilon}}$ of the general strain field (4.47). To justify the association with the *enhanced assumed strain* concept and assure variational consistency of the approach, the fundamental L_2-orthogonality between the enhanced strain variation and stress field (cf. Section 2.3.6) is to be addressed.

To this end, consider the enhanced strain test function space $\delta\tilde{\boldsymbol{\varepsilon}}$ according to $(3.10)_2$ and let $\boldsymbol{\sigma}$ denote the assumed variable stress field. Then, the L_2-orthogonality condition (2.49) for the discretized setting is enforced on element level according to

$$\int_{\Omega_e} \delta\tilde{\boldsymbol{\varepsilon}} : \boldsymbol{\sigma} \, dV \stackrel{!}{=} 0 \, . \tag{4.49}$$

Furthermore, in order to satisfy the *patch-test*, the assumed stress field is required to contain at least piecewise constant functions. Thus, equation (4.49) implies

$$\int_{\Omega_e} \delta\tilde{\boldsymbol{\varepsilon}} \, dV \stackrel{!}{=} \mathbf{0} \, . \tag{4.50}$$

Now addressing the question of choosing admissible functions for $\delta\tilde{\boldsymbol{\varepsilon}}$, it can be shown, that a standard Bubnov-Galerkin approach for the enhanced strain test functions of the form

$$\delta\tilde{\boldsymbol{\varepsilon}} = -\left(\delta\boldsymbol{\mu} \otimes \boldsymbol{\nabla}\varphi\right)^{\mathrm{sym}} + \left(\delta\boldsymbol{\mu} \otimes \boldsymbol{N}\right)^{\mathrm{sym}} \delta_{\mathrm{s}} \tag{4.51}$$

proves to be insufficient — equation (4.51) is obtained by simply adopting the same approach as for the enhanced strain trial space (4.47). For such a scheme, it is evident that condition (4.50) is only satisfied in special situations. To remedy this deficiency, we slightly modify the above equation (4.51) and propose in accordance with Simo & Oliver [115] and Oliver [87, 88]

$$\delta\tilde{\boldsymbol{\varepsilon}} = -\frac{A_s^e}{V^e}\,(\delta\boldsymbol{\mu}\otimes\boldsymbol{N})^{\mathrm{sym}} + (\delta\boldsymbol{\mu}\otimes\boldsymbol{N})^{\mathrm{sym}}\,\delta_{\mathrm{s}}\;; \tag{4.52}$$

vector $\delta\boldsymbol{\mu}$ be arbitrary to define the test function space for the enhanced strain field. This choice still reflects the split in a regular and a singular contribution; it is, however, independent of the transmission function $\varphi(\boldsymbol{X})$. Using the property (A.2) of the Dirac-delta distribution, see Appendix A, it can readily be verified that for this particular form of $\delta\tilde{\boldsymbol{\varepsilon}}$, condition (4.50) is satisfied. It should be noted, that by introducing (4.52) — instead of (4.51) — for the enhanced strain variation Ansatz, we obviously depart from the notion of a Bubnov-Galerkin scheme and instead migrate to a more general Petrov-Galerkin approach.

If we now adopt (4.52) and insert it into the internal equilibrium condition $(2.51)_2$ of the underlying variational problem,we have

$$\int_{\Omega_e} \hat{\boldsymbol{\sigma}} : \delta\tilde{\boldsymbol{\varepsilon}}\; dV = 0 \tag{4.53}$$

$$\Leftrightarrow \quad \frac{1}{V^e}\int_{\Omega_e} \hat{\boldsymbol{\sigma}} : (\delta\boldsymbol{\mu}\otimes\boldsymbol{N})\; dV = \frac{1}{A_s^e}\int_{\Omega_e} \hat{\boldsymbol{\sigma}} : (\delta\boldsymbol{\mu}\otimes\boldsymbol{N}\delta_s)\; dV\;, \tag{4.54}$$

which can equivalently [4] be written as

$$\frac{1}{V^e}\int_{\Omega_e} \delta\boldsymbol{\mu}\bullet(\hat{\boldsymbol{\sigma}}\boldsymbol{N})\; dV = \frac{1}{A_s^e}\int_{\Omega_e} \delta\boldsymbol{\mu}\bullet(\hat{\boldsymbol{\sigma}}\boldsymbol{N}\delta_s)\; dV\;. \tag{4.55}$$

With $\delta\boldsymbol{\mu}$ being arbitrary and again accounting for the properties of the Dirac-delta distribution (A.2), it follows from (4.55), that

$$\begin{aligned}\frac{1}{V^e}\int_{\Omega_e} \hat{\boldsymbol{\sigma}}\boldsymbol{N}\; dV &= \frac{1}{A_s^e}\int_{\Omega_e} \hat{\boldsymbol{\sigma}}\boldsymbol{N}\delta_s\; dV \\ &= \frac{1}{A_s^e}\int_{\partial_{\mathrm{s}}\Omega_e} \hat{\boldsymbol{\sigma}}\boldsymbol{N}\; dA \\ &= \frac{1}{A_s^e}\int_{\partial_{\mathrm{s}}\Omega_e} \boldsymbol{t}_{\mathrm{s}}\; dA\;.\end{aligned} \tag{4.56}$$

Identifying $\boldsymbol{t}_{\mathrm{s}}$ as the traction vector on the discontinuity surface $\delta_{\mathrm{s}}\Omega$, identity (4.56) renders, in an integral sense, the condition of traction continuity (4.21) at the discontinuity surface. This means, the variational basis (2.51) can be interpreted as the classical condition of weak

[4] consider the identity $\boldsymbol{A} : (\boldsymbol{a}\otimes\boldsymbol{b}) = \boldsymbol{a}\bullet(\boldsymbol{A}\boldsymbol{b})$

equilibrium for the bulk material enhanced by the additional requirement of traction continuity across the discontinuity surface in an integral sense

$$\begin{aligned} &\int_{\Omega} \boldsymbol{\nabla}^{\mathrm{sym}} \delta\boldsymbol{u} : \hat{\boldsymbol{\sigma}} \; dV - \mathcal{W}_{\mathrm{ext}}(\delta\boldsymbol{u}) = 0 \\ &- \frac{A_s^e}{V^e} \int_{\Omega_e} \boldsymbol{\delta\mu} \bullet \hat{\boldsymbol{\sigma}} \boldsymbol{N} \; dV + \int_{\partial_{\mathrm{s}}\Omega_e} \boldsymbol{\delta\mu} \bullet \boldsymbol{t}_{\mathrm{s}} \; dA = 0 \end{aligned} \tag{4.57}$$

Hence, from a mechanical point of view, the approach possesses the advantageous quality of reproducing *both* the *kinematics* (4.47) induced by the strong discontinuity *and* the *statical* requirement of traction continuity (4.21) — giving rise to its classification as a *statically and kinematically optimal nonsymmetric* (SKON) method, Jirásek [52]. The attribute "non-symmetric" identifies the price for these distinguished features: the loss of symmetry of the condensed stiffness matrix $\tilde{\mathbf{K}}_e$ (cf. Section 3.1.2).

We summarize as follows:

Proposition 4.4.1 (Weak traction continuity)**.** Using the particular choice (4.52) for the enhanced gradient variation Ansatz $\delta\tilde{\boldsymbol{\varepsilon}}$, the internal equilibrium condition $(2.51)_2$ of the underlying variational equations inherently — and variationally consistent — constitutes *traction continuity* along the discontinuity surface $\delta_s\Omega$ in a *weak* (integral) sense, see equation (4.56).

4.4.2 Stability considerations

Of further interest is the discussion of stability of the formulation. In the context of the adopted general Petrov-Galerkin discretization, the stability condition is equivalent to the condition of unique solvability of the linearized system of equations (3.14), provided that appropriate boundary conditions are applied, i.e., the system is not kinematically unstable. This notion shall be explored in the following.

Rendering the linearized system of equations (3.14) uniquely solvable, poses the requirement of regularity on the stiffness matrix $\mathbf{K}_e$, respectively its condensed form $\tilde{\mathbf{K}}_e$ (4.48). Using equations (3.14) and (3.15), the enhanced stiffness matrix is recast here as

$$\mathbf{K}_e = \begin{bmatrix} \mathbf{B}^T\mathbf{C}\mathbf{B} & \mathbf{B}^T\mathbf{C}\mathbf{G} \\ \hat{\mathbf{G}}^T\mathbf{C}\mathbf{B} & \hat{\mathbf{G}}^T\mathbf{C}\mathbf{G} \end{bmatrix} , \tag{4.58}$$

where integral signs have been omitted for the sake of clarity.

Assuming the material matrix $\mathbf{C}$ to be regular, the conventional element stiffness matrix ${}^{\mathrm{bb}}\mathbf{K}_e$ according to equation $(3.15)_1$ is considered to be regular, as well. A closer investigation of the enhanced stiffness matrix (4.58) by comparison of the respective terms in the first and second row reveals: In order to render the equations represented by the entries in $\mathbf{K}_e$ linear

independent, i.e., to maintain the regularity of $\mathbf{K}_e$, matrix $\mathbf{B}$ — representing the gradient of the displacement trial function space $\boldsymbol{\nabla}^{\mathrm{sym}}\mathcal{V}^h$ — and matrix $\hat{\mathbf{G}}^T$ — representing the function space of the enhanced strain test functions $\tilde{\mathcal{E}}^h_\delta$ — must be linear independent.

Furthermore, as already noted in Section 3.1.2, the derivation of the condensed system of equations (4.48) is based on the assumption of regularity of matrix ${}^{\mathrm{gg}}\mathbf{K}_e$. Recalling from equation (3.15), that

$$ {}^{\mathrm{gg}}\mathbf{K}_e = \int_{\Omega_e} \hat{\mathbf{G}}^T \mathbf{C}\mathbf{G}\, dV $$

and noting that $\mathbf{C}$ is regular, we conclude, that the regularity condition is met, if the columns of $\hat{\mathbf{G}}$ and $\mathbf{G}$ are each linearly independent.

The foregoing considerations can be summarized in accordance with Simo & Oliver [115] and Simo & Rifai [117]:

Proposition 4.4.2 (Stability)**.** With ${}^{\mathrm{bb}}\mathbf{K}_e$ being regular, the system of equations (3.14), respectively its condensed form (4.48), is uniquely solvable if, and only if,

(i) ${}^{\mathrm{gg}}\mathbf{K}_e$ is regular; satisfied, if the columns of $\hat{\mathbf{G}}$ and $\mathbf{G}$, respectively, are linearly independent.

(ii) $\tilde{\mathcal{E}}^h_\delta \cap \boldsymbol{\nabla}^{\mathrm{sym}}\mathcal{V}^h = \varnothing$; equivalently, the enhanced strain test function space must be linearly independent of the compatible strain field stemming from the displacement trial functions [5].

In the present setting, the adopted choice for the enhanced strain test functions reads (cf. (4.52))

$$ \delta\tilde{\boldsymbol{\varepsilon}} = -\frac{A^e_s}{V^e}\,(\delta\boldsymbol{\mu}\otimes\boldsymbol{N})^{\mathrm{sym}} + (\delta\boldsymbol{\mu}\otimes\boldsymbol{N})^{\mathrm{sym}}\,\delta_{\mathrm{s}}\ . \tag{4.59} $$

For this choice, it can readily be verified that the spaces of enhanced strain test functions $\tilde{\mathcal{E}}^h_\delta$ and compatible strain field trial functions $\boldsymbol{\nabla}^{\mathrm{sym}}\mathcal{V}^h$ are linearly independent — and therefore, requirement (ii) of Proposition 4.4.2 is satisfied. Requirement (i) is rather a technical issue, which is met likewise by the adopted approaches for $\tilde{\boldsymbol{\varepsilon}}$ and $\delta\tilde{\boldsymbol{\varepsilon}}$.

4.4.3 Transition to an equivalent continuum formulation

In the following, the close affinity of the precedent approach to a pure continuum formulation shall be illustrated. To begin with, the discretized form of the variational basis (3.12) — in view of the advocated enhanced strain trial and test functions (4.47) and (4.52), respectively — shall be devised.

[5] Note, that this restriction applies to the function space $\tilde{\mathcal{E}}^h_\delta$ of the enhanced strain test functions and *not* to the function space $\tilde{\mathcal{E}}^h$ of the corresponding trial functions!

4.4.3.1 Discretized weak form

Using matrix notation (cf. Section 3.1.2), and with view of decomposition (4.46), the strain rate at a point $\boldsymbol{X} \in \Omega_e^{\pm}$ in a finite element is recalled as

$$\dot{\boldsymbol{\varepsilon}}(\boldsymbol{X}) \;=\; \mathbf{B}(\boldsymbol{X})\dot{\mathbf{d}} + \mathbf{G}(\boldsymbol{X})\dot{\boldsymbol{\mu}}\,, \tag{4.60}$$

where now, from the strain field definition (4.47), matrix $\mathbf{G}$ of an element can be cast as

$$\mathbf{G} \;=\; -\mathbf{L}\,\boldsymbol{\nabla}\varphi \;=\; -\begin{bmatrix} \frac{\partial\varphi}{\partial X} & 0 & 0 \\ 0 & \frac{\partial\varphi}{\partial Y} & 0 \\ 0 & 0 & \frac{\partial\varphi}{\partial Z} \\ \frac{\partial\varphi}{\partial Y} & \frac{\partial\varphi}{\partial X} & 0 \\ 0 & \frac{\partial\varphi}{\partial Z} & \frac{\partial\varphi}{\partial Y} \\ \frac{\partial\varphi}{\partial Z} & 0 & \frac{\partial\varphi}{\partial X} \end{bmatrix}\,. \tag{4.61}$$

Further, considering the enhanced strain test function Ansatz (3.10), from equation (4.52), we express matrix $\hat{\mathbf{G}}$ as composed of a regular and a singular contribution:

$$\hat{\mathbf{G}} \;=\; -\frac{A_s^e}{V^e}\,\mathbf{g} + \mathbf{g}\,\delta_s\,, \tag{4.62}$$

where

$$\mathbf{g} \;:=\; \begin{bmatrix} N_1 & 0 & 0 \\ 0 & N_2 & 0 \\ 0 & 0 & N_3 \\ N_2 & N_1 & 0 \\ 0 & N_3 & N_2 \\ N_3 & 0 & N_1 \end{bmatrix}\,. \tag{4.63}$$

Introducing the above definitions into the variational basis (3.12), the discretized weak form of equilibrium reads

$$\begin{aligned} &\mathop{\mathsf{A}}_{e=1}^{n_{el}} \left| \int_{\Omega_e} \mathbf{B}^T\,\hat{\boldsymbol{\sigma}}\;dV - \int_{\Omega_e} \mathbf{N}^T\,\mathbf{b}\;dV - \int_{\partial\Omega_e} \mathbf{N}^T\,\mathbf{t}^*\;dA = 0 \right. \\ &\mathop{\mathsf{A}}_{e=1}^{n_{el}} \left| -\frac{A_s^e}{V^e}\int_{\Omega_e} \mathbf{g}^T\,\hat{\boldsymbol{\sigma}}\;dV + \int_{\partial_{\mathrm{s}}\Omega} \mathbf{t}_{\mathrm{s}}\;dA = 0\,. \right. \end{aligned} \tag{4.64}$$

Naturally, the above system of equations represents the discretized counterpart to equations (4.57).

4.4.3.2 Linearized weak form

In the same manner, i.e., by employing the definitions of $\mathbf{G}$ (4.61) and $\hat{\mathbf{G}}$ (4.62), the linearized system of equations (3.14) is rewritten as

$$\mathop{\mathsf{A}}_{e=1}^{n_{el}} \left| \begin{bmatrix} {}^{\mathrm{bb}}\mathbf{K}_e & {}^{\mathrm{bg}}\mathbf{K}_e \\ {}^{\mathrm{g}_r\mathrm{b}}\mathbf{K}_e & {}^{\mathrm{g}_r\mathrm{g}}\mathbf{K}_e + {}^{\mathrm{h}}\mathbf{K}_e \end{bmatrix} \right. \begin{Bmatrix} \dot{\mathbf{d}} \\ \dot{\boldsymbol{\mu}} \end{Bmatrix} = \begin{Bmatrix} \mathbf{f}_e^{\mathrm{ext}} - \mathbf{f}_e^{\mathrm{int}} \\ -\mathbf{h}_e \end{Bmatrix} , \tag{4.65}$$

where matrices ${}^{\mathrm{bb}}\mathbf{K}_e$ and ${}^{\mathrm{bg}}\mathbf{K}_e$ already have been defined in (3.15). Matrices ${}^{\mathrm{g}_r\mathrm{b}}\mathbf{K}_e$ and ${}^{\mathrm{g}_r\mathrm{g}}\mathbf{K}_e$ are determined by the *regular* portion of $\hat{\mathbf{G}}$, so that we have

$$\begin{aligned} {}^{\mathrm{bb}}\mathbf{K}_e &:= \int_{\Omega_e} \mathbf{B}^T\mathbf{C}\mathbf{B}\, dV & {}^{\mathrm{bg}}\mathbf{K}_e &:= \int_{\Omega_e} \mathbf{B}^T\mathbf{C}\mathbf{G}\, dV \\ {}^{\mathrm{g}_r\mathrm{b}}\mathbf{K}_e &:= -\frac{A_s^e}{V^e}\int_{\Omega_e} \mathbf{g}^T\mathbf{C}\mathbf{B}\, dV & {}^{\mathrm{g}_r\mathrm{g}}\mathbf{K}_e &:= -\frac{A_s^e}{V^e}\int_{\Omega_e} \mathbf{g}^T\mathbf{C}\mathbf{G}\, dV \ . \end{aligned} \tag{4.66}$$

Matrix ${}^{\mathrm{h}}\mathbf{K}_e$ is assembled from contributions stemming from the *singular* portion of $\hat{\mathbf{G}}$. Considering that

$$\begin{aligned} \int_{\Omega_e} \mathbf{g}^T\mathbf{C}\mathbf{B}\,\delta_{\mathrm{s}}\, dV\, \dot{\mathbf{d}} + \int_{\Omega_e} \mathbf{g}^T\mathbf{C}\mathbf{G}\,\delta_{\mathrm{s}}\, dV\, \dot{\boldsymbol{\mu}} &= \int_{\partial_{\mathrm{s}}\Omega_e} \mathbf{g}^T\mathbf{C}\underbrace{\left(\mathbf{B}\dot{\mathbf{d}} + \mathbf{G}\dot{\boldsymbol{\mu}}\right)}_{=\dot{\boldsymbol{\varepsilon}}\ (4.60)}\, dA \\ &= \int_{\partial_{\mathrm{s}}\Omega_e} \mathbf{g}^T\dot{\hat{\boldsymbol{\sigma}}}\, dA = \int_{\partial_{\mathrm{s}}\Omega_e} \dot{\mathbf{t}}_{\mathrm{s}}\, dA \ , \end{aligned} \tag{4.67}$$

and assuming the rate form constitutive of the tractions at the discontinuity being given by $\dot{\mathbf{t}}_{\mathrm{s}} := \mathbf{H}\,\dot{\boldsymbol{\mu}}$, we arrive at the definition

$${}^{\mathrm{h}}\mathbf{K}_e := \int_{\partial_{\mathrm{s}}\Omega_e} \mathbf{H}\, dA \ . \tag{4.68}$$

Matrix $\mathbf{H}$ can readily be interpreted as tangential constitutive assembled from the softening moduli of the respective directions. The remaining quantities are accordingly rendered as

$$\begin{aligned} \mathbf{f}_e^{\mathrm{ext}} &:= \int_{\Omega_e} \mathbf{N}^T\mathbf{b}\, dV + \int_{\partial\Omega_e} \mathbf{N}^T\,\mathbf{t}^*\, dA \\ \mathbf{f}_e^{\mathrm{int}} &:= \int_{\Omega_e} \mathbf{B}^T\hat{\boldsymbol{\sigma}}\, dV \\ \mathbf{h}_e &:= \int_{\Omega_e} \hat{\mathbf{G}}^T\hat{\boldsymbol{\sigma}}\, dV = -\frac{A_s^e}{V^e}\int_{\Omega_e} \mathbf{g}^T\hat{\boldsymbol{\sigma}}\, dV + \int_{\partial_{\mathrm{s}}\Omega_e} \dot{\mathbf{t}}_{\mathrm{s}}\, dA \ , \end{aligned} \tag{4.69}$$

cf. definitions (3.16).

Remark. Notably, the element related cross-sectional area A_s^e of the discontinuity surface is not necessarily required to be computed explicitly. Assuming the tractions along the elemental discontinuity surface to be constant, the second integral term in $(4.64)_2$ can be recast as

$$\int_{\partial_s\Omega_e} \mathbf{t}_s \, dA = A_s^e \, \mathbf{t}_s \; , \tag{4.70}$$

so that A_s^e can be eliminated from the discretized weak form (4.64) and the corresponding linearized equations (4.65). □

4.4.3.3 Equivalent continuum formulation

In analogy to Section 3.1.2 the system of equations (4.65) can equivalently be expressed in a statically condensed format. In view of equations (3.17), we obtain

$$\begin{aligned} \tilde{\mathbf{K}}_e &= {}^{\mathrm{bb}}\mathbf{K}_e - {}^{\mathrm{bg}}\mathbf{K}_e \left[{}^{\mathrm{g}_r\mathrm{g}}\mathbf{K}_e + {}^{\mathrm{h}}\mathbf{K}_e\right]^{-1} {}^{\mathrm{g}_r\mathrm{b}}\mathbf{K}_e \quad \text{and} \\ \dot{\boldsymbol{\mu}} &= -\left[{}^{\mathrm{g}_r\mathrm{g}}\mathbf{K}_e + {}^{\mathrm{h}}\mathbf{K}_e\right]^{-1} \left(\mathbf{h}_e + {}^{\mathrm{g}_r\mathrm{b}}\mathbf{K}_e \dot{\mathbf{d}}\right) \; . \end{aligned} \tag{4.71}$$

The affinity to a pure continuum formulation can be illustrated when expanding the above expression for the condensed stiffness matrix:

$$\begin{aligned} \tilde{\mathbf{K}}_e = & \int_{\Omega_e} \mathbf{B}^T \mathbf{C} \mathbf{B} \, dV \\ & - \int_{\Omega_e} \mathbf{B}^T \mathbf{C} \mathbf{G} \, dV \left[-\frac{A_s^e}{V^e} \int_{\Omega_e} \mathbf{g}^T \mathbf{C} \mathbf{G} \, dV + \int_{\partial_s\Omega_e} \mathbf{H} \, dA \right]^{-1} \left(-\frac{A_s^e}{V^e} \int_{\Omega_e} \mathbf{g}^T \mathbf{C} \mathbf{B} \, dV \right) \end{aligned} \tag{4.72}$$

Assuming, for the moment, a constant strain state over the element domain, the integrals can be eliminated from the formulation, yielding

$$\begin{aligned} \tilde{\mathbf{K}}_e &= V^e \mathbf{B}^T \left[\mathbf{C} - \mathbf{C}\mathbf{G} \left[-A_s^e \mathbf{g}^T \mathbf{C} \mathbf{G} + A_s^e \mathbf{H} \right]^{-1} \left(-A_s^e \mathbf{g}^T \mathbf{C} \right) \right] \mathbf{B} \\ &= V^e \mathbf{B}^T \underbrace{\left[\mathbf{C} - \mathbf{C}(-\mathbf{G}) \left[\mathbf{g}^T \mathbf{C}(-\mathbf{G}) + \mathbf{H} \right]^{-1} \mathbf{g}^T \mathbf{C} \right]}_{\tilde{\mathbf{C}}} \mathbf{B} \; ; \end{aligned} \tag{4.73}$$

matrix $\tilde{\mathbf{C}}$ representing the equivalent continuum tangent. This notion can be further explored, if the direction of the displacement jump is assumed to be fixed, so that the enhanced variable vector $\boldsymbol{\mu}$ reduces to a scalar magnification of $\mathbf{m}$ according to

$$\boldsymbol{\mu} = \zeta \mathbf{m} \; . \tag{4.74}$$

Then, $\mathbf{g}$ and $\mathbf{G}$ are substituted by $\mathbf{gm}$ and $\mathbf{Gm}$, respectively, finally rendering the equivalent continuum tangent as

$$\tilde{\mathbf{C}} = \mathbf{C} - \frac{\mathbf{C}\,(-\mathbf{G}\mathbf{m})\,(\mathbf{g}\mathbf{m})^T\,\mathbf{C}}{(\mathbf{g}\mathbf{m})^T\,\mathbf{C}\,(-\mathbf{G}\mathbf{m}) + H} \; , \tag{4.75}$$

see also Wells [128]. Identifying **gm** as the gradient of the yield function and $(-\mathbf{Gm})$ as the gradient of the plastic potential, equation (4.75) identically reflects the, generally unsymmetric, continuum tangent of an elasto-plastic material with non-associative flow rule and hardening modulus H; compare to $\mathbb{C}_{\text{ep}}$, as defined by equation (2.80).

This finding suggests the possibility of a treatment of strong discontinuities within a pure continuum formulation, as it was already motivated in Section 4.3. Although the formal equivalence as derived above is exact only for the case of constant strain elements — due to the elimination of the integrals in (4.73) — the continuum notion can be adopted in order to develop a generalization of the concept. As will be elaborated in Section 4.5.1, this finally facilitates a convenient algorithmic formulation for arbitrary finite elements. Furthermore, as a consequence of the continuum concept, the enhanced degrees of freedom $\dot{\boldsymbol{\mu}}$ can be eliminated on integration point level — featuring the particular advantage that a static condensation procedure on element level renders dispensable.

Remark. It should be noted that the non-symmetric character of the affine continuum tangent (4.75) is a direct consequence of the adopted Petrov-Galerkin approach. The continuum notion once more reveals the essential properties of the adopted SKON approach (cf. Section 4.4.1): statical and kinematical optimality, due to different choices regarding enhanced strain trial and test function spaces (cf. equations (4.47) and (4.52), or alternatively, the respective matrix forms (4.61) and (4.62)) — gained at the cost of symmetry. □

4.5 Adaptation to a high-order finite element approach

With particular focus to a possible application within a high-order finite element framework, the present section is dedicated to extending the so far developed concept. To this end, Section 4.5.1 takes the discussion of Section 4.4.3 on and initially casts the strong discontinuity formulation in a pure continuum format which dispenses with the restriction of one localization plane per finite element. Subsequently, Section 4.5.2 presents a consequent reassessment of the strong discontinuity kinematics, proving essential for the extension to high-order finite element approximations.

4.5.1 Generalization of the concept

Based on the notion that each integration point of a finite element represents a volume of finite size, the present section abandons the restriction of one localization plane per finite element — instead, the possibility of separate and independent localization planes is postulated for each integration point under consideration. An equivalent setting is adopted by Mosler & Meschke [78, 80] and Mosler [75].

Subsequently, the basic lines of the formulation regarding Gauss point associated discontinuities in dependence on Mosler & Meschke [78, 80] are developed. That followed, an alternative notion to the problem is presented in Section 4.5.1.2.

4.5.1.1 Formulation for GAUSS point associated discontinuities

To begin with, we consider a material point in $\Omega^{\pm}$ whose response is determined by deformation localization in the adjacent discontinuity surface $\partial_{\mathrm{s}}\Omega_e$ with normal $\boldsymbol{N}$. The behavior in the bulk material be subject to HOOKE's law. Then, according to equation (4.35), the evolution of stress in the bulk material is described by

$$\dot{\boldsymbol{\sigma}} = \mathbb{C} : \left(\boldsymbol{\nabla}^{\mathrm{sym}} \dot{\boldsymbol{u}} - \lambda \left(\partial_{,\boldsymbol{t}} g \otimes \boldsymbol{\nabla} \varphi \right)^{\mathrm{sym}} \right) , \tag{4.76}$$

where the term $\lambda \, \partial_{,\boldsymbol{t}} g$ reflects the enhanced displacements rates $\dot{\boldsymbol{\mu}}$, i.e., the jump $[\![\boldsymbol{u}]\!]_{\mathrm{s}}$ at the discontinuity surface, cf. equation $(4.25)_1$. Furthermore, satisfaction of the previously derived weak traction continuity condition $(4.57)_2$ requires [6]

$$\frac{1}{V^e} \int_{\Omega_e} \dot{\boldsymbol{\sigma}} \boldsymbol{N} \, dV = \frac{1}{A_s^e} \int_{\delta_{\mathrm{s}}\Omega_e} \dot{\boldsymbol{t}}_{\mathrm{s}} \, dA \, . \tag{4.77}$$

In the present setting, the statement of weak traction continuity (4.77) must hold for every considered GAUSS point i with associated localization surface $\partial_{\mathrm{s}}\Omega^{(i)}$ [78]. Figure 4.5 schematically depicts the situation of a quadrilateral element with two GAUSS points exhibiting localized response.

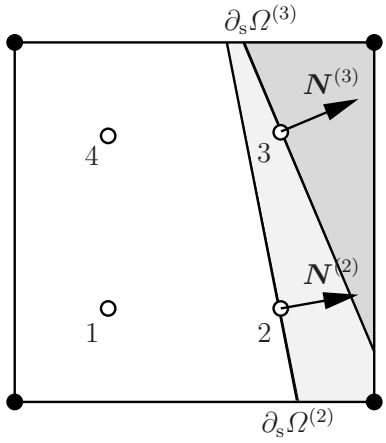

Figure 4.5: Schematic sketch of a quadrilateral element with two localization surfaces associated to GAUSS points 2 and 3, respectively.

Considering a particular GAUSS point and adopting equation (4.76), the left hand side of the

[6] To improve readability, the superscript $\hat{\bullet}$, denoting the stress field computed from the assumed strain by evaluation of the respective constitutive law, is omitted here and in the remainder of the work. Since the asssumed variable stress field has been removed from the formulation by means of the L_2-orthogonality (see Section 2.3.6) there is no further risk of confusion.

weak traction continuity condition (4.77) can be reformulated as [7]

$$\begin{aligned}
&\frac{1}{V^e}\int_{\Omega_e} \dot{\boldsymbol{\sigma}}\boldsymbol{N}\, dV \\
=&\frac{1}{V^e}\int_{\Omega_e} \left[\mathbb{C} : \left(\boldsymbol{\nabla}^{\mathrm{sym}}\dot{\bar{\boldsymbol{u}}} - \lambda\left(\partial_{,\boldsymbol{t}} g \otimes \boldsymbol{\nabla}\varphi\right)^{\mathrm{sym}}\right)\right]\boldsymbol{N}\, dV \\
=&\underbrace{\left[\mathbb{C} : \left(\boldsymbol{\nabla}^{\mathrm{sym}}\dot{\bar{\boldsymbol{u}}} - \lambda\,\frac{1}{V^e}\left(\partial_{,\boldsymbol{t}} g \otimes \int_{\Omega_e}\boldsymbol{\nabla}\varphi\, dV\right)^{\mathrm{sym}}\right)\right]}_{\dot{\boldsymbol{\sigma}}}\boldsymbol{N}\,,
\end{aligned} \tag{4.78}$$

such that the rate form constitutive law now can equivalently be cast as

$$\dot{\boldsymbol{\sigma}} = \mathbb{C} : \left(\boldsymbol{\nabla}^{\mathrm{sym}}\dot{\bar{\boldsymbol{u}}} - \lambda\,\left(\partial_{,\boldsymbol{t}} g \otimes \overline{\boldsymbol{\nabla}\varphi}\right)^{\mathrm{sym}}\right)\,, \tag{4.79}$$

where

$$\overline{\boldsymbol{\nabla}\varphi}(\boldsymbol{X}) := \frac{1}{V^e}\int_{\Omega_e}\boldsymbol{\nabla}\varphi(\boldsymbol{\xi})\, dV\,. \tag{4.80}$$

Considering Proposition 4.4.1, we conclude: Adopting the so modified constitutive law (4.79) together with equation (4.80) at integration point level, facilitates satisfaction of the weak traction continuity condition (4.77) and hence, fulfills the variational equation $(4.57)_2$.

A particular asset of this approach is the elimination of the enhanced degrees of freedom $\dot{\boldsymbol{\mu}}$ on integration point level, which consequently renders dispensable an otherwise required static condensation procedure on element level. This also means that the overall structure of the finite element algorithm remains unchanged by the incorporation of strong discontinuities in the proposed manner — which features a distinct computational advantage. Adversely assessed, on the other hand, can be the fact that evaluation of the constitutive response via $\overline{\boldsymbol{\nabla}\varphi}$ now incorporates element information — hence, a clear distinction between element and material information is lost.

4.5.1.2 An alternative notion to the problem

Definition of the transmission function gradient $\overline{\boldsymbol{\nabla}\varphi}$ according to equation (4.80) closely resembles the concept of *nonlocal models* (Pijaudier-Cabot & Bažant [95, 9]). The fundamental idea of nonlocal models is manifested by replacing a certain local variable by its nonlocal counterpart and so allowing for the influence of the neighborhood on the considered material particle. In general, the nonlocal counterpart $(\bar{\bullet})$ of some local quantity $(\bullet)$ is specified by

$$(\bar{\bullet})(\boldsymbol{X}) = \int_{\Omega} a(\boldsymbol{X},\boldsymbol{\xi})\,(\bullet)(\boldsymbol{\xi})\, dV\,, \tag{4.81}$$

[7] Note, that for the considered integration point the quantities $\boldsymbol{t}_{\mathrm{s}}$, $\boldsymbol{m}$, $\boldsymbol{N}$ and $\boldsymbol{\nabla}^{\mathrm{sym}}\bar{\boldsymbol{u}}$ are independent of $\boldsymbol{X}$!

where $a(\boldsymbol{X}, \boldsymbol{\xi})$ represents the *nonlocal weight function*, which frequently is taken as a function of the distance between *source point* position $\boldsymbol{\xi}$ and considered material point (*effect point*) position $\boldsymbol{X}$, see e.g., JIRÁSEK [51]. Characteristical, this distance is related to an *internal length* scale l that is considered as a material parameter; further, the weight function is constructed such that it attains its positive maximum at $\boldsymbol{X}$ and fades, often monotonically, with increasing distance $|\boldsymbol{\xi} - \boldsymbol{X}|$. In addition, to facilitate the correct reproduction of a constant local field, the nonlocal weight function must suffice condition

$$\int_{\Omega} a(\boldsymbol{X}, \boldsymbol{\xi})\, dV = 1 \quad , \forall \boldsymbol{X} \in \Omega \, . \tag{4.82}$$

When adopting such a nonlocal model to materials that exhibit strain softening (see, e.g., references [8], [103] and [57]), the internal length scale l directly influences the extension of the localization zone. The nonlocal formulation thus is employed as a *localization limiter* by preventing the localized zone from contracting with further refinement of the discretization and is therefore qualified as a regularization technique. Noteworthy, apart from the localization limiter capability, nonlocal formulations also provide for a smoothing effect [41], which of course directly correlates with the type of employed weight function.
To transfer this notion to our present setting we specify a nonlocal weight function as

$$a(\boldsymbol{X}, \boldsymbol{\xi}) := \frac{\chi_e}{V_e} \quad , \forall \boldsymbol{X} \in \Omega \, , \tag{4.83}$$

where χ_e is defined according to (3.9); obviously, this definition suffices condition (4.82). Then, with this weight function at hand, due to equation (4.81), the modified transmission function gradient $\overline{\boldsymbol{\nabla}\varphi}$ according to equation (4.80) can readily be identified as the *nonlocal average* to $\boldsymbol{\nabla}\varphi$.

Adopting this view, nonlocal averaging motivates an alternative perception of the traction continuity condition (4.77). To this end, the domain of a finite element is notionally split into finite portions $\Omega^{(i)}$ associated with the respective GAUSS points, such that $\Omega_e = \bigcup_{i=1}^{n_{\mathrm{gp}}} \Omega^{(i)}$, where n_{gp} denotes the number of elemental GAUSS points (Figure 4.6a). For each of these subdomains the possible formation of a discontinuity plane $\delta_{\mathrm{s}}\Omega^{(i)}$ is accounted for. Then, considering this partitioning for the formulation of the L_2-orthogonality condition (4.49) and the approach for the enhanced strain test functions (4.52), the traction continuity condition (4.77) can finally be recast as

$$\frac{1}{V^{(i)}} \int_{\Omega^{(i)}} \dot{\boldsymbol{\sigma}} \boldsymbol{N}^{(i)}\, dV = \frac{1}{A_s^{(i)}} \int_{\delta_{\mathrm{s}}\Omega^{(i)}} \dot{\boldsymbol{t}}_{\mathrm{s}}\, dA \, , \tag{4.84}$$

with $V^{(i)}$ and $A_s^{(i)}$ representing volume respectively discontinuity surface area associated to GAUSS point i. Equation (4.84) must be fulfilled for each affected GAUSS point.

Figure 4.6b schematically depicts the situation of a planar quadrilateral element, where two GAUSS points are subject to discontinuous response.

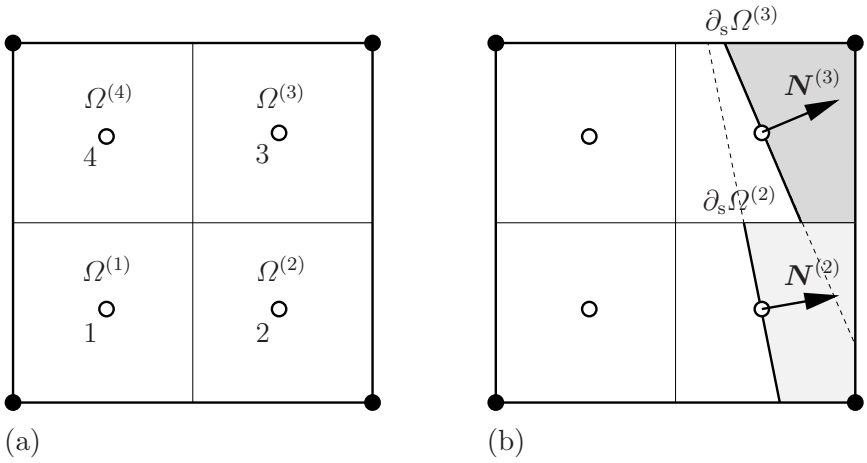

Figure 4.6: (a) Schematic sketch of a quadrilateral element partitioned into GAUSS point associated subdomains $\Omega^{(i)}$. (b) Formation of two localization surfaces associated to GAUSS points 2 and 3, respectively.

Assuming a sufficiently high order of integration, rates of stress and traction can be considered as approximately constant over the correspondingly small domains $\Omega^{(i)}$ and $\delta_s\Omega^{(i)}$. In consequence, equation (4.84) reduces to

$$\dot{\boldsymbol{\sigma}}\boldsymbol{N}^{(i)} = \dot{\boldsymbol{t}}_s \; ; \tag{4.85}$$

constituting a completely independent and GAUSS point local treatment of the former integral type traction continuity condition.

For the evaluation of the stress rate $\dot{\boldsymbol{\sigma}}$ in equation (4.85) now the notion of *nonlocal averaging* of the transmission function gradient $\boldsymbol{\nabla}\varphi$ is adopted. Accordingly the stress rates are determined subject to (4.79) using the nonlocal average (4.80). As an important aspect of the nonlocal averaging procedure a smoothing of the transmission function gradient $\boldsymbol{\nabla}\varphi$ is introduced. On the one hand, this smoothing effect indeed proves beneficial from a numerical point of view; tests show that it considerably contributes to the robustness of the approach. On the other hand, nonlocal averaging reflects the *physical property* that the kinematics of multiple localization surfaces within one finite element are in fact *not* mutually independent.

The notion of nonlocal averaging also substantiates that via the transmission function under the terms of (4.80) an element size related internal length scale is implicitly introduced into the formulation.

4.5.2 Reassessment of the strong discontinuity kinematics

With special attention to a high-order finite element framework, this section resumes the discussion and motivation of a suitable choice for the transmission function $\varphi(\boldsymbol{X})$, respectively its gradient $\boldsymbol{\nabla}\varphi(\boldsymbol{X})$, put forth by the strong discontinuity kinematics of Section 4.1. There,

it was already indicated, that the choice of $\varphi(\boldsymbol{X})$ is not completely arbitrary — subsequently, the decisive characteristics are elaborated and discussed thoroughly.

4.5.2.1 Equivalence of standard and reformulated discontinuity kinematics

Again, let us assume the situation of a body Ω with a localization surface $\partial_{\mathrm{s}}\Omega$. Then, in view of the previously described rate form constitutive framework, we restate the modified version of the strong discontinuity kinematics (4.14) and write the enhanced strain rates within the domain Ω as

$$\dot{\boldsymbol{\varepsilon}} = \boldsymbol{\nabla}^{\mathrm{sym}}\dot{\boldsymbol{u}} - (\llbracket\dot{\boldsymbol{u}}\rrbracket_{\mathrm{s}} \otimes \boldsymbol{\nabla}\varphi)^{\mathrm{sym}} + (\llbracket\dot{\boldsymbol{u}}\rrbracket_{\mathrm{s}} \otimes \boldsymbol{N})^{\mathrm{sym}}\ \delta_{\mathrm{s}} \ . \tag{4.86}$$

We recall that the modified version of strong discontinuity kinematics was initially motivated by a more convenient treatment of the DIRICHLET constraints (Section 4.1.2), furnished by the displacement field decomposition (4.11):

$$\dot{\boldsymbol{u}}(\boldsymbol{X},t) = \dot{\tilde{\boldsymbol{u}}}(\boldsymbol{X},t) + \llbracket\dot{\boldsymbol{u}}\rrbracket(\boldsymbol{X},t)\ \underbrace{(H_{\mathrm{s}}(\boldsymbol{X}) - \varphi(\boldsymbol{X}))}_{=:M_{\mathrm{s}}\ (4.9)} \ , \qquad \forall \boldsymbol{X} \in \Omega \tag{4.87}$$

The departure point for its development, however, was the standard form of strong discontinuity kinematics, derived from a *physically* justified decomposition of the displacement field into regular and jump terms according to (4.4):

$$\dot{\boldsymbol{u}}(\boldsymbol{X},t) = \underbrace{\dot{\tilde{\boldsymbol{u}}}(\boldsymbol{X},t)}_{\text{regular}} + \underbrace{\llbracket\dot{\boldsymbol{u}}\rrbracket(\boldsymbol{X},t)\, H_{\mathrm{s}}(\boldsymbol{X})}_{\text{jump term}} \ , \qquad \forall \boldsymbol{X} \in \Omega \tag{4.88}$$

To elaborate on the equivalence between the two formulations (4.88) and (4.87), it is important to realize that in a general three-dimensional setting, the decompositions are relevant only to those components of the displacement field that represent the direction of the displacement jump $\boldsymbol{m}(\boldsymbol{X},t)$, which in a general setting can be a function of space and time. Thus, as necessary conditions to assure the equivalence between the physical formulation (4.1) and the algorithmically motivated formulation (4.8), we require the above equations (4.88) and (4.87), respectively, to yield the *same rates for the displacement component falling together with the direction of the displacement jump* $\boldsymbol{m}$. At a given instant t, considering identity (4.7), we formally enforce [8]

$$\Big(\big(\dot{\tilde{\boldsymbol{u}}}(\boldsymbol{X}) - \llbracket\dot{\boldsymbol{u}}\rrbracket(\boldsymbol{X})\,\varphi(\boldsymbol{X})\big) \bullet \boldsymbol{m}(\boldsymbol{X})\Big)\boldsymbol{m}(\boldsymbol{X}) \overset{!}{=} \Big(\dot{\tilde{\boldsymbol{u}}}(\boldsymbol{X}) \bullet \boldsymbol{m}(\boldsymbol{X})\Big)\boldsymbol{m}(\boldsymbol{X}) \ , \tag{4.89}$$

from which immediately follows, that

$$\varphi(\boldsymbol{X}) = \frac{\Big(\dot{\tilde{\boldsymbol{u}}}(\boldsymbol{X}) - \dot{\tilde{\boldsymbol{u}}}(\boldsymbol{X})\Big) \bullet \boldsymbol{m}(\boldsymbol{X})}{\llbracket\dot{\boldsymbol{u}}\rrbracket(\boldsymbol{X}) \bullet \boldsymbol{m}(\boldsymbol{X})} \ . \tag{4.90}$$

[8] The vector $\boldsymbol{u}_m$ resulting from the projection of $\boldsymbol{u}$ on the unit vector $\boldsymbol{m}$ is computed according to $\boldsymbol{u}_m = \frac{\boldsymbol{u}\bullet\boldsymbol{m}}{|\boldsymbol{m}|}\,\frac{\boldsymbol{m}}{|\boldsymbol{m}|} = (\boldsymbol{u}\bullet\boldsymbol{m})\,\boldsymbol{m}$

In the present case we have, consistent with definition (4.32), $\boldsymbol{m}$ = const. with respect to space; therefore equation (4.90) can be rendered in the alternative form

$$\varphi(\boldsymbol{X}) = \frac{1}{\dot{\zeta}} \left(\dot{\boldsymbol{u}}(\boldsymbol{X}) - \dot{\breve{\boldsymbol{u}}}(\boldsymbol{X}) \right) \bullet \boldsymbol{m} \,, \tag{4.91}$$

where advantage was taken of the fact that $\boldsymbol{m} \bullet \boldsymbol{m} = 1$.

4.5.2.2 Discretized setting

In the following, for further development of the approach within the framework of a finite element context, we consider — as in Section 3.1.2 — the body Ω being represented by means of a union of finite elements Ω_e, so that $\Omega = \bigcup_{e=1}^{n_{elm}} \Omega_e$. Then, the standard finite element assembly procedure outlined in Section 3.1.2, manifests the continuum body's response as independently determined and subsequently assembled contributions of the individual finite elements. Consequently, and conforming with this approach, we now associate the previously derived strong discontinuity kinematics with the domain of one finite element Ω_e, more precisely we set $\Omega_\varphi \equiv \Omega_e$. The advantage of this specific choice is twofold. First, as already alluded to in Section 4.1.2, since $\boldsymbol{u}_h(\boldsymbol{X}, t) = \bar{\boldsymbol{u}}_h(\boldsymbol{X}, t)\,,\ \forall \boldsymbol{X} \in \partial\Omega_e$, the DIRICHLET conditions on $\partial\Omega_e$ can conveniently be incorporated. Second, adopting this view, from equation (4.87) we readily identify $\dot{\breve{\boldsymbol{u}}}$ as the compatible displacement field spanned by the element basis functions. At a given instant t we have:

$$\begin{aligned} \dot{\breve{\boldsymbol{u}}}_h(\boldsymbol{X}) = &\sum_{i=1}^{n_N} N_i^N(\boldsymbol{X})\ \dot{\boldsymbol{d}}_i^N + \sum_{i=1}^{n_E} N_i^E(\boldsymbol{X})\ \dot{\boldsymbol{d}}_i^E + \\ &+ \sum_{i=1}^{n_F} N_i^F(\boldsymbol{X})\ \dot{\boldsymbol{d}}_i^F + \sum_{i=1}^{n_B} N_i^B(\boldsymbol{X})\ \dot{\boldsymbol{d}}_i^B \,, \end{aligned} \tag{4.92}$$

where superscripts N, E, F and B denote the nodal, edge, face and internal (bubble) modes, respectively.

Finally, to complete a formulation for $\varphi(\boldsymbol{X})$, respectively its discretized form $\varphi_h(\boldsymbol{X})$, that satisfies both conditions (4.10) and (4.90), it remains to address the nature of the function $\dot{\breve{\boldsymbol{u}}}(\boldsymbol{X})$ contained in (4.90). To this end, we consider a continuum body Ω subjected to a displacement rate $\dot{\boldsymbol{u}}(\boldsymbol{X})$. Let $\dot{\boldsymbol{u}}(\boldsymbol{X})$ effect an *active* localization surface $\partial_{\mathrm{s}}\Omega$ within the body, i.e., an increase of the jump amplitude ζ. Then, in virtue of the fundamental displacement field decomposition (4.87), $\dot{\breve{\boldsymbol{u}}}(\boldsymbol{X})$ describes the change of the displacement field in the domains Ω_φ^+ and Ω_φ^- adjacent to the discontinuity surface $\partial_{\mathrm{s}}\Omega$ (cf. Figure 4.2). Furthermore, consistent with Proposition 4.3.1, deformation is concentrated into the localization zone, resulting in an increase of the discontinuity, i.e., the displacement jump. This, in turn, reduces the amount of traction that can be transferred across the localization surface — a result of the progressing softening response. The important point is, that the adjacent domains Ω_φ^+ and Ω_φ^- must then unload to satisfy the traction continuity condition stated in Proposition 4.2.1. Notably, this unloading behavior is of *passive* character since it is completely induced by the softening response of the localization surface $\partial_{\mathrm{s}}\Omega$. As a consequence, higher-order displacement rates

$\dot{\tilde{\boldsymbol{u}}} \bullet \boldsymbol{m}$ in the adjacent regions Ω_φ^+ and Ω_φ^- will not be stimulated. This situation is comparable to a prestrained continuum body that is subject to a change (release) of the prestraining traction on its boundary.

From the foregoing argumentation we conclude:

Hypothesis 4.5.1. *The order of interpolation for $\dot{\tilde{\boldsymbol{u}}} \bullet \boldsymbol{m}$ should be linear at most, a higher-order interpolation would tend to enforce unphysical unloading patterns in the regions Ω_φ^+ and Ω_φ^- adjacent to the softening localization surface.*

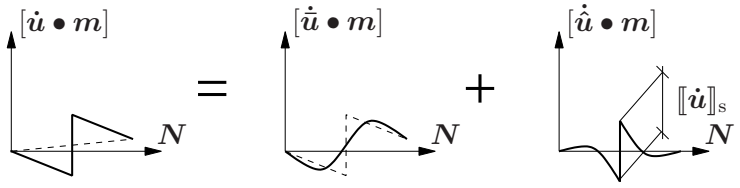

Figure 4.7: Decomposition of higher-order displacement rates with jump discontinuity

Additionally, equations (4.10) — which assure a proper representation of the DIRICHLET conditions at the element boundary $\partial\Omega_e$ — together with equation (4.7) imply that

$$\dot{\tilde{\boldsymbol{u}}}_h(\boldsymbol{X}) \stackrel{!}{=} \begin{cases} \dot{\tilde{\boldsymbol{u}}}_h(\boldsymbol{X}) - \dot{\boldsymbol{\mu}} & \forall \boldsymbol{X} \in \partial\Omega_\varphi^+ \\ \dot{\tilde{\boldsymbol{u}}}_h(\boldsymbol{X}) & \forall \boldsymbol{X} \in \partial\Omega_\varphi^- \end{cases} . \tag{4.93}$$

As before, the displacement jump $[\![\dot{\boldsymbol{u}}]\!]_\mathrm{s}$ at the discontinuity surface is reflected in the element local enhanced variables $\dot{\boldsymbol{\mu}} := \dot{\zeta}\boldsymbol{m}$. An interpolation for $\dot{\tilde{\boldsymbol{u}}}(\boldsymbol{X})$ that both accounts for (4.93) and reflects the low order interpolation requirement of hypothesis 4.5.1 can conveniently be constructed from the element Ansatz functions as

$$\begin{aligned} \dot{\tilde{\boldsymbol{u}}}_h(\boldsymbol{X}) = \underbrace{\sum_{i=1}^{n_N} N_i^N(\boldsymbol{X})\ \dot{\boldsymbol{d}}_i^N + \sum_{i=1}^{n_{E,F,B}} N_i^{E,F,B}(\boldsymbol{X})\ \dot{\boldsymbol{d}}_i^{E,F,B}}_{\dot{\boldsymbol{u}}_h(\boldsymbol{X})} - \\ - \sum_{i=1}^{n_{\Omega^+}} N_i^N(\boldsymbol{X})\ \dot{\boldsymbol{\mu}} \ - \sum_{i=1}^{n_{E,F,B}} N_i^{E,F,B}(\boldsymbol{X})\ \left(\dot{\boldsymbol{d}}_i^{E,F,B} \bullet \boldsymbol{m}\right) \boldsymbol{m} . \end{aligned} \tag{4.94}$$

Observe, that the first subtracted term involves the nodal shape functions only of those nodes that are associated with Ω^+ — and therefore assures compatibility with the DIRICHLET constraint (4.93). The last term, in turn, effectively eliminates the high-order contributions for $\dot{\tilde{\boldsymbol{u}}} \bullet \boldsymbol{m}$, and thus satisfies the low-order interpolation requirement stated in Hypothesis 4.5.1.

With this definition at hand the transmission function $\varphi_h(\boldsymbol{X})$, as defined by (4.91), is finally

obtained as

$$\begin{aligned}\varphi_h(\boldsymbol{X}) &= \frac{1}{\dot{\zeta}}\left(\dot{\tilde{\boldsymbol{u}}}_h(\boldsymbol{X}) - \dot{\breve{\boldsymbol{u}}}_h(\boldsymbol{X})\right) \bullet \boldsymbol{m} \\ &= \frac{1}{\dot{\zeta}}\left(\sum_{i=1}^{n_{\Omega^+}} N_i^N(\boldsymbol{X})\ \dot{\boldsymbol{\mu}} + \sum_{i=1}^{n_{E,F,B}} N_i^{E,F,B}(\boldsymbol{X})\ \dot{\boldsymbol{d}}_i^{E,F,B}\right) \bullet \boldsymbol{m} \\ &= \underbrace{\sum_{i=1}^{n_{\Omega^+}} N_i^N(\boldsymbol{X})}_{\varphi_{h,\text{base}}} + \underbrace{\frac{1}{\dot{\zeta}} \sum_{i=1}^{n_{E,F,B}} N_i^{E,F,B}(\boldsymbol{X}) \left(\dot{\boldsymbol{d}}_i^{E,F,B} \bullet \boldsymbol{m}\right)}_{\varphi_{h,\text{int}}}\ ,\end{aligned} \tag{4.95}$$

where once more the identity $\boldsymbol{m} \bullet \boldsymbol{m} = 1$ was exploited.

The so obtained definition of φ_h is constituted of a term $\varphi_{h,\text{base}}$ reflecting the transmission function commonly adopted for low-order finite elements (see, e.g., references [87], [100], [130], [79] and [41]) and an additional $\varphi_{h,\text{int}}$ term accounting for the possible effect due to higher-order modes. It should be noted, that expression (4.95) represents a generalization of the standard concept — in the absence of higher-order contributions it simply reduces to

$$\varphi_h(\boldsymbol{X}) = \sum_{i=1}^{n_{\Omega^+}} N_i^N(\boldsymbol{X})\ . \tag{4.96}$$

Remark. An alternative motivation for the derivation of function φ_h is set out as follows. As alluded to in Section 4.1, φ_h essentially transmits the effect of the displacement jump to the boundaries of the numerical localization zone, which in the model is represented by Ω_φ. For low order finite elements with $p = 1$ due to the constrained kinematics the element essentially localizes as a whole, such that the boundaries of the numerical localization zone indeed coincide with the element boundaries $\partial\Omega_e$. Higher-order modes, on the contrary, are qualified to resolve the discontinuity in a more localized manner, such that localization is restricted to a portion of the element domain only. Consequently, the actual numerical localization zone no longer is congruent with the assumed domain $\Omega_\varphi \equiv \Omega_e$ — an effect which must be reflected in the transmission function φ_h. Viewed in this light, formula (4.95) exploits the higher-order contributions as an adaptive measure for the extension of the actual numerical localization zone and thus adjusts to the localization response independent of finite element size and displacement field's order of polynomial approximation. If we further consider, that in the present approach the effect of the discontinuity is captured on continuum level, it appears natural that the discontinuity's actual discretization, possibly reproduced by higher-order polynomial contributions, in some way must enter the continuum formulation.

Following up Hypothesis 4.5.1 and the argument outlined above, the commonly accepted notion that φ_h only has to suffice conditions (4.10) *— which facilitate a consistent representation of the* Dirichlet *conditions at the element boundary $\partial\Omega_e$ — and otherwise is arbitrary, appears improper in a generalized framework.* □

The 'base' contribution to the transmission function $\varphi_h(\boldsymbol{X})$ depends according to equation (4.95) on the number of element nodes n_{Ω^+} located in Ω^+. In order to distinguish the various

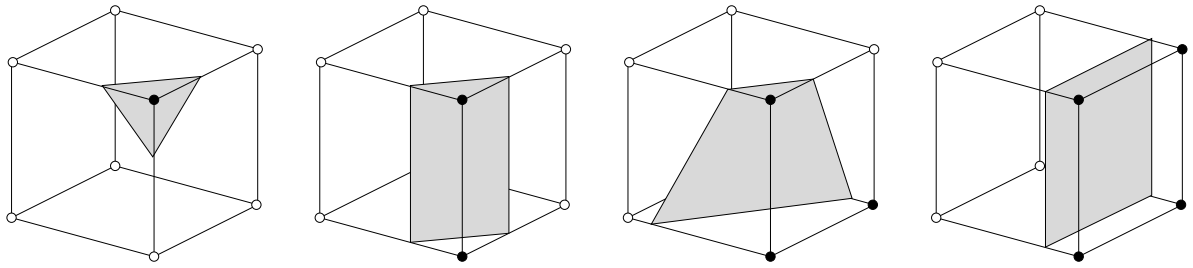

Figure 4.8: Schematic representation of four possible numerical localization modes for a hexahedral element. Nodes in Ω^+ are marked black, nodes in Ω^- are marked white. (a) One node in Ω^+. (b) Two nodes in Ω^+. (c) Three nodes in Ω^+. (d) Four nodes in Ω^+.

possible configurations, MOSLER [75] introduced the term *numerical localization mode*. Figure 4.8 qualtitatively illustrates possible configurations for a hexahedral element.

Depending on the actual prevailing numerical localization mode, diverse definitions of the regularizing function M_s (4.87) emerge. Figure 4.9 demonstrates two possible configurations for M_s for the two-dimensional case by means of a quadrilateral element.

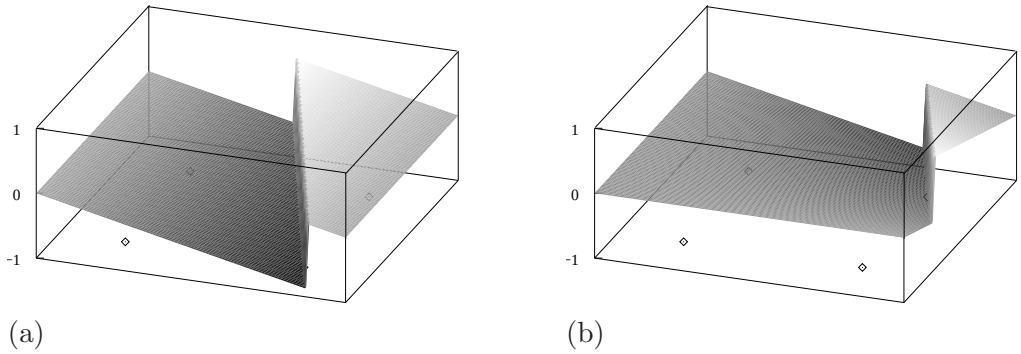

Figure 4.9: Two possible numerical localization modes for a quadrilateral element. Shape of M_s exemplified in the absence of higher-order contributions. (a) Discontinuity $\partial_\mathrm{s}\Omega$ crossing two opposite element edges. (b) Discontinuity $\partial_\mathrm{s}\Omega$ crossing adjacent element edges.

With a view to the enhanced strain formulation according to (4.86), the derivation is finally completed by establishing the corresponding gradient to φ_h as

$$\boldsymbol{\nabla}\varphi_h(\boldsymbol{X}) = \underbrace{\sum_{i=1}^{n_{\Omega^+}} \boldsymbol{\nabla} N_i^N(\boldsymbol{X})}_{\boldsymbol{\nabla}\varphi_{h,\mathrm{base}}} + \underbrace{\frac{1}{\dot{\zeta}} \sum_{i=1}^{n_{E,F,B}} \boldsymbol{\nabla} N_i^{E,F,B}(\boldsymbol{X}) \left(\dot{\boldsymbol{d}}_i^{E,F,B} \bullet \boldsymbol{m} \right)}_{\boldsymbol{\nabla}\varphi_{\mathrm{h,int}}} . \tag{4.97}$$

The actual numerical evaluation of (4.95) and (4.97), respectively, is treated in Section 5.2.1.

Chapter 5

A model for the simulation of brittle mode-I material failure

The line between failure and success
is so fine that we scarcely know when we pass it.
– Elbert Hubbard.

In Section 4.3, a general framework for coupling embedded strong discontinuities with a plasticity type discrete traction-separation law has already been discussed. The present chapter finally carries over this concept to a specific formulation suitable for the simulation of brittle mode-I material failure. The chapter is split into two main parts. The first part describes the essential characteristics of the adopted model while the second part is devoted to algorithmic aspects of the implementation.

5.1 Model characteristics

5.1.1 The Rankine criterion

Following up Section 4.3 we start with the adoption of the general form of admissible stress space $\mathbb{E}_{\boldsymbol{\sigma}}$ according to (4.26):

$$\phi(\boldsymbol{\sigma}, q) = \|\boldsymbol{t}\| - q(\alpha) \tag{5.1}$$

Equation (5.1) can be further refined as

$$\begin{aligned} \phi(\boldsymbol{\sigma}, q) &= \boldsymbol{t} \bullet \boldsymbol{m} - q(\alpha) \\ &= (\boldsymbol{\sigma}\, \boldsymbol{N}) \bullet \boldsymbol{m} - q(\alpha) \\ &= \underbrace{(\boldsymbol{m} \otimes \boldsymbol{N}) : \boldsymbol{\sigma}}_{t_m} - q(\alpha) \end{aligned} \tag{5.2}$$

— i.e., by selecting an appropriate norm, the first term on the right hand side of (5.2) now represents the traction component t_m in the direction $\boldsymbol{m}$ at the discontinuity surface, where the discontinuity surface is described by its normal $\boldsymbol{N}$. If we further choose $q = \|\boldsymbol{t}_\mathrm{s}\|$ and require $\phi(\boldsymbol{\sigma}, q) \leqslant 0$, the local form (5.2) then effectively poses a restriction on the traction component t_m, in dependence of the kinematic variable α (cf. [75, 41]).

Subsequent derivations are based on the assumption of associative plasticity, i.e., hardening law and flow rule are determined by the potentials $h \equiv \phi$ and $g \equiv \phi$, compare equations (2.72), (2.71) and (4.29). For this choice, we observe that

$$\partial_{,\boldsymbol{\sigma}} g \equiv \partial_{,\boldsymbol{\sigma}} \phi = \boldsymbol{m} \otimes \boldsymbol{N} \,, \tag{5.3}$$

so that in view of (4.37) we confirm the identity (4.38), i.e., $\lambda = \dot{\zeta}$. Further, from the evolution equation $(4.29)_2$ together with (5.2) and (4.38), we obtain

$$\dot{\alpha} = \lambda \, \frac{\partial \phi(\boldsymbol{\sigma}, \boldsymbol{q})}{\partial \boldsymbol{q}} \equiv \lambda \, \frac{\partial \phi(\boldsymbol{\sigma}, q)}{\partial q} = -\lambda = -\dot{\zeta} \,. \tag{5.4}$$

With ζ denoting the amplitude of the displacement discontinuity, which in the context of brittle material failure corresponds the the actual crack opening, equation (5.2) can be recast in a physically motivated form:

$$\phi(\boldsymbol{\sigma}, q) = (\boldsymbol{m} \otimes \boldsymbol{N}) : \boldsymbol{\sigma} - q(\zeta) \tag{5.5}$$

In this form, for the limit case $\phi(\boldsymbol{\sigma}, q) = 0$, it is obvious that equation (5.5) indeed describes a discrete interface law.

Recalling $\boldsymbol{m}$ as the direction of the displacement jump, compare (4.32), an interface law describing the behavior for mode-I separation is readily obtained by setting

$$\boldsymbol{m} \equiv \boldsymbol{N} \,. \tag{5.6}$$

Doing so, the discrete form of the well-known Rankine yield criterion is recovered as

$$\phi(\boldsymbol{\sigma}, q) = \underbrace{(\boldsymbol{N} \otimes \boldsymbol{N}) : \boldsymbol{\sigma}}_{t_n} - \underbrace{q(\zeta)}_{f_\mathrm{t}(\zeta)} \,, \tag{5.7}$$

where the admissible traction vector normal component t_n is related to the tensile strength of the material f_t. The tensile strength in turn depends on the amplitude of the displacement jump ζ, i.e., the crack opening, across the discontinuity surface $\partial_\mathrm{s}\Omega$. Hence, the discrete Rankine interface law furnishes a unique relationship between the admissible traction across the (crack) interface, represented by the discontinuity surface $\partial_\mathrm{s}\Omega$ and the separation of the disjoint parts Ω^+ and Ω^-.

Figure 5.1a depicts the Rankine yield function in the two-dimensional principal stress space. Conforming with (5.7), the onset of inelastic deformation localization is characterized as the instant when the maximum principal stress for the first time attains the tensile strength of the material. Prior to that moment the material is — in a simplified manner — assumed to exhibit purely linear elastic response.

5.1.2 Softening relationship

A typical example for material failure is the formation of a crack in brittle materials. In this context, the magnitude of the displacement jump represents the crack opening. Typically, the amount of traction that can be transferred across the crack directly depends on its current opening state. For mode-I material failure, the tensile strength f_t is employed as equivalent stress or rather equivalent traction. Since it is considered to be a decaying function in terms of crack opening, it is usually referred to as *softening relationship*. As already alluded to in Sections 1.1 and 1.2, for many materials the specific fracture energy G_f can be regarded as a material constant. According to CEB-FIB Model Code [32] the specific fracture energy for plain concrete is defined as the *energy required to propagate a tensile crack of unit area*. Adopting the notion of constant fracture energy, softening relationships are based on the requirement

$$\int_0^\infty q(\zeta)\, d\zeta = G_f \ . \tag{5.8}$$

In this work, two variants of softening relationships obeying (5.8) are employed, a linear and an exponential one. The exponential relationship, Figure 5.1b, is given as

$$q(\zeta) = f_\mathrm{tu} \exp\left(-\frac{\zeta}{\zeta_u}\right) \ , \tag{5.9}$$

whereas the linear relationship reads

$$q(\zeta) = \begin{cases} f_\mathrm{tu}\, \left(1 - \frac{\zeta}{\zeta_u}\right) & \text{for} \quad 0 < \zeta \leqslant \zeta_u \\ 0 & \text{for} \quad \zeta > \zeta_u \ . \end{cases} \tag{5.10}$$

In both relations f_tu denotes the uniaxial tensile strength and the auxiliary parameter ζ_u is computed as

$$\zeta_u := \frac{G_f}{f_\mathrm{tu}} \tag{5.11}$$

for the exponential law and

$$\zeta_u := 2\, \frac{G_f}{f_\mathrm{tu}} \tag{5.12}$$

in the linear softening case, respectively.

5.1.3 Determining the discontinuity normal

The considered constitutive model of Rankine type is characterized by a linear elastic pre-peak behavior. Evaluation of the strong discontinuity condition (4.43) for the Rankine case turns out to be particular convenient. It can be shown (see, e.g, Mosler [75]) that in this case the strong discontinuity condition is identically satisfied for the direction of maximum principal stress. The vector $\boldsymbol{N} \equiv \boldsymbol{m}$ is therefore obtained as the direction of maximum principal stress, an explicit evaluation of the strong discontinuity condition (4.43) is dispensable.

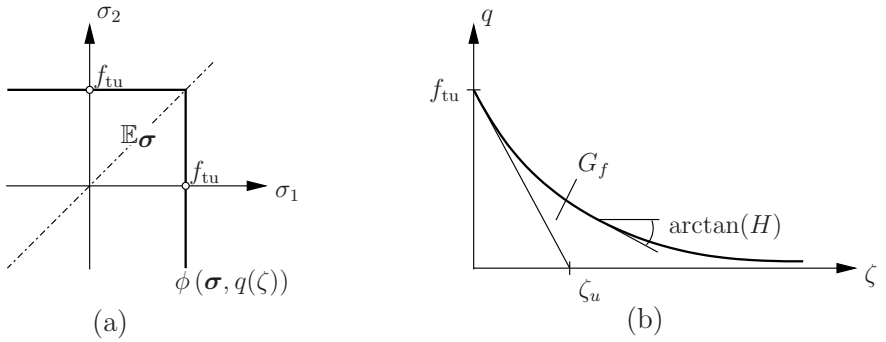

Figure 5.1: Representative constitutive model for mode-I material failure: (a) RANKINE failure surface in the two-dimensional principal stress space, (b) fracture energy objective exponential softening law

5.2 Algorithmic treatment

The principal objective of the constitutive algorithm is the evaluation of the previously established constitutive relationship (4.79). Introducing the equivalences $\partial_{,\boldsymbol{t}} g = \boldsymbol{m}$ and $\lambda = \zeta$ developed above, the constitutive relation is recast as:

$$\dot{\boldsymbol{\sigma}} = \mathbb{C} : \left(\boldsymbol{\nabla}^{\mathrm{sym}}\dot{\boldsymbol{u}} - \dot{\boldsymbol{\varepsilon}}_{\varphi}\right) \qquad \forall \boldsymbol{X} \in \Omega \setminus \partial_{\mathrm{s}}\Omega \tag{5.13}$$

In equation (5.13), the symmetric second-order strain tensor $\dot{\boldsymbol{\varepsilon}}_{\varphi}$ is determined by the flow rule

$$\dot{\boldsymbol{\varepsilon}}_{\varphi} = \dot{\zeta}\ \left(\boldsymbol{m} \otimes \overline{\boldsymbol{\nabla}\varphi}_h\right)^{\mathrm{sym}}\ , \tag{5.14}$$

with $\overline{\boldsymbol{\nabla}\varphi}_h$ being defined subject to (4.80) as

$$\overline{\boldsymbol{\nabla}\varphi}_h(\boldsymbol{X}) := \frac{1}{V^e}\int\limits_{\Omega_e} \boldsymbol{\nabla}\varphi_h(\boldsymbol{\xi})\, dV\ . \tag{5.15}$$

The rate of the displacement jump amplitude $\dot{\zeta}$ takes over the role of the LAGRANGE multiplier λ in standard flow theory of plasticity. It is determined from the traction continuity requirement in $\partial_{\mathrm{s}}\Omega$, represented by the condition $\phi(\boldsymbol{\sigma}, q) \leqslant 0$, where the yield function ϕ is defined according to (5.7). In Section 4.3.2.1, we have already pointed out the formal equivalence of this setting to a formulation resulting from the classical flow theory of plasticity. As a consequence, standard algorithms of computational plasticity such as described, e.g., in ORTIZ & MARTIN [93], SIMO & HUGHES [114], ZIENKIEWICZ & TAYLOR [135], CRISFIELD [23, 24] or JIRÁSEK [51], can be adopted with minor modifications. Due to the notion of assuring the admissibility of the stress state subject to some yield condition, this class of algorithms frequently goes by the name *return mapping* strategies or simply *stress return* algorithms. In this work, an implicit scheme is employed and will be described in detail in Section 5.2.2.

5.2.1 Computing the transmission function φ

In view of equation (5.13) we start by establishing the transmission function φ_h (4.95), respectively its gradient $\boldsymbol{\nabla}\varphi_h$ (4.97). Following the composition of equation (4.95), computation of the transmission function φ_h is carried out in two steps — related to the respective contributions of $\varphi_{h,\text{base}}$ and $\varphi_{h,\text{int}}$.

5.2.1.1 Identification of the nodal shape function basis contributions

Focusing for the moment on the nodal shape function contributions to φ_h, computation of $\varphi_{h,\text{base}}$ can be realized in a straight-forward and convenient manner. To clarify this, we consider a sampling point — typically a GAUSS integration point — with position vector $\boldsymbol{X}$, located inside a finite element with domain Ω_e. We assume that for this integration point localization is signaled and the discontinuity surface normal direction $\boldsymbol{N}$ is established according to Section 5.1.3. Then, the element nodes i lying in the direction of $\boldsymbol{N}$, i.e., $\boldsymbol{X}_i^N \in \Omega_e^+$, can be identified by a simple scalar product operation. Summing up the contributions of the associated shape functions N_i^N, finally furnishes $\varphi_{h,\text{base}}$. The structure of the resulting algorithm is illustrated in Algorithm 5.1. The algorithm renders very efficient since no additional effort is required to evaluate the nodal shape functions N_i^N at the position $\boldsymbol{X}$ of the considered GAUSS point — the respective contributions are already available from the finite element displacement approximation.

Algorithm 5.1: Computation of the transmission function φ

```
initialize ∀X ∈ ∂_s Ω_e :   φ_h,base = 0
for i = 0 to n_N do
    proj = (X_i^N − X) • N
    if proj > 0 then
        φ_h,base = φ_h,base + N_i^N
    end
end
```

The procedure for computation of the actually required gradient $\boldsymbol{\nabla}\varphi_{h,\text{base}}$ follows completely analogous lines, with the only difference that in place of the nodal shape function contributions N_i^N, contributions of the respective gradients $\boldsymbol{\nabla}N_i^N$ are summed up.

The required average $\overline{\boldsymbol{\nabla}\varphi}_{h,\text{base}}$ according to equation (5.15) is numerically obtained by GAUSS integration. To this end, the above procedure is repeated separately for all GAUSS points within the element domain Ω_e, the weighted contributions are summed up and finally divided by the element volume V^e.

Depending on the orientation of the discontinuity surface within the element and the element geometry, the resulting transmission function gradient $\overline{\boldsymbol{\nabla}\varphi}_{h,\text{base}}$ may not be aligned with $\boldsymbol{N}$. As a consequence spurious strains might develop, such that a normal displacement in direction

$\boldsymbol{N}$ of the discontinuity also induces significant lateral sliding along the discontinuity surface. This, in turn holds the potential of spurious stress generation *(stress locking)*. But even if stress locking is avoided, the undesired sliding behavior can be the source of instabilities and spoils the robustness of the procedure, also refer to [128]. The effect becomes particular severe if the discontinuity surface is considered fixed and is not allowed to rotate with time, i.e., $\dot{\boldsymbol{N}} = \boldsymbol{0}$. An *ad hoc* remedy to overcome this pathological behavior, is the elimination of the spurious lateral contributions from the transmission function gradient $\overline{\boldsymbol{\nabla}\varphi}_{h,\text{base}}$ by a coercive alignment of $\overline{\boldsymbol{\nabla}\varphi}_{h,\text{base}}$ to $\boldsymbol{N}$. Numerical tests confirm that this modification crucially improves on the convergence behavior of the method, see also [128].

5.2.1.2 Higher-order contributions

From an algorithmic point of view it proves convenient to slightly revise the definition of $\boldsymbol{\nabla}\varphi_h$ subject to (4.97). For this purpose, we recall that the essential characteristic of the higher-order contributions is the adaptive scaling of the transmission function in order to account for the kinematically improved representation of the discontinuity (cf. Section 4.5.2.2). Exploiting this interpretation, we introduce a scalar factor $c(\dot{\zeta})$ to the previously established basis contribution $\overline{\boldsymbol{\nabla}\varphi}_{h,\text{base}}$, such that

$$\overline{\boldsymbol{\nabla}\varphi}_h = \overline{\boldsymbol{\nabla}\varphi}_{h,\text{base}}\, c(\dot{\zeta}) \,, \tag{5.16}$$

where

$$\begin{aligned} c(\dot{\zeta}) &:= 1 + \overbrace{h(\dot{\zeta})}^{\approx 1}\, \dot{\zeta}\, \frac{\boldsymbol{\nabla}\varphi_{h,\text{int}} \bullet \boldsymbol{m}}{\overline{\boldsymbol{\nabla}\varphi}_{h,\text{base}} \bullet \boldsymbol{m}} \\ &= 1 + h(\dot{\zeta})\, \frac{\left[\sum_{i=1}^{n_{E,F,B}} \boldsymbol{\nabla} N_i^{E,F,B}(\boldsymbol{X})\, (\dot{\boldsymbol{d}}_i^{E,F,B} \bullet \boldsymbol{m})\right] \bullet \boldsymbol{m}}{\overline{\boldsymbol{\nabla}\varphi}_{h,\text{base}} \bullet \boldsymbol{m}} \,. \end{aligned} \tag{5.17}$$

The auxiliary function $h(\dot{\zeta})$ is introduced for numerical reasons in order to guarantee a well defined behavior for $\dot{\zeta} = 0$. It is constructed such, that for values $\dot{\zeta} > 0$ it converges fast and asymptotically against $1/\dot{\zeta}$. Possible definitions are, e.g.,

$$h(\dot{\zeta}) := \frac{1}{\dot{\zeta} + \epsilon \exp(-\dot{\zeta})} \tag{5.18}$$

or

$$h(\dot{\zeta}) := \frac{1}{\sqrt{\dot{\zeta}^2 + \epsilon}} \,, \tag{5.19}$$

where $\epsilon \ll 1 \in \mathbb{R}^+$ denotes a small numerical constant.

Given the definitions (5.17) and (5.18) respectively (5.19), equation (5.16) represents an algorithmically equivalent form of the original definition (4.97) of the transmission function gradient $\overline{\boldsymbol{\nabla}\varphi}_h$ — regarding its effect in the direction $\boldsymbol{m}$ of the displacement jump.

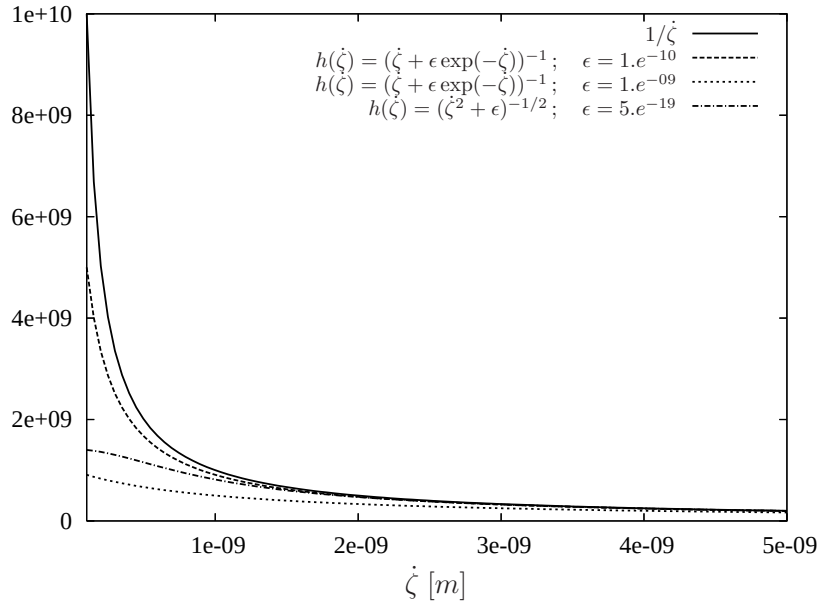

Figure 5.2: Family of auxiliary functions $h(\dot{\zeta})$ for different choices of parameter ϵ in comparison with the graph of $1/\dot{\zeta}$.

Figure 5.2 shows the graphs of a family of auxiliary functions $h(\dot{\zeta})$ for different choices of parameter ϵ over a range $0 < \dot{\zeta} \ll 1$. With a view to the required linearization, the exponential type function (5.18) is preferable over type (5.19) due to the consistent curvature of the graph. For the numerical analyses, equation (5.18) is adopted with a choice of parameter ϵ equal to $1.e^{-10}$.

5.2.2 Stress evaluation

Within the adopted finite element framework, for time t_{n+1} the incremental iterative overall solution procedure provides an updated displacement field $\bar{\boldsymbol{u}}_{n+1}$, the corresponding strains $\bar{\boldsymbol{\varepsilon}}_{n+1}$ and the state variables $(q, \boldsymbol{\varepsilon}_\varphi)_n$, which are related to the previous converged equilibrium state at time t_n. For this new deformation state now the corresponding updated fields $\boldsymbol{\sigma}_{n+1}$ and $(q, \boldsymbol{\varepsilon}_\varphi)_{n+1}$ are sought.

Hence, the intrinsic task of the stress return algorithm can be described as a mapping of the form

$$(\bar{\boldsymbol{\varepsilon}}_{n+1}, \boldsymbol{\sigma}_n, \boldsymbol{\varepsilon}_n^\varphi, q_n) \longrightarrow \left(\bar{\boldsymbol{\varepsilon}}_{n+1}, \boldsymbol{\sigma}_{n+1}, \boldsymbol{\varepsilon}_{n+1}^\varphi, q_{n+1}\right) \qquad \forall \boldsymbol{X} \in \Omega \setminus \partial_{\mathrm{s}}\Omega \,. \tag{5.20}$$

Notably, the mapping is performed for $\boldsymbol{X} \in \Omega \setminus \partial_{\mathrm{s}}\Omega$. By employing the traction continuity condition for the interface law in $\partial_{\mathrm{s}}\Omega$ the need to explicitly consider the singular strains $\boldsymbol{\varepsilon}_\delta \in \partial_{\mathrm{s}}\Omega$ is avoided. Instead, the effect of the discontinuity on the adjacent bulk material is modeled. As a consequence, the otherwise required approximation of the DIRAC-delta distribution by numerical regularization [88] becomes completely dispensable.

In order to establish such a mapping, the integration of the rate form constitutive relationship (5.13) over the interval t_n to t_{n+1} is required. In general, a closed form solution is — due to the complexity of the constitutive relation — impossible to obtain, hence a numerical solution procedure must be adopted. Such a scheme can be written generically as

$$\begin{aligned} x_{n+1} &= x_n + \int_{t_n}^{t_{n+1}} \dot{x} dt \\ &\approx x_n + (t_{n+1} - t_n)\ (\beta\, \dot{x}_n + (1-\beta)\dot{x}_{n+1}) \end{aligned} \tag{5.21}$$

with $0 \leqslant \beta \leqslant 1$.

Depending on the choice of β different strategies are recovered. For $\beta = 1$ an explicit method is established (Forward-Euler), where computation of the unknown state x_{n+1} is based exclusively on information available from the known state x_n. Such a procedure is computationally convenient, it exhibits however all the well-known drawbacks regarding conditional stability, i.e., sensitivity to the pseudo time step size $\Delta t = t_{n+1} - t_n$. Moreover, when transferred to the present context, admissibility of the computed stress state at time t_{n+1}, i.e., satisfaction of $\phi(\boldsymbol{\sigma}_{n+1}, q_{n+1}) \leqslant 0$, is not guaranteed [135]. Choosing $\beta = 0$ on the other hand, renders a fully implicit scheme (Backward-Euler) which offers the distinct feature of unconditional stability. In addition, for this approach the admissibility of the computed stress state at time t_{n+1} inherently is assured. The price for these benefits lies in the fact that now computation of the unknown state x_{n+1} requires information of the unknown state itself, and therefore indespensably entails an iterative process. Combined approaches with $0 < \beta < 1$ are possible, as well — this issue shall, however, not be further addressed in this work. Instead, owing to the advantageous characteristics set out above, for the present context the notion of a fully implicit Backward-Euler scheme is adopted. Due to its superior stability features, the implicit scheme has gained increasing popularity and a huge amount of literature is available on this topic. A comprehensive algorithmic overview is given, e.g., in Crisfield [23, 24], Zienkiewicz & Taylor [135] and the work of Simo & Hughes [114] can be regarded as a definitive book on this topic.

The essential ingredients of the implicit approach shall subsequently be elaborated. To this end, we start by rewriting the constitutive relationship (5.13) in a corresponding incremental form. At time t_{n+1} the stress state is dermined by

$$\boldsymbol{\sigma}_{n+1} = \mathbb{C} : \left(\boldsymbol{\nabla}^{\mathrm{sym}} \bar{\boldsymbol{u}}_{n+1} - \boldsymbol{\varepsilon}^{\varphi}_{n+1} \right) \ . \tag{5.22}$$

Adopting the Backward-Euler integration scheme, the inelastic strain $\boldsymbol{\varepsilon}^{\varphi}_{n+1}$ is computed subject to the flow rule (5.14) as

$$\boldsymbol{\varepsilon}^{\varphi}_{n+1} = \boldsymbol{\varepsilon}^{\varphi}_{n} + \Delta\zeta\ \boldsymbol{G}_{n+1} \ , \tag{5.23}$$

where the symmetric second-order tensor $\boldsymbol{\varepsilon}^{\varphi}_{n}$ denotes the accumulated inelastic strains in the localization surface $\partial_{\mathrm{s}}\Omega$ at the previous time step t_n and the, likewise symmetric, second-order tensor

$$\boldsymbol{G} := \left(\boldsymbol{m} \otimes \overline{\boldsymbol{\nabla} \varphi_h} \right)^{\mathrm{sym}} \tag{5.24}$$

has been introduced to simplify notation. Due to the Backward-Euler assumptions, the increment of inelastic strain in (5.23) is completely determined by the state at time t_{n+1}. [1] Analogously, we write the flow rule for the displacement like internal variable α according to $(4.29)_2$ as

$$\alpha_{n+1} = \alpha_n + \Delta\zeta \ \left(\partial_{,\boldsymbol{q}}\phi\right)_{n+1} \ . \tag{5.25}$$

With $\bar{\boldsymbol{u}}_{n+1}$ and state variables $(q, \boldsymbol{\varepsilon}_\varphi)_n$ being given, a *trial stress* state can simply be established by assuming a non-localized response, i.e., taking $\Delta\zeta = 0$ in equation (5.23). If the so obtained stress state suffices condition $\phi(\boldsymbol{\sigma}^{\text{trial}}_{n+1}, q_n) \leqslant 0$, it is admissible and the assumption of a non-localized response was justified. If on the other hand localization is signaled, then $\Delta\zeta > 0$ holds and from the Karush-Kuhn-Tucker conditions (4.30) we have the constraint

$$\phi(\boldsymbol{\sigma}_{n+1}, q_{n+1}) = 0 \ . \tag{5.26}$$

Equations (5.22), (5.23) and (5.25) then form a nonlinear system of equations that can be solved for the unknowns $\boldsymbol{\sigma}_{n+1}$, q_{n+1} and $\Delta\zeta$ using any suitable iterative technique.

With the objective of developing such an iterative scheme, in what follows the Newton-Raphson procedure is adopted due to its favorable quadratic convergence properties. Thereby, we follow the basic lines given in [114] and later particularize the formulation with a view to the present setting. We start by defining from equations (5.22), (5.23) and (5.25) the residuals

$$\boldsymbol{R}^\varepsilon := \boldsymbol{\nabla}^{\text{sym}}\bar{\boldsymbol{u}}_{n+1} - \boldsymbol{\varepsilon}^\varphi_n - \mathbb{C}^{-1} : \boldsymbol{\sigma}_{n+1} - \Delta\zeta \ \boldsymbol{G}_{n+1} \tag{5.27}$$

and

$$R^\alpha := \alpha_{n+1} - \alpha_n - \Delta\zeta \ \left(\partial_{,q}\phi\right)_{n+1} \tag{5.28}$$

For subsequent use we also recall the previously established correlation $\boldsymbol{H} = -\partial\boldsymbol{q}/\partial\boldsymbol{\alpha}$, cf. equation (2.78), which — accounting for the scalar character of q and α — in the present context reduces to

$$H_{n+1} := -\left(\frac{\partial q}{\partial \alpha}\right)_{n+1} \quad \Longleftrightarrow \quad H^{-1}_{n+1} := -\left(\frac{\partial \alpha}{\partial q}\right)_{n+1} \ . \tag{5.29}$$

Hence, a solution $(\boldsymbol{\sigma}, q, \Delta\zeta)$ [2] to the nonlinear system of equations must satisfy the yield condition (5.26) in consideration of the additional constraints posed by relations (5.27) and (5.28) according to

$$\begin{Bmatrix} \boldsymbol{R}^\varepsilon\left(\boldsymbol{\sigma}, \Delta\zeta\right) \\ R^\alpha\left(q, \Delta\zeta\right) \\ \phi\left(\boldsymbol{\sigma}, q\right) \end{Bmatrix} = \begin{Bmatrix} \boldsymbol{0} \\ 0 \\ 0 \end{Bmatrix} \ . \tag{5.30}$$

[1] It should further be noted, that in the most general case $\boldsymbol{G}$ depends on the stresses $\boldsymbol{\sigma}$ via $\boldsymbol{m}$, the jump rate $\dot{\zeta}$ and also on the displacement gradient rates via the enhancement (5.17), which accounts for the internal mode contributions.

[2] To clarify notation, the index $(\bullet)_{n+1}$ is omitted here and in the following. Within the Backward-Euler approach, it is unambigous that all quantities are related to the instant t_{n+1}.

Assuming equations (5.30) are not satified for the current state $(\boldsymbol{\sigma}, q, \Delta\zeta)_k$, an improved state

$$\begin{aligned} \big(\boldsymbol{\sigma}, q, \Delta\zeta\big)_{k+1} &= \big(\boldsymbol{\sigma}, q, \Delta\zeta\big)_k + \big(\Delta\boldsymbol{\sigma}, \Delta q, \Delta^2\zeta\big)_k \\ \big(\alpha\big)_{k+1} &= \big(\alpha\big)_k + \big(H^{-1}\,\Delta q\big)_k \end{aligned} \tag{5.31}$$

can be obtained by a linear extension around the state k. To this end, a truncated TAYLOR series is applied to equations (5.27), (5.28) and (5.26) to finally render the linearized system of equations

$$\begin{Bmatrix} \boldsymbol{R}^\varepsilon \\ R^\alpha \\ \phi \end{Bmatrix}_{k+1} = \begin{Bmatrix} \boldsymbol{R}^\varepsilon \\ R^\alpha \\ \phi \end{Bmatrix}_k + \begin{Bmatrix} \Delta\boldsymbol{R}^\varepsilon \\ \Delta R^\alpha \\ \Delta\phi \end{Bmatrix}_k \overset{!}{=} \begin{Bmatrix} \boldsymbol{0} \\ 0 \\ 0 \end{Bmatrix} \tag{5.32}$$

with [3]

$$\begin{Bmatrix} \Delta\boldsymbol{R}^\varepsilon \\ \Delta R^\alpha \\ \Delta\phi \end{Bmatrix}_k = \begin{bmatrix} -\left(\mathbb{C}^{-1} + \partial_{,\boldsymbol{\sigma}}\boldsymbol{G}\,\Delta\zeta\right) & -\partial_{,q}\boldsymbol{G}\,\Delta\zeta & -\left(\boldsymbol{G} + \partial_{,\zeta}\boldsymbol{G}\,\Delta\zeta\right) \\ -\partial_{,\boldsymbol{\sigma}}\partial_{,q}\phi\,\Delta\zeta & -\left(H^{-1} + \partial_{,q}\partial_{,q}\phi\,\Delta\zeta\right) & -\partial_{,q}\phi \\ \partial_{,\boldsymbol{\sigma}}\phi & \partial_{,q}\phi & 0 \end{bmatrix}_k \begin{Bmatrix} \Delta\boldsymbol{\sigma} \\ \Delta q \\ \Delta^2\zeta \end{Bmatrix}_k . \tag{5.33}$$

The linear system of equations (5.32) could now be solved for $(\Delta\boldsymbol{\sigma}, \Delta q, \Delta^2\zeta)$, the current state k would be updated according to (5.31) and the whole process iteratively repeated until condition (5.30) is satisfied within a specified tolerance. For the considered family of yield surfaces (5.2), however, the linearized system of equations (5.32) can be further tapered, furnishing a more efficient implementation. Employing (5.29) in accordance with the flow rule $(4.29)_2$, we note that

$$\Delta q = -H\,\Delta\alpha = -H\,\frac{\partial\phi}{\partial q}\,\Delta^2\zeta \tag{5.34}$$

Substituting this equivalence into (5.33) and accounting for $\partial_{,q}\boldsymbol{G} = \partial_{,\boldsymbol{\sigma}}\partial_{,q}\phi \equiv \boldsymbol{0}$, furthermore $\partial_{,q}\partial_{,q}\phi \equiv 0$, the system of equations (5.32) is cast in an equivalent reduced form

$$\begin{bmatrix} \left(\mathbb{C}^{-1} + \partial_{,\boldsymbol{\sigma}}\boldsymbol{G}\,\Delta\zeta\right) & \left(\boldsymbol{G} + \partial_{,\zeta}\boldsymbol{G}\,\Delta\zeta\right) \\ \partial_{,\boldsymbol{\sigma}}\phi & -\partial_{,q}\phi\,H\,\partial_{,q}\phi \end{bmatrix}_k \begin{Bmatrix} \Delta\boldsymbol{\sigma} \\ \Delta^2\zeta \end{Bmatrix}_k = \begin{Bmatrix} \boldsymbol{R}^\varepsilon \\ -\phi \end{Bmatrix}_k . \tag{5.35}$$

The just developed procedure can — due to its close connection to the principle of maximum dissipation, cf. Section 2.4.2.1 — be interpreted as *closest point projection* strategy. This notion is particularly justified in case of associated flow and hardening rules for which a geometrical interpretation of the return mapping procedure is readily available, as illustrated in Figure 5.3.

A compact strucure chart of the complete return mapping algorithm is provided in Algorithm 5.2.

[3] In the present tensorial notation, the matrix product in equation (5.33) must be interpreted in a slightly different manner: components related to $\Delta\boldsymbol{\sigma}$ are multiplied subject to a double contraction ":", while for components related to Δq and $\Delta^2\zeta$ a standard single contraction "·" applies. For the actual numerical implementation, of course, the tensorial components are transferred to their respective matrix equivalents.

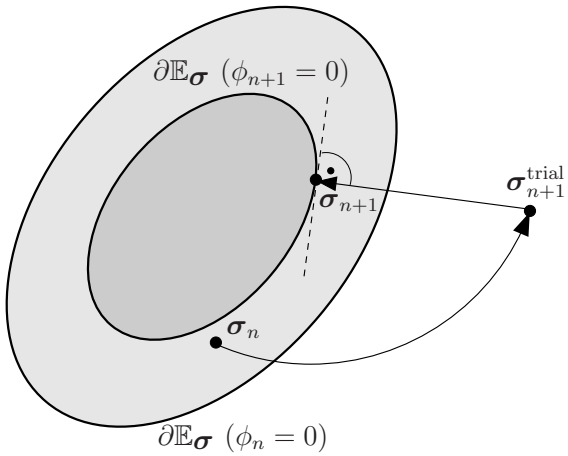

Figure 5.3: Geometrical interpretation of the closest point projection algorithm.

5.2.3 Algorithmic constitutive tangent

In order to maintain the quadratic convergence properties of the global incremental-iterative NEWTON-RAPHSON solution process, it is essential to assure the consistency of the employed material tangent operator with the actual algorithmic formulation of the constitutive integration algorithm. The notion of a *consistent tangent stiffness* was established by SIMO & TAYLOR [118], it is frequently also referred to as *algorithmic tangent stiffness* [51]. In this work we prefer the term *algorithmic* over *consistent* to emphasize the inherent difference to the (also consistently derived) continuum tangent stiffness, which for the elastoplastic case has already been defined by (2.80). Due to the popularity of implicit return mapping schemes, the available literature on the topic of algorithmic tangent stiffness is just as comprehensive. Representatively, the early work of ORTIZ & MARTIN [93], dealing with the aspect of symmetry-preservation of the approach, shall be mentioned.

As already alluded to in the previous section, starting from an equilibrium state at time t_n with a corresponding strain state $\bar{\boldsymbol{\varepsilon}}_n$, the global solution process with each iteration k provides an iteratively updated state $\bar{\boldsymbol{\varepsilon}}_{n+1,k}$ related to the current time t_{n+1} until convergence is reached, i.e., equilibrium is fulfilled. The essential role of the constitutive algorithm in this framework is the mapping of the strain state $\bar{\boldsymbol{\varepsilon}}_{n+1,k}$ to a corresponding stress state $\boldsymbol{\sigma}_{n+1,k} = \boldsymbol{\theta}_{n+1}(\bar{\boldsymbol{\varepsilon}}_{n+1,k})$, resulting from a strain increase from $\bar{\boldsymbol{\varepsilon}}_n$ to $\bar{\boldsymbol{\varepsilon}}_{n+1,k}$ — where the mapping function $\boldsymbol{\theta}_{n+1}(\bar{\boldsymbol{\varepsilon}})$ generally depends on the state variables of the previous equilibrium state at time t_n. In place of the continuum tangent (2.80)

$$\mathbb{C}_{\text{ep}}(\bar{\boldsymbol{\varepsilon}}) := \frac{\partial \boldsymbol{\sigma}}{\partial \bar{\boldsymbol{\varepsilon}}}$$

the algorithmic tangent is then defined as

$$\mathbb{C}_{\text{alg}}^{n+1}(\bar{\boldsymbol{\varepsilon}}) := \frac{\partial \boldsymbol{\theta}_{n+1}(\bar{\boldsymbol{\varepsilon}})}{\partial \bar{\boldsymbol{\varepsilon}}} \,. \tag{5.36}$$

It is important to note that due to its dependency on the previous equilibrium state, the mapping function $\boldsymbol{\theta}_{n+1}$ reflects the incremental character of the approach and therefore, in

general

$$\mathbb{C}_{\text{alg}}^{n+1}(\bar{\boldsymbol{\varepsilon}}) \neq \mathbb{C}_{\text{ep}}(\bar{\boldsymbol{\varepsilon}}) \ , \tag{5.37}$$

unless $\bar{\boldsymbol{\varepsilon}} \equiv \bar{\boldsymbol{\varepsilon}}_n$.

To derive an algorithmic tangent formulation for the present setting, we extend the basic lines set out in [114]. Differentiating the algorithmic constitutive relationship (5.22) and the algorithmic flow rule (5.23), we obtain

$$d\boldsymbol{\sigma}_{n+1} = \mathbb{C} : \left(d\bar{\boldsymbol{\varepsilon}}_{n+1} - d\boldsymbol{\varepsilon}_{n+1}^{\varphi} \right) \tag{5.38}$$

$$d\boldsymbol{\varepsilon}_{n+1}^{\varphi} = \Delta\zeta \, \partial_{,\boldsymbol{\sigma}} \boldsymbol{G}_{n+1} : d\boldsymbol{\sigma}_{n+1} + \left(\boldsymbol{G}_{n+1} + \Delta\zeta \, \partial_{,\zeta} \boldsymbol{G}_{n+1} \right) d\Delta\zeta + \Delta\zeta \, \partial_{,\bar{\boldsymbol{\varepsilon}}} \boldsymbol{G}_{n+1} : d\bar{\boldsymbol{\varepsilon}}_{n+1} \ . \tag{5.39}$$

Substituting (5.39) into (5.38) yields

$$d\boldsymbol{\sigma}_{n+1} = \boldsymbol{\Xi}_{n+1} : \left[\left(\boldsymbol{I} - \Delta\zeta \, \partial_{,\bar{\boldsymbol{\varepsilon}}} \boldsymbol{G}_{n+1} \right) : d\bar{\boldsymbol{\varepsilon}}_{n+1} - \left(\boldsymbol{G}_{n+1} + \Delta\zeta \, \partial_{,\zeta} \boldsymbol{G}_{n+1} \right) d\Delta\zeta \right] \ , \tag{5.40}$$

where the algorithmic fourth-order tensor $\boldsymbol{\Xi}_{n+1}$ is defined according to

$$\boldsymbol{\Xi}_{n+1} := \left(\mathbb{C}^{-1} + \Delta\zeta \, \partial_{,\boldsymbol{\sigma}} \boldsymbol{G}_{n+1} \right)^{-1} \ . \tag{5.41}$$

In analogy to the continuum case, the result (5.40) is inserted into the algorithmic form of the consistency condition (2.76)

$$\partial_{,\boldsymbol{\sigma}} \phi_{n+1} : d\boldsymbol{\sigma}_{n+1} + \partial_{,q} \phi_{n+1} \, \partial_{,\alpha} q_{n+1} \, \partial_{,\zeta} \alpha_{n+1} \, d\Delta\zeta = 0 \tag{5.42}$$

$$\Leftrightarrow \partial_{,\boldsymbol{\sigma}} \phi_{n+1} : d\boldsymbol{\sigma}_{n+1} + \partial_{,q} \phi_{n+1} \, (-H) \, \partial_{,q} \phi_{n+1} \, d\Delta\zeta = 0 \tag{5.43}$$

in order to obtain the incremental LAGRANGE multiplier as

$$d\Delta\zeta = \frac{\partial_{,\boldsymbol{\sigma}} \phi_{n+1} : \boldsymbol{\Xi}_{n+1} : \left(\boldsymbol{I} - \Delta\zeta \, \partial_{,\bar{\boldsymbol{\varepsilon}}} \boldsymbol{G}_{n+1} \right) : d\bar{\boldsymbol{\varepsilon}}_{n+1}}{\partial_{,\boldsymbol{\sigma}} \phi_{n+1} : \boldsymbol{\Xi}_{n+1} : \left(\boldsymbol{G}_{n+1} + \Delta\zeta \, \partial_{,\zeta} \boldsymbol{G}_{n+1} \right) + \partial_{,q} \phi_{n+1} \, H \, \partial_{,q} \phi_{n+1}} \ . \tag{5.44}$$

Finally, substituting (5.44) into (5.40) furnishes the expression for the algorithmic tangent modulus as

$$\begin{aligned} \mathbb{C}_{\text{alg}}^{n+1} &:= \left. \frac{\partial \boldsymbol{\sigma}}{\partial \bar{\boldsymbol{\varepsilon}}} \right|_{n+1} \\ &= \boldsymbol{\Xi}_{n+1} - \frac{\boldsymbol{\Xi}_{n+1} : \left(\boldsymbol{G}_{n+1} + \Delta\zeta \, \partial_{,\zeta} \boldsymbol{G}_{n+1} \right) \otimes \partial_{,\boldsymbol{\sigma}} \phi_{n+1} : \boldsymbol{\Xi}_{n+1} : \left(\boldsymbol{I} - \Delta\zeta \, \partial_{,\bar{\boldsymbol{\varepsilon}}} \boldsymbol{G}_{n+1} \right)}{\partial_{,\boldsymbol{\sigma}} \phi_{n+1} : \boldsymbol{\Xi}_{n+1} : \left(\boldsymbol{G}_{n+1} + \Delta\zeta \, \partial_{,\zeta} \boldsymbol{G}_{n+1} \right) + \partial_{,q} \phi_{n+1} \, H \, \partial_{,q} \phi_{n+1}} \ . \end{aligned} \tag{5.45}$$

5.2.3.1 Peculiarity for higher-order mode contributions

In the derivation of (5.45), we have tacitly assumed a dependency of $\boldsymbol{G}$ on $\bar{\boldsymbol{\varepsilon}}$, giving rise to the term $\partial_{,\bar{\boldsymbol{\varepsilon}}} \boldsymbol{G}$. This dependency is due to the scaling factor $c(\dot{\zeta})$ (5.17) previously introduced into equation (5.16), which accounts for the influence of higher-order modes. The nominator

of (5.17) can be identified as the contribution of the internal modes to the normal strain rate in the direction of the displacement jump $\boldsymbol{m}$:

$$\left[\sum_{i=1}^{n_{E,F,B}} \boldsymbol{\nabla} N_i^{E,F,B}(\boldsymbol{X})\ (\dot{\boldsymbol{d}}_i^{E,F,B} \bullet \boldsymbol{m})\right] \bullet \boldsymbol{m} = (\boldsymbol{m} \otimes \boldsymbol{m}) : \dot{\bar{\boldsymbol{\varepsilon}}}^{E,F,B} = \dot{\bar{\varepsilon}}_{\mathrm{mm}}^{E,F,B} \ . \tag{5.46}$$

Using this cognition along with definitions (5.24) and (5.16), we rewrite the derivative $\partial_{,\bar{\boldsymbol{\varepsilon}}}\boldsymbol{G}$ as

$$\frac{\partial \boldsymbol{G}}{\partial \bar{\boldsymbol{\varepsilon}}} = \left(\boldsymbol{m} \otimes \overline{\boldsymbol{\nabla}\varphi}_{h,\mathrm{base}}\right)^{\mathrm{sym}} \otimes \left(\frac{\partial c(\dot{\bar{\varepsilon}}_{\mathrm{mm}}^{E,F,B})}{\partial \bar{\varepsilon}_{\mathrm{mm}}} \frac{\partial \bar{\varepsilon}_{\mathrm{mm}}}{\partial \bar{\boldsymbol{\varepsilon}}}\right) \ . \tag{5.47}$$

In the form of (5.47), the only term which can not be computed offhand, is the derivative $\partial_{,\bar{\varepsilon}_{\mathrm{mm}}} c$. To emphasize the dependency for the present context, the scaling factor c is denoted as a function of the internal mode contributions, i.e., $c = c(\dot{\bar{\varepsilon}}_{\mathrm{mm}}^{E,F,B})$. Hence, in view of (5.17) it is evident that evaluation of

$$\frac{\partial \dot{\bar{\varepsilon}}_{\mathrm{mm}}^{E,F,B}}{\partial \bar{\varepsilon}_{\mathrm{mm}}} \tag{5.48}$$

is required to finally compute the sought derivative (5.47).

The coherence between strain rate contributions from internal modes and total strain rate can, however, not be described analytically on the level of observation, i.e., material point level. Hence, it is not possible to compute an exact algorithmic tangent in case internal mode contributions are present.

Nevertheless, introducing the *approximation*

$$\frac{\partial \dot{\bar{\varepsilon}}_{\mathrm{mm}}^{E,F,B}}{\partial \bar{\varepsilon}_{\mathrm{mm}}} \approx \frac{\dot{\bar{\varepsilon}}_{\mathrm{mm}}^{E,F,B}}{\dot{\bar{\varepsilon}}_{\mathrm{mm}}} \ , \tag{5.49}$$

i.e., assuming the portion of higher-order strain rate contributions to be constant, it is finally possible to establish an approximate algorithmic tangent also for this extended case.

Clearly, the approximative character of the derivative (5.47) to a certain extent antagonizes the quadratic convergence properties of the overall Newton-Raphson iteration process on structural level. Therefore, in order to stabilize and accelerate the iterative process, the standard Newton-Raphson procedure is enhanced by a secant-related Quasi-Newton stabilization technique according to Crisfield [23] for the actual implementation. The scheme is closely related to Quasi-Newton techniques such as the popular BFGS-method, named after Broyden [19], Fletcher [42], Goldfarb [44] and Shanno [111]; for an overview see, e.g., Luenberger [67].

5.3 Fixed or rotating discontinuity?

The plasticity formulation for mode-I failure in a strong discontinuity context developed in preceding sections, relies on the basic assumptions of

Algorithm 5.2: General closest point projection (Backward-EULER)

compute elastic trial stress $\boldsymbol{\sigma}_{n+1}^{\text{trial}} = \mathbb{C} : (\boldsymbol{\nabla}^{\text{sym}} \bar{\boldsymbol{u}}_{n+1} - \boldsymbol{\varepsilon}_n^{\varphi})$
compute yield function $\phi(\boldsymbol{\sigma}_{n+1}^{\text{trial}}, q_n)$
if $\phi(\boldsymbol{\sigma}_{n+1}^{trial}, q_n) \leqslant 0$ **then**
  (elastic response)
  update:
  $\boldsymbol{\varepsilon}_{n+1}^{\varphi} = \boldsymbol{\varepsilon}_n^{\varphi}$
  $\alpha_{n+1} = \alpha_n$
  $\boldsymbol{\sigma}_{n+1} = \boldsymbol{\sigma}_n$
  $q_{n+1} = q_n$
  $\mathbb{C}_{\text{alg}}^{n+1} = \mathbb{C}$
  return good
else
  (localized response)
  initialize:
  $\boldsymbol{\varepsilon}_{n+1,0}^{\varphi} = \boldsymbol{\varepsilon}_n^{\varphi}$
  $\boldsymbol{\sigma}_{n+1,0} = \boldsymbol{\sigma}_{n+1}^{\text{trial}}$
  $\alpha_{n+1,0} = \alpha_n$
  $q_{n+1,0} = q_n$
  $\Delta\zeta_0 = 0$
  for $k = 0$ **to** MaxIter **do**
    compute $\boldsymbol{R}_k^{\varepsilon}$ subject to (5.27)
    if $\|\Phi\| < \epsilon$ *and* $\|\boldsymbol{R}_k^{\varepsilon}\| < \epsilon$ **then**
      update:
      $\boldsymbol{\varepsilon}_{n+1}^{\varphi} = \boldsymbol{\varepsilon}_{n+1,k}^{\varphi}$
      $\alpha_{n+1} = \alpha_{n+1,k}$
      $\boldsymbol{\sigma}_{n+1} = \boldsymbol{\sigma}_{n+1,k}$
      $q_{n+1} = q_{n+1,k}$
      compute $\mathbb{C}_{\text{alg}}^{n+1}$ subject to (5.45)
      return good
    end
    compute coefficent matrix subject to (5.35)
    solve LSE (5.35) for $(\Delta\boldsymbol{\sigma}, \Delta^2\zeta)_k$
    update:
    $\boldsymbol{\sigma}_{n+1,k+1} = \boldsymbol{\sigma}_{n+1,k} + \Delta\boldsymbol{\sigma}_k$
    $\Delta\zeta_{k+1} = \Delta\zeta_k + \Delta^2\zeta_k$
    $\boldsymbol{\varepsilon}_{n+1,k+1}^{\varphi} = \boldsymbol{\varepsilon}_{n+1,k}^{\varphi} + \Delta^2\zeta\, \boldsymbol{G}_{n+1,k}$
    $\alpha_{n+1,k+1} = \alpha_{n+1,k} + (\partial_{,q}\Phi)_{n+1,k}\, \Delta^2\zeta_k$ subject to (5.25)
    $q_{n+1,k+1} = q_{n+1,k} - H\, \frac{\partial\phi}{\partial q}\, \Delta^2\zeta$ subject to (5.34)
    compute $\phi(\boldsymbol{\sigma}_{n+1,k+1}, q_{n+1,k+1})$
  end
  return bad
end

- a general yield function of degree one according to equation (5.2),
- an associated flow rule and
- an associated hardening law.

However, the issue of characterizing the discontinuity itself has not yet been tackled, which still offers the possibility for various sub-formulations of the model.

5.3.1 Rotating discontinuity

For the algorithmic derivation established so far, it has been tacitely assumed that both the direction of the discontinuity normal $\boldsymbol{N}$ and the direction of the displacement jump $\boldsymbol{m}$ can change with time, i.e., $\boldsymbol{N} = \boldsymbol{N}(t)$ and $\boldsymbol{m} = \boldsymbol{m}(t)$. In effect, also the tensor $\boldsymbol{G}$ (5.24) introduced to the stress evaluation algorithm (Section 5.2.2) has to be considered as time dependent. This general concept of a *rotating discontinuity* reflects the characteristics of *rotating crack models* commonly adopted in the context of *smeared crack models* (e.g., Oliver [86], Jirásek [58]).

In the framework of strong discontinuities such a general concept is advocated by Mosler [75, 76] and Mosler & Meschke [80].

To some extent, the concept of a rotating discontinuity contradicts the assumptions made for derivation of the strong discontinuity kinematics, cf. Section 4.1, where the shape of the discontinuity surface is assumed to remain unchanged over time. Based on this notion, algorithmic formulations commonly rely on the assumption of stationarity regarding discontinuity orientation and displacement jump direction, i.e., $\boldsymbol{N} = \text{const.}$ and $\boldsymbol{m} = \text{const.}$ (see, e.g., Oliver [88], Wells & Sluys [130], Feist [41]).

5.3.2 Fixed discontinuity

In the following, formulation of the model shall be specialized to the case of discontinuity orientation and displacement jump direction being considered as invariant with respect to time.

As already alluded to in Section 5.1.3, in case of the adopted Rankine yield condition with linear elastic pre-peak range, the discontinuity normal $\boldsymbol{N} \equiv \boldsymbol{m}$ is simply determined as the direction of maximum principal stress. For the fixed discontinuity concept, this implies that $\boldsymbol{N}$ is determined solely by the direction of principal stress at the onset of localization — and remains unchanged in the further process. Hence, from $\partial_{\boldsymbol{\sigma}} \boldsymbol{m}_{n+1} = \boldsymbol{0}$ it follows that $\boldsymbol{G}_{n+1} = \boldsymbol{G} = \text{const.}$ (5.24), meaning that the direction of plastic flow remains constant. As a consequence, the algorithmic modulus (5.41) reduces to

$$\boldsymbol{\Xi}_{n+1} = \boldsymbol{\Xi} = \mathbb{C} \,. \tag{5.50}$$

5.3.2.1 Modified kinematics

Once localization is initiated, the fixed discontinuity approach entails progress of localization along the fixed direction $\boldsymbol{m}$ of the displacement jump. However, in all but the simplest cases, in the progress of further loading stress redistribution effects will induce rotation of principal stress axes. Thus, in the context of the adopted RANKINE criterion for mode-I failure, without further modification spurious shear stress transfer over the discontinuity may develop and induce significant shear-locking effects. As a remedy, displacements tangential to the discontinuity surface may be permitted which in effect prevents spurious shear stress transfer. With $\boldsymbol{N}$ as the unit normal vector to the discontinuity surface $\partial_{\mathrm{s}}\Omega$, the tangent unit vectors $\boldsymbol{T}_i$ with $i = 1, \ldots, 1 - n_{\mathrm{dim}}$ must suffice

$$\begin{aligned} &\boldsymbol{N} \bullet \boldsymbol{T}_i = 0 && \text{for } i = 1, \ldots, 1 - n_{\mathrm{dim}} \\ &\boldsymbol{T}_i \bullet \boldsymbol{T}_j = 0 \quad \text{for } i \neq j && \text{and } i, j = 1, \ldots, 1 - n_{\mathrm{dim}} \ . \end{aligned} \tag{5.51}$$

The amplitude of the displacement jump in normal direction is denoted as ζ_n while the respective amplitudes of the tangential components are defined as $\zeta_{t,i}$. Adopting these specifications, the displacement jump across the discontinuity (4.32) is then rephrased as

$$[\![\boldsymbol{u}]\!]_{\mathrm{s}} = \zeta_n \, \boldsymbol{N} + \sum_{i=1}^{n_{\mathrm{dim}}-1} \zeta_{t,i} \, \boldsymbol{T}_i \ . \tag{5.52}$$

As before, the evolution of the normal traction component $t_n = (\boldsymbol{N} \otimes \boldsymbol{N}) : \boldsymbol{\sigma}$ is ruled by the traction separation law (5.7)

$$\phi_n(\boldsymbol{\sigma}, q) = t_n - q_n(\zeta_n) \ . \tag{5.53}$$

Accordingly, for the tangential traction components $t_{t,i} = (\boldsymbol{T}_i \otimes \boldsymbol{N}) : \boldsymbol{\sigma}$ a corresponding interface relationship is defined as

$$\phi_{t,i}(\boldsymbol{\sigma}, q) = t_{t,i} - q_{t,i}(\zeta_n, \zeta_{t,i}) \ , \tag{5.54}$$

where in general the stress like hardening variable $q_{t,i}$ also may depend on the amplitude of the displacement jump in normal direction ζ_n. Under the the assumption of dominating mode-I loading states, equation (5.54) may be simplified by setting

$$q_{t,i}(\zeta_n, \zeta_{t,i}) = 0 \ , \tag{5.55}$$

which corresponds to a zero shear retention factor (MOSLER & MESCHKE [80]). It is important to realize that for the considered mode-I failure the interface law for the normal traction component is the primary condition which controls evolution of the discontinuity. The secondary interface laws for the tangential traction components are therefore activated only in case mode-I induced localization has already occurred.

In compliance with the decomposition of the displacement jump (5.52), the rate of the enhanced strain tensor (5.14) is rewritten as

$$\begin{aligned}\dot{\boldsymbol{\varepsilon}}_{\varphi} &= \dot{\boldsymbol{\varepsilon}}_{\varphi_n} + \sum_{i=1}^{n_{\text{dim}}-1} \dot{\boldsymbol{\varepsilon}}_{\varphi_{t,i}} \\ &= \dot{\zeta}_n \, \boldsymbol{G}_n + \sum_{i=1}^{n_{\text{dim}}-1} \dot{\zeta}_{t,i} \, \boldsymbol{G}_{t,i} \ , \end{aligned} \tag{5.56}$$

where the second order tensors $\boldsymbol{G}_n$ and $\boldsymbol{G}_{t,i}$ are defined due (5.24) as

$$\boldsymbol{G}_n := \left(\boldsymbol{N} \otimes \overline{\boldsymbol{\nabla}\varphi}_h\right)^{\text{sym}} \tag{5.57}$$

$$\boldsymbol{G}_{t,i} := \left(\boldsymbol{T}_i \otimes \overline{\boldsymbol{\nabla}\varphi}_h\right)^{\text{sym}} \quad \text{for } i = 1, \dots, 1 - n_{\text{dim}} \ . \tag{5.58}$$

5.3.2.2 Analogy to multisurface plasticity algorithms

Utilizing above definitions for the stress evaluation algorithm, the strain residual (5.27) and the residuals of the strain like internal variable (5.28) are redefined as

$$\boldsymbol{R}^{\varepsilon} := \boldsymbol{\nabla}^{\text{sym}} \bar{\boldsymbol{u}}_{n+1} - \boldsymbol{\varepsilon}_n^{\varphi} - \mathbb{C}^{-1} : \boldsymbol{\sigma}_{n+1} - \Delta\zeta_n \, \boldsymbol{G}_{n,n+1} - \sum_{i=1}^{n_{\text{dim}}-1} \Delta\zeta_{t,i} \, \boldsymbol{G}_{t,i,n+1} \tag{5.59}$$

and

$$\begin{Bmatrix} R_n^{\alpha} \\ R_{t,i}^{\alpha} \end{Bmatrix} := \begin{Bmatrix} \alpha_{n,n+1} - \alpha_{n,n} - \Delta\zeta_n \ \left(\partial_{,q_n}\phi_n\right)_{n+1} \\ \alpha_{t,i,n+1} - \alpha_{t,i,n} - \Delta\zeta_{t,i} \ \left(\partial_{,q_{t,i}}\phi_{t,i}\right)_{n+1} \end{Bmatrix} \qquad i = 1, \dots, n_{\text{dim}} - 1 \ , \tag{5.60}$$

respectively. The extended system of equations is finally complemented by the constraints due the active interface conditions:

$$\begin{aligned} &\phi_n(\boldsymbol{\sigma}_{n+1}, q_{n,n+1}) = 0 \\ &\phi_{t,i}(\boldsymbol{\sigma}_{n+1}, q_{t,i,n+1}) = 0 \qquad i = 1, \dots, n_{\text{dim}} - 1 \end{aligned} \tag{5.61}$$

The fixed discontinuity setting with extension to tangential sliding presented so far, is completely equivalent to the framework of multisurface plasticity. Consequently, the actual implementation facilitates adoption of concepts readily established in this context, see, e.g., Simo & Hughes [114]. To this end, the solution of the system of equations determined by (5.59), (5.60) and (5.61) for the updated stress state $\boldsymbol{\sigma}_{n+1}$, softening state represented by $q_{n,n+1}$, $q_{t,i,n+1}$ and jump amplitudes $\zeta_{n,n+1}$ and $\zeta_{t,i,n+1}$ in normal and tangential directions, respectively, follows the same lines as set forth in Section 5.2.2 — i.e., by consistent linearization and adopting a Newton-Raphson iterative procedure. Details of the algorithm are given, e.g., in Simo & Hughes [114] or Lackner [66].

5.3.3 Hybrid approach

The primary goal of the present strong discontinuity modeling approach is simulation and tracing of non-intersecting macroscopic discontinuities within a continuum body. In this regard, the fixed discontinuity concept would be the natural approach.

Decisive for the success of the fixed discontinuity approach, however, is the correct identification of the macroscopic discontinuity's orientation at the onset of localization. A flawed determination of the discontinuity's orientation entails a high risk of introducing spurious stress locking in the progress of further loading and even can completely block further propagation of the localization zone.

In particular for brittle materials it can be observed that formation of a macroscopic discontinuity (crack), in general is preceded by the development of secondary localization (microcracks) which must not necessarily be aligned with the macroscopic discontinuity path. Only on further loading, these microcracks give rise to propagation of the macroscopic discontinuity; either by alignment (rotation) and aggregation of multiple microcracks or by inducing propagating stress and strain states, respectively. This cognition clarifies that identification of the *macroscopic* discontinuity direction based on local stress and strain states, respectively, can be misleading. Furthermore, in the context of the finite element method a material point (e.g., Gauss point) in fact aggregates the effects within a finite *volume*, hence, this notion becomes even more pronounced.

As a remedy, multiple cracking could be allowed for in the algorithmic implementation, see, e.g., Jirásek & Zimmermann [58] for application in the context of a smeared model with rotating cracks. Such an approach increases the algorithmic complexity, and at the same time also considerably complicates the establishment of a numerically robust procedure.

An alternative conept is provided by strategies that employ additional *nonlocal* information in order to correctly identify the macroscopic discontinuity direction. These strategies are further discussed in Chapter 6.

In this work, a third approach is pursued. Accounting for the characteristic formation process of a macroscopic discontinuity, a hybrid approach, combining rotating and fixed discontinuity concepts, is devised. The model comprises two phases:

- *Initiation phase:*
  After onset of localization has been signaled at a material point, a macroscopic discontinuity starts to form. During this phase, the discontinuity's orientation adapts to the locally prevailing stress or rather strain state *(rotating discontinuity approach)*.

- *Propagation phase:*
  After a certain threshold is passed, the discontinuity is considered as macroscopic. From now on, the orientation of the discontinuity is kept constant *(fixed discontinuity approach)*. During the propagation phase, further loading will solely affect the amplitude

of the displacement jump across the discontinuity, not the orientation of the discontinuity itself.

A suitable threshold marking the transition between the two phases could be based on the magnitude of the displacement jump across the discontinuity. For the actual implementation, however, a dimensionless related quantity, identifying the decrease of the transmissible normal traction across the discontinuity, is preferred:

$$\omega := \frac{q_n(\zeta_n)}{f_{\mathrm{tu}}} \,, \tag{5.62}$$

with f_{tu} denoting the uniaxial tensile strength of the material and q_n reflecting the current softening state of the normal traction interface law (5.53). The initiation phase is then bounded by $\omega \geqslant \omega_{\mathrm{thr}}$ while the propagation phase corresponds to values $\omega < \omega_{\mathrm{thr}}$.

Numerical tests indicate that $\omega_{\mathrm{thr}} \in [0.5, 0.8]$ represents a suitable range for the threshold value ω_{thr}. For analyses carried out in Chapter 6 a uniform value of $\omega_{\mathrm{thr}} = 0.5$ is adopted.

Simulations performed in Chapter 6 are based on the adoption of tangential interface conditions according to (5.55), corresponding to a zero shear retention factor, for the propagation phase.

The actual implementation of the proposed hybrid approach offers the advantageous feature of maintaining the single discontinuity concept on algorithmic level, which also significantly enhances numerical stability. As illustrated further in Chapter 6, it contributes to stress locking free propagation of the discontinuity under avoidance of elaborate nonlocal strategies.

Related concepts can be found in Jirásek & Zimmermann [59, 60]. In [59] the authors advocate a rotating crack approach with transition to scalar damage in order to overcome stress locking effects in the context of smeared crack modeling. A combination of smeared crack and strong discontinuity formulation for triangular constant strain elements is presented in [60].

Chapter 6

Numerical studies

Everything will work just as you expect it to.
Unless your expectations are incorrect.
– Hyman Rosen.

The aim of the present chapter is the investigation of the capability of the embedded strong discontinuity approach developed in foregoing Chapters 4 and 5 — with particular focus on its application within a high-order finite element framework. To this end, numerical analyses on various examples of structures exhibiting mode-I failure are carried out and discussed.

All simulations are performed on basis of a three-dimensional finite element discretization using hexahedral elements. For the purpose of numerical simulation, the embedded strong discontinuity modeling approach is implemented into the high-order finite element code *AdhoC* [34] which is used exclusively for subsequent analyses.

6.1 Uniaxial tensile test

In dependence on the setting adopted in Section 1.1, we start with a simple model problem of a bar loaded in uniaxial tension.

The model properties and the employed three-dimensional finite element discretization are depicted in Figure (6.1). The bar has a uniform cross-sectional area of $A = 0.5\ m \times 0.5\ m$. In order to enforce a localized response despite the uniform geometry, the bar is supplied with an 'artificial' imperfection zone — a region of extension $0.4\ m$ with a slightly lower tensile strength. For the numerical analyses this is realized, by assigning an increased tensile strength by 1.25 % for the material outside the imperfection zone. The bar is clamped at one end. The other end is subjected to a prescribed axial displacement load $\boldsymbol{u}$ which is applied uniformly over the cross-sectional area in order to provide for a purely uniaxial response.

During the analysis, the prescribed axial displacement $\boldsymbol{u}$ is increased monotonically up to a maximum value of $u_{\max} = 0.349\ m$, which corresponds approximately to the 8.72-fold value of the theoretical crack initiation end section displacement of $u_{\mathrm{cr}} = \frac{f_{\mathrm{tu}}}{E} l = 0.04\ m$.

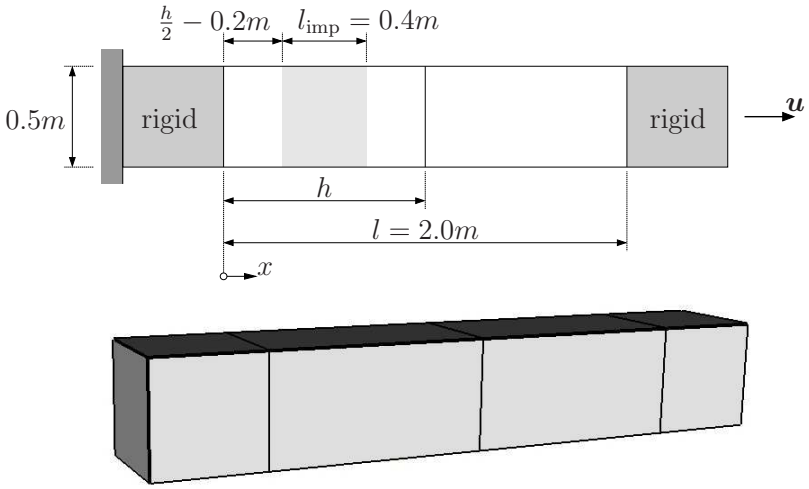

Elastic properties:	
YOUNG's modulus	$E = 500.0\ kN/m^2$
POISSON's ratio	$\nu = 0.0$
Exponential softening law:	
Tensile strength	$f_{\mathrm{tu}} = 10.0\ kN/m^2$
Fracture energy	$G_f = 1.0\ kNm/m^2$

Figure 6.1: Bar with imperfection: System and three-dimensional discretization

The purpose of this example is the elaboration of the basic assets and drawbacks of different modeling approaches: classical continuum modeling without regularization, standard embedded strong discontinuity and embedded strong discontinuity using the advocated p-adaptivity. Subsequently, these are discussed in detail.

6.1.1 Classical continuum approach

In order to emphasize the notion set out in Section 1.1, a classical continuum modeling approach without any regularization is employed for the analysis of the problem outlined above.

To this end, we investigate in a first step three different discretizations, characterized by different lengths $h = 0.5\ m$, $h = 1.0\ m$ and $h = 1.5\ m$ for the localizing element, see Figure 6.1. The polynomial degree is kept constant with $p = 1$. Due to the simplicity of the model problem, an analytical solution can readily be derived, which allows for a straight-forward

assessment of the numerically computed response. Figure 6.2 plots axial stress over axial displacement at the bar end section both for the theoretical and the numerically obtained responses. It is evident that the numerical solution is not objective with respect to the finite element size h. In complete accordance with the argumentation pictured in Section 1.1, the numerical responses evidence an increasingly localized behavior with decreasing h. It should be noted that due to the low-order polynomial approximation of the regular displacement field with $p = 1$, the finite element which incorporates the imperfection zone localizes as a whole, such that the extension of the numerical localization zone coincides with the element dimension h. Therefore, for $h = 1.0\ m$, the size of the numerical localization zone is by coincidence 'correct', such that the fracture energy G_f can be reproduced and consequentially the theoretical softening response is matched, see Figure 6.2.

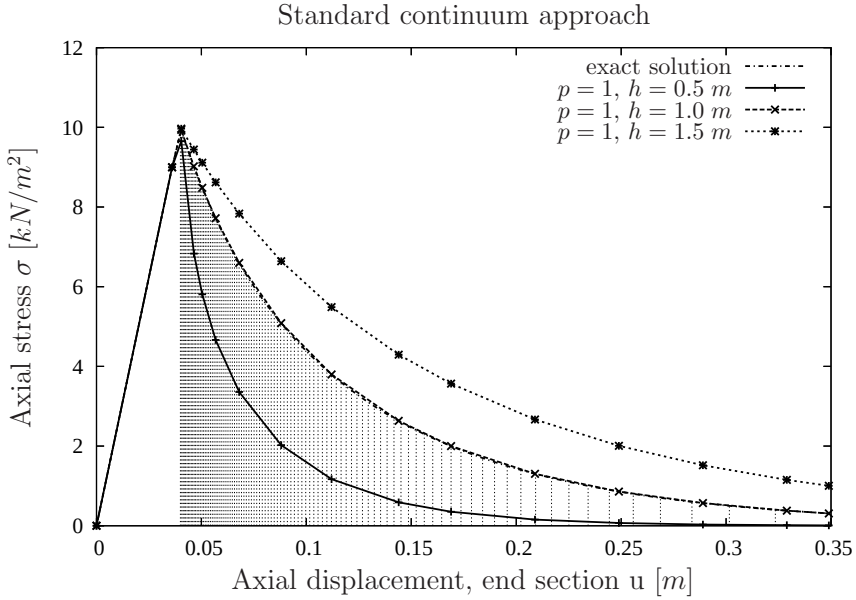

Figure 6.2: h-sensitivity of the standard continuum approach

Next, in order to investigate the sensitivity regarding the order of polynomial approximation, a sequence of analyses is carried out with varying polynomial degree $p = 1, 2, 3, 5$ and constant element size $h = 1.0\ m$. The response curves in Figure 6.3 reveal a strong dependency on the actual order of polynomial approximation p — such that with higher-order p the obtained response is more localized. Higher-order polynomial approximation enhances the kinematic capabilities of the respective finite element; thus, with increasing p the extension of the simulated softening zone decreases, furnishing a correspondingly decreased simulated fracture energy. In conclusion, also in case of strain softening, an *increasing* order of polynomial approximation p qualitatively corresponds to a *decreasing* finite element dimension h.

To summarize, simulation of material softening behavior with a non-regularized continuum approach exhibits the well-known defects already discussed in Section 1.1. In particular it is both

- not objective with respect to the finite element size h and

- not objective with respect to the order of polynomial approximation p.

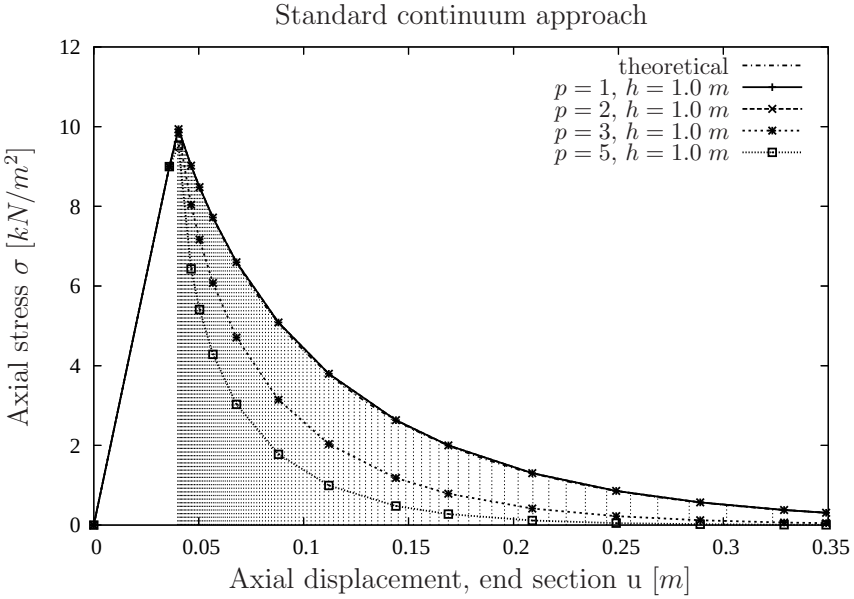

Figure 6.3: p-sensitivity of the standard continuum approach

6.1.2 Embedded strong discontinuity approach

Having illustrated the deficiencies of the standard continuum approach, the present section is devoted to investigating the capability of the embedded strong discontinuity approach (ESD) by means of the same model problem.

6.1.2.1 Standard approach

We start by adopting the standard approach, i.e., employing the transmission function φ_h as defined by equation (4.96). A sequence of analyses with fixed polynomial degree $p = 1$ and varying element size $h = 0.5\ m$, $h = 1.0\ m$ and $h = 1.5\ m$ supports the expected invariance with respect to the size of the localizing finite element, see Figure (6.4). The embedded strong discontinuity formulation properly captures the kinematics of the displacement jump independently of the dimensions of the parent finite element and hence, reproduces the theoretical fracture energy and softening path.

A sensitivity analysis regarding the order of polynomial approximation p, however, discloses a strong dependency of the simulated softening response on the chosen polynomial degree p, cf. Figure (6.5).

Explanation of this behavior is again based on the increased kinematic capability of higher-order polynomials to approximate the displacement jump across the discontinuity surface.

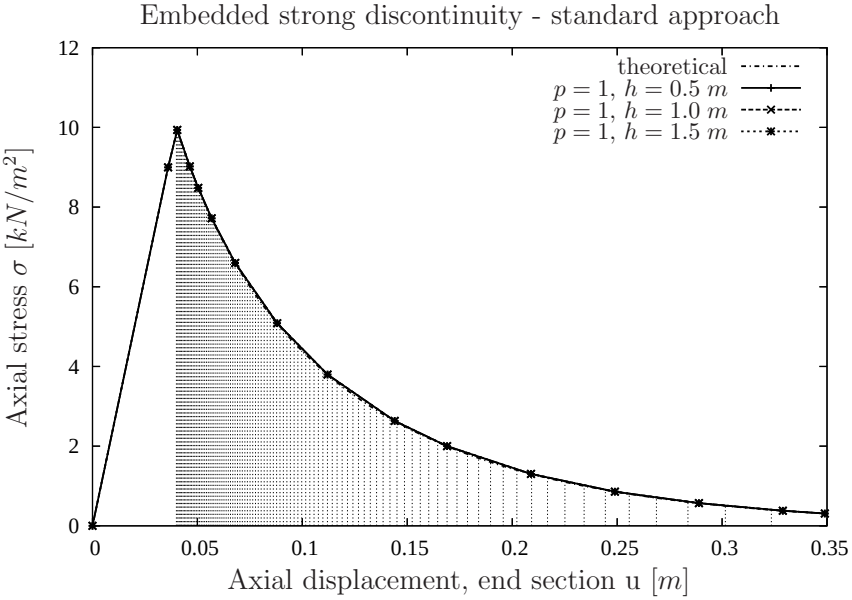

Figure 6.4: h-objectivity of the standard ESD approach

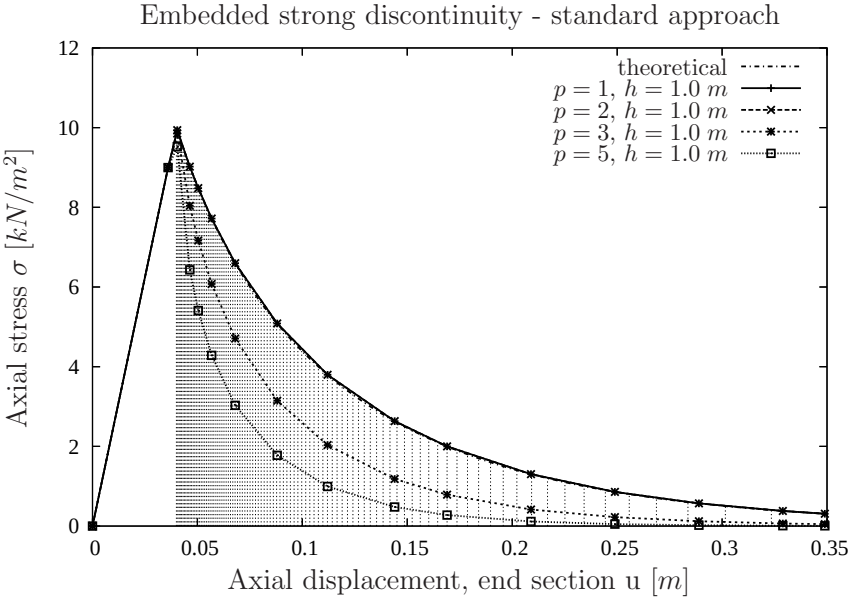

Figure 6.5: p-sensitivity of the standard ESD approach

As a consequence, the numerical localization zone does not extend over the whole element domain anymore. This notion is confirmed by Figure 6.6. There, GAUSS integration points that exhibit localized response are visualized for two representative choices regarding the order of polynomial approximation, namely $p = 1$ and $p = 5$. It is evident that for $p = 1$ all GAUSS points of the respective element respond localized in a uniform manner. By contrast, for $p = 5$, the localized response is concentrated on a portion of the element domain, represented by two GAUSS point layers only. The effect of deformation concentration within a *portion* of the finite element, however, is not accounted for by the embedded strong discontinuity approach in its standard form, i.e., with transmission function φ_h being defined according to (4.96). As a consequence, the regularizing effect of the approach is lost for higher-order polynomial approximations of the regular displacement field.

Remark. It is exactly this observation on which the advocated p-adaptive extension of the transmission function φ_h is founded; compare the discussion given in Section 4.5.2.2. □

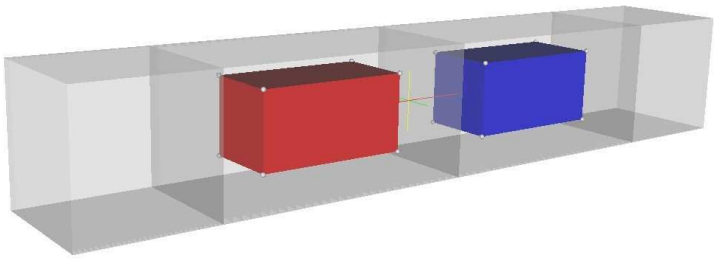

(a)

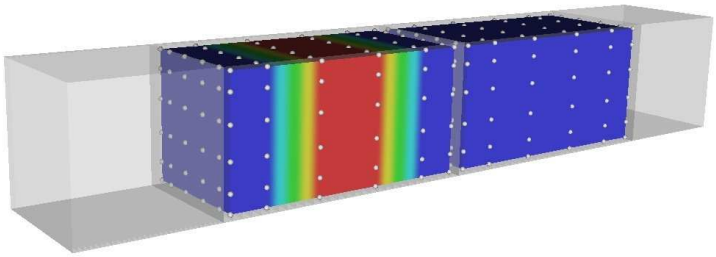

(b)

Figure 6.6: Extension of the numerical localization zone in dependence on the order of polynomial approximation p. GAUSS integration points exhibiting localized response for (a) $p = 1$ and (b) $p = 5$.

Interestingly, for $p = 2$ the theoretical softening path is reproduced by the numerical simulation, see Figure 6.5. This is obviously achieved despite the neglection of higher-order contributions to the transmission function φ_h — which, at first, poses a contradiction to the foregoing argumentation. Can this apparent inconsistency in rationale be resolved? Closer inspection motivates an answer that is as simple as it is self-evident: the quadratic modes are not activated at all for this model problem, which means that the computed responses for $p = 1$ and $p = 2$ are completely identical, compare also Figure 6.3. The reason for this

behavior lies in the fact that quadratic modes are qualified only to a limited extent to contribute to an improved kinematic representation of the jump discontinuity. In the present case, where the discontinuity surface is located at mid-span of the localizing element, the quadratic modes completely fall short of improving the kinematic representation of the discontinuity. This notion is graphically illustrated in Figure 6.7.

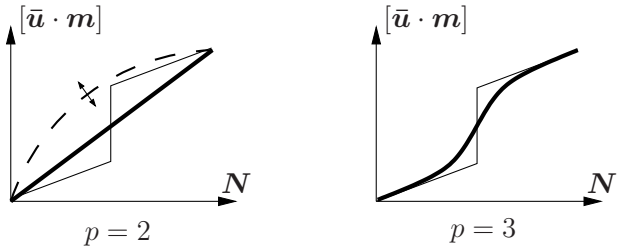

Figure 6.7: Poor qualification of quadratic modes to approximate displacement jump

In view of the above considerations, finite element formulations that rely on a formally independent treatment of the regular and the discontinuous parts $\bar{\boldsymbol{u}}$ and $\hat{\boldsymbol{u}}$ of the displacement field (4.8), investigated, e.g., in [78] and [75], appear prone to exhibit a problematic behavior.

We conclude that — within the framework of embedded strong discontinuities — formally independent approaches for the approximation of the regular and the discontinuous parts of the displacement field are not admissible in general: As shown above, this procedure does not guarantee objectivity of the results with respect to the order of polynomial approximation p adopted for the regular displacement field. For the special case of $p = 2$ in conjunction with a standard approach for the transmission function φ_h, this effect is less apparent — due to the poor qualification of quadratic modes to improve the kinematic representation of a displacement jump.

6.1.2.2 p-adaptive extension

In order to round out the picture, the model problem is finally reanalyzed employing the embedded strong discontinuity formulation in conjunction with the p-adaptive extension, which was developed previously in Section 4.5.

In the previous section, on the one hand the regularizing effect of the standard ESD-approach regarding the elemental discretization h could be affirmed, on the other hand however, a failure of regularization with respect to the order of polynomial approximation p was identified. Following up these outcomes and with a focus on the elimination of this deficiency, now the capability of the advocated p-adaptive extension to the embedded strong discontinuity shall be investigated.

To this end, analyses with different polynomial degrees $p = 1, 2, 3, 5, 7, 9$ are executed. The obtained results show that with increasing order of polynomial approximation p of the regular displacement field, also the approximation of the kinematics of the displacement jump

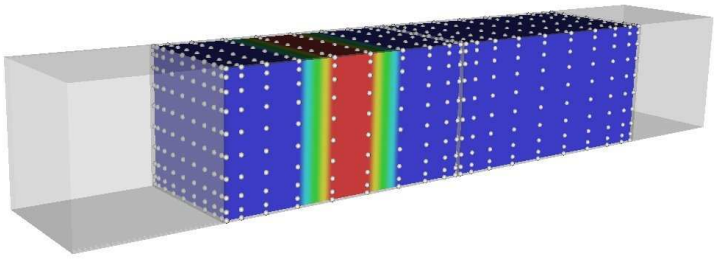

(a)

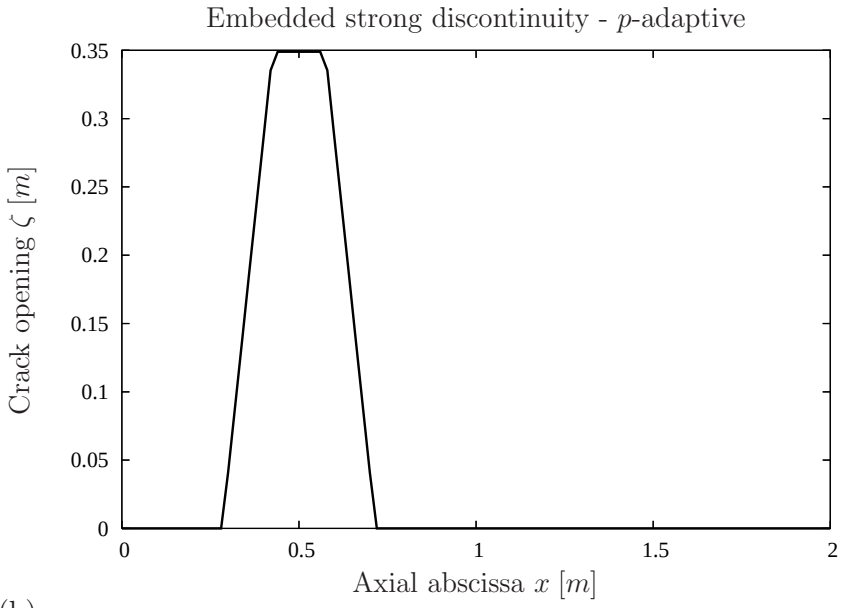

(b)

Figure 6.8: Simulation with order of polynomial approximation $p = 9$ for the regular displacement field. (a) Numerical localization zone and 'crack opening' at the final loading stage $u_{\max} = 0.349\ m$. (b) 'Crack opening' distribution along the bar.

is improved — giving rise to a 'contraction' of the simulated softening zone; compare Figure 6.6 for $p = 1,5$ and Figure 6.8 for $p = 9$. Considering the regular displacement field, the distribution of the axial component approaches the theoretical discontinuous distribution with increasing degree of polynomial approximation. Accordingly, the obtained axial strain distribution represents an increasingly refined approximation of the theoretical singular strain distribution. Figure 6.9 depicts the respective distributions obtained for the simulation with $p = 9$; qualitatively, they should be compared to the distributions that originated from the initial theoretical reflections, see Figure 1.4.

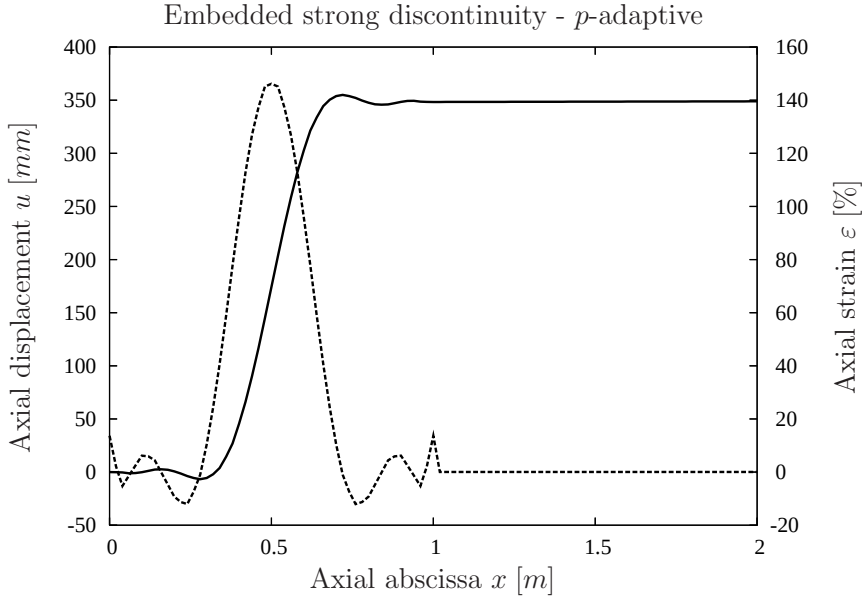

Figure 6.9: Simulation with order of polynomial approximation $p = 9$ for the regular displacement field. Axial displacement and axial continuum strain distribution along the bar at final loading stage $u_{\max} = 0.349\ m$.

In contrast to the ESD standard approach, the advocated p-adaptive extension accounts for this improved kinematic representation of the displacement field. In consequence, it accomplishes a reproduction of the theoretical fracture energy and softening path, independent of the order of polynomial approximation; Figure 6.10 gives a synopsis of the computed numerical responses for the different choices of p and the theoretical softening path, which are apparently congruent.

Due to the traction continuity condition, which is inherent to the strong discontinuity approach, the resulting stress field is expected to be regularly distributed — also and in particular across the discontinuity surface, represented by the numerical localization zone. This notion is confirmed by Figure 6.11 rendering a uniformly constant distribution of the axial stress component along the bar.

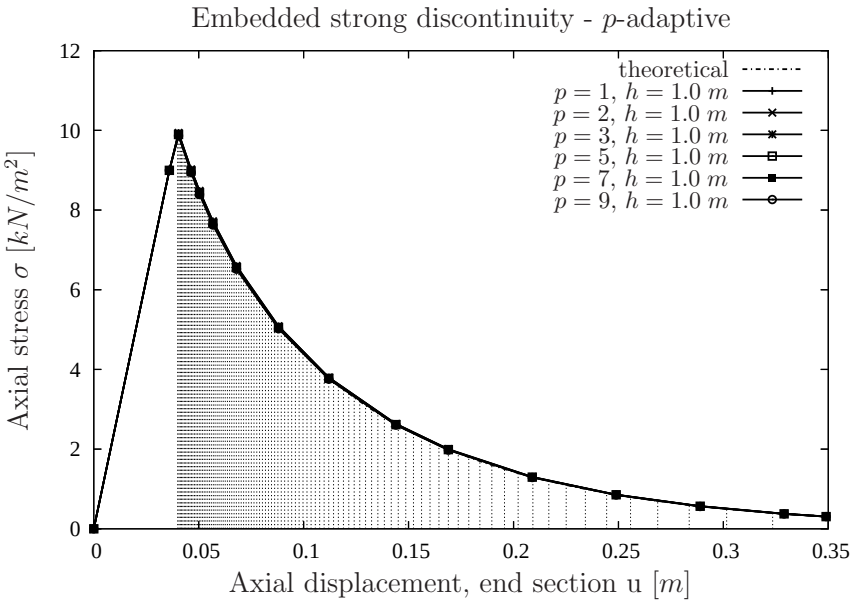

Figure 6.10: Objectivity of the p-adaptive ESD approach

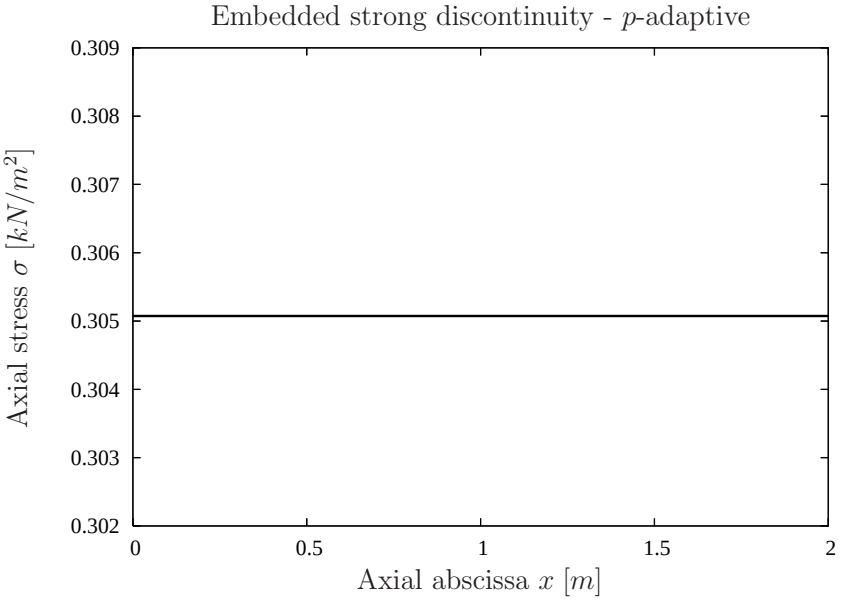

Figure 6.11: Simulation with order of polynomial approximation $p = 9$ for the regular displacement field. Axial stress distribution along the bar at final loading stage $u_{\max} = 0.349\ m$.

6.2 Notched bar

For the preceding model problem, due to the regular geometry, a localized response had to be enforced by artificially introducing an imperfection zone with slightly reduced material strength. In order to explore the case of a 'natural' discontinuity formation and evolution, the present section analyzes a second model problem featuring a geometrical imperfection. To this end, a notched bar which is again subjected to uniaxial tension is considered. Configuration and adopted material properties can be seen from Figure 6.12.

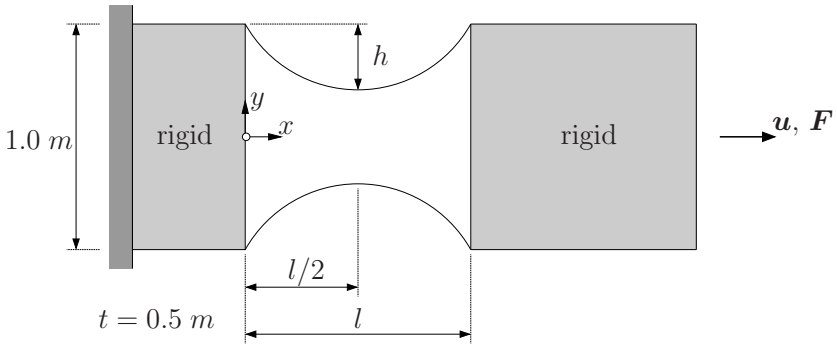

Elastic properties:	
YOUNG's modulus	$E = 500.0\ kN/m^2$
POISSON's ratio	$\nu = 0.0$
Exponential softening law:	
Tensile strength	$f_{\mathrm{tu}} = 10.0\ kN/m^2$
Fracture energy	$G_f = 0.2\ kNm/m^2$

Figure 6.12: Symmetrically notched bar: System configuration and material properties. The boundary edges in the notch region are of quadratic shape with ordinates according to $y = \pm\left(0.5 - h + \frac{4h}{l^2}(x - \frac{l}{2})^2\right)$. For the actually investigated configuration, $h = 0.3\ m$ and $l = 1.0\ m$.

As before, the geometry is discretized by three-dimensional hexahedral finite elements. Two spatial discretizations are investigated, see Figure 6.13. For the refined mesh with 148 elements the curved boundary is approximated in a polygonal manner and for the corresponding finite element geometry a standard trilinear mapping is adopted, cf. Section 3.3.2. Analysis on this mesh is carried out using a polynomial degree of $p = 1$ for the approximation of the regular displacement field. The second mesh consists of 5 elements, only. Here, the element edges affected by the notch are no longer straight but reparametrized according to their quadratic shape, cf. Figure 6.12. Mapping of the corresponding elements is then performed using the blending function method as described in Section 3.3.2. The second mesh is employed for analyses with higher-order polynomial degrees $p = 3, 5, 7, 9$ for the approximation of the regular displacement field.

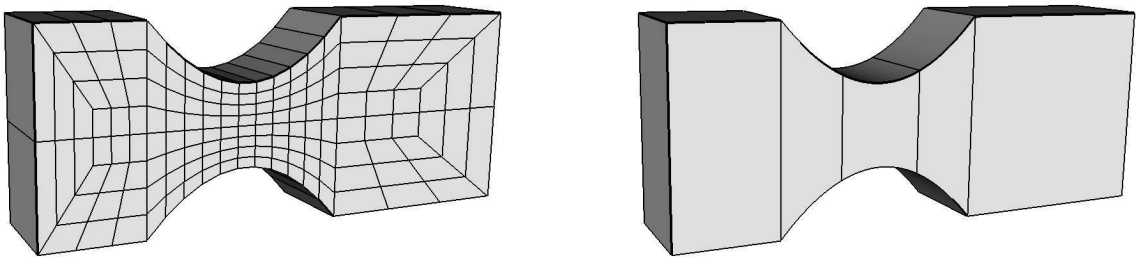

(a) (b)

Figure 6.13: Symmetrically notched bar, three-dimensional discretization. (a) h-refined mesh with 148 elements. (b) finite element mesh with 5 elements used for higher-order polynomial approximation of the regular displacement field.

The objective of the investigation is threefold. As a consequence of the tapered shape of the bar, stress concentration at the notches occurs upon loading. Therefore, initiation of failure is expected to take place at the notches, succeeded by a vertical progress of the failure zone towards the center of the bar. In contrast to the preceding model problem, the present model problem involves both phases, namely crack initiation and crack propagation. Hence, the first objective is to investigate the capability of the ESD p-adaptive approach in view of the extended issue. Further, the curved geometry puts forth non-constant JACOBIAN matrices (cf. Section 3.1.2.1) for the corresponding finite elements — which directly incorporates into the strong discontinuity formulation via the adopted approach for the transmission function φ_h (4.95). Therefore, the second objective is to assess the quality of the ESD p-adaptive formulation in view of this aspect. Finally, due to the relative simplicity of the model problem, results obtained by the ESD standard approach for $p = 1$ on the h-refined mesh (Figure 6.13a) are expected to be essentially equivalent to results of respective simulations with higher-order poylnomial approximations of the regular displacement field using the ESD p-adaptive extension on the coarse mesh, Figure 6.13b.

The analyses are performed under displacement control. Instead of increasing the loading by a constant increment size, an automatic adaptive stepping scheme according to CRISFIELD [22, 23] is applied as an efficient action to reduce the number of load increments that are required to sufficiently fine resolve the failure process. To this end, as a simple heuristic measure for the 'degree of nonlinearity', the actual number n_n^i of required global level NEWTON-RAPHSON iterations to achieve equilibrium for the current load increment is adopted. The step length for the subsequent load increment $\Delta\lambda_{n+1}^g$ [1] is then obtained by scaling the current one according to

$$\Delta\lambda_{n+1}^g = \Delta\lambda_n^g \left(\frac{n_n^i}{n_{\text{des}}}\right)^\kappa , \tag{6.1}$$

[1] In the context of the overall incremental iterative solution procedure, the total load vector, given by $\mathbf{f}^{\text{ext}}$, to be applied to the dicretized initially unloaded system is scaled by a factor λ_n^g, which is then successively increased. In order to avoid confusion with the plastic multiplier λ introduced in Section 2.4.2, the superscript $(\bullet)^g$ has been introduced, here.

where the input parameter n_{des} represents the number of 'desired' iterations. Exponent κ is motivated by SCHWEIZERHOF [110] who successfully introduced $\kappa = 0.5$ in order to smooth possible strong oscillations in the computed step length. Following this approach, the same choice was adopted for the present analyses.

Figure 6.14 shows a synopsis of the numerically computed structural responses for all performed analyses. In case of a uniform cross-sectional stress distribution, the theoretical load carrying capacity of the considered model problem would amount to $A_c \cdot f_{\text{tu}} = 2.0\ kN$. However, as a consequence of stress concentration at the notches, this theoretical value can never be reached but represents an upper bound. As Figure 6.14 demonstrates, this notion is confirmed by all numerical simulations. Due to stress concentration effects at the notches, crack initiation starts already well before the capacity limit is reached, cf. Figure 6.16a. As a consequence of the henceforth decreasing traction capacity of the 'cracked' regions, further stress concentration develops at the tips of these regions — finally enforcing a propagation of the localization zone towards the center of the bar until a through-going crack has formed. This mechanism of localization initiation and successive propagation is nicely resolved by all numerical analyses — both for the ESD standard approach with $p = 1$ on the refined mesh and for the ESD p-adaptive approach for higher-order polynomial approximations p of the regular displacement field, for which the higher-order contributions directly incorporate into the strong discontinuity formulation via the transmission function φ_h (4.95). Exemplarily, Figure 6.16 depicts the evolution of the localization zone up to the formation of a straight through-going crack for the analysis with $p = 9$. Likewise, a plot of stress evolution along the centerline of the bar, see Figure 6.15, illustrates both a *decrease* of traction transferred over the discontinuity (crack) with *increasing* amplitude of the discontinuity (crack opening) and an associated homogenization of the stress state along the bar.

Considering the responses according to Figure 6.14 it emerges that the different simulations essentially yield equivalent results. Remaining differences can be attributed to the degree of resolution of the initial stress concentration at the notches leading to localization initiation. In consequence, it appears that the rather coarse approach with $p = 3$ for the approximation of the regular displacement field somewhat overpredicts the structural load carrying capacity. Higer-order approximations with $p = 5, 7, 9$ on the other hand show a convergent behavior. When compared to the results of the analysis, executed on the refined mesh using a low-order $p = 1$ approximation for the regular displacement field, the high-order analysis results represent a higher degree of resolution of the localization initiation process.

Corresponding to the straight evolution of the discontinuity, Figure 6.17 illustrates the normal vectors $\boldsymbol{N}$ of the GAUSS point related discontinuity planes for different loading stages.

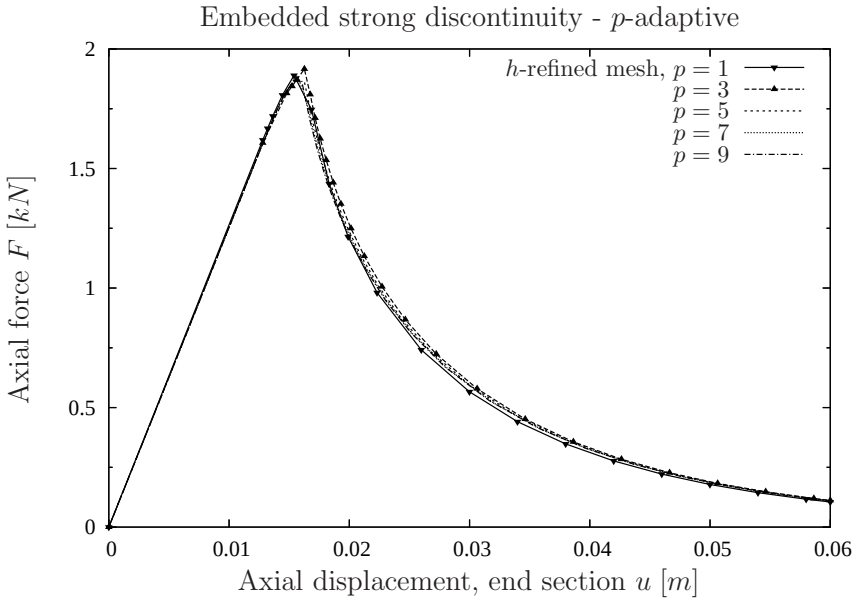

Figure 6.14: Notched bar in axial tension. Synopsis of numerical response for h-refined mesh and responses for different degrees p of polynomial approximation for the regular displacement field.

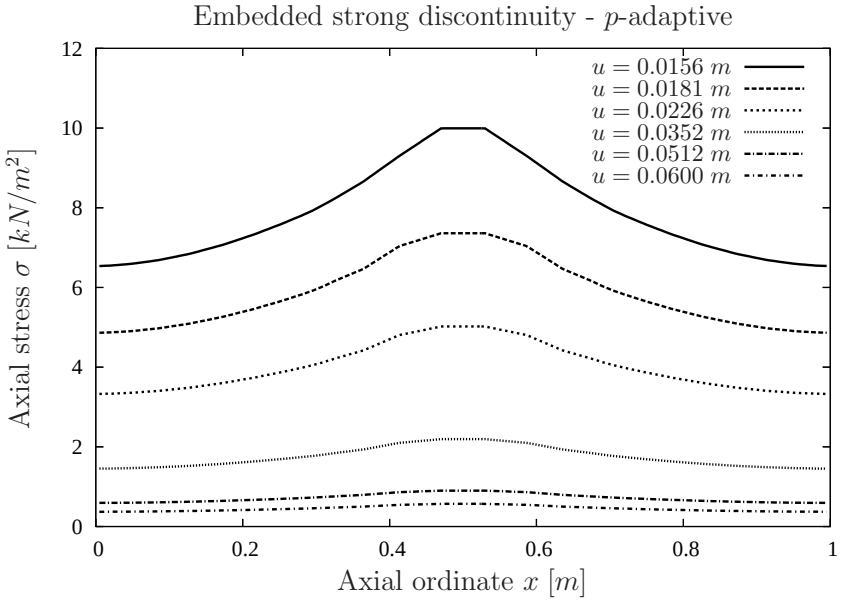

Figure 6.15: Notched bar in axial tension. Axial stress distribution along the centerline, evolution and homogenization with increasing axial displacement u at the free bar end. Analysis with order of polynomial approximation $p = 9$ for the regular displacement field.

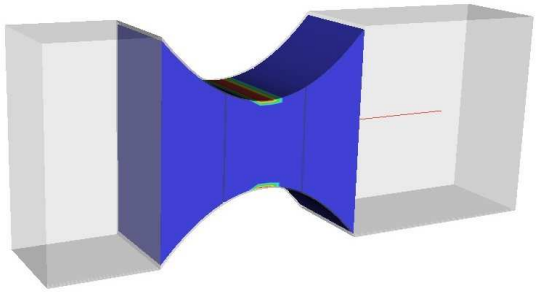

(a) $u = 0.01344\ m$

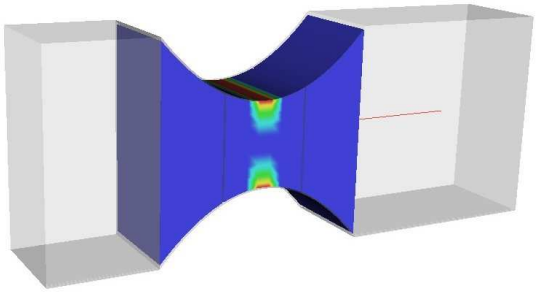

(b) $u = 0.01604\ m$

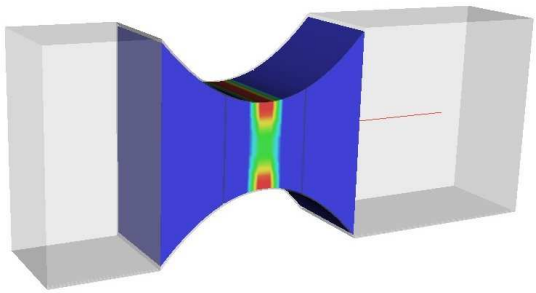

(c) $u = 0.01671\ m$

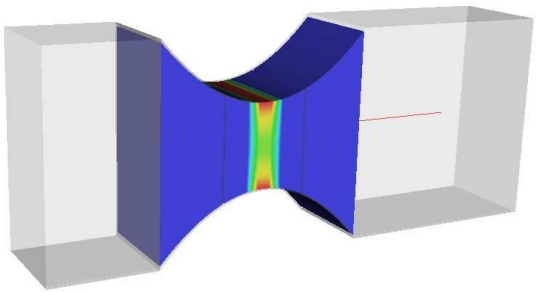

(d) $u = 0.01855\ m$

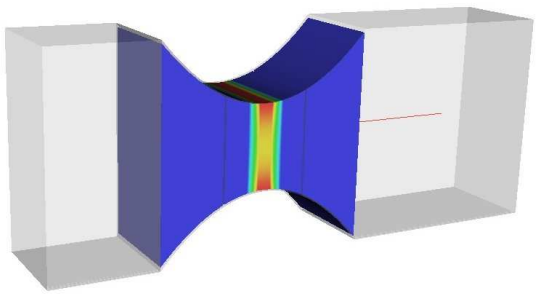

(e) $u = 0.02298\ m$

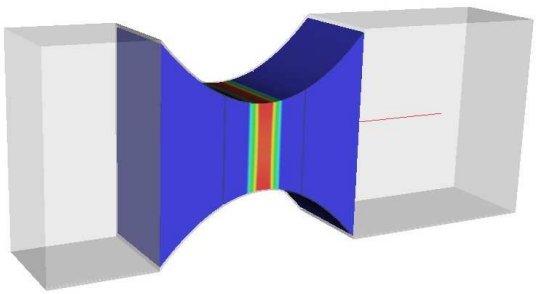

(f) $u = 0.0600\ m$

Figure 6.16: Notched bar in axial tension. Evolution of the discontinuity band with increasing axial displacement u at the free bar end. Analysis with order of polynomial approximation $p = 9$ for the regular displacement field.

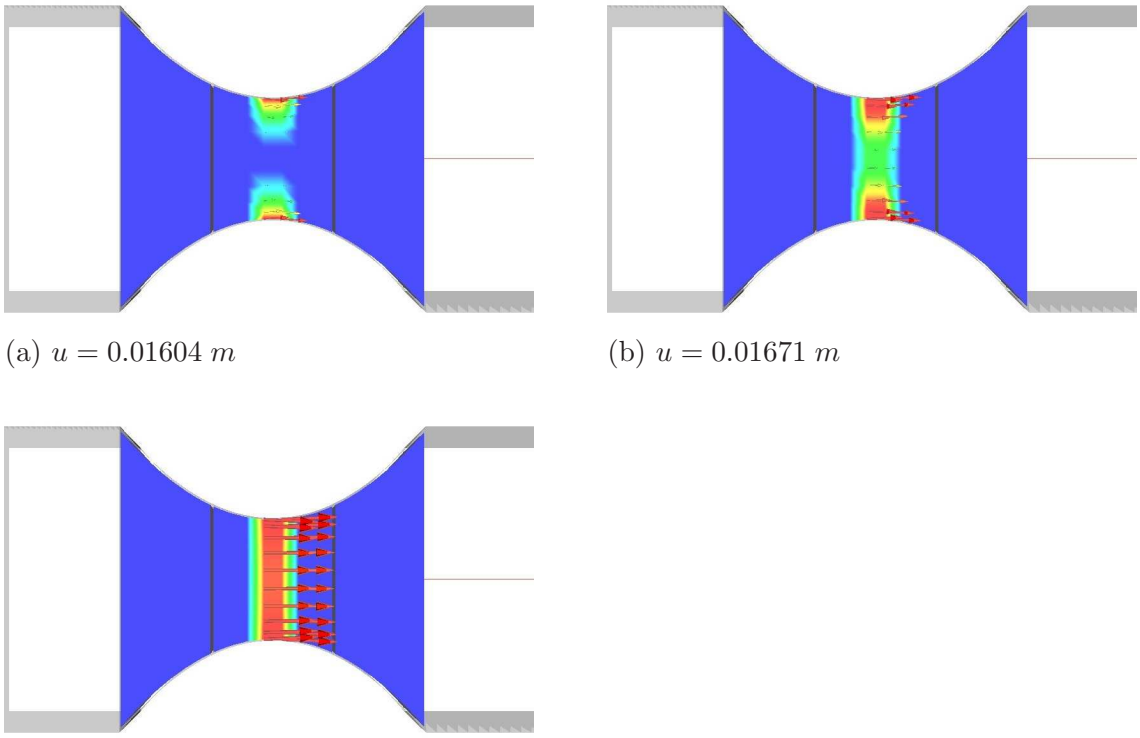

(a) $u = 0.01604\ m$

(b) $u = 0.01671\ m$

(c) $u = 0.0600\ m$

Figure 6.17: Notched bar in axial tension. Normal vectors of the GAUSS point related discontinuity planes at different loading stages. Analysis with order of polynomial approximation $p = 9$ for the regular displacement field.

6.3 Three point bending test

For the preceding examples, both the instantaneous formation of an end-to-end localization zone as well as the gradual propagation of the discontinuity until a continuous localization zone is established, have been analyzed. The prevailing stress state in these tests, however, was still of predominantly uniaxial character. To carry on the discussion to a more general situation, in the present section a three point bending test is analyzed.

The three point bending test represents a standard benchmark for the validation of numerical models for tensile failure, see, e.g., MESCHKE et al. [71]. The principal system setup and the adopted geometry are illustrated in Figure 6.18. The beam is affixed by pinned supports arranged at the left and right hand side endings of its bottom side. One support is left free to move horizontally in order to prevent the development of consequential constraint forces. The beam is loaded by an imposed vertical displacement applied at midspan at the beam's topside.

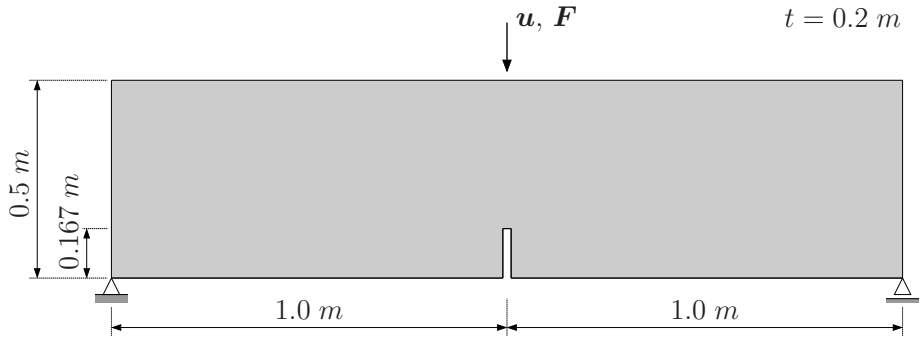

Elastic properties:		
YOUNG's modulus	$E =$	30000.0 MPa
POISSON's ratio	$\nu =$	0.2
Exponential softening law:		
Tensile strength	$f_{\mathrm{tu}} =$	1.0 MPa
Fracture energy	$G_f =$	0.1 kNm/m^2

Figure 6.18: Three point bending test: System configuration and adopted material properties.

As a result of the loading conditions, the beam is predominantly subjected to bending, with the highest tensile stresses developing in axial direction at the bottom side of the midspan cross-section. This effect is yet amplified by the notch. In consequence, localization is expected to be naturally induced at the tip of the notch and to subsequently progress in vertical direction towards the point of load application.

Following up the discussion of Section 5.3, the objective of the investigation is the assessment and extended motivation of the advocated hybrid discontinuity approach.

To this end, for analysis of the three point bending test two models are contrasted;

- the *fixed discontinuity approach* (FDA) assuming zero shear retention due equation (5.55), and
- the *hybrid discontinuity approach* (HDA), where for the propagation phase likewise zero shear retention is assumed.

Analyses are based on a three-dimensional hexahedral finite element discretization, see Figure 6.19. Regarding the order of polynomial approximation for the regular displacement field, a uniform degree of $p = 1$ is adopted. [2] Simulations are performed under pure displacement control up to a final vertical displacement of $u = 0.5\ mm$ at the point of load application. Adopted material properties are given in Figure 6.18.

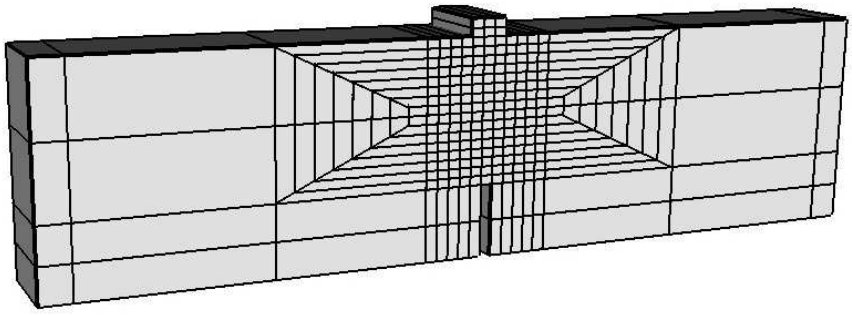

Figure 6.19: Three point bending test, three-dimensional discretization using hexahedral elements.

6.3.1 Simulated structural response

In a first step, the analysis is run employing the fixed discontinuity approach. In order to prevent spurious shear transfer across the discontinuity, zero shear retention according to (5.55) is adopted.

Due to observed stability problems, the solution process is terminated at a stage corresponding to a vertical displacement of $u = 0.31\ mm$ at the point of load application. By this time, the obtained response curve, depicting load over vertical displacement at the point of load application (Figure 6.20), does not exhibit a distinct maximum. Instead, it shows a monotonically increasing behavior such that neither a structural load carrying capacity nor structural softening response can be identified.

[2] The chosen finite element mesh along with the adopted low-order polynomial approximation yields a rather coarse discretization of the problem at hand; it is, however, emphasized that the primary goal of the investigation is a qualitative assessment of the respective characteristics of fixed and hybrid discontinuity approach. Since quantitative aspects are of minor relevance in this context, the chosen discretization is regarded as sufficiently fine to illustrate the principal differences inherent to the two approaches.

The analysis is rerun, this time adopting the hybrid discontinuity approach with a threshold value of $\omega_{\text{thr}} = 0.5$ (5.62) and likewise zero shear retention. As opposed to the foregoing analysis stability problems are not observed and the simulation is continued up to a final vertical displacement of $u = 0.5\ mm$ at the point of load application. Differences are also manifest in the computed structural response. This time the corresponding response curve clearly shows the expected pronounced maximum and softening response, cf. Figure 6.20.

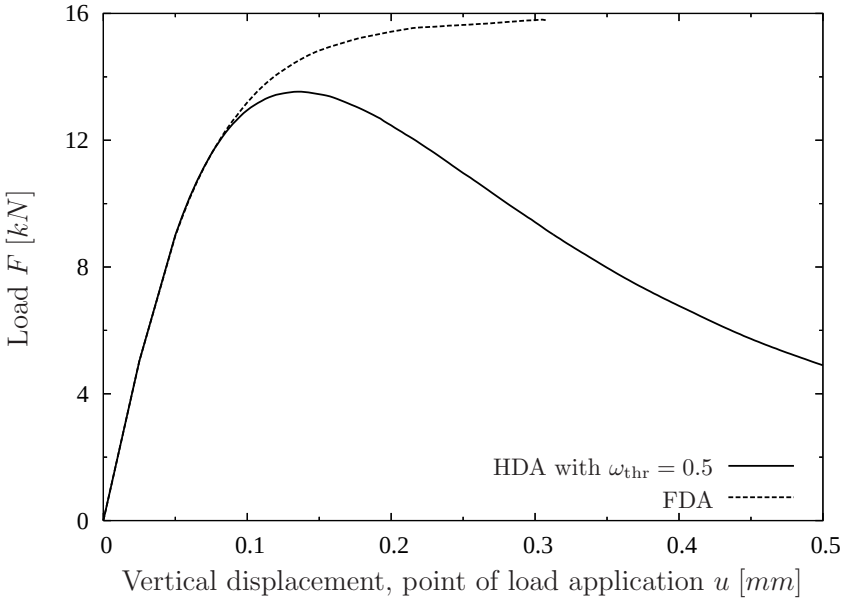

Figure 6.20: Three point bending test, load vs. vertical displacement at the point of load application. Stress-locking for fixed discontinuity approach (FDA). Locking free response for the advocated hybrid discontinuity approach (HDA).

6.3.2 Fixed discontinuity approach

Closer investigation of the numerical localization path reveals that localization indeed is triggered at the notch tip and starts propagating vertically towards the load application point. At a certain point, however, the localization pattern bifurcates in a diffuse manner. Figure 6.21 exemplarily depicts the state at a loading of $u = 0.195\ mm$, where the initially unique localization path has clearly branched out. The solution procedure obviously has bifurcated to a secondary, spurious equilibrium path.

Upon thorough inspection, the reason for this behavior emerges as follows.

Figure 6.23 provides a magnification of the localization domain and illustrates the evolution of the localization path with increasing loading of the beam. Depicted are the GAUSS points, grouped according to their finite element association. Shaded areas indicate localizing response and lines represent normal directions of actual and potential localization planes at the respective GAUSS points. Potential localization planes are identified by the direction of maximum principal tensile strain.

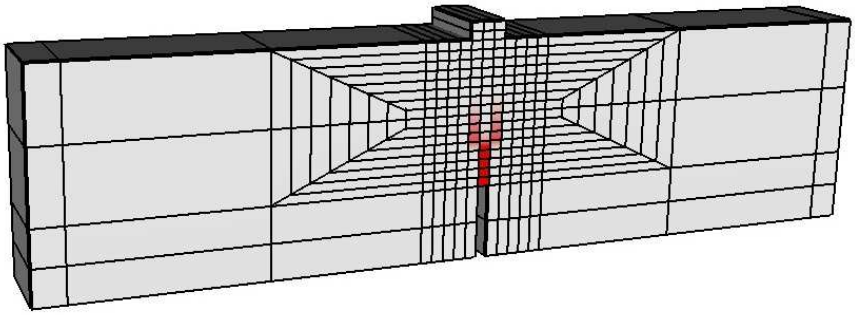

Figure 6.21: Three point bending test, fixed discontinuity approach. Spurious localization pattern at loading state $u = 0.195\ mm$.

Clearly visible, already during the initial phase, the GAUSS point related discontinuity planes are not perfectly aligned with the macroscopic discontinutiy direction (Figure 6.23a–c). Moreover, it is noticable that the potential discontinuity planes ahead of the localization tend towards a *horizontal* alignment, i.e., the respective normals are oriented (nearly) vertically. The increasing misalignment of the GAUSS point related discontinuity planes with the macroscopic discontinuity direction, finally blocks propagation of the discontinuity and triggers the evolution of *unphysical* diffuse localization patterns, see Figure 6.23d–f. These localization patterns are characterized by inconsistent orientation of the respective GAUSS point discontinuity normals.

It is important to note that this pathological behavior can only to a very limited extent be alleviated by a refined discretization of the problem, as an illustration of the principal structural load carrying behavior innervates. Figure 6.22 schematically sketches the flow of forces through the structure by means of a simplified strut and tie model. The important aspect is that due to the presence of the notch, the lower tie, representing the tensile zone induced by bending, cannot proceed horizontally. This, on the other hand, entails the necessity of a vertical tie positioned right above the notch in order to bybass it.

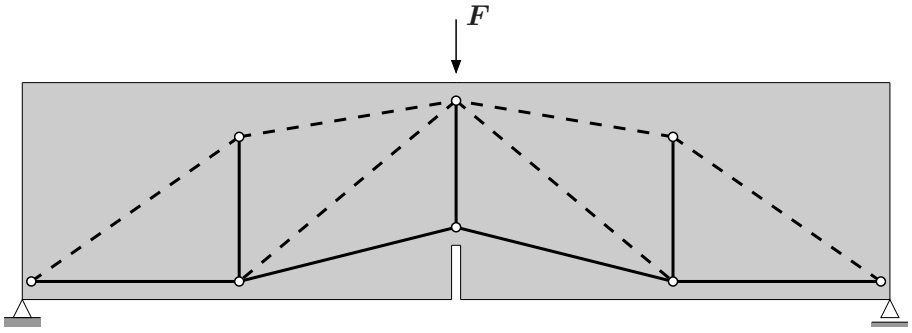

Figure 6.22: Three point bending test. Principal load carrying scheme illustrated by a simplified strut (dashed lines) and tie (solid lines) model.

The effect is even amplified if starting from the notch tip a vertically propagating localization path forms, such that the capacity of horizontal tensile stress stress transfer is continuously

decreased — which would correspond to an extension of the notch; propagation therefore additionally boosts the "by-passing effect".

These considerations clarify, that presence of the notch (or corresponding localization zone) indeed induces the formation of a predominantly vertically aligned tensile band above the notch region. At a later loading stage these tensile strains may increase in such a way that they even are responsible for localization initiation, giving rise to a nearly horizontally aligned discontinuity ahead of the vertically aligned macroscopic discontinuity. In the context of the FDA such a situation then would completely block propagation of the macroscopic discontinuity. Figure 6.23f indeed illustrates the situation, where at the front of the localization zone almost horizontally aligned GAUSS point discontinuity planes have formed. Moreover, the image of inclined lower ties (Figure 6.22) also illustrates that corresponding tensile strains and stresses are not necessarily perfectly horizontal at the onset of localization.

In summary, the observations further encourage the perviously motivated notion (cf. Section 5.3.3) that identification of the macroscopic discontinuity direction based on the local strain states at the onset of localization — as it is the case for the considered fixed discontinuity approach — is not an appropriate means; instead the procedure is very likely to introduce locking effects which can easily yield spurious localization patterns.

6.3.3 Hybrid discontinuity approach

Since the so far observed behavior for the fixed discontinuity concept exactly reflects the considerations which led to the development of the hybrid discontinuity concept, it is interesting to shed some more light on the behavior of the hybrid approach for this example.

In dependence on the discussion given in Section 5.3.3, the advocated hybrid approach distinguishes between *initation phase* and *propagation phase*. During the initiation phase, the microscopic character of the discontinuity is accounted for by permitting continuous adaptation of the discontinuity direction to the possibly rotating direction of maximum principal strain. This characteristic is maintained until a threshold, marking the onset of the propagation phase, is passed, cf. equation (5.62). Not until this point, the discontinuity is considered as macroscopic and its orientation remains fixed.

Closer investigation reveals that the hybrid approach resolves previously observed problems of locking and spurious localization. As evidenced by Figure 6.24a–c, the approach facilitates the alignment of GAUSS point related discontinuity planes with the vertical macroscopic discontinuity path in the process of further loading. As a consequence, locking effects are avoided and localization propagates towards the point of load application along the expected vertical path.

Figure 6.25 illustrates the progress of localization at the final loading state of $u = 0.5\ mm$. A unique localization pattern along the expected vertical path is observed. As can clearly be seen, at this state of loading almost all deformation is concentrated into the localization zone, which indicates a strong degree of energy dissipation as a result of the localization process.

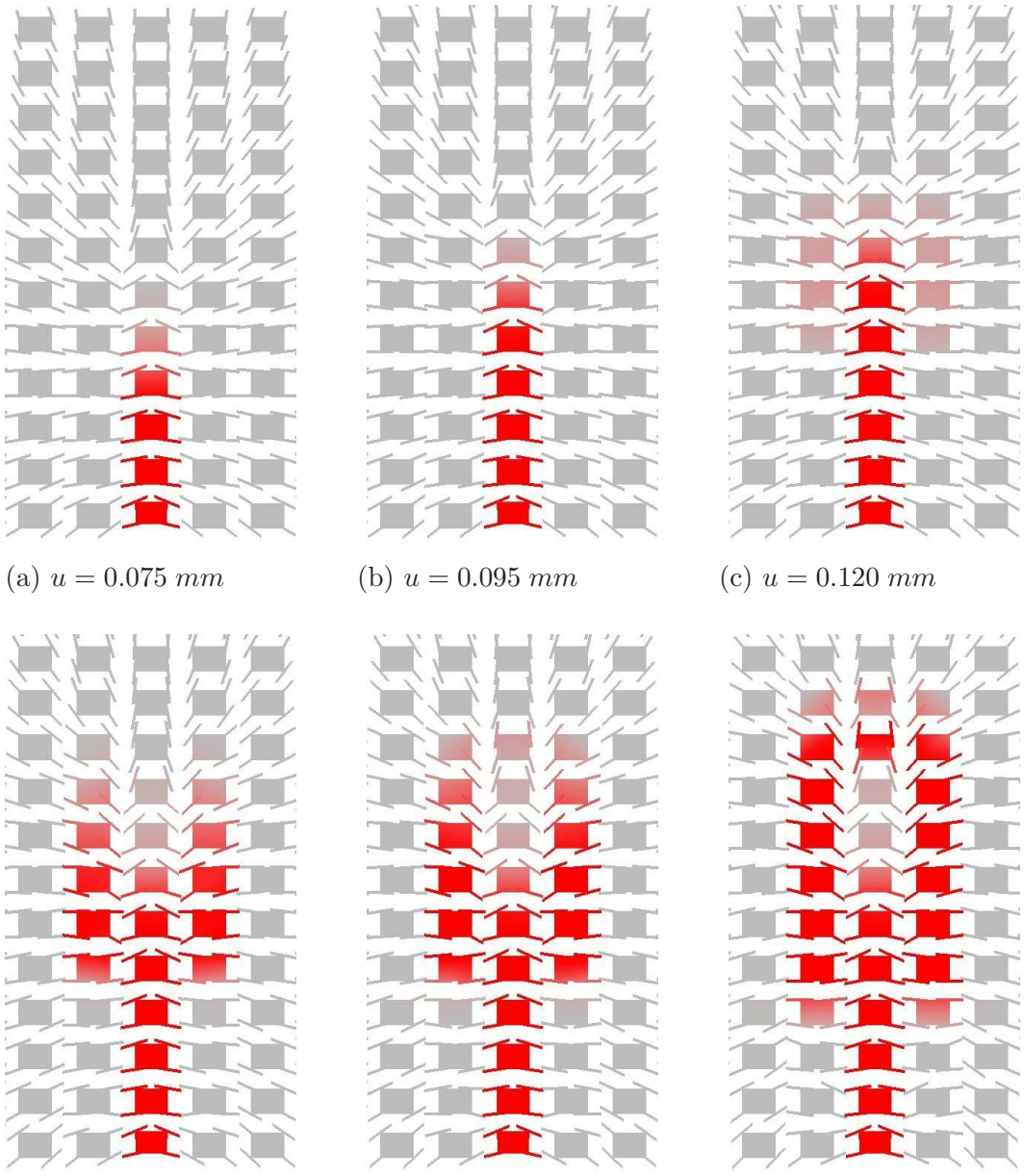

(a) $u = 0.075\ mm$ (b) $u = 0.095\ mm$ (c) $u = 0.120\ mm$

(d) $u = 0.145\ mm$ (e) $u = 0.158\ mm$ (f) $u = 0.195\ mm$

Figure 6.23: Three point bending test, fixed discontinuity approach. Spurious localization evolves as a result of constrained adaptation of discontinuity orientation, leading to severe stress-locking effects. (a)–(f) GAUSS points in the vicinity of the localization domain illustrating localization patterns at various loading stages. Lines indicate normal directions of actual and potential localization planes (direction of maximum principal tensile strain).

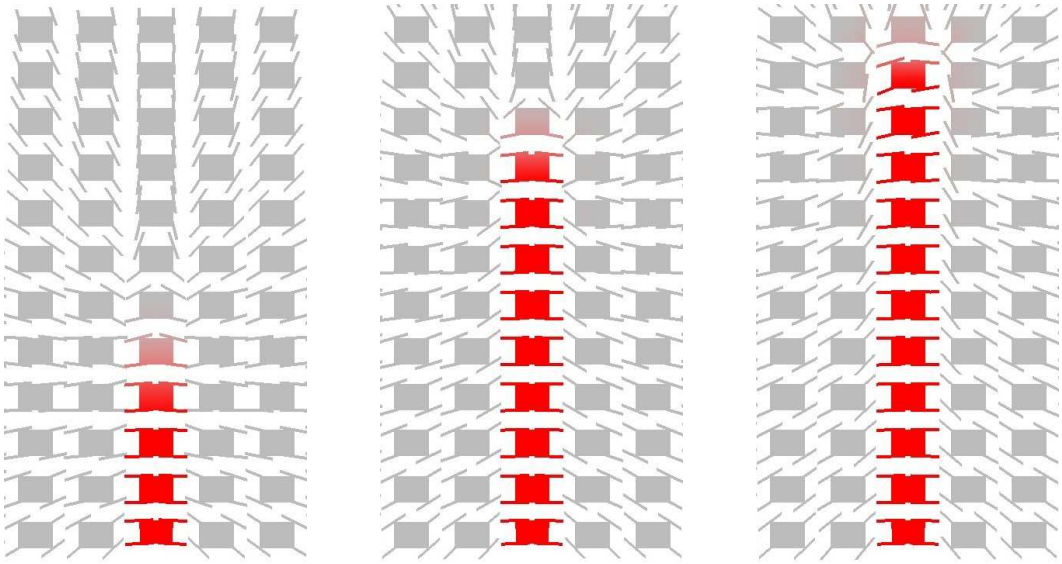

(a) $u = 0.075\ mm$ (b) $u = 0.145\ mm$ (c) $u = 0.195\ mm$

Figure 6.24: Three point bending test, hybrid discontinuity approach. Correct representation of macroscopic discontinuity orientation by orientation adaptation of microscopic discontinuity planes, facilitating locking free propagation of the macroscopic discontinuity. (a)–(c) GAUSS points in the vicinity of the localization domain illustrating localization patterns at various loading stages. Lines indicate normal directions of actual and potential localization planes (direction of maximum principal tensile strain).

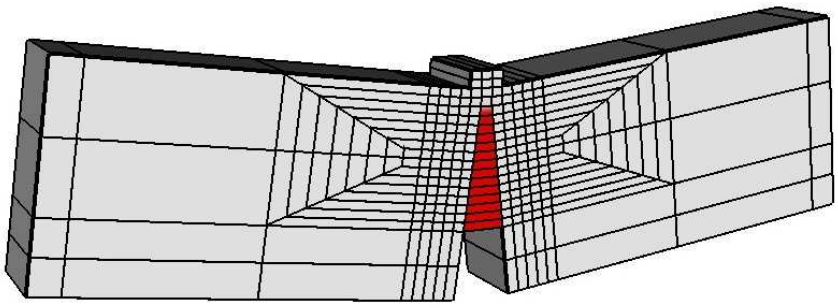

Figure 6.25: Three point bending test, hybrid discontinuity approach. Deformed configuration at final loading state $u = 0.5\ mm$ (displacements scaled by a factor of 250).

The advocated hybrid approach accounts for the multi-level character of the formation process of a macroscopic discontinuity and, in conclusion, facilitates a locking-free self propagation of the localization zone.

6.4 L-shaped panel

The L-shaped panel test has become a standard benchmark for validation of computational models aiming at the numerical simulation of brittle, predominant mode-I failure. It has been investigated by numerous researchers, both experimentally and numerically (e.g., Lackner [66], Mosler [75], Oliver et al. [89] and Feist [41]).

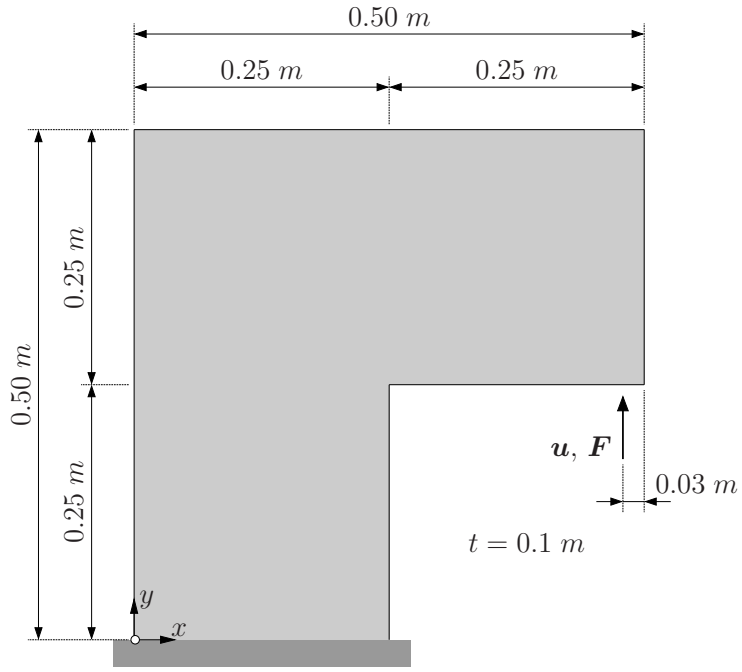

Elastic properties:		
Young's modulus	$E =$	$25850.0\ MPa$
Poisson's ratio	$\nu =$	0.18
Exponential softening law:		
Tensile strength	$f_{\mathrm{tu}} =$	$2.7\ MPa$
Fracture energy	$G_f =$	$0.065 - 0.090\ kNm/m^2$

Figure 6.26: L-shaped panel: System configuration and material properties according to Winkler [131].

Numerical analyses carried out subsequently are based on the setting adopted by Winkler [131] for his test series A, which were executed on a plain concrete test specimen. Winkler's

experimental results have also been incorporated into the data base, set up by the Task Group 2.2 of the EU-*Network Integrity Assessment of Large Concrete Dams (IALAD)* [3].

The system setup and material properties determined by WINKLER [131] are given in Figure 6.26. The lower horizontal edge of the specimen is clamped. A vertically acting point load F is applied under displacement control at a distance of 30 mm to the end of the horizontal leg. The chosen shape and loading conditions effect the onset of localization at the re-entrant corner. Upon further loading, the localization zone (crack) starts to propagate into the interior of the plate. As opposed to preceding examples, which yielded planar localization zones, for the present case a curved shape is expected. Due to the — with regard to the panel's boundaries — non-aligned principal stress state prevailing in the vicinity of the re-entrant corner, the localization zone initially propagates towards the interior of the plate at an angle. At later loading stages progress is nearly horizontal. This behavior is also confirmed experimentally, a detailed description of the observed crack propagation process is given in WINKLER [131].

The objective of the present investigation covers two aspects. First, the capability of the proposed p-adaptive ESD formulation to reproduce a curved discontinuity shall be assessed. Of particular interest in this context is the evaluation of mesh bias sensitivity. As, e.g., reported by LACKNER [66] and WINKLER [131] the numerically obtained crack paths are to a strong degree attracted by the horizontal mesh lines and fall short of reproducing the theoretical — and experimentally confirmed — initially curved shape of the localization zone. As for the second aspect, the available test data also facilitates a quantitative conclusion regarding the quality of simulated structural load carrying capacity and post-peak response.

For the analyses, again a three-dimensional finite element discretization using hexahedral elements is adopted. Three different finite element meshes, illustrated in Figure 6.27, are employed. All simulations are performed under displacement control using a constant increment size of $\Delta u = 0.01\ mm$. Since the investigation is not aiming at best possibly fitting the numerical analyses to the experimentally obtained data, from the reported rather wide scatter for the fracture energy $G_f = 0.065 - 0.09\ kNm/m^2$ simply an intermediate value of $G_f = 0.075\ kNm/m^2$ is chosen and retained unchanged for all analyses.

6.4.1 Low-order polynomial approximation of the regular displacement field

A first approach of the problem is based on simulations employing the three different finite element meshes M-434, M-857 and M-1315 (Figure 6.27) along with a constant degree of $p = 1$ for the polynomial approximation of the regular displacement field. The obtained numerical responses are illustrated in Figure 6.28, where the applied load F is plotted over the vertical displacement u at the point of load application. It emerges that analyses carried out on the refined meshes M-857 and M-1315 yield almost identical response, with a somewhat increased load carrying capacity and a slightly more pronounced ductile post-peak behavior than analysis M-434. When compared to the experimental spectrum documented by IALAD,

[3] NW-IALAD Network Integrity Assessment of Large Concrete Dams. `http://nw-ialad.uibk.ac.at`

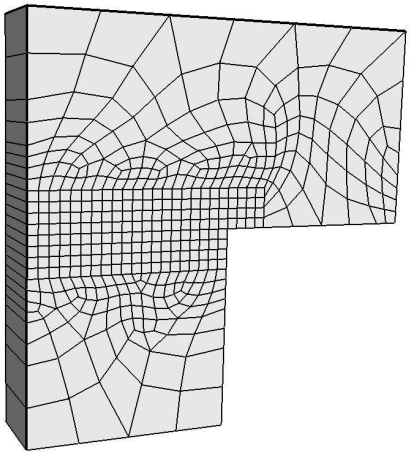

(a) M-434

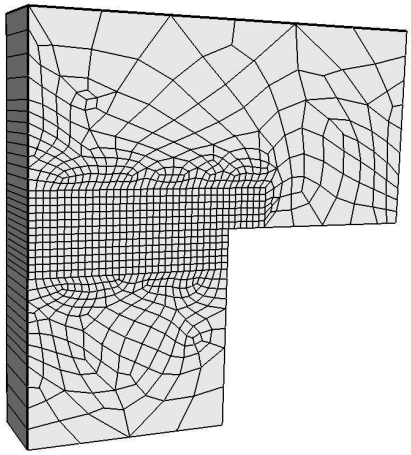

(b) M-857

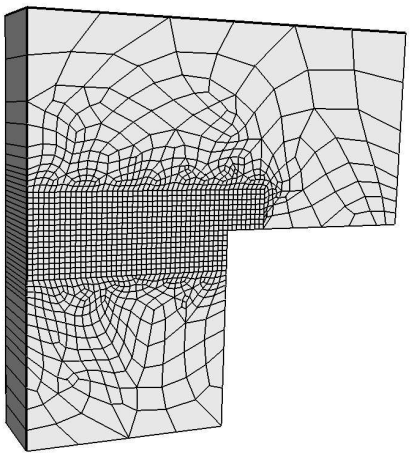

(c) M-1315

Figure 6.27: L-shaped panel, three-dimensional discretization. Finite element meshes with (a) 434, (b) 857 and (b) 1315 hexahedral elements.

cf. Figure 6.28, the numerically computed load carrying capacity complies remarkably well in all three cases.

Investigation of the numerically identified localization zones — which represent the physical crack paths — reveals that analysis M-434 fails to reproduce the curved shape of the crack path in the vicinity of the re-entrant corner. The simulated localization zone extends from the corner towards the opposite edge in a horizontal manner aligned with the finite element mesh, see Figure 6.29b. The reason for this behavior is twofold. First, the chosen discretization is not capable of resolving the stress and strain state around the re-entrant corner sufficiently fine. In effect, localization planes associated with the respective GAUSS points at the onset of cracking are almost horizontal. Furthermore, due to the limited kinematic capabilities of finite elements with low-order polynomial approximation of the regular displacement field, once a localization plane at an element's GAUSS point is activated, orientation of the plane

tends to dominate the behavior of the whole finite element. Therefore, if the initial direction of the localization plane is aligned or almost aligned with the element edges, propagation of the discontinuity is prone to follow the orientation of the finite element mesh. This effect is frequently referred to as *mesh bias*, see e.g., JIRÁSEK [59].

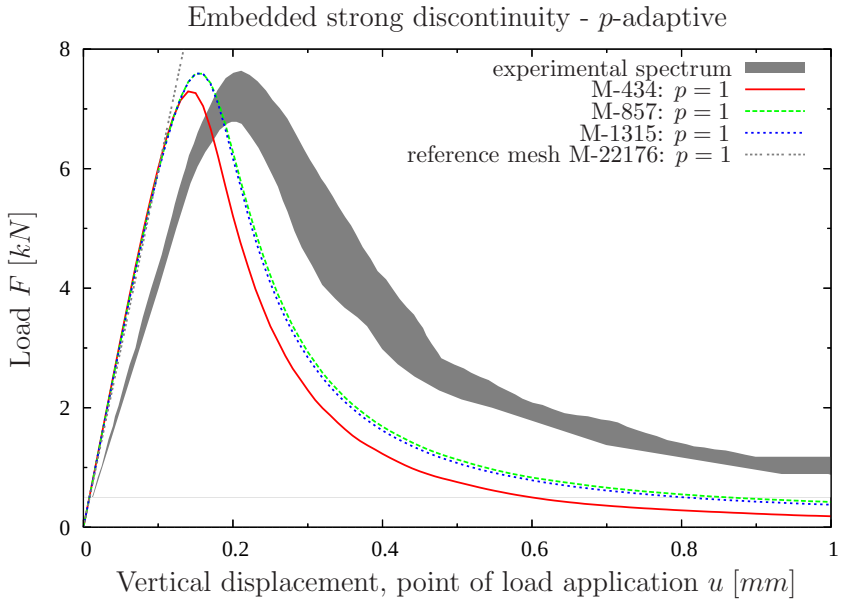

Figure 6.28: L-shaped panel, load vs. vertical displacement at the point of load application. Illustration of the computed numerical response for meshes M-434, M-857 and M-1315 using polynomial degree $p = 1$ for the approximation of the regular displacement field; experimental spectrum according to IALAD. Elastic stiffness obtained from reference solution using 22176 hexahedral elements and $p = 1$.

With further refinement of the finite element mesh, the strain and stress states leading to onset of localization are approximated increasingly more accurate, such that the unfavourable mesh bias effect is partially overcome. This notion is supported by the simulated localization zones using the refined meshes M-857 and M-1315, see Figures 6.29c and 6.29d. Still, in evidence there is some remaining alignment of the numerical localization zone to the element topology in the vicinity of the re-entrant corner. In agreement with the already observed almost identical response of analyses M-857 and M-1315 (Figure 6.28), also the computed shapes of the respective localization zones show no qualitative difference, cf. Figures 6.29c and 6.29d.

It is noticeable that the simulated initial pre-peak response is considerably stiffer than the experimentally observed one; a fortiori, if one considers the initial loading stage to be ruled by predominantly linear elastic material behavior, where localization effects are yet of minor significance. In order to exclude locking effects due to insufficient resolution of the descretized system, a convergence study for the linear elastic case is performed; on the one hand by increasing the order of polynomial approximation p for the regular displacement field and on the other hand by h-refinement of the employed finite element mesh. As a result, it is concluded that analysis based on the chosen discretizations M-434, M-857 and M-1315 using

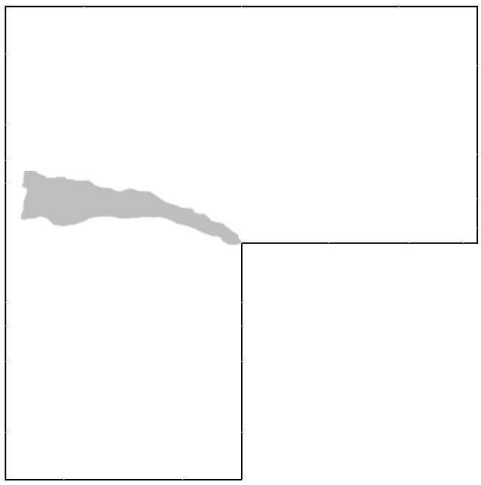

(a) experimental scatter

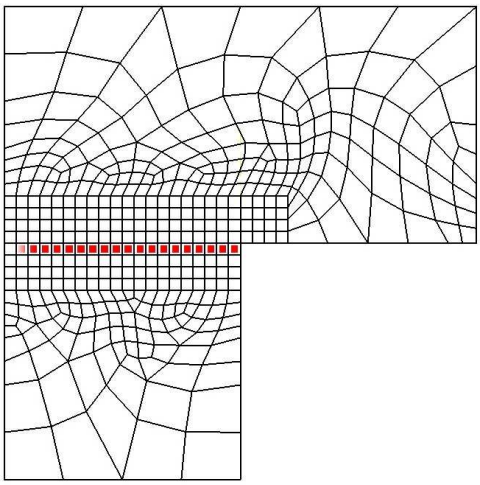

(b) M-434: $p = 1$

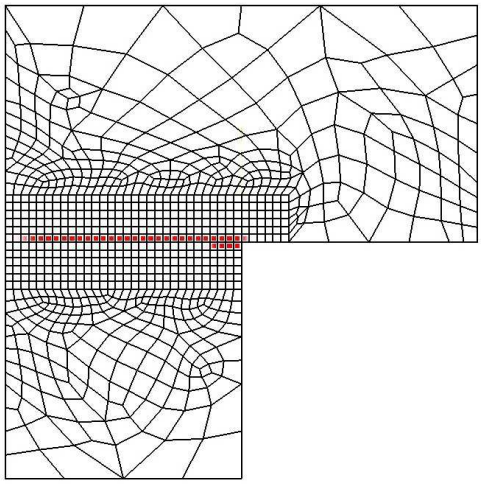

(c) M-857: $p = 1$

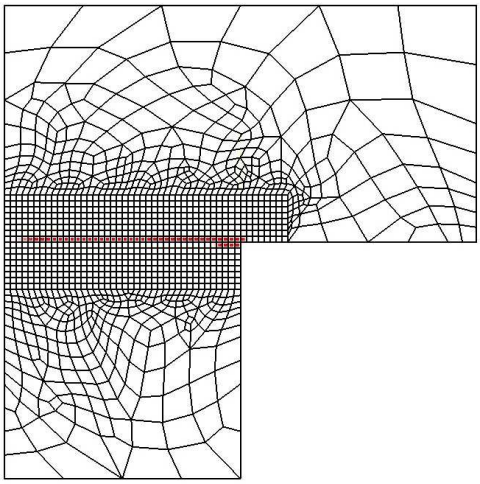

(d) M-1315: $p = 1$

Figure 6.29: L-shaped panel, numerically obtained crack patterns for finite element mesh M-434, M-857 and M-1315 using order of polynomial approximation $p = 1$ for the regular displacement field.

a polynomial degree of $p = 1$ indeed approximates the initial elastic stiffness fairly well. For comparison, the linear elastic response obtained from a reference mesh with 22176 hexahedral elements, arranged in three layers over the thickness of the panel, using $p = 1$ is plotted in Figure 6.28.

From this investigation, it is also confirmed that stress evolution in thickness direction of the panel is of minor relevance, so that the plane stress assumption made by other analysts, see e.g., [131], [89] and [41], poses an admissible simplification. In conclusion, differences regarding the initial slope between analysis and experimental results cannot be explained by numerical errors due to locking effects or insufficient refinement of the discretization; using the *given material properties*, it is believed that the initial stiffness of the structure is reproduced correctly by the chosen discretizations. Hence, for the following investigations, no attempt is made to adapt the numerical solution to the experimentally obtained initial stiffness.

6.4.2 Discontinuity tracking

As set out in Chapter 4, the strain induced by the occurrence of displacement jumps is incorporated as incompatible *elemental enrichment* within the framework of enhanced assumed strain methods. The embedded strong discontinuity approach therefore correctly captures the effect of a discontinuity intersecting a finite element on the displacement field. Due to the incompatible character of the enrichment, however, an inter elemental geometric continuity of the discontinuity surface is external to the assumptions of the embedded strong discontinuity approach.

In the context of fixed discontinuity approaches using low-order finite elements, the element local character of the enrichment may trigger kinematic incompatibility of neighboring finite elements, which may lead to severe locking, see, e.g., Jirásek [52], Wells [128].

As a remedy to avoid these situations and at the same time alleviate mesh bias effects mentioned above, strategies aiming at the reestablishment of a geometrically continuous discontinuity path have been devised and applied in the context of low-order finite element approximations. These strategies commonly go by the name *tracking strategies*. Concepts can be distinguished into *local* and *global* tracking strategies, respectively (Oliver et al. [91]), and hybrid methods (Feist [41]).

It is emphasized that these strategies are extraneous to the embedded strong discontinuity approach and rely on nonlocal information, i.e., information in addition to the one supplied by the considered material point and finite element, respectively.

Subsequently, a short highlight of the different strategies' essential characteristics shall be given.

Provided that information about the direction of propagation is given for all finite elements, the local tracking strategy traces the discontinuity starting from a root element, where localization was triggered, by exploiting knowledge about the element connectivity. This method

is reported to be robust for two-dimensional cases exhibiting a single discontinuity line, in case of three-dimensional settings, however, huge topological difficulties are encountered [91] and this strategy is not practically applicable.

The global tracking strategy, on the other hand, relies on the establishment of a global potential field from the likewise globally held information about the direction of propagation. The potential field is constructed such that level sets then represent all admissible discontinuity surfaces [91]. This strategy is consistently applicable both in two-dimensional and three-dimensional settings, it is, however, not free of stability problems [41]. Moreover, computational effort is increased considerably, since for every time increment identification of the corresponding potential field requires the solution of a set of partial differential equations which is in formal analogy to a stationary heat conduction boundary value problem [91].

The hybrid approach proposed by Feist [41] and applied in a two-dimensional setting, finally, maintains the idea of the global tracking strategy, but circumvents the need for solution of a large system of equations by also incorporating information about the element connectivity. The algorithm is, however, to a fairly strong degree dependent on the topology of the adopted type of finite element and likewise not easily extended to three-dimensional situations. Additional expense is entailed by the fact that required information about the direction of propagation is established by a nonlocal averaging procedure. This procedure is based on the cognition that the strain and stress states computed locally at a material point only represent a crude approximation to the actual ones, e.g., Jirásek & Zimmermann [60], therefore calculation of the direction of propagation based on local information only, can lead to locally erroneous results (Feist [41]).

The bottom line of the diverse tracking strategies can be described as the identification of those material points and corresponding directions for which localization is considered feasible in order to ensure a continuous localization path. In essence, tracking procedures are means to restrict the occurrence of localization to those elements or material points which are indicated by the algorithm. Implicitly, this also may lead to exclusion zones in which localization, e.g., due to secondary cracking, is artificially prevented.

The overall rather expensive character of discontinuity tracking strategies, has triggered recent research efforts towards formulations that aim at circumventing the need for those strategies, see, e.g., Oliver et al. [90], Sancho et al. [107, 106, 108]. Also from a theoretical point of view, it is not obvious that localization path continuity must be *enforced* in order to provide for a meaningful discontinuity propagation and avoid locking.

In fact, as for the proposed p-adaptive ESD approach we devise the expectancy that *enforcement* of a continuous localization path is dispensable for the following reasons:

- Raising the order of polynomial approximation for the regular displacement field provides for an increased quality of resolution of strain and stress states. Therefore, localization initiation is expected to be captured with increased precision both regarding the onset of localization and its direction of propagation. This holds in particular, when compared to approaches based on constant strain finite element discretizations.

- Due to the increased kinematic capability, higher-order finite elements are much less prone to locking behavior. As discussed in preceding examples, the proposed p-adaptive ESD formulation facilitates a concentration of the localization zone to a portion of the element. Shape of the discontinuity path is therefore less sensitive to mesh topology. In consequence, mesh bias issues are anticipated to have an inferior impact.

- The advocated concept of a combined rotating – fixed discontinuity approach (cf. Sections 5.3 and 6.3) allows for initial secondary cracking without prevention of macroscopic crack propagation.

6.4.3 Higher-order polynomial approximation of the regular displacement field

In order to shed further light on the expectations motivated in the preceding section, the numerical study of the L-shaped panel is continued by increasing the order of polynomial approximation p for the regular displacement field.

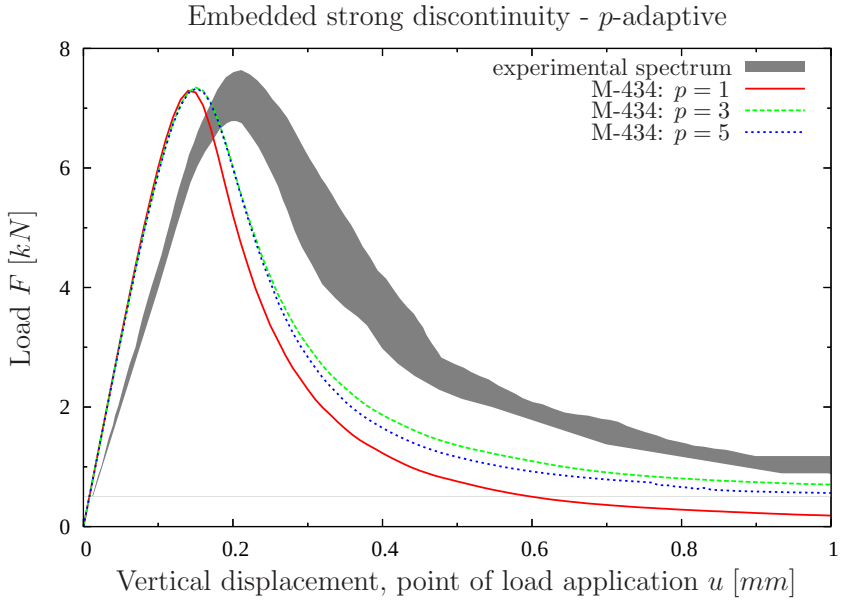

Figure 6.30: L-shaped panel, load vs. vertical displacement at the point of load application. Illustration of the computed numerical response for mesh M-434 using polynomial degree $p = 1$, $p = 3$ and $p = 5$ for the approximation of the regular displacement field; experimental spectrum according to IALAD.

Starting with finite element mesh M-434, the respective response curves obtained for polynomial degree $p = 3$ and $p = 5$ show a very similar post-peak behavior, see Figure 6.30. When compared to the response obtained by adopting $p = 1$ on the same mesh, post-peak behavior proves to be slightly more ductile for the higher-order polynomial approximations. The simulated load-carrying capacity is marginally increased (Figure 6.30).

As for the refined meshes M-857 and M-1315 the situation is similar. Increasing the order of polynomial approximation yields a more pronounced ductile post-peak behavior and at the same time the predicted load carrying capacity is slightly reduced when compared to the respective analyses with polynomial degree $p = 1$ (Figure 6.31). The slight reduction in load carrying capacity for the higher-order p analyses can be attributed to the improved numerical resolution of the localization initiation process. Notably, computed responses for all higher-order p analyses show a convergent behavior, manifested by good correspondence of the obtained response curves, cf. Figure 6.31. The computed load carrying capacity of $\sim 7.4\ kN$ fits the experimentally observed range very well (Figure 6.31).

Assessing the simulated localization patterns, it is observed that the expected curved shape of the localization path in the vicinity of the re-entrant corner is resolved considerably better with higher-order polynomial approximations p of the regular displacement field. Adopting a polynomial degree of $p = 3$ on the initial mesh M-434 features already a significantly improved representation of the localization path (Figure 6.33c) — even when compared to patterns obtained by low-order polynomial approximations $p = 1$ on the *refined* meshes (Figures 6.34b and 6.35a). This observation also holds for the simulated structural response: Even a moderate increase of the order of polynomial approximation from $p = 1$ to $p = 3$ leads to an almost congruent prognosis of structural load carrying capacity and very similar post-peak responses for all three investigated finite element meshes, cf. Figure 6.32.

The already constituted convergent behavior of the response curves is also reflected in the obtained localization patterns for the analyses on refined meshes M-857 and M-1315. As Figures 6.34c, 6.34d and 6.35b illustrate, the respective shapes of localization zones are nearly identical — moreover, they represent a fairly good approximation to the experimental scatter according to IALAD (Figure 6.34a). The slightly increased ductility in response, inherent to the analyses with higher-order polynomial approximation p, can be attributed to the improved resolution of the localization path and is likewise supported by experimental data.

Figure 6.36 exemplarily depicts the deformed configurations at the final loading state $u = 1\ mm$, obtained from meshes M-857 and M-1315 using an order of polynomial approximation of $p = 5$ and $p = 3$, respectively. It is evident that almost all deformation concentrates into the localization zone. The portions of the panel (almost) separated by the localization zone essentially undergo rigid body motion — indicating that the stored energy is dissipated almost completely by the localization process.

In conclusion, the performed analyses support the assumptions set forth above. Raising the order of polynomial approximation for the regular displacement field significantly enhances the quality of the predicted shape of the localization zone, fairly insensitive to mesh topology. No locking effects are observed and the solution shows a convergent behavior both regarding structural response and predicted localization pattern. The important point is, that this is achieved while maintaining a high degree of locality of the algorithmic formulation — in fact, the only nonlocal ingredient is the smoothed transmission function $\overline{\boldsymbol{\nabla}\varphi}_h$ according to (5.15), which still is of element local character. The proposed p-adaptive ESD formulation dispenses with algorithmically and computationally elaborate, highly nonlocal tracking strategies, instead a self propagating discontinuity can be established.

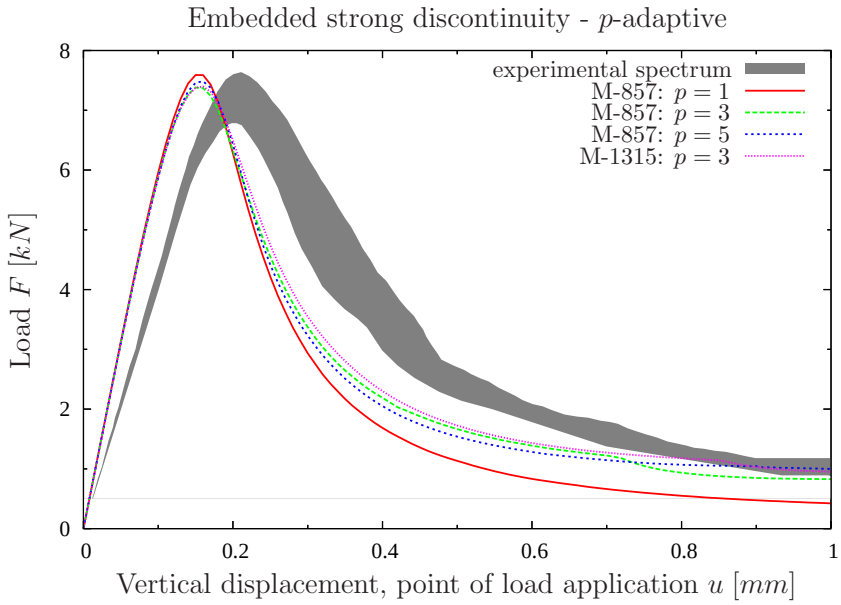

Figure 6.31: L-shaped panel, load vs. vertical displacement at the point of load application. Illustration of the computed numerical response for refined meshes M-857 and M-1315 with increasing order of polynomial approximation for the regular displacement field; experimental spectrum according to IALAD.

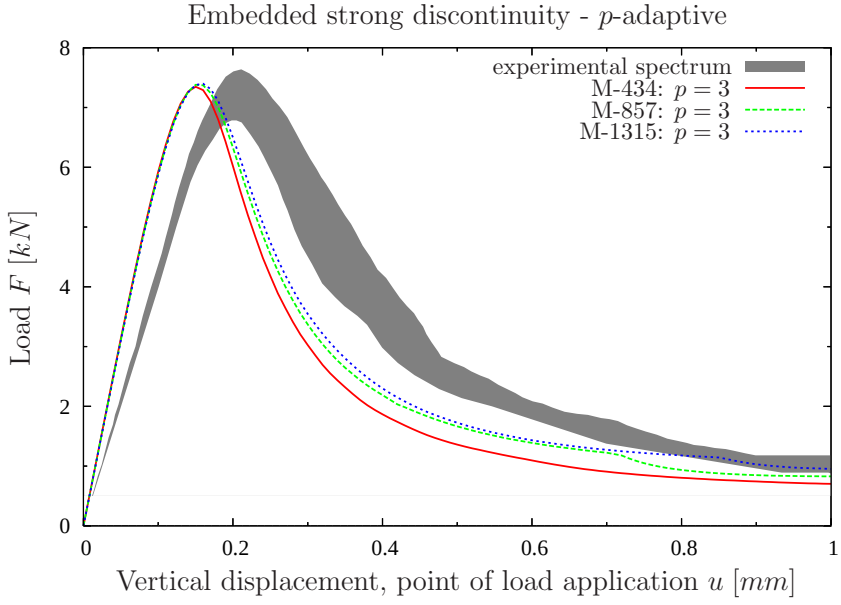

Figure 6.32: L-shaped panel, load vs. vertical displacement at the point of load application. Illustration of the computed numerical response for meshes M-434, M-857 and M-1315 using polynomial degree $p = 3$ for the approximation of the regular displacement field; experimental spectrum according to IALAD.

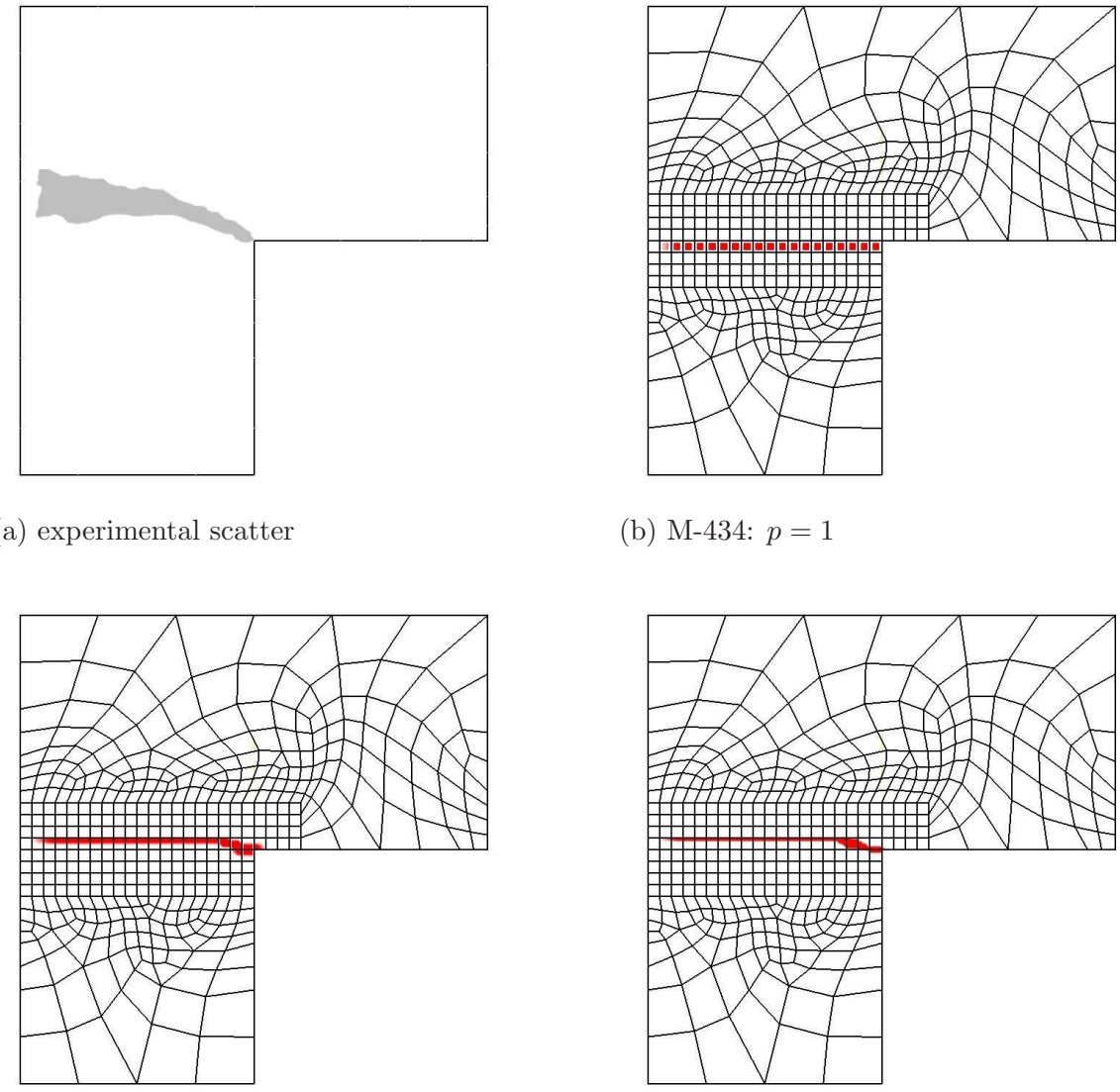

(a) experimental scatter

(b) M-434: $p = 1$

(c) M-434: $p = 3$

(d) M-434: $p = 5$

Figure 6.33: L-shaped panel, numerically obtained crack patterns for finite element mesh M-434 and varying order of polynomial approximation $p = 1$, $p = 3$ and $p = 5$ for the regular displacement field.

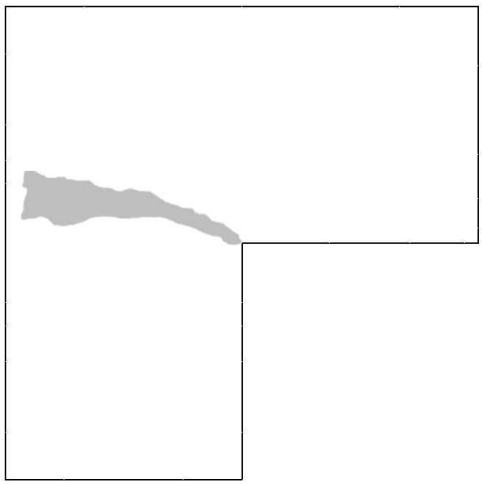

(a) experimental scatter

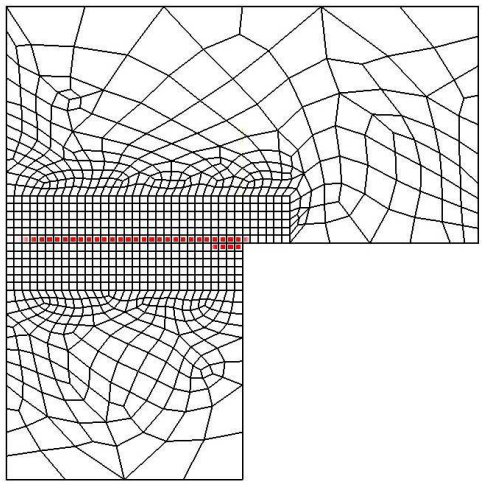

(b) M-857: $p = 1$

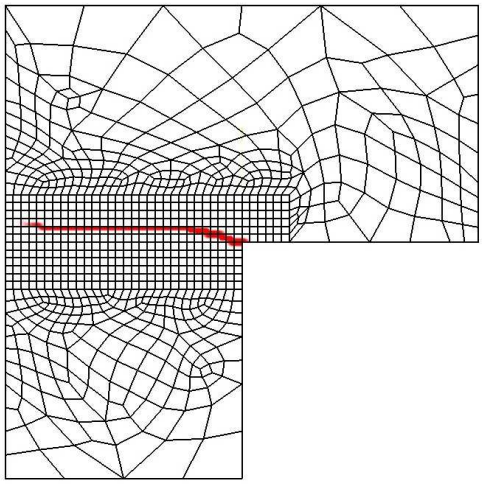

(c) M-857: $p = 3$

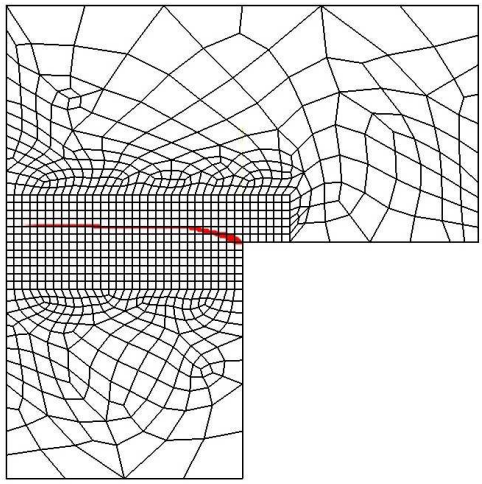

(d) M-857: $p = 5$

Figure 6.34: L-shaped panel, numerically obtained crack patterns for finite element mesh M-857 and varying order of polynomial approximation $p = 1$, $p = 3$ and $p = 5$ for the regular displacement field.

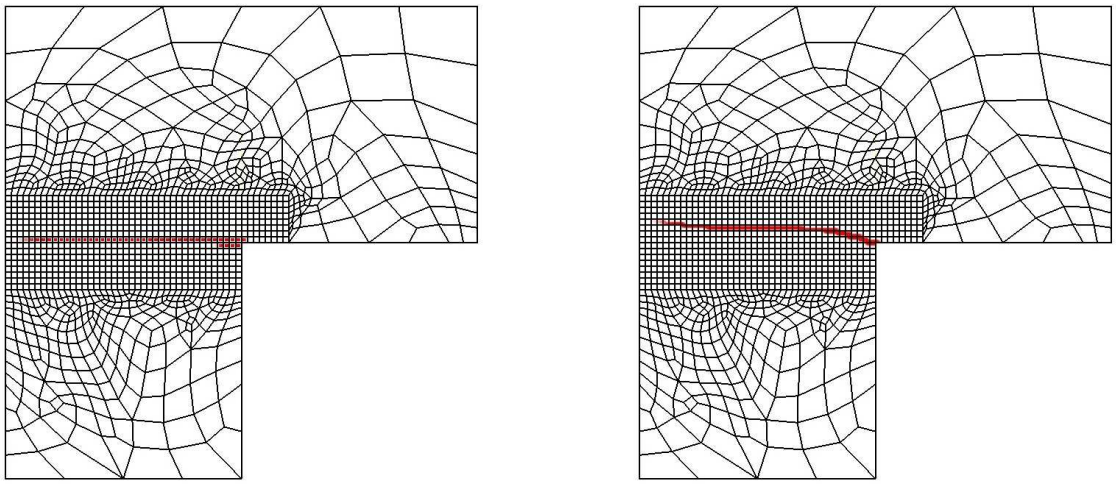

(a) M-1315 $p = 1$ (b) M-1315: $p = 3$

Figure 6.35: L-shaped panel, numerically obtained crack patterns for finite element mesh M-1315 and varying order of polynomial approximation $p = 1$, $p = 3$ for the regular displacement field.

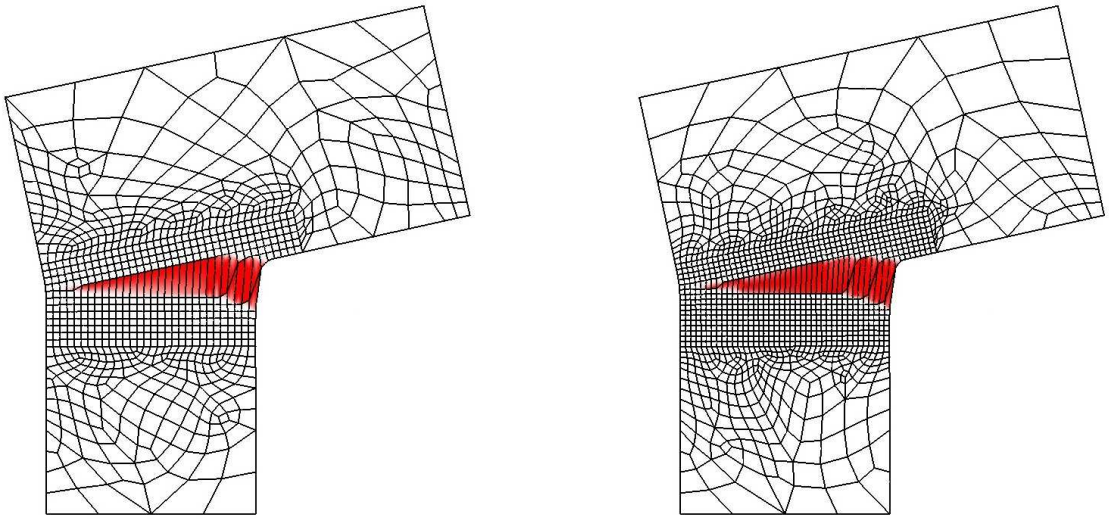

(a) (b)

Figure 6.36: L-shaped panel, deformed configuration at final loading state $u = 1\ mm$ for (a) mesh M-857 with a polynomial degree of $p = 5$ for the approximation of the regular displacement field and (b) M-1315 with a polynomial degree of $p = 3$ for the approximation of the regular displacement field (displacements scaled by a factor of 100).

In order to give an idea of the number of degrees of freedom and corresponding computational cost, Figure 6.37 compares the observed CPU times for various refinement degrees and order of polynomial approximation. It should be noted, however, that the number of corresponding linear equation system solution sequences considerably scatters as a result of the iterative solution procedure (cf. also the discussion in Section 5.2.3.1). Therefore, assessment of these numbers should be made with care.

M-434	DOF	CPU-time [s]	time/DOF [s]
$p = 1$	2770	862	0.31
$p = 3$	5842	6428	1.10
$p = 5$	11026	34781	3.15

M-857	DOF	CPU-time [s]	time/DOF [s]
$p = 1$	5362	2475	0.46
$p = 3$	12082	16448	1.36
$p = 5$	11186	35021	3.13

M-1314	DOF	CPU-time [s]	time/DOF [s]
$p = 1$	8134	4242	0.52
$p = 3$	19910	37761	1.90

Figure 6.37: CPU-times for various refinement degrees and order of polynomial approximation p

Chapter 7

Conclusive remarks

Daring ideas are like chessmen moved forward;
they may be beaten but they may start a winning game.
– Johann Wolfgang von Goethe.

Today, the finite element method along with its various specifications is an indispensable tool in many engineering disciplines. As computer power increases and numerical models get further refined, its field of application is extended more and more towards complex scenarios — with the goal of highly realistic simulations of the underlying physical or chemical processes. In the field of structural analysis, which was focused in this work, safety and profitability issues determine the increasing importance of numerical assessment of structural failure or failure of structural components. To this end, the extension of modeling approaches is required with respect to loading regimes far beyond the spectrum of serviceability loads.

The present work concentrated on material induced failure phenomena. Closer investigation of these processes reveals, that failure is often preceeded by the formation of a process zone in which damage and other inelastic effects accumulate, and in which high strain gradients prevail. As illustrated in Chapter 1, it is this phenomenon of *strain localization* or *deformation localization* which substantiates the insufficiency of the classical continuum mechanical approach to this class of problems. Modeling approaches to overcome this deficiency are presently almost exclusively developed in a low-order, mostly constant-strain, finite element framework. Investigations for linear and nonlinear elliptic boundary value problems, however, have shown that high-order finite elements yield very efficient discretizations when compared to low-order h-version finite element approximations [37, 38, 36, 97, 84]. So, it was two essential aspects that constituted the motive force for this work:

- The argument, that it is not only desirable from an academic point of view to extend the scope of high-order finite elements to the field of deformation localization and material failure and

- the notion, that a high-order finite element approximation, due to its robust and rich kinematics, is qualified to contribute to an effective *locking-free* modeling approach also for the considered problem field of deformation localization and material failure.

Consistent advancement of both thoughts finally led to the development of the proposed p-adaptive embedded strong discontinuity formulation (Chapter 4).

- With particular focus on large scale analyses, a macroscopic view of the failure process was adopted; leading to enhancement of the classical continuum model by the possible incindence of *strong discontinuities*, i.e., jumps in the displacement field. This procedure also reflects the multi-scale character of the failure process.
- The effect of these discontinuities was incorporated into the three-dimensional finite element formulation in terms of an *element enrichment*; this mathematical incorporation offers the particular advantage of a widely discontinuity independent finite element topology; it dispenses, e.g., with elaborate mesh adaption strategies [66]. The variational framework for this formulation is posed by the generalized Hu-Washizu functional and closely follows the concept of *enhanced assumed strains*.
- As opposed to previous works, a consistent formulation regarding the adoption of a *high-order* finite element basis was established as a generalization of the standard approach. It could be shown that the commonly accepted strategy for incorporation of strong discontinuities is no longer sufficient in a generalized context. The extended p-adaptive formulation was then deduced based on a novel reassessment of the strong discontinuity kinematics.
- The formulation is cast on continuum level, which features an efficient elimination of the additional degrees of freedom, associated with strong discontinuities, already within the scope of the constitutive algorithm.

The p-adaptive embedded strong discontinuity approach was then specialized for the case of brittle predominant mode-I material failure in Chapter 5. Accounting for the multi-phase character of the failure zone formation process, the idea of a *hybrid discontinuity approach* was developed. Numerical examples presented in Chapter 6, demonstrate the advocated approach's consistency in a high-order finite element framework. In interaction with the *hybrid discontinuity* concept, an approach was established that allows for a virtually locking-free softening response. Notably, the algorithmic formulation maintains a high degree of locality and does *not* rely on elaborate strategies of highly nonlocal character. A benchmark simulation of a plain concrete test, not only supports validity of the model, it also confirms that *mesh bias* issues are significantly alleviated by increasing the polynomial order of displacement approximation. Finally, as the example illustrates, high-order p-extensions yield a superior resolution of the failure process compared to corresponding low-order finite element approaches.

Future directions

Inspired by the work on this topic and based on the findings of this thesis, several aspects of desirable future research evolve:

- **Extension of the material model**
  The present model for brittle predominant mode-I material failure could be adapted to a more realistic representation of plain concrete characteristics. This could as a first step, e.g., involve the incorporation of damage effects on the elastic stiffness which would extend the range of application from montonic to cyclic loading conditions. As a second aspect, of course, combination with nonlinear response under compressive stress states would have to be considered. Furthermore, range of application could be extended in a straight-forward manner to a different context by accounting for situations of predominant mode-II or combined mode material failure; as it is, e.g., the case in shear banding in metals or soils.

- **Algorithmic variation**
  Instead of casting the p-adaptive embedded strong discontinuity approach in a pure continuum format, the enhanced degrees of freedom of the GAUSS point associated discontinuities could be treated on element level in analogy to the *enhanced assumed strain* approach. Though this would entail the necessity of statical condensation of the enhanced degrees of freedom on element level, such a procedure could be beneficial for the performance of the solution process since then a consistent linearization of the problem is feasible.

- **Extension to a finite deformation setting**
  Due to the fact that in many cases structural failure is accompanied by large deformations, it appears reasonable to extend the approach to the geometrically nonlinear case.

- **Enrichment based on the *partition-of-unity* concept**
  A completely different strategy is provided by the *partition-of-unity* concept [70, 5]. It is attractive since it offers the possibility to incorporate arbitrary functions into the finite element Ansatz space, i.e., discontinuous functions representing displacement jumps render an admissible option. In a two-dimensional setting, such a procedure has successfully been adopted for constant-strain elements [128]; generalization to three dimensions, however, proves complex. Moreover, the approach does not seem to be easily extended to a high-order finite element framework. Nevertheless, the appealing option of completely mesh independent simulation of deformation localization and failure justifies further research efforts in this direction.

Appendix A

The Dirac-delta distribution

The Dirac-delta function is sometimes referred to as *unit impulse function*. It was introduced by the British theoretical physicist Paul Dirac. The Dirac-delta does not represent a function in a strict mathematical sense, in fact it is classified as a distribution.

In a one-dimensional setting the Dirac-delta can informally be thought of a function $\delta(x)$ that is infinite at $x = 0$ and adopts the value zero everywhere else, such that the total integral over the interval $(-\infty, +\infty)$ amounts to the value one (Figure A.1).

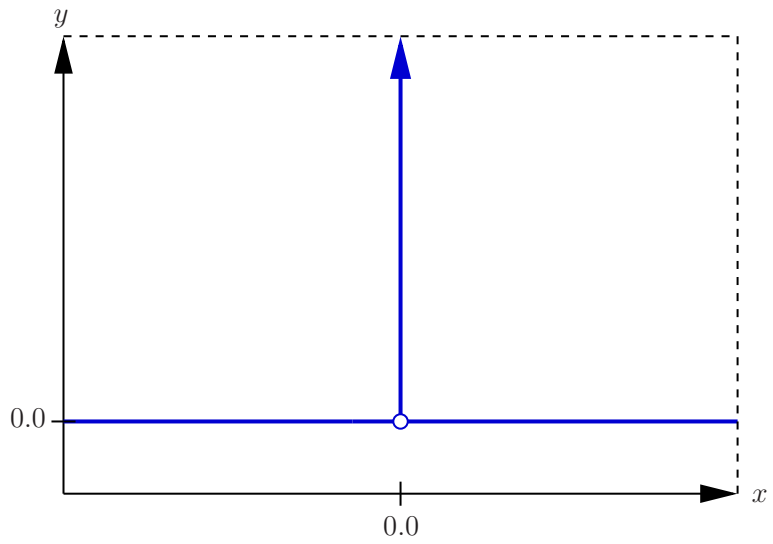

Figure A.1: Schematic representation of the Dirac-delta distribution.

More formally, the Dirac-delta is introduced by the property

$$\int_{-\infty}^{+\infty} f(x)\,\delta x\,dx := f(0) \tag{A.1}$$

for any continuous function $f(x)$.

Extending this property to three dimensions yields

$$\int_{\Omega} f(\boldsymbol{X}) \underbrace{\delta\left(\boldsymbol{X}-\boldsymbol{X}_{\mathrm{s}}\right)}_{=:\delta_{\mathrm{s}}} \, dV := \int_{\partial_{\mathrm{s}}\Omega} f(\boldsymbol{X}) \, dA \,, \tag{A.2}$$

where $\boldsymbol{X}_{\mathrm{s}} \in \partial_{\mathrm{s}}\Omega$.

Appendix B

The blending function method

B.1 Mapping for quadrilateral elements

Edge terms for the quadrilateral element depicted in Figure 3.8:

$$\begin{aligned}
\mathbf{e}_1(\xi,\eta) &= \left[\mathbf{E}_1(\xi) - \frac{(1-\xi)\mathbf{X}_1 + (1+\xi)\mathbf{X}_2}{2}\right]\left(\frac{1-\eta}{2}\right) \\
\mathbf{e}_2(\xi,\eta) &= \left[\mathbf{E}_2(\eta) - \frac{(1-\eta)\mathbf{X}_2 + (1+\eta)\mathbf{X}_3}{2}\right]\left(\frac{1+\xi}{2}\right) \\
\mathbf{e}_3(\xi,\eta) &= \left[\mathbf{E}_3(\xi) - \frac{(1-\xi)\mathbf{X}_4 + (1+\xi)\mathbf{X}_3}{2}\right]\left(\frac{1+\eta}{2}\right) \\
\mathbf{e}_4(\xi,\eta) &= \left[\mathbf{E}_4(\eta) - \frac{(1-\eta)\mathbf{X}_1 + (1+\eta)\mathbf{X}_4}{2}\right]\left(\frac{1-\xi}{2}\right)
\end{aligned} \tag{B.1}$$

B.2 Mapping for hexahedral elements

Edge and face terms for the hexahedral element depicted in Figure 3.9:

B.2.1 Edge terms according to [63]

$$\mathbf{e}_1(\xi,\eta,\zeta) = \left[\mathbf{E}_1(\xi) - \frac{(1-\xi)\mathbf{X}_1 + (1+\xi)\mathbf{X}_2}{2}\right]\left(\frac{1-\eta}{2}\right)\left(\frac{1-\zeta}{2}\right)$$

$$
\begin{aligned}
\mathbf{e}_2(\xi,\eta,\zeta) = &\quad \left[\mathbf{E}_2(\eta) - \frac{(1-\eta)\mathbf{X}_2 + (1+\eta)\mathbf{X}_3}{2}\right]\left(\frac{1+\xi}{2}\right)\left(\frac{1-\zeta}{2}\right)\\
\mathbf{e}_3(\xi,\eta,\zeta) = &\quad \left[\mathbf{E}_3(\xi) - \frac{(1-\xi)\mathbf{X}_4 + (1+\xi)\mathbf{X}_3}{2}\right]\left(\frac{1+\eta}{2}\right)\left(\frac{1-\zeta}{2}\right)\\
\mathbf{e}_4(\xi,\eta,\zeta) = &\quad \left[\mathbf{E}_4(\eta) - \frac{(1-\eta)\mathbf{X}_1 + (1+\eta)\mathbf{X}_4}{2}\right]\left(\frac{1-\xi}{2}\right)\left(\frac{1-\zeta}{2}\right)\\
\mathbf{e}_5(\xi,\eta,\zeta) = &\quad \left[\mathbf{E}_5(\zeta) - \frac{(1-\zeta)\mathbf{X}_1 + (1+\zeta)\mathbf{X}_5}{2}\right]\left(\frac{1-\xi}{2}\right)\left(\frac{1-\eta}{2}\right)\\
\mathbf{e}_6(\xi,\eta,\zeta) = &\quad \left[\mathbf{E}_6(\zeta) - \frac{(1-\zeta)\mathbf{X}_2 + (1+\zeta)\mathbf{X}_6}{2}\right]\left(\frac{1+\xi}{2}\right)\left(\frac{1-\eta}{2}\right)\\
\mathbf{e}_7(\xi,\eta,\zeta) = &\quad \left[\mathbf{E}_7(\zeta) - \frac{(1-\zeta)\mathbf{X}_3 + (1+\zeta)\mathbf{X}_7}{2}\right]\left(\frac{1+\xi}{2}\right)\left(\frac{1+\eta}{2}\right)\\
\mathbf{e}_8(\xi,\eta,\zeta) = &\quad \left[\mathbf{E}_8(\zeta) - \frac{(1-\zeta)\mathbf{X}_4 + (1+\zeta)\mathbf{X}_8}{2}\right]\left(\frac{1-\xi}{2}\right)\left(\frac{1+\eta}{2}\right)\\
\mathbf{e}_9(\xi,\eta,\zeta) = &\quad \left[\mathbf{E}_9(\xi) - \frac{(1-\xi)\mathbf{X}_5 + (1+\xi)\mathbf{X}_6}{2}\right]\left(\frac{1-\eta}{2}\right)\left(\frac{1+\zeta}{2}\right)\\
\mathbf{e}_{10}(\xi,\eta,\zeta) = &\quad \left[\mathbf{E}_{10}(\eta) - \frac{(1-\eta)\mathbf{X}_6 + (1+\eta)\mathbf{X}_7}{2}\right]\left(\frac{1+\xi}{2}\right)\left(\frac{1+\zeta}{2}\right)\\
\mathbf{e}_{11}(\xi,\eta,\zeta) = &\quad \left[\mathbf{E}_{11}(\xi) - \frac{(1-\xi)\mathbf{X}_8 + (1+\xi)\mathbf{X}_7}{2}\right]\left(\frac{1+\eta}{2}\right)\left(\frac{1+\zeta}{2}\right)\\
\mathbf{e}_{12}(\xi,\eta,\zeta) = &\quad \left[\mathbf{E}_{12}(\eta) - \frac{(1-\eta)\mathbf{X}_5 + (1+\eta)\mathbf{X}_8}{2}\right]\left(\frac{1-\xi}{2}\right)\left(\frac{1+\zeta}{2}\right)
\end{aligned}
\tag{B.2}
$$

B.2.2 Face terms according to [63]

$$
\begin{aligned}
\mathbf{f}_1(\xi,\eta,\zeta) = &\left[\mathbf{F}_1(\xi,\,\eta) - \frac{1}{4}\Big[(1-\xi)(1-\eta)\mathbf{X}_1 + (1+\xi)(1-\eta)\mathbf{X}_2 + \right.\\
&\left.(1+\xi)(1+\eta)\mathbf{X}_3 + (1-\xi)(1+\eta)\mathbf{X}_4\Big]\right]\left(\frac{1-\zeta}{2}\right)\\
\mathbf{f}_2(\xi,\eta,\zeta) = &\left[\mathbf{F}_2(\xi,\,\zeta) - \frac{1}{4}\Big[(1-\xi)(1-\zeta)\mathbf{X}_1 + (1+\xi)(1-\zeta)\mathbf{X}_2 + \right.\\
&\left.(1+\xi)(1+\zeta)\mathbf{X}_6 + (1-\xi)(1+\zeta)\mathbf{X}_5\Big]\right]\left(\frac{1-\eta}{2}\right)
\end{aligned}
$$

$$
\begin{aligned}
\mathbf{f}_3(\xi,\eta,\zeta) = \Big[\mathbf{F}_3(\eta,\,\zeta) - \; & \frac{1}{4}\Big[(1-\eta)(1-\zeta)\mathbf{X}_2 + (1+\eta)(1-\zeta)\mathbf{X}_3 + \\
& (1+\eta)(1+\zeta)\mathbf{X}_7 + (1-\eta)(1+\zeta)\mathbf{X}_6\Big]\Big]\left(\frac{1+\xi}{2}\right) \\
\mathbf{f}_4(\xi,\eta,\zeta) = \Big[\mathbf{F}_4(\xi,\,\zeta) - \; & \frac{1}{4}\Big[(1-\xi)(1-\zeta)\mathbf{X}_4 + (1+\xi)(1-\zeta)\mathbf{X}_3 + \\
& (1+\xi)(1+\zeta)\mathbf{X}_7 + (1-\xi)(1+\zeta)\mathbf{X}_8)\Big]\Big]\left(\frac{1+\eta}{2}\right) \\
\mathbf{f}_5(\xi,\eta,\zeta) = \Big[\mathbf{F}_5(\eta,\,\zeta) - \; & \frac{1}{4}\Big[(1-\eta)(1-\zeta)\mathbf{X}_1 + (1+\eta)(1-\zeta)\mathbf{X}_4 + \\
& (1+\eta)(1+\zeta)\mathbf{X}_8 + (1-\eta)(1+\zeta)\mathbf{X}_5\Big]\Big]\left(\frac{1-\xi}{2}\right) \\
\mathbf{f}_6(\xi,\eta,\zeta) = \Big[\mathbf{F}_6(\xi,\,\eta) - \; & \frac{1}{4}\Big[(1-\xi)(1-\eta)\mathbf{X}_5 + (1+\xi)(1-\eta)\mathbf{X}_6 + \\
& (1+\xi)(1+\eta)\mathbf{X}_7 + (1-\xi)(1+\eta)\mathbf{X}_8\Big]\Big]\left(\frac{1+\zeta}{2}\right)
\end{aligned}
\tag{B.3}
$$

Bibliography

[1] U. Andelfinger. *Untersuchungen zur Zuverlässigkeit hybrid-gemischter Finiter Elemente für Flächentragwerke*. PhD thesis, Universtät Stuttgart, 1991.

[2] F. Armero. Localized anisotropic damage of brittle materials. In D.R.J. Owen, E. Oñate, and E. Hinton, editors, *Computational plasticity: Fundamentals and applications*, pages 635–640, 1997.

[3] F. Armero. Large-scale modeling of localized dissipative mechanisms in a local continuum: applications to the numerical simulation of strain localization in rate-dependent inelastic solids. *Mechanics of Cohesive-frictional Materials*, 4:101–131, 1999.

[4] F. Armero and K. Garikipati. Recent advances in the analysis and numerical simulation of strain localization in inelastic solids. In D.R.J. Owen, E. Oñate, and E. Hinton, editors, *Proceedings of the 4th International Conference on Computational Plasticity, COMPLAS IV*, volume 1, pages 547–561, 1995.

[5] I. Babuška and J.M. Melenk. The partition of unity method. *International Journal for Numerical Methods in Engineering*, 40:727–758, 1997.

[6] I. Babuška and T. Strouboulis. *The finite element method and its reliability*. Oxford University Press, 2001.

[7] Z.P. Bažant and L. Cedolin. *Stability of structures*. Oxford University Press, 1991.

[8] Z.P. Bažant and F.-B. Lin. Nonlocal smeared cracking model for concrete fracture. *Journal of structural engineering*, 114:2493–2510, 1988.

[9] Z.P. Bažant and G. Pijaudier-Cabot. Nonlocal damage, localization, instability and convergence. *Journal of Applied Mechanics*, 55:287–293, 1988.

[10] T. Belytschko, J. Fish, and B.E. Engelmann. A finite element with embedded localization zones. *Computer Methods in Applied Mechanics and Engineering*, 70:59–89, 1988.

[11] T. Belytschko, W.K. Lui, and B. Moran. *Nonlinear Finite Elements for Continua and Structures*. Wiley, 2000.

[12] M. Bischoff. Advanced Finite Element Methods. Lecture-Notes, Lehrstuhl für Statik, Technische Universität München, 2005.

[13] K.-U. Bletzinger. *Formoptimierung von Flächentragwerken*. PhD thesis, Institut für Baustatik der Universität Stuttgart, 1990.

[14] G. Bolzon and A. Corigliano. An interface variables formulation for embedded-cack finite elements. In D.R.J. Owen, E. Oñate, and E. Hinton, editors, *Computational plasticity: Fundamentals and applications*, Proc. COMPLAS V, pages 1617–1624, International Center for Numerical Methods in Engineering, Barcelona, 1997.

[15] J. Bonet and R.D. Wood. *Nonlinear continuum mechanics for finite element analysis*. Cambridge University Press, New York, 1997.

[16] R.I. Borja. A finite element model for strain localization analysis of strongly discontinuous fields based on standard galerkin approximation. *Computer Methods in Applied Mechanics and Engineering*, 190:1529–1549, 2000.

[17] R.I. Borja and A.R. Regueiro. Strain localization in frictional materials exhibiting displacement jumps. *Computer Methods in Applied Mechanics and Engineering*, 190:2555–2580, 2001.

[18] H. Bröker. *Integration von geometrischer Modellierung und Berechnung nach der p-Version der FEM*. PhD thesis, Lehrstuhl für Bauinformatik, Fakultät für Bauingenieur- und Vermessungswesen, Technische Universität München, 2001.

[19] C.G. Broyden. The Convergence of a Class of Double Rank Minimization Algorithms: Parts I and II. *Journal of the Institute of Mathematics and Its Applications*, 6:76–90, 222–231, 1970.

[20] Q. Chen and I. Babuška. Approximate optimal points for polynomial interpolation of real functions in an interval and in a triangle. *Computer Methods in Applied Mechanics and Engineering*, 128:405–417, 1995.

[21] E. Cosserat and F. Cosserat. *Theorie des Corps Deformables*. Herman et fils, Paris, 1909.

[22] M.A. Crisfield. A fast Incremental/Iterative Solution Procedure that Handles "Snap-Through". *Computers & Structures*, 13:55–62, 1981.

[23] M.A. Crisfield. *Non-linear finite element analysis of solids and structures*, volume 1. John Wiley & Sons, 1991.

[24] M.A. Crisfield. *Non-linear finite element analysis of solids and structures*, volume 2. John Wiley & Sons, 2003.

[25] G.A. D'Adetta. *Discrete Models for Cohesive Frictional Materials*. PhD thesis, Institut für Baustatik der Universtät Stuttgart, 2004.

[26] R. de Borst. *Non-linear analysis of frictional materials*. PhD thesis, Technical University Delft, 1986.

[27] R. de Borst. Simulation of strain localization: A reappraisal of the cosserat continuum. *Engineering Computations*, 8:317–332, 1991.

[28] R. de Borst. Some recent issues in computational mechanics. *International Journal for Numerical Methods in Engineering*, 52:63–95, 2001.

[29] R. de Borst and H.B. Mühlhaus. Gradient-dependent plasticity: Formulation and algorithmic aspects. *International Journal for Numerical Methods in Engineering*, 35:521–539, 1992.

[30] L. Demkowicz. Finite Element Methods for Maxwell Equations. In E. Stein, R. de Borst, and T.J.R. Hughes, editors, *Encyclopedia of Computational Mechanics*, pages 723–737. John Wiley & Sons, 2004.

[31] L. Demkowicz. *Computing with hp-Adaptive Finite Elements (Preprint)*, volume 1: One- and Two-Dimensional Elliptic and Maxwell Problems. Taylor & Francis, 2005.

[32] Comité Euro-International du Béton. *CEB-FIP Model Code 90*. Thomas Telford Services Ltd., London, 1993.

[33] A. Düster. *High order finite elements for three-dimensional, thin-walled nonlinear continua*. PhD thesis, Lehrstuhl für Bauinformatik, Fakultät für Bauingenieur- und Vermessungswesen, Technische Universität München, http://www.inf.bv.tum.de/~ duester, 2001.

[34] A. Düster, H. Bröker, H. Heidkamp, U. Heißerer, S. Kollmannsberger, R. Krause, A. Muthler, A. Niggl, V. Nübel, M. Rücker, and D. Scholz. *AdhoC^4 – User's Guide*. Lehrstuhl für Bauinformatik, Technische Universität München, 2004.

[35] A. Düster, H. Bröker, and E. Rank. The p-version of the finite element method for three-dimensional curved thin walled structures. *International Journal for Numerical Methods in Engineering*, 52:673–703, 2001.

[36] A. Düster, A. Niggl, V. Nübel, and E. Rank. A numerical investigation of high-order finite elements for problems of elasto-plasticity. *Journal of Scientific Computing*, 17:429–437, 2002.

[37] A. Düster and E. Rank. The p-version of the finite element method compared to an adaptive h-version for the deformation theory of plasticity. *Computer Methods in Applied Mechanics and Engineering*, 190:1925–1935, 2001.

[38] A. Düster and E. Rank. A p-version finite element approach for two- and three-dimensional problems of the J_2 flow theory with non-linear isotropic hardening. *International Journal for Numerical Methods in Engineering*, 53:49–63, 2002.

[39] E.N. Dvorkin, A.M. Cuitiño, and G. Gioia. Finite elements with displacement interpolated embedded localization lines insensitive to mesh size and distortions. *International Journal for Numerical Methods in Engineering*, 30:541–564, 1990.

[40] W. Ehlers and W. Volk. Cosserat-Theorie für gesättigte poröse Festkörper. *Zeitschrift für Angewandte Mathematik und Mechanik*, 77:83–84, 1997.

[41] C. Feist. *A Numerical Model for Cracking of Plain Concrete Based on the Strong Discontinuity Approach*. PhD thesis, Institut für Baustatik, Festigkeitslehre und Tragwerkslehre, Universität Innsbruck, 2004.

[42] R. Fletcher. A New Approach to Variable Metric Algorithms. *Computer Journal*, 13:317–322, 1970.

[43] K. Garikipati. *On strong discontinuities in inelastic solids and their numerical simulation*. PhD thesis, Stanford University, 1996.

[44] D. Goldfarb. A Family of Variable Metric Methods Derived by Variational Means. *Mathematics of Computation*, 24:23–26, 1970.

[45] W.J. Gordon and Ch.A. Hall. Construction of curvilinear co-ordinate systems and applications to mesh generation. *International Journal for Numerical Methods in Engineering*, 7:461–477, 1973.

[46] W.J. Gordon and Ch.A. Hall. Transfinite element methods: Blending function interpolation over arbitrary curved element domains. *Numerische Mathematik*, 21:109–129, 1973.

[47] J. Hadamard. *Lecon sur la Propagation des Ondes*. Herman et Fils, Paris, 1903.

[48] R. Hill. A general theory of uniqueness and stability in elastic-plastic solids. *Journal of the Mechanics and Physics of Solids*, 6:236–249, 1958.

[49] A. Hillerborg, M. Modeer, and P.E. Petersson. Analysis of crack formation and crack growth in concrete by means of fracture mechanics and finite elements. *Cement and Concrete Research*, 6:773–782, 1976.

[50] H.C. Hu. On some variational principles in the theory of elasticity and plasticity. *Scintia Sinica*, 4:33–54, 1955.

[51] M. Jirásek. Numerical Modeling of Deformation and Failure of Materials. Lecture-Notes, 1999.

[52] M. Jirásek. Comparative study on finite elements with embedded discontinuities. *Computer Methods in Applied Mechanics and Engineering*, 188:307–330, 2000.

[53] M. Jirásek. Conditions of uniqueness for finite elements with embedded cracks. In E. Oñate, G. Bugeda, and B. Suárez, editors, *Proceedings of the European Congress of Computational Methods in Applied Sciences and Engineering, ECCOMAS*, 2000.

[54] M. Jirásek. Objective modeling of strain localization. *Revue française de génie civil*, 6:1119–1132, 2002.

[55] M. Jirásek and Z.P. Bažant. *Inelastic Analysis of Structures*. John Wiley & Sons, 2002.

[56] M. Jirásek and T. Belytschko. Computational resolution of strong discontinuities. In H.A. Mang, F.G. Rammerstorfer, and J. Eberhardsteiner, editors, *Proceedings of the Fifth World Congress on Computational Mechanics, WCCM V*, 2002.

[57] M. Jirásek and S. Rolshoven. Comparison of integral-type nonlocal plasticity models for strain-softening materials. *International journal of engineering science*, 41:1553–1602, 2003.

[58] M. Jirásek and T. Zimmermann. Analysis of rotating crack model. *Journal of Engineering Mechanics (ASCE)*, 124:842–851, 1998.

[59] M. Jirásek and T. Zimmermann. Rotating crack model with transition to scalar damage. *Journal of Engineering Mechanics (ASCE)*, 124:277–284, 1998.

[60] M. Jirásek and T. Zimmermann. Embedded crack model: Part I: Basic formulation, Part II: Combination with smeared cracks. *International Journal for Numerical Methods in Engineering*, 50:1269–1305, 2001.

[61] C. Johnson. Existence theorems for plasticity problems. *Journal de Mathematiques Pures et Appliquées*, 55:431–444, 1976.

[62] C. Johnson and R. Scott. A finite element method for problems in perfect plasticity using discontinuous trial functions. In W. Wunderlich, E. Stein, and K.J. Bathe, editors, *Nonlinear finite element analysis in structural mechanics*, pages 307–324. 1981.

[63] G. Királyfalvi and B.A. Szabó. Quasi-regional mapping for the p-version of the finite element method. *Finite Elements in Analysis and Design*, 27:85–97, 1997.

[64] S. Klinkel and W. Wagner. A geometrical non-linear brick element based on the eas-method. *International Journal for Numerical Methods in Engineering*, 40:4529–4545, 1997.

[65] M. Klisinski, K. Runesson, and S. Sture. Finite element with inner softening band. *Journal of Engineering Mechanics (ASCE)*, 117(3):575–587, 1991.

[66] R. Lackner. *Adaptive finite element analysis of reinforced concrete plates and shells.* PhD thesis, Institut für Festigkeitslehre, Technische Universität Wien, 1999.

[67] D.G. Luenberger. *Linear and Nonlinear Programming.* Springer, 2nd edition, 2005.

[68] J. Mandel. Conditions de stabilité et postulat de drucker. In *Proceedings of the IUTAM Symposium on Rheology and Soil Mechanics*, pages 58–68. Springer, Berlin, 1966.

[69] H. Matthies, G. Strang, and E. Christiansen. The saddle point of a differential program. In Glowinski, Robin, and Zienkiewicz, editors, *Energy methods in finite element analysis*, pages 309–318. John Wiley & Sons, London, 1979.

[70] J.M. Melenk and I. Babuška. The partition of unity finite element method: Basic theory and applications. *Computer Methods in Applied Mechanics and Engineering*, 139:289–314, 1996.

[71] G. Meschke. An anisotropic elatoplastic-damage model for plain concrete. *International Journal for Numerical Methods in Engineering*, 42:703–727, 1998.

[72] C. Miehe. *Kanonische Modelle multiplikativer Elasto-Plastizität. Thermodynamische Formulierung und numerische Implementation.* Postdoctoral thesis, Institut für Baumechanik und Numerische Mechanik, Universität Hannover, 1993.

[73] N. Moës, J. Dolbow, and T. Belytschko. A finite element method for crack growth without remeshing. *International Journal for Numerical Methods in Engineering*, 64:131–150, 1999.

[74] M. Mooney. A theory of large elastic deformations. *Journal of Applied Mechanics*, 11:582–592, 1940.

[75] J. Mosler. *Finite Elemente mit sprungstetigen Abbildungen des Verschiebungsfeldes für numerische Analysen lokalisierter Versagenszustände in Tragwerken.* PhD thesis, Lehrstuhl für Statik und Dynamik, Fakultät für Bauingenieurwesen, Ruhr-Universität Bochum, 2002.

[76] J. Mosler. On advanced solution strategies to overcome locking effects in strong discontinuity settings. *International Journal for Numerical Methods in Engineering*, 63:1313–1341, 2005.

[77] J. Mosler and G. Meschke. 3D FE analysis of cracks by means of the strong discontinuity approach. In E. Oñate, G. Bugeda, and B. Suárez, editors, *Proceedings of the European Congress of Computational Methods in Applied Sciences and Engineering, ECCOMAS*, 2000.

[78] J. Mosler and G. Meschke. Analysis of mode-I failure in brittle materials using the strong discontinuity approach with higher order elements. In *Proceedings of the 2nd European Conference on Computational Mechanics, ECCM*, 2001.

[79] J. Mosler and G. Meschke. An elasto-plastic damage model for quasi-brittle materials in the framework of the strong discontinuity approach. In *Proceedings of the 4th International Conference on Fracture Mechanics of Concrete and Concrete Structures*, pages 817–822, 2001.

[80] J. Mosler and G. Meschke. 3D modeling of strong discontinuities in elastoplastic solids: Fixed and rotating localization formulations. *International Journal for Numerical Methods in Engineering*, 57:1553–1576, 2003.

[81] H.B. Mühlhaus and E.C. Aifantis. A variational principle for gradient plasticity. *International Journal of Solids and Structures*, 28:845–857, 1991.

[82] A. Muthler. *Berechnung der elastischen Rückfederung von Tiefziehbauteilen mit der p-Version der Finite-Elemente-Methode.* PhD thesis, Lehrstuhl für Bauinformatik, Fakultät für Bauingenieur- und Vermessungswesen, Technische Universität München, 2005.

[83] A. Nádai. *Plasticity.* McGraw-Hill, New York, 1931.

[84] V. Nübel. *Die adaptive rp-Methode für elastoplastische Probleme.* PhD thesis, Lehrstuhl für Bauinformatik, Technische Universität München, 2005.

[85] R.W. Ogden. Large Deformation Isotropic Elasticity — On the Correlation of Theory and Experiment for Incompressible Rubberlike Solids. *Proceedings of the Royal Society London*, A326:565–584, 1972.

[86] J. Oliver. A consistent characteristic length for smeared cracking models. *International Journal for Numerical Methods in Engineering*, 28:461–474, 1989.

[87] J. Oliver. Continuum modelling of strong discontinuities in solid mechanics using damage models. *Computational Mechanics*, 17(1-2):49–61, 1995.

[88] J. Oliver. Modelling strong discontinuities in solid mechanics via strain softening constitutive equations part 1: Fundamentals. part 2: Numerical simulations. *International Journal for Numerical Methods in Engineering*, 39:3575–3623, 1996.

[89] J. Oliver, A. Huespe, M.D.G. Pulido, and S. Blanco. Computational modeling of cracking of concrete in strong discontinuity settings. *Computers and Concrete*, 1:61–76, 2004.

[90] J. Oliver, A. Huespe, and E. Samaniego. A study of finite elements for capturing strong discontinuities. *International Journal for Numerical Methods in Engineering*, 56:2135–2161, 2003.

[91] J. Oliver, A.E. Huespe, E. Samaniego, and E.W.V. Chaves. On strategies for tracking strong discontinuities in computational failure mechanics. In H.A. Mang, F.G. Rammerstorfer, and J. Eberhardsteiner, editors, *Proceedings of the Fifth World Congress on Computational Mechanics, WCCM V*, 2002.

[92] M. Ortiz, Y. Leroy, and A. Needleman. A finte element method for localized failure analysis. *Computer Methods in Applied Mechanics and Engineering*, 61:189–214, 1987.

[93] M. Ortiz and J.B. Martin. Symmetry-preserving return mapping algorithms and incrementally extremal paths: A unification of concepts. *International Journal for Numerical Methods in Engineering*, 28:1839–1853, 1989.

[94] S. Pietruszczak and Z. Mroź. Finite element analysis of deformation of strain-softening materials. *International Journal for Numerical Methods in Engineering*, 17:327–334, 1981.

[95] G. Pijaudier-Cabot and Z.P. Bažant. Nonlocal damage theory. *Journal of Engineering Mechanics (ASCE)*, 113:1512–1533, 1987.

[96] E. Rank, H. Bröker, A. Düster, R. Krause, and M. Rücker. The p-version of the finite element method for structural problems. In E. Stein, editor, *Error-controlled Adaptive Finite Elements in Solid Mechanics*, pages 263–307. John Wiley & Sons, 2002.

[97] E. Rank and A. Düster. h- versus p-version finite element analysis for J_2 flow theory. In *Proceedings of the First M.I.T Conference on Computational Fluid and Solid Mechanics*, Cambridge, USA, 2001.

[98] E. Rank, A. Düster, V. Nübel, K. Preusch, and O.T. Bruhns. High order finite elements for shells. *submitted to Computer Methods in Applied Mechanics and Engineering*, 2003.

[99] E. Rank, A. Düster, V. Nübel, K. Preusch, and O.T. Bruhns. High order finite elements for shells. *Computer Methods in Applied Mechanics and Engineering*, 194:2494–2512, 2005.

[100] A.R. Regueiro and R.I. Borja. A finite element model of localized deformation in frictional materials taking a strong discontinuity approach. *Finite Elements in Analysis and Design*, 33:283–315, 1999.

[101] J.R. Rice and J.W. Rudnicki. A note on some features of the theory of localization of deformation. *International Journal of Solids and Structures*, 16:597–605, 1980.

[102] R.S. Rivlin. Large Elastic Deformations of Isotropic Materials. IV. Further Developments of the General Theory. *Philosophical Transactions of the Royal Society London*, A241:379–397, 1948.

[103] S. Rolshoven and M. Jirásek. Nonlocal formulations of softening plasticity. In H.A. Mang, F.G. Rammerstorfer, and J. Eberhardsteiner, editors, *Proceedings of the Fifth World Congress on Computational Mechanics, WCCM V*, 2002.

[104] J.W. Rudnicki and J.R. Rice. Conditions for localization of deformation in pressure-sensitive dilatant materials. *Journal of the Mechanics and Physics of Solids*, 23:371–394, 1975.

[105] E. Samaniego. *Contributions to the Continuum Modelling of Strong Discontinuities in Two-dimensional Solids*. PhD thesis, UPC Barcelona, 2003.

[106] J.M. Sancho, J. Planas, D.A. Cendón, and J. Gálvez. On the need of crack path continuity in the simulation of concrete fracture using embedded crack elements. In *Proceedings of the EUROMECH Colloquium 460, Numerical Modelling of Concrete Cracking*, 2005.

[107] J.M. Sancho, J. Planas, J. Gálvez, D.A. Cendón, and A. Fathy. Three-dimensional simulation of concrete fracture using embedded crack elements without enforcing crack path continuity. In D.R.J. Owen and E. Oñate, editors, *Proceedings of the 8th International Conference on Computational Plasticity, COMPLAS VIII*, 2005.

[108] J.M. Sancho, J. Planas, J. Gálvez, E. Reyes, and D.A. Cendón. An embedded cohesive crack model for finite element analysis of mixed mode fracture of concrete. *Fatigue & Facture of Engineering Materials & Structures*, 29:1056–1065, 2006.

[109] H.R. Schwarz. *Numerische Mathematik*. B.G. Teubner, 4th edition, 1997.

[110] K. Schweizerhof. *Nichtlineare Berechnung von Tragwerken unter verformungsabhängiger Belastung mit finiten Elementen*. PhD thesis, Institut für Baustatik der Universität Stuttgart, 1982.

[111] D.F. Shanno. Conditioning of Quasi-Newton Methods for Function Minimization. *Mathematics of Computation*, 24:647–656, 1970.

[112] J.C. Simo and F. Armero. Geometrically non-linear enhanced strain mixed methods and the method of incompatible modes. *International Journal for Numerical Methods in Engineering*, 33:1413–1449, 1992.

[113] J.C. Simo and T.J.R. Hughes. On variational foundations of assumed strain methods. *Journal of Applied Mechanics*, 53:51–54, 1986.

[114] J.C. Simo and T.J.R. Hughes. *Computational Inelasticity*. Springer-Verlag, New York, 1998.

[115] J.C. Simo and J. Oliver. A new approach to the analysis and simulation of strain softening in solids. In Z.P. Bažant, Z. Bittnar, M. Jirásek, and J. Mazars, editors, *Fracture and Damage in Quasibrittle Structures*, pages 25–39. E. & F.N. Spon, London, 1994.

[116] J.C. Simo, J. Oliver, and F. Armero. An analysis of strong discontinuities induced by strain softening in rate-independent inelastic solids. *Computational Mechanics*, 12:277–296, 1993.

[117] J.C. Simo and M.S. Rifai. A class of mixed assumed strain methods and the method of incompatible modes. *International Journal for Numerical Methods in Engineering*, 29:1595–1638, 1990.

[118] J.C. Simo and R.L. Taylor. Consistent tangent operators for rate independent elastoplasticity. *Computer Methods in Applied Mechanics and Engineering*, 48:101–118, 1985.

[119] E. Stein. *Progress in computational analysis of inelastic structures*. Springer, 1993.

[120] P. Steinmann and K.J. Willam. Localization within the framework of micropolar elastoplasticity. In V. Mannl, J. Najar, and O. Brüller, editors, *Advances in continuum mechanics*, pages 296–313. Springer, Berlin-Heidelberg, 1991.

[121] B.A. Szabó and I. Babuška. *Finite element analysis*. John Wiley & Sons, 1991.

[122] B.A. Szabó, A. Düster, and E. Rank. The p-version of the Finite Element Method. In E. Stein, R. de Borst, and T.J.R. Hughes, editors, *Encyclopedia of Computational Mechanics*, volume 1, chapter 5, pages 119–139. John Wiley & Sons, 2004.

[123] Y. Thomas. *Plastic Flow and Fracture of Solids*. Academic Press, New-York, 1961.

[124] C. Truesdell and W. Noll. *The non-linear field theories of mechanics*. Springer, 3rd edition, 2004.

[125] W. Volk. *Cosserat-Theorie für gesättigte poröse Festkörper*. PhD thesis, Institut für Mechanik (Bauwesen), Universität Stuttgart, 1999.

[126] W.A. Wall, M. Bischoff, and E. Ramm. A deformation dependent stabilization technique, exemplified by EAS elements at large strains. *Computer Methods in Applied Mechanics and Engineering*, 188:859–871, 2000.

[127] K. Washizu. On the variational principles of elasticity and plasticity. Technical Report 25-18, Aeroelastic and Structures Reserach Laboratory, MIT Press, Cambridge, 1955.

[128] G.N. Wells. *Discontinuous modelling of strain localisation and failure*. PhD thesis, Technical University Delft, 2001.

[129] G.N. Wells and L.J. Sluys. A new method for modelling cohesive cracks using finite elements. *International Journal for Numerical Methods in Engineering*, 50:2667–2682, 2001.

[130] G.N. Wells and L.J. Sluys. Three-dimensional embedded discontinuity model for brittle fracture. *International Journal of Solids and Structures*, 38:897–913, 2001.

[131] B.J. Winkler. *Traglastuntersuchungen von unbewehrten und bewehrten Betonstrukturen auf der Grundlage eines objektiven Werkstoffgesetzes für Beton.* PhD thesis, Innsbruck University Press, 2001.

[132] P. Wriggers. *Nichtlineare Finite-Element Methoden.* Springer-Verlag, 2001.

[133] P. Wriggers. *Computational Contact Mechanics.* John Wiley & Sons, 2002.

[134] C.R. Wylie and L.C. Barret. *Advanced engineering mathematics.* McGraw-Hill Inc., 1995.

[135] O.C. Zienkiewicz and R.L. Taylor. *The Finite Element Method – Solid Mechanics*, volume 2. Butterworth-Heinemann, 5th edition, 2000.